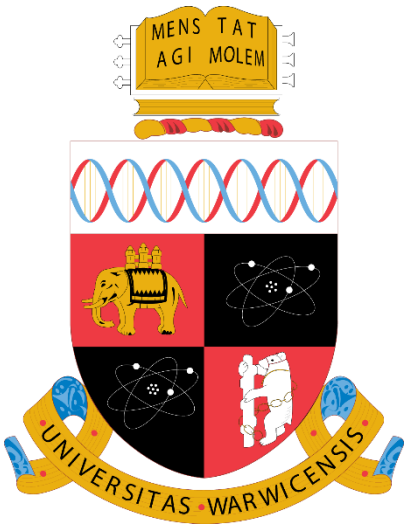

Characterising molecular self-assembly using high-resolution ^{1}H solid-state NMR spectroscopy

by

Aiden James Robertson

Thesis

Submitted to the University of Warwick

for the degree of

Doctor of Philosophy

Department of Physics

June 2016

Contents

List of Tables

List of Figures

Acknowledgements

First and foremost I would like to thank Professor Steven Brown, not only for his constant support and advice over the course of this project, but for giving me the opportunity to travel, at home and abroad, to many different places to present my research and attend workshops, and to my second supervisor, Dr Andrew Marsh for his support in the lab and the many discussions we have had around supramolecular chemistry. I would also like to thank Yusuke Nishiyama and Manoj Pandey at JEOL, Tokyo, for providing me with the opportunity to travel to Japan and to carry out experiments on their facilities, as well as allowing me access to their immeasurable expertise. Thanks also to Dr Dmytro Dudenko and Dr Stephen Day for helping me set things up during the dark early days of my adventure into the world of CASTEP (as well as answering my annoying questions), and to Dr Ann-Christin Pöppler for providing help and support with regards to GIPAW calculations as well as her time and energy in X-ray. Financial support from EPSRC is also gratefully acknowledged.

On a personal note, I would like to thank all the lost souls of the Warwick solid-state NMR group, who have made (for the most part) the last 3 ½ years thoroughly enjoyable, to my friends back home in Burnley, and to my family without whose love and support (and 2008-style financial bailouts) completion of this thesis would not have been possible.

Declarations

The work presented in this thesis is a result of my own original research carried out between October 2012 and April 2016, under the supervision of Professor Steven P. Brown and Dr Andrew Marsh at the University of Warwick. Where contributions of others are included, these are indicated within the text. This work has not been submitted as part of another degree. Chapter 7 presents work published by the author:

A. J. Robertson, M. K. Pandey, A. Marsh, Y. Nishiyama and S. P. Brown. The use of a selective saturation pulse to suppress t_1 noise in two-dimensional ^{1}H fast magic angle spinning solid-state NMR spectroscopy. *J. Magn. Reson*., 260, 89 (2015).

Abstract

Supramolecular chemistry, the domain of chemistry 'beyond the molecule', is finding increasing application in a diverse range of scientific fields. A key concept in this field, termed molecular self-assembly, has important applications ranging from nanotechnology to medicine, and refers to the intermolecular assembly of individual molecules *via* non-covalent forces, most importantly hydrogen bonding and $\pi - \pi$ stacking interactions. Specifically, this thesis considers the self-assembling arrangements of synthetic pyrimidine-based heterocyclic systems, which present guanine/cytosine DDA/AAD hydrogen bonding motifs. Characterisation of such systems is well documented in the liquid phase, but there exists a general paucity of solid-state analytical data for such materials. Owing to the inherent difficulty in crystallising these systems, typically due to disordered alkyl and aryl sidechains, high-resolution ^{1}H MAS NMR is uniquely placed to elucidate hydrogen bonding arrangements in these systems, given the sensitivity of the ^{1}H chemical shift to its local atomic environment. For cases where single-crystal X-ray structures can be obtained, a so-called NMR crystallographic approach can be used to complement the existing single-crystal X-ray data. By comparison of GIPAW calculated ^{1}H chemical shielding parameters to experimentally observed chemical shifts and, more specifically, through comparison of calculated shielding values for the full crystal versus the isolated molecule, an analysis of the strength of non-covalent phenomenon present in a given system can be presented.

This thesis applies fast MAS ^{1}H detected 2D NMR methods to a range of structural problems concerning pyrimidine-based synthetic organic molecules. Specifically, ^{1}H – ^{1}H DQ/SQ MAS, ^{14}N – ^{1}H HMQC and ^{1}H – ^{13}C techniques, such as the refocused INEPT and well-known CP MAS methods, are used, where applicable, in conjunction with GIPAW calculated NMR parameters to provide a comprehensive study of the solid-state packing arrangements of a series of guanine/cytosine synthetic derivatives which exhibit a diverse range of self-assembling architectures, including helical and stacking trimeric motifs. It is shown that, for crystalline compounds, confirmation of chemical shift assignments *via* the GIPAW method can be used to infer the structure of related systems for which diffraction data is not available, through comparison of the observed experimental NMR data. In addition, it is demonstrated that, for a series of pyrimidine and pyridopyrimidine intermediates which form non-crystalline powdered solids, high-resolution ^{1}H MAS NMR methods can be applied alone to elucidate likely hydrogen bonding motifs in the absence of crystallographic data, thereby allowing the observer to speculate on likely modes of self-assembly in the solid state. Interestingly, this study involves the relatively novel investigation (by means of solid-state NMR) of aldehyde and, in particular, oxime containing organic molecules, for which (in the case of the latter functional group) no published ^{1}H MAS NMR studies have been presented at the time of writing.

Finally, in collaboration with the spectrometer company JEOL, it is shown that a selective saturation pulse can be employed to supress excessive t_1 noise in two-dimensional ^{1}H MAS NMR spectra, at fast MAS frequencies. To demonstrate this effect, the intense methyl resonance of a synthetic nucleoside derivative is suppressed, whilst reduced spin diffusion rates at higher MAS frequencies ensure that the effect on nearby spins is minimised.

Abbreviations

AAD: acceptor/acceptor/donor (hydrogen bonding)

AHT: average Hamiltonian theory

BABA: back-to-back

BOC: *t*-butyloxycarbonyl

CD: circular dichroism

COSY: correlation spectroscopy

CP: cross polarisation

CRAMPS: combined rotation and multiple pulse spectroscopy

CSA: chemical shift anisotropy

CW: continuous wave

DDA: donor/donor/acceptor (hydrogen bonding)

DFT: density functional theory

DNA: deoxyribonucleic acid

DOR: double rotation (spectroscopy)

DOSY: diffusion-ordered spectroscopy

DRAMA: dipolar recoupling at the magic angle

DQ/DQC: double-quantum coherence

DUMBO: decoupling under mind boggling optimisation

EFG: electric field gradient

FID: free induction decay

FSLG: frequency switched Lee-Goldburg

FT: Fourier transform

GGA: generalised gradient approximation

GIPAW: gauge-including projector augmented wave

GPC: gel permeation chromatography

HMQC: heteronuclear multiple-quantum coherence

INEPT: insensitive nuclei enhanced by polarisation transfer

L: laboratory frame (of reference)

LDA: local density approximation

MAS: magic angle spinning

M/k/Hz: mega/kilo/hertz

MQC: multiple-quantum coherence

NMR: nuclear magnetic resonance

NOESY: nuclear Overhauser effect spectroscopy

PAS: principal axis system

PBE: Perdew-Burke-Ernzerhof (functional)

PFG: pulsed field gradient

PMLG: phase modulated Lee-Goldburg

POST-C7: permutationally offset stabilised-C7

2Q-HORROR: double-quantum homonuclear rotary resonance

R^3: rotary resonance recoupling

rf: radiofrequency

RFDR: radiofrequency driven recoupling

RNA: ribonucleic acid

SR4: supercycled R4

SQ/SQC: single-quantum coherence

T: Tesla

TIPS: triisopropylsilyl

TMS: trimethylsilyl

TPPI: two pulse phase incremented

TPPM: two pulse phase modulated

UV: ultra violet

WATERGATE: water suppression by gradient-tailored excitation

ZQ: zero-quantum

Chapter 1 : Thesis Introduction

1.1 Introduction

This project concerns itself with the structural elucidation of a range of synthetic analogues of the nucleobases guanine and cytosine, by means of high-resolution ^{1}H magic angle spinning (MAS) nuclear magnetic resonance (NMR) techniques. In section 1.2, a brief history of NMR and the development of modern day solid-state NMR is introduced, highlighting the significant and relevant advances in the field. Section 1.3 introduces the concepts and principles of molecular self-assembly, and discusses the suitability of solid-state NMR for the purposes of structural characterisation of such systems.

1.2 Introduction to solid-state NMR

The foundations of nuclear magnetic resonance (NMR) were first developed in the late 19th century, many decades before the first experiments were attempted. The discovery of the Zeeman effect, in which an optical spectral line can be split into several components in the presence of an external magnetic field, by the Dutch physicist Pieter Zeeman in 1896 (1902 Nobel Prize in Physics),(1) and the subsequent attempt to explain the phenomenon by Sir Joseph Larmor in 1897,(2) resulted in the introduction of two fundamental concepts: the Zeeman interaction and the Larmor frequency. The subsequent development of experimental NMR was a natural consequence of the evolution of the field of nuclear physics, which began in earnest with Rutherford's model of the atom in 1911. The model described a dense positive core, in which the majority of the particle's mass resided, surrounded by negative electrons. The subsequent discovery of the neutron by Sir James Chadwick, in 1932, was to directly influence Isidor Isaac Rabi who, in the late 1930s, observed for the first time the resonance effect of nuclear matter (1944 Nobel Prize in Physics).(3-5) These discoveries in the late 19th and early 20th centuries set the scene for over 70 years of progress in theoretical and experimental NMR. (Note, the first purely magnetic experiment concerning nuclear moments was actually performed in the Soviet Union in the late 1930's, in which the magnetic susceptibility of liquid hydrogen was measured).(6)

The first attempts to measure an NMR signal were made some years before Rabi's discovery, in 1936, by two scientists, Gorter and Broer. These experiments attempted, and failed, to measure the ^{7}Li signal in LiF and the ^{1}H signal in $KAl(SO_4)_2\ 12H_2O$. A further attempt was made in 1942, again to no avail.(7) Indeed it was not until the conclusion of the Second World War, and benefitting from the military technologies made during the conflict, that the first successful attempts to measure an NMR spectrum were made. The first solid and solution state spectra were published independently by two groups, those of Purcell (8) (Harvard) and Bloch (9-11) (Stanford) respectively. Both groups noted the importance of relaxation in their measurements (it is widely agreed that the 1936 and 1942 experiments of Gorter and Broer failed due to saturation of the NMR signal). Although not fully understood at the time, the two different methods employed by each group had actually described the two ways to understand NMR as a concept. Purcell's method was best described by quantum mechanics, whilst Bloch's method was more classical in nature, relying on the theory of electromagnetic induction. Both descriptions, as will be described in the next chapter, have their advantages (and disadvantages!). Purcell and Bloch were to

share the Nobel Prize for physics in 1952 *"for their development of new methods for nuclear magnetic precision measurements and discoveries in connection therewith".* One year later, inspired by these experiments, Rollin and Hatton reported the first low temperature NMR experiments, measuring both longitudinal (T_1) and transverse (T_2) relaxation times in solid hydrogen and other samples.(12) These seminal papers were to greatly influence subsequent developments in the field.

The power of the NMR method in elucidating the solid-state structure of materials derives from the form of the spatial dependence of the magnetic dipolar interaction:$(3\cos\theta - 1)r^{-3}$. The inverse cube dependence on the internuclear separation (r) means that near neighbour interactions dominate, hence it is possible to extract distance information from the appropriate NMR experiment. The importance of the dipolar coupling interaction, and hence the motivation for all high resolution ^{1}H solid-state NMR, was first described in 1948 by George Pake. In this classic experiment, performed on a single crystal of gypsum ($CaSO_4$ $2H_2O$) (due to well isolated proton pairs in the water molecules), the observed pair of doublets corresponded to the fact that each proton could 'observe' the two states of its coupled neighbour, up and down (with respect to the static field).(13) Expansion of his work to powdered samples lead to the famous Pake doublet pattern which arises from the fact that, over the whole sample volume, the microcrystals in the powder experience all possible orientations with respect to the applied magnetic field. Starting from these experiments, ^{1}H solid-state NMR has grown today into an extremely useful tool, especially in the last two decades, given the difficulty of determining proton positions with high accuracy in other high-resolution techniques, notably single-crystal X-ray diffraction. For instance, solid-state NMR is a particularly useful probe of hydrogen bonded systems, as will be demonstrated by the work presented in this thesis.

The true power of NMR however, namely the chemical shift, was not realised until 1951 when Arnold, Dharmatti and Packard observed the NMR spectrum of ethanol.(14) They observed three distinct resonances with height ratios of 1:2:3, which provided direct evidence for the first time of the CH_3CH_2OH formula. This discovery revolutionised NMR. No longer the occupation only of physicists, the technique started to attract chemists, biologists and the wider scientific community. With this increasing demand came more user-friendly set-ups, with the first commercial spectrometers (operating at a proton Larmor frequency of 30 MHz corresponding to a field of 0.7 T) becoming available in the 1950s. Further developments came in the 1960s and 1970s when the first superconducting magnets were designed.

During the same period, the traditional method of detection, continuous wave (CW) detection, which consisted of sweeping the magnetic field over a large range to acquire the signal, gave way to more time efficient pulsed NMR methods. This technique was heavily influenced by the accidental discovery in the late 1940s of the spin echo by Erwin Hahn,(15,16) and work by Henry Torrey at the same time on the concept of nutation.(17) Concurrently, the idea of the free induction decay (FID) was developed,

with this concept now underpinning the whole of modern NMR spectroscopy. The significance of the idea was first demonstrated when Lowe and Norberg proved, in 1957, that the FID is simply the Fourier transform (FT) of the NMR CW spectrum.(18) The proof was general and could be applied to solids, liquids and gases. The proof is not valid at temperatures below 1 Kelvin, when the high temperature approximation of the Boltzmann factor is no longer valid. It was Ernst and Anderson, however, who provided the first full treatment of the FT and realised the full implications of the FID.(19)

The development of pulsed NMR techniques, actually first suggested by Bloch in his aforementioned 1946 Physical Review paper, had a massive impact on the usefulness of experimental NMR by drastically reducing the time needed to run a simple experiment and obtain a signal. Fortunately, this development occurred simultaneously with advances in computing facilities, where fast FT algorithms were becoming available. These methods were applied first to solution-state NMR, and only became applicable to solids much later. This was due to the broad nature of a solid-state spectrum, which requires microsecond excitation pulses, and which in turn requires more technologically advanced transmitters and receivers, which were not available until somewhat later.

At approximately the same time, a new discovery was made, independently, by Andrew and Lowe, which was eventually to bring solid-state NMR back into the scientific mainstream. It had been evident in the early solid-state spectra recorded in the 1940s and 50s that the broadening of lineshapes due to anisotropic internal interactions often rendered effective analysis futile, especially with powdered samples. Andrew (20,21) and Lowe (22) separately demonstrated that by rapidly spinning the sample at a specific angle, the so called magic angle, it was possible to remove some of this anisotropic broadening. They observed that, experimentally and theoretically, all sources of broadening were described by second rank tensor interactions, which are reduced by rapid rotation by a factor $\left|\frac{1}{2}3\cos^2\beta - 1\right|$, where β is the angle between the axis of rotation and the applied field. If the angle β is chosen to be $1/\sqrt{3}$ (which requires $\beta = 54°74'$) then the broadening interactions may be removed (this concept will be described in greater detail in chapter 2).

These developments quickly combined to yield the type of complex NMR experiments routinely used today. The spin echo discovered by Hahn in the late 1940s was the first example of a multiple pulse NMR sequence. The experiment utilises two closely spaced pulses and has become an integral part of many modern NMR pulse sequences, e.g., allowing transverse relaxation times to be measured. It was not until the mid-1960s, however, that the field of pulsed NMR really gained momentum. Two independent groups, Mansfield and Ware,(23) and Ostroff and Waugh,(24) applied a train of pulses, thus obtaining a set of solid echoes with a prolonged envelope, which effectively narrowed the solid-state NMR spectrum. Since these developments, much effort has been made in solid-state NMR to devise multiple pulse sequences for several key reasons: to average specific interactions to zero, as well as reducing the effects of *rf* inhomogeneity.

Another important milestone was the development of average Hamiltonian theory (AHT).(25) In simplistic terms, AHT is a mathematical formalism which allows for the analysis of how pulse sequences affect internal spin interactions. This theory yielded important sequences such as WAHUHA,(26) one of the first homonuclear decoupling sequences, and, when combined with the theory of MAS, forms the basis of the important concept of recoupling. The idea of dipolar recoupling, which will be discussed in further detail in chapter 3, is to find a pulse sequence for which the time-averaged dipole-dipole coupling is non-zero under MAS, whilst simultaneously averaging other terms (e.g. CSA, heteronuclear decoupling) to zero. It is therefore a method of reintroducing, for example, the homonuclear dipolar coupling back into the system in order to extract structural constraints. Manifold sequences have been developed which effectively achieve this, such as the DRAMA (Dipolar Recovery At the Magic Angle) (27), POST-C7 (Permutationally Offset STabilised C7) (28) and BABA (BAck-to-BAck) (29-31) sequences, the latter of which plays a central role in the work presented herein.

Further advances at this time included the idea of double-resonance, i.e., at a basic level, the application of a second irradiation field at the same time as the observing field. This led to the famous cross-polarisation (CP) experiment. This ingenious experiment was proposed in 1962 by Hartman and Hahn,(32) with the method being used to improve the sensitivity of a low abundance spin species *S*, such as ^{13}C, ^{15}N, by transferring polarisation from an abundant spin *I*, such as ^{1}H, whilst heteronuclear decoupling is implemented to suppress unwanted broadening from undesired interactions.(33) In the CP method, polarisation transfer is mediated *via* the heteronuclear dipolar couplings. Further experimental work in this area was presented by Pines, Gibby and Waugh in the 1970s.(34,35) A critical improvement of the CP method was made in 1975 when the sequence was combined with MAS to yield the important CP MAS method,(36) now a routine solid-state experiment. Incidentally, this work represented the first time that a multiple pulse sequence had been combined successfully with MAS. Importantly, this idea of double-resonance underpins all heteronuclear NMR experiments.

At the same time, the concept of two-dimensional experiments was developed by Jeener who, unfortunately, did not publish his work. What he suggested, however was what is now commonly known as the COSY (COrrelation SpectroscopY) experiment. Jeener's ideas were experimentally implemented in a 1976 paper by Richard Ernst,(37) in which he laid down the basic theoretical groundwork and discussed the potential applications. Modern NMR now relies heavily upon higher dimensional experiments, in particular two-dimensional experiments, since exploiting multiple dimensions allows for additional information to be obtained (for instance employment of a 2D heteronuclear NMR experiment often means exploiting the greater chemical shift range of the second nucleus, at the same time as revealing heteroatomic connectivities). These developments subsequently led to quadrature detection, a method of sign discrimination in a spectrum, and lead to the evolution of more elegant pulse sequences. Importantly, the product operator formalism (a simple way to understand a NMR experiment) was introduced by Sorensen *et al*. (38) Other work in this area, by Bodenhausen,

Kogler and Ernst, introduced the concept of the coherence-transfer pathway, thus greatly expanding our understanding of how an NMR experiment works.(39)

Historically speaking, the advent of high-resolution ^{1}H solid-state NMR is a fairly recent concept, developing rapidly only in the last two decades. This rise has, not by coincidence, coincided with simultaneous advances achieved in MAS technology. The strength of homonuclear $^{1}H - {}^{1}H$ dipolar couplings, of magnitude tens of kilohertz (kHz), is often such that it cannot be fully removed under MAS due partially to its magnitude (available spinning rates are not high enough, especially for the strongly coupled alkyl and aryl regions of the ^{1}H spectrum) and the quantum mechanical effects of an ensemble of coupled protons (this will be described in more detail in chapter 2). As available MAS frequencies have increased, so too has the applicability of ^{1}H solid-state NMR. In this respect, the 1990s was an important decade for the development of this field. Not only did it see the development of robust recoupling schemes (BABA etc.), but the idea of homonuclear decoupling sequences (developed much earlier) gained significant traction, due to the intrinsic limits of MAS at the time (~30 kHz in the late 1990s). These sequences built upon the work performed by Lee and Goldburg (LG) in the mid-1960s, in which they showed that continuous off-resonance *rf* irradiation could be used to effectively decouple strong ^{19}F homonuclear interactions in the static spectrum of CaF_2.(40) Subsequent modifications to the LG approach yielded the frequency-switched (FSLG) and phase-modulated (PMLG) approaches.(41,42) The important CRAMPS (Combined Rotation And Multiple Pulse Spectroscopy) method, which was proposed in the late 1970s when decoupling schemes were initially combined with MAS,(43) entered the forefront of the field in the mid-to-late 1990s. Indeed this method has proven extremely useful in the study of small organic molecules.(44) More complex, high-performance, decoupling sequences such as DUMBO (Decoupling Under Mind-Boggling Optimisation), originally developed for broadband heteronuclear decoupling purposes, were experimentally optimised for homonuclear decoupling at moderate MAS frequencies.(45,46) The development and theory of decoupling shall be described in detail later.

Solution-state NMR has been central and routine to chemistry, biology and many other fields of science for half a century and more. Solid-state NMR, and in particular high resolution ^{1}H solid-state NMR, despite the technical difficulties arising primarily due to the retention of internal anisotropic interactions over the NMR timescale, is fast becoming an active area of research in the more general scientific community. This is due to technological developments, for example the option of routinely available MAS rates up to and exceeding 100 kHz,(47) and the evolution of complex pulse sequences, decoupling and recoupling schemes and the availability of larger superconducting magnets (up to ~1 GHz at the time of writing). Solid-state NMR is now perhaps the most powerful tool (alongside single-crystal X-ray diffraction, electron microscopy etc.) with which to investigate the structure of materials in the solid state.

1.3 Introduction to molecular self-assembly

"*The chemist finds illustration, inspiration, and stimulation in natural processes, as well as confidence and reassurance since they are proof that such highly complex systems can indeed be achieved on the basis of molecular components."*

Jean-Marie Lehn, Nobel Laureate, 1995

The overall purpose of supramolecular chemistry "*is to gain progressive control over the complex spatial (structural) and temporal (dynamic) features of matter through self-organisation*".(48) An ever central theme of the field, often described as "chemistry beyond the molecule",(49) self-assembly can be defined as the ordered, reversible and spontaneous association of building blocks (molecules, ions etc.) into larger suprastructures and entities of high complexity, according to the information encoded into the molecule at the design stage.(48,50) Importantly, the information encoded into the individual molecules allows for assembly without external input i.e. it is truly spontaneous. Such materials are built from a limited array of noncovalent interactions including hydrogen bonding, $\pi - \pi$ interactions, ionic bonds, van der Waals interactions etc. Designing self-assembling systems from only one subunit means that the "*lexicon of interactions employed*" is kept to a minimum, which is highly economical in a chemical sense (especially because of the high convergence of self-assembly processes).(49) The work in this thesis concerns only assemblies consisting of one subunit. Multi-component systems, such as the hexameric assembly of melamine and cyanuric acid,(51) can be more complex to study, particularly from an NMR perspective in the absence of X-ray diffraction data (the difficulty arises in determining assignments for individual molecules). Using the basic principles of noncovalency, it is possible to transform simple molecular 'units' with limited properties into highly sophisticated dynamic structures with manifold potential materials applications (see Fig. 1.1).(52-63) Importantly these materials are, in the overwhelming majority of cases, beyond the scope of more traditional covalent chemistry.(64)

More broadly, the following criteria can be thought of as characteristics of self-assembly, as defined by Fredericks and Hamilton:(65)

1. Self-assembling units are held together *via* noncovalent interactions.
2. The assembly of these subunits into larger suprastructures is selective, i.e., subunits bind *cooperatively* to form the most stable aggregate.
3. The aggregates can be recognised by their properties which differ from those of the individual components.
4. The aggregates are not infinite lattices, but rather of a definitive size and molecular composition.

In a non-trivial manner, modern self-assembly borrows heavily from fundamental principles in coordination chemistry, namely the concepts of cooperativity, which arises from "*the interplay of two or more interactions, so that the system as a whole behaves differently from expectations based on the properties of the individual interactions acting in isolation*" (i.e. individual hydrogen bonds are weak, multiple hydrogen bonds acting together are strong and influence one another),(66) and more broadly multivalency,(67) which describes the interaction between multiple sites on one entity and complementary sites on another (such as the DDA – AAD hydrogen bonding interface between guanosine and cytidine in DNA). Biological cooperativity is important in allosteric protein - ligand binding for instance, where the binding of one ligand directly effects the binding of subsequent ligands. The classic example is that of oxygen binding to haemoglobin: binding of the first oxygen increases the oxygen affinity of the other sites.(68) From a thermodynamic perspective, when several molecules come together to form suprastructures, the drop in entropy must be compensated for by enthalpic contributions from noncovalent interactions (i.e. hydrogen bonds). Individually, these interactions are not sufficient to offset the drop in entropy upon self-assembly, but taken together they promote aggregation, i.e., multiple hydrogen bonds (for instance) offset the entropy change. Molecules may also undergo conformational changes to drive self-assembly. In this sense, cooperativity can be thought of as involving both multiple noncovalent interactions and conformational changes to offset the decrease in entropy upon aggregation into more complex assemblies.

Cooperativity and multivalency are central topics in biochemistry, since they govern many important biological processes. Both ideas are also important for understanding supramolecular self-assembly from an energetic perspective. Multivalency is particularly interesting because it represents a pathway to self-assembly that combines the favourable characteristics of the process (i.e. reversibility, self-sorting) with the opportunity to achieve thermodynamic and/or kinetic stability of suprastructures even at low concentrations: a fundamental principle in biological self-assembly processes in cells for instance. Cooperativity and self-assembly, which is a non-trivial idea,(69,70) was first proposed by Lehn *et al* in 1987, whilst describing the spontaneous assembly of inorganic double helicates, because it "*opens ways to the design and study of self-assembling systems presenting cooperativity and regulation features*".(71) Since these ideas influence the thermodynamic and kinetic control of self-assembling processes, they are beyond the scope of this project which concerns itself with synthesis and characterisation only. However, from a synthetic perspective, these considerations are important since, when compared to their covalent cousins, structures built from noncovalent association of several molecular components are relatively weak and labile. Particularly for molecules which, in principle, have multiple possible avenues to molecular self-assembly (i.e. ribbons, cyclic trimers, helices etc.) these thermodynamic challenges are considerable, if complete selectivity (high fidelity) is required.

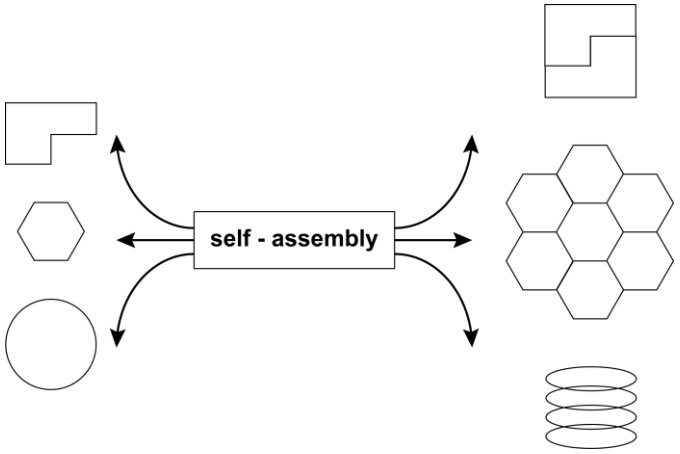

Figure 1.1 The basic concept of molecular self-assembly, whereby single 'building blocks' (molecules/ions etc.) can reversibly and spontaneously form higher order discrete structures via noncovalent interactions (hydrogen bonds, $\pi - \pi$ stacking etc.). The magnitude of the higher order structure i.e. dimer, trimer, hexamer etc. is determined by the intrinsic capacities for intermolecular interaction programmed into the building blocks at the design stage (for synthetic materials).

(Note that from a design perspective, cyclic structures are more useful for the preparation of nanostructures in solution since unlike ribbon/tape-like structures, they are more soluble and their size and shape can be more easily defined.(64)) In response to these challenges, noncovalent synthetic methods are gaining significant traction in the field, but require careful design of molecular building blocks.(64,72-74)

Apart from materials science, self-assembly processes are vital in the wider world,(50) particularly in biological systems. Cell membranes (lipid bilayer), multi-component enzymes, proteins, viruses etc. are all examples of nature's ability to control and tune highly complex processes and functions with a limited number of simple noncovalent interactions, often exploiting the concepts of cooperativity and multivalency. An interesting example is that of the tobacco mosaic virus, which is built from 2130 identical protein units assembled around an RNA strand to form a rod like structure.(75,76) The structure can be dismantled, isolated and reconstructed *in vitro* to form the intact virus,(77) demonstrating the flexible and reversible nature of self-assembly processes. The ultimate paradigm in biological self-assembly, the formation of the DNA double helix structure, has provided much inspiration to chemists. By exploiting the rich hydrogen bonding properties of the four DNA bases (guanine, cytosine, adenine and thymine (note uracil replaces thymine in RNA)), it is possible to design and synthesise novel materials. Specifically, much of the literature has focused on the guanine nucleobase, whose corresponding nucleoside, guanosine, was first observed to form hydrogen bonded tetrameric structures (the famous hydrogen bonded ionophore known as the G-quartet) in the early 1960s, when Gellert *et al* published an X-ray diffraction study of a fibre obtained from a gel of guanosine-3'-phosphate.(78) This tetrameric arrangement was again observed in the 1970s, after additional diffraction studies of several guanosine derivatives,(79) and independent reports on the self-

assembled structures of polyguanylic acid and polyinosinic acid were made.(80,81) (Note, quartet structures are typically templated by metal cations such as sodium or potassium, although examples of non-metal templated quartet formation have also been reported.(82)) Deoxyguanosine derivatives are also known to form liquid crystalline phases in solvents such as water, which was first reported in 1988,(83) with other studies following quickly.(84,85) Detailed studies of these phases has provided fundamental structural information regarding the well characterised columnar species (in which several quartets stack on top of each other *via* $\pi - \pi$ interactions). G-quartet formation and structure has subsequently been well studied and is the topic of several reviews.(86-89) Incidentally, guanosine derivatives had been known to form gels since the early years of the 20th century, some 52 years before the first observation of the G-quartet, when Ivar Christian Bang published a study on concentrated solutions of guanylic acid (guanosine monophosphate).(90) Research around nucleic acid gels is still very active to this day, over a century after the first reports, for their bioanalytical and biomedical applications.(91-93) In addition to tetramers, guanosine can also form hydrogen bonded molecular ribbons,(94,95) which have additional potential applications. Synthetic guanosine derivatives remain of interest for the tuning of structure,(96) and their (potential) use as anticancer agents,(97) gelators (98) and components of molecular electronics,(99) amongst other diverse areas.

In the solid state, interest in self-assembly processes of synthetic guanosine derivatives (the basic guanosine unit with synthetic additions normally to the ribose sugar moiety) has grown in the last decade. This interest has been directly complemented by advances in high-resolution ^{1}H MAS NMR, which is capable of directly probing the important hydrogen bonding interactions prevalent in such systems, with high precision. Indeed, there are now several relevant studies in the literature.(100-104) Solid state studies of non-crystalline synthetic structural analogues however, which incorporate the hydrogen bonding motifs of DNA bases whilst often changing the entire structural backbone of the molecule, are underrepresented in the literature. Hence, the work contained within this thesis attempts to address this issue, by applying high-resolution ^{1}H MAS NMR techniques to the structural elucidation of a range of synthetic nucleobase inspired materials. Specifically, molecules incorporating guanine and/or cytosine hydrogen bonding motifs are presented herein, thereby taking advantage of the natural propensity for GC hydrogen bonding interactions in structures such as DNA. Designing such molecules from pseudo-first principles allows for even greater scope of new materials properties, whilst simultaneously fulfilling the mandate of the bottom-up fabrication of supramolecular systems.

1.3.1 Examples and solid-state characterisation of self-assembled materials

Nucleobases are perhaps nature's finest example of molecular hydrogen bonding units, it is therefore logical that chemists would try to adapt such materials for their own purposes. Examples of self-assembled systems which derive inspiration from nucleobase chemistry are manifold, particularly in solution. Famous examples include the simple metal templated G-quartet and related structures,(86,87)

to more complex synthetic guanine/cytidine Janus-type pyridopyrimidine systems.(105-115) Other notable examples in the literature include ditopic hydrazide-based synthons,(116) pyridine-based trimeric structures,(117,118) self-assembled dendrimers, (119-122) self-assembled star polymers(123,124) and hydrogel based materials.(101,102) Interest in such systems has remained unabated despite thousands of examples because of the versatility of the individual nucleobase and the near unlimited potential for synthetic adaptation.

Characterisation of synthetic self-assembling systems is a prerequisite of any serious discussion of the properties of a given material. Methods for doing so are numerous in solution: gel permeation chromatography (GPC), circular dichroism (CD), ultra-violet (UV) spectroscopy, high-resolution mass spectrometry, calorimetry and NMR being among the most popular choices.(125) Given the simplicity and ease of access of most of these techniques, at most academic and industrial institutions, the overwhelming majority of self-assembling (and indeed supramolecular) systems are studied in solution. However, it is often prudent to study such systems in their solid form, particularly in materials chemistry. In the field of supramolecular chemistry, the solid state 'supermolecule' acts as a model for the less precise more flexible solution state system, which is not bound by the strict rules of crystal-packing. Solution state systems can be studied only indirectly by NMR or other spectroscopic methods. In the case of solid state characterisation there exist two main 'high-resolution' options. The first and (by far) most popular is single-crystal X-ray/neutron diffraction, which produces highly accurate 3D structures, from simple organic/inorganic compounds, to large sophisticated proteins. With the advent of ever more sophisticated computational technologies, analysis of diffraction data is now (in most cases) a routine and simple process. The technique is well established and well trusted in the larger academic community. However the technique is not without some serious drawbacks, most notably the requirement for high periodic order (which depends on the nature of the system in question), preference for particular crystal morphologies with good diffraction properties (cuboid-like crystals diffract better than thin needle-type shapes for instance which include some orientational bias), the requirement for recrystallization (known for its lack of reproducibility under seemingly identical conditions) and the 'snapshot' nature of the technique wherein static and dynamic disorder in the system are projected back into the unit cell (it therefore becomes difficult to distinguish between different types of disorder). In spite of these issues, in the case of small organic molecules (i.e., those below a molecular weight of around 700 g/mol), crystallisation techniques are now well optimised and produce structures with highly accurate bond lengths and angles, allowing for direct extraction of structural parameters. In the case of the very large, such as large transmembrane protein complexes (molecular weight of tens of thousands to millions of g/mol (126,127)), the process is much less accurate, sufficient for locating the positions of individual amino acids but not atoms. Supramolecular systems, such as self-assembled materials, are in the intermediate range (often several thousands of g/mol), which presents problems. The problem is particularly acute in non-metal templated assemblies, which lack the heavy atoms which diffract more

efficiently than lighter elements (due to more electrons). Therefore, systems containing only light elements (H, C, O, N) such as many of the compounds presented in this thesis, require extremely high periodicity in order to diffract well and produce a high quality structure. In many compounds, particularly moderately sized organics which contain one or more flexible moieties (such as long alkyl chains), high periodicity is often beyond reach due to the high mobility and dynamic nature of such substituents. Finally, crystal stability plays an important role in determining a material's suitability for diffraction. In many systems, the recrystallization solvent is incorporated into the crystallographic structure, or the so-called 'mother solvent' may protect against decomposition. It is therefore impractical to change or optimise the laboratory conditions. In addition, self-assembled systems are sensitive and fragile by their very definition, since the intermolecular forces which bind them can be relatively labile (in this respect, it is also necessary to consider the solvent of recrystallization since solvents such as H_2O, DMSO and DMF are highly competitive hydrogen bond acceptors). In light of this, much effort has been made in the field of crystal engineering,(128) incidentally developed in order that efficient organic topochemical reactions could be designed,(129) whereby the individual components are engineered to organise into specific crystals with desired properties (which requires an understanding of intermolecular interactions in the broader context of crystal packing, which is obviously nontrivial). Whole PhD theses have been dedicated to such studies and as such it is beyond the scope of this work. As this thesis will demonstrate, in the instance of powdered or microcrystalline samples, high-resolution ^{1}H MAS NMR is the only other viable solid state technique capable of providing structural information with high atomic precision.

1.3.2 Noncovalent interactions and solid-state NMR

There exist four general types of noncovalent forces: electrostatic interactions (ionic bonding, hydrogen bonding, halogen bonding) (130-134), van der Waals forces (dipole-dipole, dipole-induced dipole, London dispersion forces) (135,136), π effects ($\pi-\pi$, CH $-\pi$, cation/anion $-\pi$) (137,138) and hydrophobic effects.(139) Note that the hydrophobic effect only influences species in solution and hence is not directly relevant to this work. Of these various interactions the most important, at least for the systems presented herein, are hydrogen bonding and $\pi-\pi$ stacking interactions. This is a consequence of the abundance of donor/acceptor moieties in the case of the former and, in the case of the latter, the existence of aromatic functionalities contained within the pyrimidine structural backbones. The hydrogen bond in particular has been well studied for the past century, given its central importance in biological and physical sciences. This interaction is remarkably complex,(132) and as such has been redefined constantly (as recently as 2011).(140,141) The ^{1}H chemical shift which, for typical organic compounds, has a total range of around 20 ppm, is highly attuned to the electronic environment about protons, this is true for systems which interact *via* π stacking phenomena,(142) but is particularly true for systems which form hydrogen bonds, with such protons usually being observed at around or above 10.0 ppm ('stronger' hydrogen bonds tend to resonate at higher shifts).(143) This

phenomenon is well studied in the literature.(144-147) This chemical shift range is unique to hydrogen bonded protons with aromatic (~6.0 – 9.0 ppm) and aliphatic (~0.0 – 6.0 ppm) protons typically appearing at lower shifts. The introduction of NMR crystallographic methods have also seen an increase in our understanding of the subtleties of hydrogen bonding and the relationship of distance and calculated chemical shielding for instance.(148) Indeed, in the case of intermolecular hydrogen bonding, the GIPAW (gauge-including projector augmented wave) approach proves useful by comparing the calculated chemical shielding parameters for the full crystal structure versus an isolated molecule (the idea being that isolated molecules experience no intermolecular noncovalent interactions, although intramolecular phenomena are still encountered). This method has proven itself to be very powerful with shift differences of several ppm being observed for various hydrogen bonding protons in amino acids and pharmaceutical formulations.(142,149-152) Note that, as per these references, even weak CH – O hydrogen bonds can be characterised in the solid state.

1.4 An experimental example

The theoretical and experimental concepts introduced here will be fully described in chapters 2 and 3.

Consider the structure of pyridopyrimidine derivative **1-1** which contains within it a cytosine motif. **1-1**, which is non crystalline, is thought to form a hydrogen bonded dimer across the cytosine hydrogen bonding interface, as shown by Fig. 1.2.

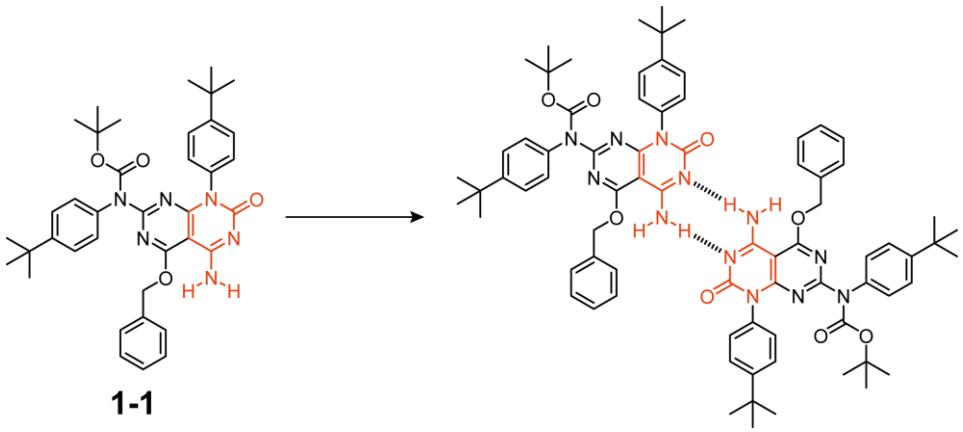

Figure 1.2 Schematic representation of the structure of compound **1-1** and the proposed dimeric arrangement postulated to exist in the solid state, with the cytosine moiety highlighted in red.

1-1 is an example of a DNA base analogue in that it contains the hydrogen bonding motif of, in this case, cytosine, whilst including other interesting chemical functionalities. **1-1** is a precursor for a more complex Janus-type molecule which forms a hexameric arrangement in solution.(105) A so-called double-quantum (DQ)/single-quantum (SQ) MAS spectrum is presented in Fig. 1.3.

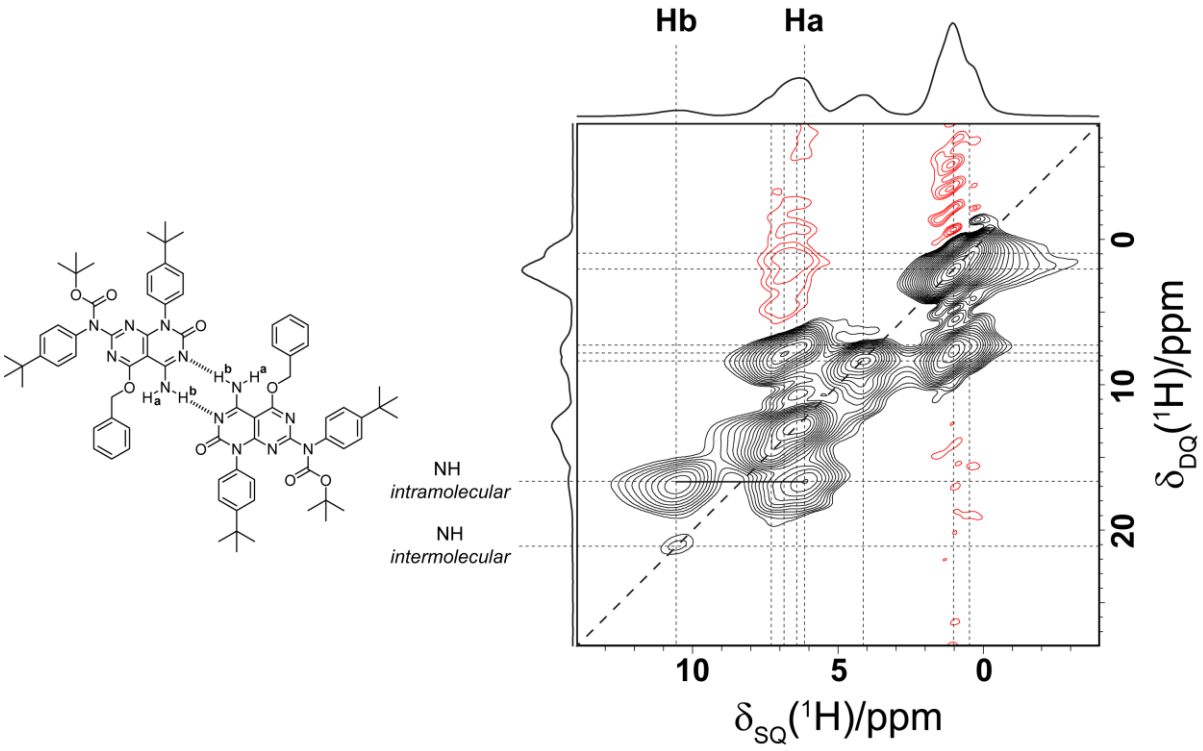

Figure 1.3 A $^{1}H - {}^{1}H$ (Larmor frequency, ω_0 = 600 MHz) DQ/SQ MAS (55 kHz spinning) spectrum, with skyline projections, of **1-1** alongside a schematic representation of the proposed dimer structure. For simplicity, only the NH protons have been assigned in this example. See Fig. 6.17 for experimental details.

Such an experiment, recouples the $^{1}H - {}^{1}H$ homonuclear dipolar coupling into the system so that it is possible to observe $^{1}H - {}^{1}H$ proximities within approximately 3.5 Å. A full description of this experiment, as well as the phenomenon of recoupling, will be provided in chapter 3.

Only the peaks corresponding to the NH protons, namely those at 6.1 (Ha) and 10.5 ppm (Hb), are shown for simplicity, although the rest of the spectrum yields important data regarding the larger molecular structure (note that the relative broadness of the individual peaks, across the spectrum, but particularly in the 3.0 – 8.0 ppm range is due primarily to the presence of multiple strongly coupled aromatic protons in **1-1**). The spectrum in Fig. 1.3 demonstrates the power of ^{1}H solid-state NMR in determining the molecular structure of hydrogen bonded solids, but also reveals its most significant limitation, namely resolution (which remains a significant problem even in the intermediate to fast MAS regime for many compounds, particularly aromatics). Two important features arise which relate to the hydrogen bonded dimeric arrangement proposed. The first is a set of strong cross peaks at δ_{DQ} = 6.1 + 10.5 = 16.6 ppm, corresponding to the intramolecular contact between the two protons in the amine NH_2 functionalities. The close proximity of these protons results in intense cross-peaks, as will be discussed later. The second and defining feature is the weak auto-peak, which lies on the diagonal, at

δ_{DQ} = 10.5 + 10.5 = 21.0 ppm, and corresponds to the intermolecular Hb – Hb contact experienced across the hydrogen bonding interface. Such ^{1}H 'signatures' are commonly encountered in the work presented in this thesis. The strong intramolecular coupling between the NH_2 protons effectively attenuate this intermolecular coupling in a process known as dipolar truncation.(153,154)

These features alone are consistent with the dimeric arrangement proposed for **1-1**, and demonstrate the ability of the ^{1}H chemical shift, as revealed by a simple two-dimensional homonuclear experiment, to probe hydrogen bonded structures in the absence of single-crystal X-ray diffraction data. As this thesis will demonstrate, ^{1}H based NMR MAS experiments are well suited to the study of synthetic nucleobase analogues, especially when exploiting homo- and heteronuclear two-dimensional experiments. For compounds which have an available high-quality diffraction structure of sufficient quality (note that ~80% of the compounds discussed in this work do not), it is possible to complement experimental NMR data with *ab initio* calculations, which is described briefly at a basic level in the following section. Compound **1-1** will be discussed in more detail in chapter 6 (compound **6-6**).

1.5 Introduction to DFT and the GIPAW method

NMR crystallography, which is an area of research gaining significant prominence in the field of solid-state NMR, can be defined as the combined use of experimental NMR methodologies and *ab initio* calculations in order to provide additional insight into the structure and dynamics of molecular solids. Specifically, the use of the GIPAW (gauge-including projector augmented wave) method,(155-158) has been used effectively for the calculation of NMR parameters (e.g. magnetic shielding, EFG tensors, *J*-coupling) on a range of inorganic and organic materials. The method is employed after the selection of the appropriate geometry (usually by some geometry optimising procedure applied to the diffraction structure), to provide the required calculated NMR tensors.(158) Directly relevant to the work presented here, several NMR crystallographic studies have been conducted on guanosine derivatives within the group of Professor Steven Brown at Warwick in the past five years.(100,103,104) The technique is useful for confirmation of chemical shift assignments, particularly in cases where significantly broadened ^{1}H lineshapes prevent independent assignment. However, therein lies the drawback of this methodology as it currently stands, i.e., the need for a high-quality single-crystal X-ray diffraction structure of the compound in question. In this regard, the technique acts only as a confirmation of the power of both diffraction and high-resolution solid-state NMR in providing detailed structural insights into the system in question. However, this being said, it is possible, as will be demonstrated by this thesis, to infer structural information in related but non-crystalline materials, for a series of compounds in which there exists a crystal structure for one of those systems. In addition, crystallographic data may be complemented by comparing the calculated magnetic shielding parameters for the full crystal (i.e., the full unit cell) with those of the isolated molecules, therefore allowing for some comment upon the strength of noncovalent interactions present in the system. The ultimate goal of the GIPAW method is

to, in essence, work backwards, i.e., to extract 3D structural detail *via* the inputting of experimental NMR parameters.

Calculations in this thesis are performed using CASTEP,(159) which is a leading code for the modelling of materials properties based on a first principles quantum mechanical description of electrons and nuclei (although it should be noted that other such codes exist, e.g. Quantum Expresso). Specifically, CASTEP uses density functional theory (DFT) to simulate desired properties (e.g. energetics, molecular structure, vibrational properties, electronic response). At a basic level, DFT provides a quantum mechanical model of a many-body system (i.e. atoms, molecules, condensed phases etc.). The spatially dependent electron density of a system is determined by employing functionals. However, since the exact functionals cannot be known it is necessary to apply approximations to the system for practical applications of DFT. Many different approximations exist from the simple local density approximation (LDA), which depends upon the electronic density at each specific point in space (hence local), to complex hybrid generalised gradient approximations (GGA) which are still local approximations but have the additional effect of factoring in the gradient of the density at a specific point, a popular example being the PBE (Perdew-Burke-Ernzerhof) functional.(160) It should, however, be noted that such approximations are not without their own specific issues, such as the overestimation of volume for instance. Another issue with DFT arises in how to treat the electrons in a given atom. The many electron Schrödinger equation is simplified if the electrons in a given system are split into two distinct groups: core and valence electrons. Since the core electrons reside near and are tightly bound to the nucleus, they can be essentially fixed during the calculation. This is the so-called frozen core approximation. The atom is therefore divided into an ionic core (core electrons + nucleus) interacting with the valence electrons. A so-called *pseudopotential* is an approximation which endeavours to replace the complex motion of core electrons of an atom and the nucleus with an effective potential which replaces the Coulombic potential term for core electrons found in the Schrödinger equation. This effective potential interacts weakly with the valence electrons which are themselves treated explicitly. This makes calculations much more efficient and hence less computationally expensive. A significant drawback of the pseudopotential approach is that it explicitly neglects the form of electronic wavefunctions around the nucleus.(155) Since the NMR chemical shift is dependent upon the all-electron wavefunction at the nucleus, it was supposed that no pseudopotential based theory of NMR could exist. However, Van de Walle and Blöchl offered a solution to this problem for the calculation of hyperfine parameters,(161) based around the projector augemented wave (PAW) approach introduced by Blöchl,(162) which was subsequently modified for systems in an external magnetic field by Pickard and Mauri (GIPAW).(155)

1.6 Thesis overview

This thesis demonstrates the suitability of high resolution ^{1}H MAS NMR techniques and, where applicable, GIPAW calculations of the relevant NMR parameters to the elucidation of a range of self-

assembling systems based around the pyrimidine heterocycle. Specifically, fast MAS frequencies are employed to resolve the experimental $^{1}H - {}^{1}H$ and $^{14}N - {}^{1}H$ correlations in order to ascertain the mode of hydrogen bonding in these molecules, whose motifs are based around the well characterised guanine and cytosine DDA/AAD interfaces, respectively.

Chapters 2 and 3 discuss the relevant theoretical and experimental concepts in NMR, respectively. Specifically, chapter 2 describes the fundamental quantum mechanical rationale on which NMR as a technique is based, including the important concepts of the density operator at equilibrium and its time dependence, before discussing in depth the appropriate Hamiltonians for the external interactions, which describe how the spectrometer and the sample interact, and internal interactions which combine to make NMR an essential tool for structural characterisation in modern chemistry. As the most important internal interaction in ^{1}H NMR, aside from the chemical shielding, the concepts of the dipole – dipole coupling interaction are described at length. The idea of frames of reference, rotations and the secular approximation, which establishes the primacy of the dominant Zeeman interaction, are also discussed. Chapter 3 establishes the important concepts required to understand modern experimental solid-state NMR introducing, for example, the key ideas of the free-induction decay (FID) and Fourier transformation, experimental lineshapes, quadrature detection and concepts of phase in NMR spectra. The chapter ends with a discussion of dipolar decoupling and recoupling techniques and presents the pulse sequences upon which the experimental data in this thesis is based. Finally, approaches used in this work for the referencing of experimental chemical shifts are described, alongside details of the GIPAW calculations performed in this work.

Chapter 4, the first of the experimental chapters, considers the self-assembling properties of a range of pterin-based synthetic analogues. The chapter is divided into two sub-chapters. The first examines the importance of a protecting pivaloyl moiety (C_5H_9O) in directing the self-assembly for a range of low molecular weight pterin analogues. The existence of a single crystal X-ray structure for one of the intermediates allows for an NMR crystallographic analysis of this series of related molecules. The importance of the aforementioned protecting group is demonstrated further when replaced by a dimethylaminomethylene (C_7H_9N) group, thereby removing the possibility to adopt a key intramolecular hydrogen bond. The second sub-chapter investigates the hydrogen bonding capacity of two higher molecular weight compounds, in which the pterin moiety, studied in the first sub-chapter, is chemically bonded to a synthetic deoxycytidine derivative. The addition of the AAD hydrogen bonding motif through the cytidine allows for a rotation of the pivaloyl protecting group to afford the DDA guanine-like hydrogen bonding face. This allows for several hypothetical self-assembling architectures to form, most notably a stacked trimeric arrangement. In the final compound in this sub-chapter, the synthetic removal of the pivaloyl group is specifically designed to allow for trimeric assembly. However, the broad $^{1}H - {}^{1}H$ DQ/SQ MAS spectrum for this compound makes analysis non-trivial.

In chapter 5, three deoxycytidine analogues (including the previously discussed cytidine analogue in chapter 4) are discussed from an experimental and computational standpoint. The highly resolved solid-state NMR data for two of the three compounds, which were measured at a ^{1}H Larmor frequency of 850 MHz, demonstrate the ability of ^{1}H MAS NMR to determine the number of crystallographically distinct molecules in the asymmetric unit cell (Z'). These two molecules form hydrogen bonded dimers and have a Z' = 2, which results in a doubling of observed ^{1}H NMR resonances for all non-alkyl and ribose protons, including the presence of four distinct NH protons, which all form hydrogen bonding interactions. The final compound, which has a crystal structure that incorporates disorder, is postulated to form helical arrays in the solid state. The highly resolved ^{1}H – ^{1}H DQ/SQ MAS spectrum, recorded at a ^{1}H Larmor frequency of 600 MHz, is consistent with a highly ordered structure.

In the absence of any crystallographic information, i.e., for a series of compounds which form non-crystalline powdered solids, ^{1}H MAS NMR alone is still capable of probing hydrogen bonding motifs. Specifically, chapter 6 describes the solid-state packing arrangement of a range of synthetic pyrimidine and pyridopyrimidine derivatives. Despite the high abundance of aromatic protons in these systems, spinning frequencies of 60 kHz MAS are sufficient to resolve the important hydrogen bonded proton resonances. A combination of ^{1}H – ^{1}H, ^{14}N – ^{1}H and (for one compound) ^{1}H – ^{13}C correlations are employed for this purpose. Importantly, rare examples of aldehyde solid-state NMR chemical shifts are discussed and the first ^{1}H MAS NMR studies of oxime containing materials are presented. At the end of the chapter some of the synthetic challenges in preparing these intermediates are discussed alongside some possible solutions.

In terms of experimental chapters, the thesis finishes with a change of emphasis. Chapter 7 describes how, through modification of relevant pulse sequences, excessive t_1 noise can be suppressed in two-dimensional ^{1}H solid-state NMR spectra by utilising a selective saturation pulse to suppress the intensity of a strong perturbing methyl peak. The work in this chapter was recently published.(163) In order to demonstrate this effect, a deoxycytidine derivative (described in chapter 5) is used. The requirement for fast MAS frequencies is critical in order to reduce the effect of spin diffusion between the suppressed methyl environment and the other proton sites within this molecule, thereby ensuring that the selective saturation pulse has minimal impact on the viewability of the 2D spectra. This reduced spin diffusion is quantified by comparing 2D ^{1}H spin diffusion spectra recorded at 30, 40, 50, 60 and 70 kHz MAS. The effect of changing the selective pulse duration and nutation frequency is separately investigated for one-pulse ^{1}H MAS NMR spectra. Finally, the effect of the selective saturation pulse on the commonly employed ^{1}H – ^{1}H DQ/SQ MAS and ^{14}N – ^{1}H HMQC (utilising SR4 recoupling of the ^{14}N – ^{1}H heteronuclear dipolar couplings) experiments (as employed in this thesis) are investigated.

Chapter 2 : Theoretical concepts in solid-state NMR spectroscopy

2.1 Spin angular momentum and the basics of an NMR experiment[1]

Magnetically active nuclei possess an intrinsic property (alongside mass, energy, charge) known as spin angular momentum. The magnitude of this property is quantised in discrete units of $\hbar$, where $\hbar = h/2\pi$ and is represented by the spin angular momentum quantum number I, where

$$I = 0, \frac{1}{2}, 1, \frac{3}{2}, 2, \ldots \tag{2.01}$$

Since spin angular momentum is a vector quantity, both the direction and magnitude is quantised such that the spin angular momentum $\boldsymbol{I}$ of a spin-I nucleus has $2I + 1$ projections onto an arbitrary axis, which by convention is z:

$$I_z = m\hbar, \tag{2.02}$$

where m, the magnetic quantum number, has $2I + 1$ values in integral steps between $+ I$ and $- I$:

$$m = I, I-1, I-2, \ldots\ldots, -I+1, -I. \tag{2.03}$$

For ^{1}H (I = ½), the angular momentum has two permitted directions, $I_z = \pm \frac{1}{2}\hbar$.

In the absence of an external applied magnetic field, all $2I + 1$ orientations of a spin-I nucleus have degenerate energy, with this condition being subsequently removed upon application of a magnetic field, B_0, as demonstrated in Fig. 2.1.

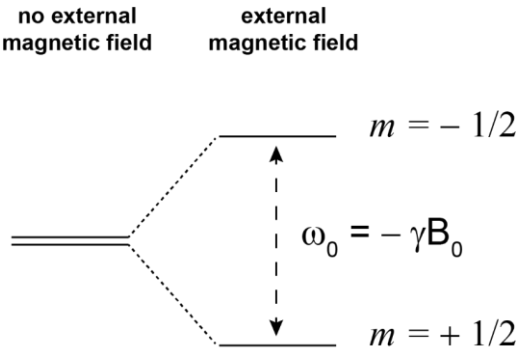

Figure 2.1 Upon the application of a magnetic field, B_0, the energy level degeneracy for an isolated spin-1/2 nucleus ($\gamma > 0$) is lifted, resulting in two energy levels denoted α and β with, m = ½ and – ½ respectively. This phenomenon is known as the Zeeman effect and the energy difference between the two levels is equal, in frequency units, to the Larmor frequency, ω_0.

[1] Unless otherwise stated, the ideas and equations presented in chapters 2 and 3 are adapted and derived from Hore, Jones and Wimperis, *164*. P. J. Hore, J. A. Jones, and S. Wimperis, *NMR, the toolkit*; Oxford University Press: Oxford ; New York, 2000., Duer,*165*. M. J. Duer, *Introduction to solid-state NMR spectroscopy*; Blackwell: Oxford, UK ; Malden, MA, 2004. and Keeler.*166*. J. Keeler, *Understanding NMR spectroscopy*; 2nd ed.; John Wiley and Sons: Chichester, U.K., 2010.

This splitting occurs due to the interaction between the magnetic moment of a nucleus and the applied field. This so called Zeeman interaction energy can be written (in terms of the Hamiltonian) as:

$$\hat{H}_Z = -\hat{\mu}B_0 \tag{2.04}$$

where $\hat{\mu}$ is the magnetic moment, defined by,

$$\hat{\mu} = \gamma\hat{I}, \tag{2.05}$$

and where γ is the magnetogyric ratio, which is simply the ratio of a system's magnetic dipole moment to its angular momentum. Convention dictates that the specified quantisation direction for the spin angular momentum is that of the external field in the *z* direction. The Zeeman Hamiltonian thus becomes:

$$\hat{H}_Z = -\gamma\hat{I}_z B_0 = \omega_0\hat{I}_z, \tag{2.06}$$

where ω_0 is the Larmor frequency,

$$\omega_0 = -\gamma B_0. \tag{2.07}$$

This frequency corresponds to the difference between energy levels (Fig. 2.1).

For systems with $I > 0$, the NMR experiment makes use of this quantisation of energy levels. Such energies are highly attuned to the electronic and hence local chemical environment of a given nucleus. The NMR experiment thus reveals site specific information and dynamics corresponding to a given system and as a result has established itself as a mainstream technique for chemical characterisation.

In order to observe a given spin system by NMR, it is necessary to rotate the spins away from their equilibrium position along the *z* axis, into the *x*/*y* plane (transverse plane) in which the probe's coil is located. This is necessary because in order to generate a signal, the spins must induce a voltage in the coil. Faraday's law states that a voltage is generated in a coil by changing the magnetic environment about that coil (time-varying magnetic field), something which is achieved (see below discussion) by first rotating the spins into the transverse plane. In modern NMR experiments, such a rotation is achieved by means of radiofrequency (*rf*) pulses with specific phases. Since an *rf* pulse is an electromagnetic wave, it has an associated magnetic field which, in addition to the strong applied magnetic field, can interact with the spins in the sample. An *rf* pulse can be off-resonance, in which

case the frequency of its oscillation will be far from the Larmor frequency of the nuclei under investigation, or it can be on-resonance, in which case this oscillation frequency will be at or close to the desired Larmor frequency. An on-resonance *rf* pulse has the effect of rotating the spins towards the transverse plane (the specific direction is determined by the phase of the *rf* pulse). The spins displaced by an *rf* pulse will immediately begin to precess about the *z* axis. This precession, in addition to the oscillation of the *rf* pulse is better visualised by introducing the concept of the rotating frame. The rotating frame assumes that the oscillating *rf* pulse or field is static. Such a model arises if the oscillating *rf* field is assumed to be comprised of two counter rotating fields, $+\omega_{rf}$ and $-\omega_{rf}$. Since only one of these components rotates in the same sense as the Larmor frequency of the spins to be manipulated, that component is retained. The other component is many hundreds of MHz off-resonance and therefore has no discernible influence on the system and can be safely ignored. In the absence of this model, i.e., when all oscillations are considered, the frame of reference is termed the laboratory frame.

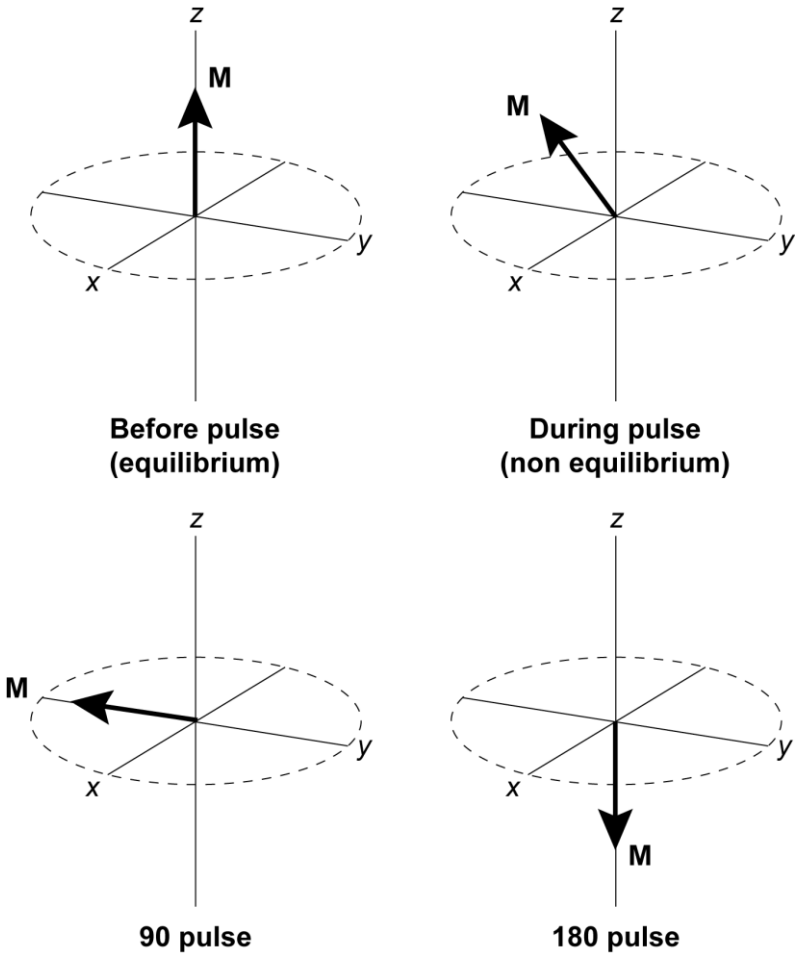

Figure 2.2 Schematic representation of what happens during the application of an *rf* pulse. Note that the so-called flip angle determines the final position of the magnetisation vector, M (spins), with typical values being 90° and 180°, in routine NMR experiments.

This has the effect that once an *rf* pulse is applied to the system, the spins 'observe' an apparently static, weak magnetic field termed B_1 and subsequently precess (nutate) about this field until the pulse is turned off. Note that pulses designed to manipulate spins in this way are usually of short duration (typically a few μs for ^{1}H, ^{13}C). The rate of the nutation, the nutation frequency, is given as the negative product of the magnetogyric ratio and the magnitude of the B_1 field. A more theoretical treatment of the influence of oscillating *rf* fields will be discussed in section 2.3.2.

Typical samples generate spectra with multiple peaks (see chapter 3 for an in-depth discussion). In this case it is not possible to set the so-called transmitter frequency (ω_{rf}) exactly equal to the Larmor frequency for all peaks. Hence, in this case the *resonance offset*, Ω, that is, the difference between ω_{rf} and ω_0, is none zero, resulting in a residual field arising in the rotating frame of reference. When the pulse is turned off, the spins will begin to precess about this residual field, with the sense and rate of precession being determined by the magnitude of Ω. Evolution under a resonance offset will be described in detail in section 2.3.3.

Signals generated in NMR evolve with time. Such signals are measured relative to the rotating frame of reference, as discussed above. Fourier transformation (FT) is used to generate a frequency domain spectrum from time domain data (free induction decay, FID). In order to generate an unambiguous frequency spectrum it is necessary to record two sets of time domain data, the so-called real and imaginary components of the time domain signal, which are offset from each other by 90°. The time domain signal is sensitive to the sign of the resonance offset, and so it is necessary to record these two components in order to ensure that the resulting frequency spectrum is sign discriminated. Since it is impractical to build two perpendicular coils into a probe, recording these two orthogonal signals is achieved *via* the use of two mixers. This technique is known as quadrature detection and will be discussed in greater length later.

Finally, it is an axiomatic concept of thermodynamics that systems displaced from thermal equilibrium will, if left alone, return to this state over time. In NMR, the *rf* pulse achieves this displacement, in which spins are moved away from the *z* axis (conventionally the direction of the B_0 magnetic field in which spins at thermal equilibrium align) into the transverse plane. Once a pulse has manipulated the magnetisation in this manner, the spins will attempt to dissipate energy in order to return to thermal equilibrium. At a basic level, which is sufficient for the work described in this thesis, this return to equilibrium or *relaxation* has two principle mechanisms. The first mechanism, transverse relaxation, which has a characteristic time T_2, describes the loss of coherence order in the transverse plane. During T_2 spins lose energy to other spins in the sample. As shall be seen in chapter 3, the rate of T_2 relaxation has important consequences for the observed linewidth in the solid state. The second mechanism, which determines the rate at which an experiment can be repeated (in order to improve the signal to noise) is

known as longitudinal relaxation, T_1, and describes how spins dissipate energy into the surrounding lattice in order to reorientate themselves along the *z* axis, i.e., return to thermal equilibrium.

In order to gain a complete understanding of the NMR experiment, it is necessary to include a basic quantum mechanical description of the processes which underpin the technique and to discuss the various spin Hamiltonians under the influence of MAS, which now follows in the subsequent sections.

2.1.1 Angular momentum operators

The wavefunction, $|\Psi\rangle$, fully describes all the properties of a quantum mechanical system. By applying an operator, $\hat{A}$, it is possible to extract information from the said wavefunction, where the operator corresponds to a measurable physical quantity. Experimentally, repeated measurements will yield an average value, the expectation value, which describes the result of a given operator acting upon the system:

$$\langle \hat{A} \rangle = \langle \Psi | \hat{A} | \Psi \rangle. \tag{2.08}$$

The angular momentum operators, $\hat{I}_x, \hat{I}_y, \hat{I}_z$, which represent the *x*, *y* and *z* components of the nuclear spin and $\hat{I}^2$, which represents the magnitude squared, can be applied to yield specific observables pertaining to the nuclear spin. The total magnitude of the spin angular momentum, squared, is given by:

$$\hat{I}^2 = \hat{I}_x^2 + \hat{I}_y^2 + \hat{I}_z^2, \tag{2.09}$$

which, in matrix form, is expressed as:

$$\hat{I}_x = \begin{pmatrix} 0 & \frac{1}{2} \\ \frac{1}{2} & 0 \end{pmatrix}, \qquad \hat{I}_y = \begin{pmatrix} 0 & -\frac{i}{2} \\ \frac{i}{2} & 0 \end{pmatrix}, \qquad \hat{I}_z = \begin{pmatrix} \frac{1}{2} & 0 \\ 0 & -\frac{1}{2} \end{pmatrix}. \tag{2.10}$$

This set of operators obey the following commutation relations:

$$\left[\hat{I}^2, \hat{I}_z\right] = 0 \tag{2.11}$$

$$\left[\hat{I}_x, \hat{I}_y\right] = i\hat{I}_z \tag{2.12}$$

The above relations imply that, as noted above, only a single component of the spin angular momentum is observable at a given time, since only a single component of the spin angular momentum commutes with the total spin angular momentum. By convention, this component is the *z* component, with the individual components not commuting with one another.

The operators $\hat{I}^2$ and $\hat{I}_z$, acting upon $|\Psi\rangle$, yield the following eigenvalues:

$$\hat{I}^2|\Psi\rangle = \hbar I(I+1)|\Psi\rangle \tag{2.13}$$

$$\hat{I}_z|\Psi\rangle = \hbar m|\Psi\rangle, \tag{2.14}$$

where m is the projection of the angular momentum onto the direction of the applied magnetic field and takes values $-I, -I+1, \ldots\ldots, I-1, +I$. There are, therefore, two possible values of m for a nucleus with spin = ½ namely, $m = +\frac{1}{2}$ and $m = -\frac{1}{2}$. These eigenstates are referred to as spin up (α) and spin down (β), respectively. The corresponding eigenvalues become:

$$\hat{I}_z\left|\alpha\right\rangle = +\frac{1}{2}|\alpha\rangle, \qquad \hat{I}_z|\beta\rangle = -\frac{1}{2}|\beta\rangle. \tag{2.15}$$

Since $\hat{H}_Z = \omega_0\hat{I}_z$, it follows that:

$$\hat{H}_Z|\alpha\rangle = +\frac{1}{2}\omega_0|\alpha\rangle \tag{2.16}$$

$$\hat{H}_Z|\beta\rangle = -\frac{1}{2}\omega_0|\beta\rangle. \tag{2.17}$$

For an isolated spin-1/2 nucleus, the wavefunction is a superposition, or linear combination, of the $|\alpha\rangle$ and $|\beta\rangle$ basis sets, such that:

$$|\Psi\rangle = c_\alpha|\alpha\rangle + c_\beta|\beta\rangle, \tag{2.18}$$

where c_α and c_β describe the relative contributions to each state. The expectation value of the $\hat{I}_z$ operator is now:

$$\langle \hat{I}_z \rangle = \frac{1}{2}\left(c_\alpha c_\alpha^* - c_\beta c_\beta^*\right) = \frac{1}{2}|c_\alpha|^2 - \frac{1}{2}|c_\beta|^2. \tag{2.19}$$

The above equation demonstrates that the longitudinal component is directly related to the probability of finding the system in either of these spin states.

The *x* and *y*-components of the spin angular momentum, which do not commute with the $\hat{I}_z$ operator, do not share $|\alpha\rangle$ and $|\beta\rangle$ eigenstates. These spin operators instead act to interconvert between the two states:

$$\hat{I}_x|\alpha\rangle = +\frac{1}{2}|\beta\rangle \tag{2.20}$$

$$\hat{I}_x|\beta\rangle = +\frac{1}{2}|\alpha\rangle \tag{2.21}$$

$$\hat{I}_y|\alpha\rangle = +\frac{1}{2}i|\beta\rangle \tag{2.22}$$

$$\hat{I}_y|\beta\rangle = -\frac{1}{2}i|\alpha\rangle. \tag{2.23}$$

The expectation values are given by:

$$\langle \hat{I}_x \rangle = \frac{1}{2}\left(c_\alpha c_\beta^* + c_\beta c_\alpha^*\right) \tag{2.24}$$

$$\langle \hat{I}_y \rangle = \frac{1}{2}i\left(c_\alpha c_\beta^* - c_\beta c_\alpha^*\right). \tag{2.25}$$

2.2 The density operator

The above description is sufficient to describe an NMR experiment for an isolated single spin $I = ½$ nucleus. However, for spins with $I > ½$ or indeed multiple spin systems, the mathematics involved in this process become increasingly tedious. Therefore, for purposes of simplification, one must construct a matrix representation for the spin system, operators and observable quantities for any value. Since the

components of the expectation values of the angular momentum are expressed as the products of two coefficients, c_α and c_β, it is possible to subject these products to the averaging process when taking ensemble averages. Such ensemble averages can be expressed in a convenient manner, hence in this context the density operator is defined as:

$$\hat{\rho} = \overline{|\Psi\rangle\langle\Psi|}, \tag{2.26}$$

where the overbar represents an ensemble average. $|\Psi\rangle$ and $\langle\Psi|$ are superposition states defined as:

$$|\Psi\rangle = c_\alpha|\alpha\rangle + c_\beta|\beta\rangle \tag{2.27}$$

$$\langle\Psi| = c_\alpha^*\langle\alpha| + c_\beta^*\langle\beta|. \tag{2.28}$$

The matrix representation of $\hat{\rho}$ is as follows:

$$\rho = \begin{pmatrix} \overline{\langle\alpha|\hat{\rho}|\alpha\rangle} & \overline{\langle\alpha|\hat{\rho}|\beta\rangle} \\ \overline{\langle\beta|\hat{\rho}|\alpha\rangle} & \overline{\langle\beta|\hat{\rho}|\beta\rangle} \end{pmatrix} = \begin{pmatrix} \rho_{11} & \rho_{12} \\ \rho_{21} & \rho_{22} \end{pmatrix} = \begin{pmatrix} \overline{c_\alpha c_\alpha^*} & \overline{c_\alpha c_\beta^*} \\ \overline{c_\beta c_\alpha^*} & \overline{c_\beta c_\beta^*} \end{pmatrix}. \tag{2.29}$$

The ensemble average of the entire spin system of wavefunctions, represented by the overbar, relates to the macroscopic average of the bulk spin system. The overbar is omitted in the following descriptions for simplicity of notation.

The matrix, ρ, which relates to the sample, can be multiplied by a matrix corresponding to a given operator, $\hat{A}$, to yield:

$$\begin{aligned} \rho A &= \begin{pmatrix} c_\alpha c_\alpha^* & c_\alpha c_\beta^* \\ c_\beta c_\alpha^* & c_\beta c_\beta^* \end{pmatrix} \begin{pmatrix} A_{\alpha\alpha} & A_{\alpha\beta} \\ A_{\beta\alpha} & A_{\beta\beta} \end{pmatrix} \\ &= \begin{pmatrix} c_\alpha c_\alpha^* A_{\alpha\alpha} + c_\alpha c_\beta^* A_{\beta\alpha} & c_\alpha c_\alpha^* A_{\alpha\beta} + c_\alpha c_\beta^* A_{\beta\beta} \\ c_\beta c_\alpha^* A_{\alpha\alpha} + c_\beta c_\beta^* A_{\beta\alpha} & c_\beta c_\alpha^* A_{\alpha\beta} + c_\beta c_\beta^* A_{\beta\beta} \end{pmatrix}. \end{aligned} \tag{2.30}$$

Inspection of this matrix reveals that the sum of the on-diagonal elements (trace) correspond to the expectation value:

$$\langle\hat{A}\rangle = Tr(\rho A). \tag{2.31}$$

Recall equations 2.19, 2.24 and 2.25. Since the expectation value of $\hat{I}_z$ is determined by $c_\alpha c_\alpha^*$ and $c_\beta c_\beta^*$, whilst those of $\hat{I}_x$ and $\hat{I}_y$ are determined by $c_\alpha c_\beta^*$ and $c_\beta c_\alpha^*$, the diagonal elements of the density matrix correspond to population states, whilst the off-diagonal elements (that represent a mixture of states) represent, in this case, single-quantum (SQ) coherences, which will be discussed later.

2.2.1 The density operator at equilibrium

The coefficients $c_\alpha c_\alpha^*$ and $c_\beta c_\beta^*$ relate to the population states n_α and n_β (where $n_\alpha + n_\beta = N$) respectively, such that:

$$c_\alpha c_\alpha^* = \frac{n_\alpha}{N} \tag{2.32}$$

$$c_\beta c_\beta^* = \frac{n_\beta}{N}. \tag{2.33}$$

The two diagonal elements of the density operator matrix, as discussed in the previous section, correspond to the population states of the system. At thermal equilibrium, the ensemble averages, $c_\alpha c_\beta^*$ and $c_\beta c_\alpha^*$, are zero (as a result of randomly distributed phases cancelling to zero in a real system). Thus the density matrix can be written as follows:

$$\hat{\rho}_{eq} = \begin{pmatrix} n_\alpha(eq)/N & 0 \\ 0 & n_\beta(eq)/N \end{pmatrix}. \tag{2.34}$$

This result provides a starting point for other calculations since all NMR experiments begin with the sample at thermal equilibrium (magnetisation aligned along the *z*-axis). However, since an NMR experiment consists, typically, of radiofrequency (*rf*) pulses combined with periods of free evolution, it is necessary to briefly consider what happens to the density operator as it evolves over time.

2.2.2 The time evolution of the density operator

The density operator can be differentiated with respect to time:

$$\frac{d}{dt}\hat{\rho}(t) = \frac{d}{dt}(|\Psi\rangle\langle\Psi|) = \left(\frac{d}{dt}|\Psi\rangle\right)\langle\Psi| + |\Psi\rangle\left(\frac{d}{dt}\langle\Psi|\right). \tag{2.35}$$

The time-dependent Schrödinger equations (which describe how the system evolves over time) for $|\Psi\rangle$ and $\langle\Psi|$ are as follows:

$$\frac{d}{dt}|\Psi\rangle = -i\hat{H}|\Psi\rangle, \tag{2.36}$$

$$\frac{d}{dt}\langle\Psi| = i\langle\Psi|\hat{H}. \tag{2.37}$$

The density operator can be thought as providing a way to read out the superposition state of a given spin system. Any new interaction which acts upon this system will change the state of the system and hence the relevant density operator description. Substituting these equations into equation 2.35 results in the so called Liouville von Neumann equation, which relates the time evolution of the density operator to the Hamiltonian (the operator of total energy of the system):

$$\frac{d}{dt}\hat{\rho}(t) = -i\big[\hat{H}, \hat{\rho}(t)\big]. \tag{2.38}$$

The solution of equation 2.38 is:

$$\frac{d}{dt}\hat{\rho}(t) = e^{-i\hat{H}t}\hat{\rho}(0)e^{i\hat{H}t} = \hat{U}(t)\hat{\rho}(0)\hat{U}(t)^{-1}, \tag{2.39}$$

where $\hat{\rho}(t)$ is the density operator at time *t*, $\hat{\rho}(0)$ is the density operator at time zero and $\hat{U}(t)$ is the propagator which simply describes the Hamiltonian acting between times $t = 0$ and $t = t$. For a constant (i.e. time-independent) Hamiltonian, the propagator can be written as:

$$\hat{U}(t) = e^{-i\hat{H}t}. \tag{2.40}$$

In the majority of cases, where the Hamiltonian is not constant between $t = 0$ and $t = t$, but where different Hamiltonians are present at different points of the experiment, the propagator can be expressed as a series of exponentials of the Hamiltonians:

$$\hat{U}(t) = e^{-iH_n t_n} \ldots e^{-iH_2 t_2} e^{-iH_1 t_1}, \tag{2.41}$$

with the individual Hamiltonians considered in chronological order. Hamiltonian descriptions of NMR relevant interactions are discussed in further detail later.

2.3 Hamiltonians

All relevant interactions acting upon a spin system during the course of an NMR experiment can be described by a total Hamiltonian operator. These interactions include external considerations, chiefly the interaction of the system with external magnetic fields, and internal interactions which describe the interaction of the spin system with its surrounding environment. A total Hamiltonian operator can be constructed such that:

$$\hat{H}_{total} = \hat{H}_{ext} + \hat{H}_{int}, \tag{2.42}$$

which can be expanded to:

$$\hat{H}_{total} = \left(\hat{H}_Z + \hat{H}_{rf}\right) + \left(\hat{H}_\sigma + \hat{H}_D + \hat{H}_Q + \hat{H}_J\right). \tag{2.43}$$

In equation 2.43:

$\hat{H}_Z$ = Zeeman interaction

$\hat{H}_{rf}$ = *rf* irradiation

$\hat{H}_\sigma$ = chemical shielding

$\hat{H}_D$ = dipolar coupling

$\hat{H}_Q$ = quadrupolar interaction

$\hat{H}_J$ = *J* coupling (scalar coupling)

The $\hat{H}_{ext}$ terms consist of the Zeeman interaction ($\hat{H}_Z$) and the perturbing effect of *rf* oscillating magnetic fields ($\hat{H}_{rf}$).

In general, a Hamiltonian used to describe an operator, $\hat{A}$, can be expressed in Cartesian coordinates as follows:

$$\hat{H}_A = \hat{I}\tilde{A}\hat{S} = \left(\hat{I}_x\hat{I}_y\hat{I}_z\right)\begin{pmatrix} A_{xx} & A_{xy} & A_{xz} \\ A_{yx} & A_{yy} & A_{yz} \\ A_{zx} & A_{zy} & A_{zz} \end{pmatrix}\begin{pmatrix} \hat{S}_x \\ \hat{S}_y \\ \hat{S}_z \end{pmatrix}, \tag{2.44}$$

where $\hat{I}$ represents a spin operator $\hat{I}$, $\tilde{A}$ describes the interaction and $\hat{S}$ can be a further interacting spin operator or an external variable, such as the magnetic field.

2.3.1 External interactions

In a fixed, uniform external magnetic field, B_0, the Hamiltonian describing the interaction between this field and a given nuclear spin, $\hat{I}$, is given by:

$$\hat{H}_Z = -\gamma B_0 \hat{I}_z = \omega_0 \hat{I}_z. \tag{2.45}$$

In solid-state NMR, and indeed NMR more generally, the B_0 magnetic field is generally of the order of 5 – 25 Tesla (T). However, conventionally, B_0 magnetic field strengths are usually referred to in terms of the ^{1}H Larmor frequency at that field strength. For instance a B_0 field operating at 14.1 T is more commonly referred to as a 600 MHz spectrometer. Spectrometers with field strengths up to and including 850 MHz are now routinely found in NMR laboratories across the world, with the absolute upper limit currently at just over 1 GHz.

2.3.2 Oscillating radiofrequency magnetic fields

Since only transverse magnetisation is observable in an NMR experiment, owing to the position of the coil in the probe-head, it is necessary to excite coherence states (the off-diagonal elements of the density matrix) by applying weak magnetic fields to the equilibrium magnetisation. If this magnetic field has an oscillation frequency comparable to that of the Larmor frequency of the nuclear spins of interest, such that $\omega_{rf} \approx \omega_0$, then this radiofrequency pulse consequently manipulates the equilibrium magnetisation. One can write this oscillating field as follows:

$$B_1(t) = 2B_1\big(cos\big[\omega_{rf}t + \phi\big]\big)\boldsymbol{i} = B_1\big[e^{i\omega_{rf}t} + e^{-i\omega_{rf}t}\big]\boldsymbol{i} \qquad if\ \phi = 0. \tag{2.46}$$

$\boldsymbol{i}$ is a unit vector along the axis under consideration and ϕ describes the initial phase of the *rf* pulse. According to the equation above, the weak magnetic field, $B_1(t)$, consists of two counter rotating fields, with characteristic frequencies $+\omega_{rf}$ and $-\omega_{rf}$. In order to simplify matters, $-\omega_{rf}$ can be ignored since only $+\omega_{rf}$ is sufficiently close to the Larmor frequency to have an effect upon the magnetisation. The corresponding Hamiltonian is thus:

$$\hat{H}_{rf} = -\gamma B_1\big[\hat{I}_x \cos\big(\omega_{rf}t + \phi\big) + \hat{I}_y \sin\big(\omega_{rf}t + \phi\big)\big]. \tag{2.47}$$

This equation is simplified by transforming from the so called laboratory frame of reference to the rotating frame, the concept of which was introduced in section 2.1. In the laboratory frame, there are two superimposed oscillations: the oscillating *rf* field and the resulting oscillation of the manipulated magnetisation about the *z*-axis (B_0). Since only $+\omega_{rf}$ rotates in the same sense as the Larmor frequency

(on-resonance as discussed above) one can view the NMR experiment in the rotating frame in which the time dependence of the various oscillations is removed i.e. the magnetisation rotates about the *z*-axis with angular frequency $+\omega_{rf}$ (the rotating *rf* field appears static). The Hamiltonian can now be written as:

$$\hat{H}_{rf}^{ROT} = -\gamma B_1\left[\hat{I}_x \cos(\phi) + \hat{I}_y \sin(\phi)\right], \tag{2.48}$$

or,

$$\hat{H}_{rf}^{ROT} = \omega_1\left[\hat{I}_x \cos(\phi) + \hat{I}_y \sin(\phi)\right], \tag{2.49}$$

where $\omega_1 = -\gamma B_1$ is the nutation frequency of the *rf* pulse. The initial phase, ϕ, defines the orientation of the pulse applied in the $x-y$ plane i.e. if we apply $\phi = 0$:

$$\hat{H}_{rf}^{ROT} = \omega_1 \hat{I}_x. \tag{2.50}$$

Therefore, the pulse appears, in the *x*-axis, as a static magnetic field in this instance.

The time dependent density operator for such an *rf* pulse is described using the solution to the Liouville von Neumann equation:

$$\hat{\rho}(t) = e^{-i\omega_1 t\hat{I}_x}\hat{\rho}(0)e^{i\omega_1 t\hat{I}_x}. \tag{2.51}$$

The nuclear spins, at equilibrium, exist in the $\hat{I}_z$ state, hence:

$$\hat{\rho}(0) = \hat{I}_z. \tag{2.52}$$

In matrix form, $\hat{\rho}(t)$ can be expressed as:

$$\hat{\rho}(t) = \frac{1}{2}\begin{pmatrix} \cos(\omega_1 t) & isin(\omega_1 t) \\ -isin(\omega_1 t) & -cos(\omega_1 t) \end{pmatrix}. \tag{2.53}$$

It can be seen, therefore, that the *rf* pulse has created both populations (diagonal elements) and coherences (off-diagonal elements). The expectation values are therefore determined as:

$$\langle \hat{I}_x \rangle = Tr[\rho I_x] = 0, \tag{2.54}$$

$$\langle \hat{I}_y \rangle = Tr[\rho I_y] = -\frac{1}{2}\sin(\omega_1 t), \tag{2.55}$$

$$\langle \hat{I}_z \rangle = Tr[\rho I_z] = \frac{1}{2}\cos(\omega_1 t). \tag{2.56}$$

An *rf* pulse applied along the *x*-direction acts to rotate the equilibrium magnetisation about the *x*-axis by an amount determined by the flip angle, β. This angle is defined as:

$$\beta = \omega_1 t_p, \tag{2.57}$$

and hence is determined by ω_1. Since an NMR experiment detects magnetisation only in the transverse plane, a pulse with a flip angle equal to $\pi/2$ applied to spin – ½ nuclei will create a single-quantum coherence state, whilst a π pulse simply inverts the equilibrium population state.

2.3.3 Evolution under a resonance offset

In a manner analogous to the external field, ω_0, the magnitude of ω_1 is dependent upon the nucleus under observation since $\omega_1 = -\gamma B_1$. Generally, ω_1 is on the order of 10 – 100s of kHz, which is much smaller than ω_0, which is of the order of 100s of MHz. The Zeeman interaction in the rotating frame can be expressed as:

$$\hat{H}_Z^{ROT} = (\omega_0 - \omega_{rf})\hat{I}_z = \Omega \hat{I}_z, \tag{2.58}$$

where $\Omega = \omega_0 - \omega_{rf}$ is known as the resonance offset. If this offset is non-zero then a residual field, $\Delta B_0 = -\Omega/\gamma$, results in the rotating frame. The magnetisation will precess about this residual field once the *rf* pulse stops. The resonance offset, therefore, conveniently describes the oscillation frequency with respect to the carrier frequency of the *rf* pulse. This means that NMR signals are observed as a frequency difference (order of kHz) instead of the MHz magnitude of the Larmor frequency.

For initial transverse magnetisation, $\hat{I}_x$, under a resonance offset, the Liouville von Neumann equation can be employed to evaluate the time dependent density operator:

$$\hat{\rho}(t) = e^{-i\Omega t\hat{I}_z}\hat{\rho}(0)e^{i\Omega t\hat{I}_z}, \tag{2.59}$$

where,

$$\hat{\rho}(0) = \hat{I}_x, \tag{2.60}$$

hence,

$$\hat{\rho}(t) = \frac{1}{2}\begin{pmatrix} 0 & e^{-i\Omega t} \\ e^{i\Omega t} & 0 \end{pmatrix}. \tag{2.61}$$

An NMR signal can be calculated by taking the trace of the above matrix and multiplying by the raising operator, $\hat{I}_+ (\equiv \hat{I}_-^\dagger)$:

$$\hat{I}_+ = \hat{I}_x + i\hat{I}_y = \begin{pmatrix} 0 & 1 \\ 0 & 0 \end{pmatrix}. \tag{2.62}$$

The raising operator relates to quadrature detection, which will be described in more detail in chapter 3. In simple terms, quadrature detection involves recording both the real and imaginary components of the free induction decay (FID) (corresponding to two components perpendicular to one another). A detected signal, under a resonance offset, is given by:

$$\begin{aligned} s(t) = Tr[\hat{I}_+, \hat{\rho}] &= Tr\left(\begin{pmatrix} 0 & 1 \\ 0 & 0 \end{pmatrix}\begin{pmatrix} 0 & \frac{1}{2}e^{-i\Omega t} \\ \frac{1}{2}e^{i\Omega t} & 0 \end{pmatrix}\right) = \begin{pmatrix} 0 & 0 \\ 0 & \frac{1}{2}e^{i\Omega t} \end{pmatrix} = \frac{1}{2}e^{i\Omega t} \\ &= \frac{1}{2}\big(\cos(\Omega t) + i sin(\Omega t)\big). \end{aligned} \tag{2.63}$$

In physical reality equation 2.63 states that transverse magnetisation, recorded as both a real and imaginary component, precesses in the $x-y$ plane of the rotating frame at the resonance offset, Ω, which consequently induces a current in the coil, which results in an NMR signal.

2.3.4 Product operators

Product operators act as a simplified representation of the density operator. The approach is a convenient method by which to describe an NMR experiment since it is fundamentally linked to

conventional geometry and the intuitive nature of the vector model. It is especially useful for systems containing more than a few coupled spins, since a description under the density operator formalism in this instance quickly becomes too complex owing to the expanding matrix calculations involved. However, this approach works only for systems evolving under weak scalar (*J*) couplings, and as such is less useful for systems under the influence of the stronger interactions which often exist between nuclei i.e. dipolar couplings, nor do product operators take into account the important effect relaxation has upon the system. That being said, the product operator approach may still be used in some cases where dipolar couplings mediate polarisation transfer, such as the ^{14}N – ^{1}H HMQC experiment. The method is also important in solid-state NMR to describe techniques in which polarisation transfer is mediated *via J*-couplings, such as the refocused ^{1}H – ^{13}C INEPT (insensitive nuclei enhanced by polarisation transfer) experiment, which uses the magnetisation advantage of high γ nuclei (such as ^{1}H) to enhance the weak NMR signals of low γ nuclei (such as ^{13}C). In such cases the standard vector model is no longer sufficient to fully describe the experiment.

For a system containing an isolated spin = ½ nucleus, four operators are required to describe an NMR experiment:

$$\frac{1}{2}E, \quad I_x, \quad I_y, \quad I_z, \tag{2.64}$$

where E is the identity operator and I_x, I_y and I_z correspond to the *x*, *y* and *z* components of the magnetisation in the rotating frame, respectively.

When an *rf* pulse is applied, about the *y*-axis, to this system, with a flip angle β, the effect on the bulk magnetisation can be written as follows:

$$I_x \overset{\beta_y}{\rightarrow} I_x cos\beta - I_z sin\beta \tag{2.65}$$

$$I_y \overset{\beta_y}{\rightarrow} I_y \tag{2.66}$$

$$I_z \overset{\beta_y}{\rightarrow} I_z cos\beta + I_x sin\beta. \tag{2.67}$$

What this means in effect is, for a flip angle, $\beta = \frac{\pi}{2}$, with phase *y*, applied to the equilibrium magnetisation, I_z, magnetisation ends up aligned with the *x*-axis. The same pulse applied to the I_x component results in magnetisation aligned along –*z*. The pulse has no effect upon the I_y component.

Evolution of the system under a resonance offset can also be described using this formalism. Consideration of the effect upon the I_x component yields:

$$I_x \overset{\Omega t}{\rightarrow} I_x cos\Omega t + I_y sin\Omega t. \tag{2.68}$$

Product operators can also be viewed in relation to energy level diagrams as demonstrated in Fig. 2.3.

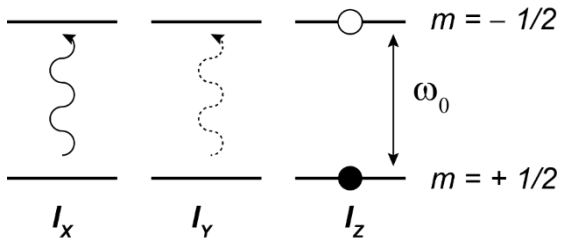

Figure 2.3 Schematic representation of the product operators for an isolated spin- ½ nucleus in terms of energy level diagrams. The solid and dashed lines represent the phase difference of π/2 between I_x and I_y. The black and white circles indicate a population excess and deficit respectively. Adapted from Hore, Jones and Wimperis.(164)

As was described previously, I_z corresponds to a population state (in the case of Fig. 2.3 at thermal equilibrium) i.e. the spin may be aligned parallel to the external static field (α) which is lower in energy or aligned anti-parallel to the field (β) which, consequently, is higher in energy. The I_x and I_y components correspond to coherences.

Product operators can describe the evolution of a system under a *J* coupling between two chemically bonded spin = ½ nuclei, *I* and *S*. The product operators for the system can be constructed by taking products of the four operators described at the start of this section.

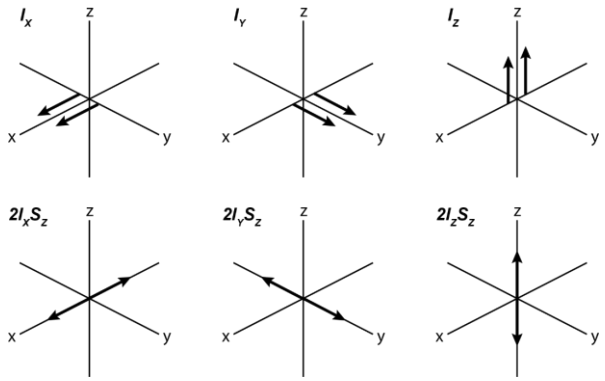

Figure 2.4 Vector representation of several product operators for a two-spin IS spin system. Adapted from ref (164).

	$\frac{1}{2}E$	S_x	S_y	S_z
$\frac{1}{2}E$	$\frac{1}{2}E$	S_x	S_y	S_z
$2I_x$	I_x	$2I_xS_x$	$2I_xS_y$	$2I_xS_z$
$2I_y$	I_y	$2I_yS_x$	$2I_yS_y$	$2I_yS_z$
$2I_z$	I_z	$2I_zS_x$	$2I_zS_y$	$2I_zS_z$

The factor of 2 on the left is a result of normalisation.

The four operators, $2I_xS_x$, $2I_xS_y$, $2I_yS_x$, $2I_yS_y$, represent multiple-quantum (MQ) coherences, which are not directly observable in an NMR experiment since they do not induce a current in the coil. The remaining operators can be viewed with respect to the vector model, as shown in Fig. 2.4.

I_x, I_y, I_z, S_x, S_y, and S_z are referred to as in-phase operators while $2I_xS_z$, $2I_yS_z$, $2I_zS_x$, $2I_zS_y$ and $2I_zS_z$ are antiphase operators (see Fig. 2.4). Considering magnetisation residing upon I_x only, then evolution under a *J* coupling is given by:

$$I_x \xrightarrow{\pi J_{IS}t} I_x cos\pi J_{IS}t + 2I_yS_z sin\pi J_{IS}t. \tag{2.69}$$

This means that magnetisation, which in this case initially resides upon the *I* spin, will evolve in time into a coupled state involving the *S* spin also. This essentially describes magnetisation transfer *via* a chemical bond i.e. *J* coupling. For systems evolving under *J* couplings only, evolution under this

coupling and a resonance offset can be treated in a sequential manner using product operators, despite evolution under these interactions occurring at the same time.

2.4 Internal interactions

The total Hamiltonian of the system, which describes the total energy and was introduced in section 2.3, contains contributions from both external interactions arising from the influence of magnetic fields upon the system, and internal interactions, which are of considerably smaller magnitude (when compared to the static B_0 field), which pertain to the interplay within the spin system under consideration and the local environment of a spin. The power of the NMR experiment lies in its ability to probe the perturbations in the system caused by the interaction between internal couplings and external stimuli, such as an *rf* pulse.

These internal interactions are, for the most part, so small when compared to the dominant Zeeman interaction, that they can in essence be treated as perturbations to first order of this energy, with the notable exception of the quadrupolar interaction, which must be considered to higher order perturbations depending on the nuclear species in question. Such an approximation is referred to as the high field or secular approximation:

$$\hat{H}_{total} = \hat{H}_0 + \hat{H}_1, \tag{2.70}$$

where $\hat{H}_0$ is the Zeeman interaction and $\hat{H}_1$ is the first order perturbation as a result of the remaining interactions acting upon the system.

2.4.1 Rotations

In section 2.3, it was shown that external interactions can be described sufficiently using the Cartesian axis system of the laboratory frame (which is subsequently simplified further to the rotating frame of reference). Since each internal interaction can be described by a second rank tensor, owing to their orientation dependence in three dimensions, each internal interaction is more correctly described with respect to their own unique frame of reference. Therefore, each interaction must be transformed from this Principal Axis System (PAS), in which only the on-diagonal elements of the interaction tensor are considered, into the laboratory frame of reference. Only then can the true effect of an internal interaction upon the spin system be correctly described.

For simplicity, such transformations are described by considering each internal interaction in terms of spherical tensor notation, thereby not requiring the more traditional Cartesian representation i.e.,

$$\hat{H}_A = \hat{I}\tilde{A}\hat{S} = \begin{pmatrix}\hat{I}_x \hat{I}_y \hat{I}_z\end{pmatrix}\begin{pmatrix}A_{xx} & A_{xy} & A_{xz}\\ A_{yx} & A_{yy} & A_{yz}\\ A_{zx} & A_{zy} & A_{zz}\end{pmatrix}\begin{pmatrix}\hat{S}_x\\ \hat{S}_y\\ \hat{S}_z\end{pmatrix}, \tag{2.71}$$

is transformed to:

$$\hat{H}_A = \sum_{j=0}^{2}\sum_{m=-j}^{+j}(-1)^m A_{jm}\hat{T}_{j-m}\,, \tag{2.72}$$

where A_{jm} is the spatial component and $\hat{T}_{j-m}$ the spin component of the irreducible spherical tensor. A_{jm} represents, therefore, the magnitude of the internal interactions, whilst $\hat{T}_{j-m}$ represents the necessary quantum mechanical operators. Under mechanical rotations (transformations), only the spatial component is affected. j and m represent the order and rank of the tensor, respectively. j can take integer values 0, 1, 2, 3, … and m can take $2j + 1$ values from $+j$ to $-j$. Since the interaction tensor is diagonalised in the PAS, the above equation is simplified to:

$$\hat{H}_A^{PAS} = A_{00}^{PAS}\hat{T}_{00} + A_{20}^{PAS}\hat{T}_{20} + A_{22}^{PAS}\hat{T}_{2-2} + A_{2-2}^{PAS}\hat{T}_{22}. \tag{2.73}$$

Note that not all components are present for all internal interactions, depending upon whether the specific interaction has isotropic, anisotropic or, in some cases, a mix of isotropic and anisotropic components. A list of properties for various NMR interaction tensors in their PASs is presented below,

$\tilde{A}$ (interaction tensor)	Trace	Anisotropy	Non-zero A_{jm}^{PAS}
$\tilde{\sigma}$ (chemical shielding)	Yes, $A_{xx} + A_{yy} + A_{zz} \neq 0$	Both isotropic and anisotropic	$A_{00}^{PAS}, A_{20}^{PAS}, A_{2\pm2}^{PAS}$
$\tilde{J}$ (J-coupling)	Yes, $A_{xx} + A_{yy} + A_{zz} \neq 0$	Only isotropic part considered (except for heavy atoms)	A_{00}^{PAS}
$\tilde{D}$ (dipolar coupling)	No $A_{xx} + A_{yy} + A_{zz} = 0$	Anisotropic only	A_{20}^{PAS}
$\tilde{V}$ (quadrupolar interaction)	No $A_{xx} + A_{yy} + A_{zz} = 0$	Anisotropic only (to first order)	$A_{20}^{PAS}, A_{2\pm2}^{PAS}$

Since the rank of a spherical tensor is invariant under a rotation, spherical tensor descriptions of the transformation from the PAS to the laboratory frame are more convenient than classical Cartesian descriptions.

It is usual to employ the three Euler angles when transforming between reference frames, as given by the so called rotation operator:

$$\hat{R}(\alpha,\beta,\gamma) = \hat{R}_z(\alpha)\hat{R}_y(\beta)\hat{R}_z(\gamma). \tag{2.74}$$

These Euler angles, as defined by Cartesian coordinates, are presented in Fig. 2.5.

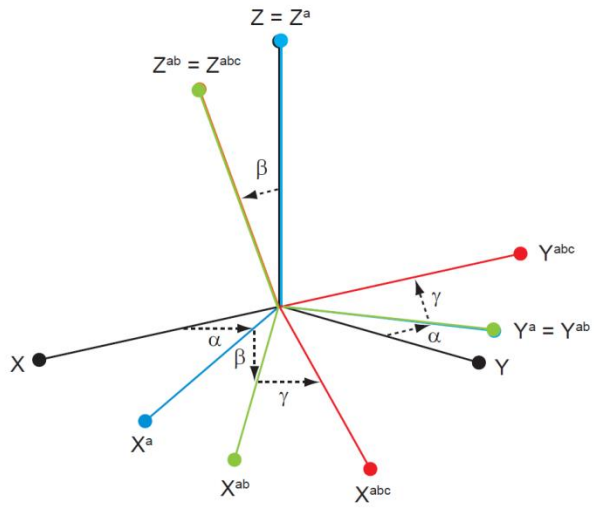

Figure 2.5 Euler angles defined in a Cartesian coordinate system.

Group theory can be employed to show that a spherical tensor component, A_{jm}, is converted by a rotation into a sum of components with identical rank, but varying order:

$$\hat{R}(A_{jm}) = \sum_{m'=-j}^{m'=+j} D^{j}_{m'm}(\alpha\beta\gamma)A'_{jm'}, \tag{2.75}$$

where $D^{j}_{m'm}(\alpha\beta\gamma)$ represents the Wigner matrix elements:

$$D^{j}_{m'm}(\alpha\beta\gamma) = e^{-im'\alpha}d^{j}_{m'm}(\beta)e^{-im\gamma}, \tag{2.76}$$

where $d^{j}_{m'm}(\beta)$ is a trigonometric function and is known as the reduced Wigner rotation matrix.

Therefore, in an NMR experiment, a rotation from the PAS to the laboratory frame (L) is given by:

$$\hat{A}^{L}_{jm'} = \sum_{m=-j}^{+j} A^{PAS}_{jm'} D^{j}_{mm'}(\alpha_{PL}, \beta_{PL}, \gamma_{PL}), \tag{2.77}$$

where $(\alpha_{PL}, \beta_{PL}, \gamma_{PL})$ describe the Euler angles between the two frames of reference. For a static sample, the expression becomes:

$$\hat{H}^{L} = \sum_{j=0}^{2} \sum_{m=-j}^{+j} (-1)^{m} A^{PAS}_{jm} D^{j}_{mm}(\alpha_{PL}, \beta_{PL}, \gamma_{PL}) \hat{T}_{j-m}. \tag{2.78}$$

2.4.2 The secular approximation

The secular approximation, introduced earlier, in which internal interactions are considered as first order perturbations of the dominant Zeeman interaction, effectively means that only spin terms which commute with the Zeeman interaction $(\hat{I}_Z)$ are retained,i.e.,

$$[\hat{I}_Z, \hat{T}_{jm}] = m\hat{T}_{jm}. \tag{2.79}$$

A commutation relation is only obtained, in this case, when $m = 0$, therefore, only A^{L}_{j0} terms are retained:

$$\hat{H}^{L} = A^{L}_{00}\hat{T}_{00} + A^{L}_{20}\hat{T}_{20}, \tag{2.80}$$

where A^{L}_{00} and A^{L}_{20} correspond to the isotropic and anisotropic part of a given internal interaction.

Note that the secular approximation only holds if the B_0 field is sufficiently high so that the Zeeman interaction dominates over all other interactions by several orders of magnitude.

2.4.3 Chemical shielding

In an experiment, the NMR frequency, in Hz, of a given nucleus is principally determined by the magnetogyric ratio and the magnetic field experienced by the nucleus, *via* the following equation:

$$|\nu| = \frac{\gamma B}{2\pi}. \tag{2.81}$$

In a B_0 magnetic field of strength 14.1 T, protons resonate at Larmor frequency of 600 MHz. However, in order to obtain site specific information from a system, one must be able to distinguish between different proton environments within a sample. This is achieved since the different local electronic environment at a given site results in a specific value of ν, close to the Larmor frequency, but crucially different when compared to other protons within the system, and is due to the interaction of the applied magnetic field and the orbital electrons within individual atoms. This is the essence of chemical shielding.

The magnetic field, B, experienced at each individual nucleus is dependent on the local electronic environment, such that:

$$B = B_0 - B' = B_0(1 - \sigma), \tag{2.82}$$

where B_0 is the external applied field and B' is the field caused by the motion of orbital electrons within individual atoms. B' is proportional to B_0, with σ being the constant of proportionality between them, referred to as the shielding constant. The resonance equation thus becomes:

$$|\nu| = \frac{\gamma B_0(1 - \sigma)}{2\pi}. \tag{2.83}$$

In terms of the Hamiltonian of this internal interaction, in Cartesian form, the expression is written as,

$$\hat{H}_{CS} = \boldsymbol{\gamma}\hat{I}\tilde{\sigma}B_0, \tag{2.84}$$

which describes the indirect effect of the electronic environment between the nuclear spin, $\hat{I}$, and the external field. $\tilde{\sigma}$ is the shielding tensor, which is of second rank, and has both a symmetric and antisymmetric component:

$$\tilde{\sigma}_s = \begin{pmatrix} \sigma_{xx} & \frac{1}{2}(\sigma_{xy} + \sigma_{yx}) & \frac{1}{2}(\sigma_{xz} + \sigma_{zx}) \\ \frac{1}{2}(\sigma_{xy} + \sigma_{yx}) & \sigma_{yy} & \frac{1}{2}(\sigma_{yz} + \sigma_{zy}) \\ \frac{1}{2}(\sigma_{xz} + \sigma_{zx}) & \frac{1}{2}(\sigma_{yz} + \sigma_{zy}) & \sigma_{zz} \end{pmatrix}, \tag{2.85}$$

and

$$\tilde{\sigma}_a = \begin{pmatrix} 0 & \frac{1}{2}(\sigma_{xy} - \sigma_{yx}) & \frac{1}{2}(\sigma_{xz} - \sigma_{zx}) \\ \frac{1}{2}(\sigma_{yx} - \sigma_{xy}) & 0 & \frac{1}{2}(\sigma_{yz} - \sigma_{zy}) \\ \frac{1}{2}(\sigma_{zx} - \sigma_{xz}) & \frac{1}{2}(\sigma_{zy} - \sigma_{yz}) & 0 \end{pmatrix}. \tag{2.86}$$

Note that only the symmetric part of the shielding tensor, $\tilde{\sigma_s}$, affects the NMR experiment to any great extent, and hence only this component is considered further.

This matrix is diagonalised in the PAS of the interaction. In spherical tensor form, the Hamiltonian in the PAS is written as:

$$\hat{H}_{CS}^{PAS} = A_{00}^{PAS}\hat{T}_{00} + A_{20}^{PAS}\hat{T}_{20} + A_{2\pm2}^{PAS}\hat{T}_{2\pm2}. \tag{2.87}$$

A transformation from the PAS to the laboratory frame is required, in order to describe the effect of chemical shielding upon the NMR spectrum. The A_{00}^{PAS} term is isotropic and hence is invariant to such a rotation. Using the secular approximation:

$$\begin{aligned} A_{20}^{L} = \sum_{m=-2}^{2} & A_{2m}^{PAS} d_{m0}^{2}(\beta_{PL}) e^{-im\alpha_{PL}} \\ & = A_{20}^{PAS} d_{00}^{2}(\beta_{PL}) + A_{22}^{PAS} d_{20}^{2}(\beta_{PL}) e^{-2im\alpha_{PL}} \\ & + A_{2\pm2}^{PAS} d_{-20}^{2}(\beta_{PL}) e^{2im\alpha_{PL}} \\ & = A_{20}^{PAS} \frac{1}{2}(3\cos^2\beta_{PL} - 1) + A_{2\pm2}^{PAS} \sqrt{\frac{3}{2}} \sin^2\beta_{PL} cos2\alpha_{PL}, \end{aligned} \tag{2.88}$$

where

$$A_{00}^{PAS} = \gamma \sqrt{\frac{1}{3}} \left(\sigma_{xx}^{PAS} + \sigma_{yy}^{PAS} + \sigma_{zz}\hat{}PAS\right) \tag{2.89}$$

$$A_{20}^{PAS} = \gamma \sqrt{\frac{1}{6}} \left(2\sigma_{zz}^{PAS} - \sigma_{xx}^{PAS} - \sigma_{yy}^{PAS}\right) \tag{2.90}$$

$$A_{2\pm2}^{PAS} = \gamma \frac{1}{2}\left(\sigma_{xx}^{PAS} - \sigma_{yy}^{PAS}\right). \tag{2.91}$$

Therefore the Hamiltonian in the laboratory frame can be written as:

$$\hat{H}_{CS}^{L} = \omega_0 \sigma_{iso} + \frac{1}{2}\omega_0 \sigma_{aniso}(3\cos^2\beta_{PL} - 1 + \eta \sin^2\beta_{PL} cos2\alpha_{PL}), \tag{2.92}$$

where σ_{iso} and σ_{aniso} correspond to the isotropic and anisotropic chemical shielding and η is the asymmetry. $\omega_0\sigma_{iso}$ is the isotropic chemical shift frequency relative to the Larmor frequency.

Experimentally the chemical shielding tensor is not measured. Instead one measures the so called chemical shift, δ,

$$\delta = \frac{\omega - \omega_{ref}}{\omega_{ref}} \times 10^6, \tag{2.93}$$

where ω is the observed resonance frequency, ω_{ref} is the reference frequency and the factor of 10^6 corresponds to parts per million (ppm). The chemical shift allows for spectra recorded at different field strengths to be directly compared. One can then define a chemical shift tensor:

$$\delta_{\alpha\beta} = \frac{\sigma_{\alpha\beta}(ref) - \sigma_{\alpha\beta}}{1 - \sigma_{\alpha\beta}(ref)}. \tag{2.94}$$

δ_{iso}, δ_{aniso} and η are defined:

$$\delta_{iso} = \frac{1}{3}\left(\delta_{xx}^{PAS} + \delta_{yy}^{PAS} + \delta_{zz}^{PAS}\right), \tag{2.95}$$

$$\delta_{aniso} = \delta_{zz}^{PAS} - \delta_{iso}, \tag{2.96}$$

$$\eta = \frac{\delta_{xx}^{PAS} - \delta_{yy}^{PAS}}{\delta_{aniso}}. \tag{2.97}$$

The relative magnitudes of the three principal components of the chemical shielding are, according to the Haeberlen convention:(167)

$$|\delta_{zz}^{PAS} - \delta_{iso}| \geq |\delta_{xx}^{PAS} - \delta_{iso}| \geq |\delta_{yy}^{PAS} - \delta_{iso}|. \quad (2.98)$$

These components can be physically represented as the dimensions of an ellipsoid. Since chemical shielding depends on the electronic ground state of a given species, it follows that elements with more electrons i.e. heavier elements, usually have larger chemical shift ranges ($\delta(^{14}N) > \delta(^{13}C) > \delta(^{1}H)$).

Since the chemical shift has both an isotropic and anisotropic component, the orientation of a nucleus with respect to the laboratory frame is important. In solution-state NMR, the rapid tumbling of molecules over the NMR timescale precludes the estimation of nuclear orientation, thereby averaging the anisotropic component to zero. As such, only isotropic values are experimentally observed. In a powdered sample, all possible orientations are sampled, leading to a distribution of chemical shifts i.e. a powder pattern is observed. In order to resolve NMR resonances, one must employ magic angle spinning (MAS) which will be discussed later.

2.4.4 Dipolar coupling

Nuclei placed within an external magnetic field will generate a secondary magnetic field. Such a field will interact directly with other fields from other nuclei, through space, with this interaction commonly referred to as the dipole – dipole interaction or dipolar coupling. Classically, this interaction can be described as the interaction between pairs of bar magnets. Note that this interaction is quite different from the indirect *J* coupling, which is mediated *via* electrons.

In solution-state NMR, the effect of dipolar couplings are not observed since the interaction is averaged to zero by fast molecular tumbling (since the dipolar coupling tensor is traceless and hence has only an anisotropic component). In the solid state however, for spin ½ nuclei, the magnitude of the interaction usually forms the major contribution to the observed line broadening. That being said, since the dipolar coupling is a direct interaction between nuclei, mediated through space, the interaction is intrinsically dependent upon the intermolecular separation between sites, and hence may be exploited to yield the structural constraints of the system.

If we now consider the quantum mechanical case for a simple isolated spin ½ pair, *I* and *S*, there exist four possible Zeeman transition states which in simplistic terms correspond to whether a spin is aligned with or against the external field. This is demonstrated in Fig. 2.6.

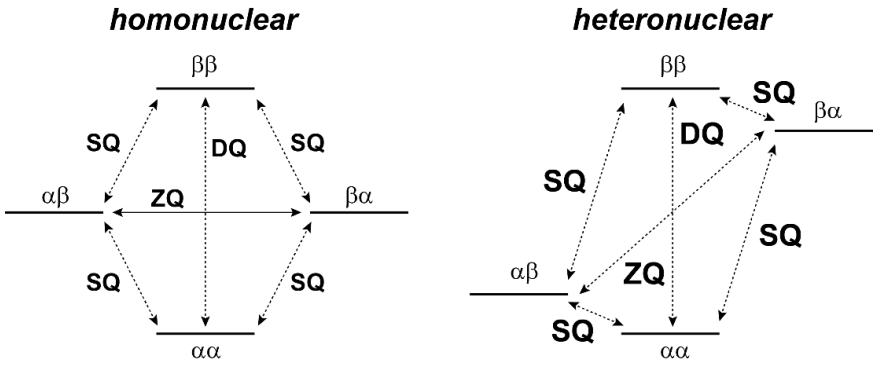

Figure 2.6 Energy level diagrams for a spin ½ pair interacting via a dipolar coupling for both the homonuclear and heteronuclear case. Note that transitions between Zeeman eigenstates correspond to coherence changes.

Transitions between the $|\alpha\alpha\rangle$ and $|\beta\beta\rangle$ energy level is referred to as double-quantum (DQ) coherence, whilst those between $|\alpha\beta\rangle$ and $|\beta\alpha\rangle$ correspond to a zero-quantum (ZQ) transition. All other possible transitions are referred to as single-quantum (SQ) coherence. Note the difference between homonuclear i.e. ^{1}H – ^{1}H and heteronuclear i.e. ^{1}H – ^{13}C, $|\alpha\beta\rangle$ and $|\beta\alpha\rangle$ energy levels. In the homonuclear case these levels have essentially degenerate energy. However in the heteronuclear case the energy difference can be of the order of 100s of MHz, meaning that the dipole-dipole interaction (of kHz magnitude) is never sufficient to drive ZQ polarisation transfer between these states. In order to solve this problem, experimentally, one must employ double-resonance pulse sequences such as cross-polarisation (CP) MAS, which transfers polarisation from, say, protons to the lower gamma nuclei. Such methods will be discussed in detail in chapter 3.

The dipolar Hamiltonian, in Cartesian coordinates, is written as:

$$\hat{H}_D = 2\sum_{i<j} \hat{I}_i \tilde{D} \hat{S}_j, \tag{2.99}$$

where $\hat{I}_i$ and $\hat{S}_j$ represent the coupled spins. Since the dipolar coupling strength, for a ^{1}H – ^{1}H pair, is usually on the order of 10s of kHz, the Zeeman interaction is still the dominant interaction influencing the system. Hence, it is necessary to rotate from the dipolar PAS, aligned along the internuclear vector between two coupled sites, into the laboratory frame. For this interaction, only the A_{20}^{PAS} term is non-zero, therefore,

$$\hat{H}_D^{PAS} = A_{20}^{PAS} \hat{T}_{20}, \tag{2.100}$$

where

$$A_{20}^{PAS} = \sqrt{6} d_{IS}, \tag{2.101}$$

where d_{IS} is defined as the dipolar coupling constant (in rad/s):

$$d_{IS} = -\hbar \left(\frac{\mu_0}{4\pi}\right) \frac{1}{r^3} \gamma_I \gamma_S. \tag{2.102}$$

Note the r^3 dependence on the internuclear distance. Dividing by an additional factor of 2π is necessary to convert from radians to hertz.

By invoking the secular approximation, only $m = 0$ terms in the laboratory frame need to be considered, therefore under static conditions:

$$A_{20}^{L} = A_{20}^{PAS} D_{00}^{2} = \sqrt{6} d_{IS} \left\{ e^{-i\alpha_{PL}0} d_{00}^{2}(\beta_{PL}) e^{-i\gamma_{PL}0} \right\} = \sqrt{6} d_{IS} \frac{1}{2} (3\cos^2 \beta_{PL} - 1), \tag{2.103}$$

and under MAS,

$$A_{20}^{L} = \sqrt{6} d_{IS} \frac{1}{2} (3\cos^2 \beta_{PR} - 1) \frac{1}{2} (3\cos^2 \beta_{RL} - 1). \tag{2.104}$$

The corresponding spin term is written as:

$$\hat{T}_{20} = \frac{1}{\sqrt{6}} \left(\hat{I}_z \hat{S}_z - \frac{1}{2} \left(\hat{I}_x \hat{S}_x + \hat{I}_y \hat{S}_y \right) \right). \tag{2.105}$$

The dipolar Hamiltonian, for a static experiment, may therefore be written (in the laboratory frame) as:

$$\hat{H}_{D,het} = d_{IS} \frac{1}{2} (\, 3\cos^2 \beta_{PL} - 1) \left(2\hat{I}_z \hat{S}_z \right) \tag{2.106}$$

for the heteronuclear case and

$$\hat{H}_{D,homo} = d_{IS} \frac{1}{2} (3\cos^2 \beta_{PL} - 1) \left(2\hat{I}_z \hat{S}_z - \left(\hat{I}_x \hat{S}_x + \hat{I}_y \hat{S}_y \right) \right) \tag{2.107}$$

for the homonuclear case. The matrix forms of the spin operators are as follows:

$$2\hat{I}_z\hat{S}_z = \begin{pmatrix} \frac{1}{2} & 0 & 0 & 0 \\ 0 & -\frac{1}{2} & 0 & 0 \\ 0 & 0 & -\frac{1}{2} & 0 \\ 0 & 0 & 0 & \frac{1}{2} \end{pmatrix}, \qquad \left(\hat{I}_x\hat{S}_x + \hat{I}_y\hat{S}_y\right) = \begin{pmatrix} 0 & 0 & 0 & 0 \\ 0 & 0 & \frac{1}{2} & 0 \\ 0 & \frac{1}{2} & 0 & 0 \\ 0 & 0 & 0 & 0 \end{pmatrix}. \tag{2.108}$$

In the case of heteronuclear dipolar coupling, the off-diagonal elements of the corresponding matrix are zero, since only the $2\hat{I}_z\hat{S}_z$ spin term is considered in this case. For a pair of spin ½ nuclei, under the influence of a heteronuclear dipolar coupling, the spin eigenstates correspond to the Zeeman product states, shown in Fig. 2.6, αα, αβ, βα, ββ. A typical lineshape, obtained under static conditions for a system under heteronuclear dipolar coupling, is known as a Pake doublet as shown in Fig. 2.7. The two horns represent two different crystallite orientations, both being perpendicular to the external field, B_0 (corresponding to the two different transitions having the opposite sign: two *I* spin and two *S* spin transitions for a heteronuclear *I* – *S* spin pair). The separation between the horns is equal to $|d_{IS}|/2\pi$ in Hz. Importantly, this means that the contribution to the line broadening from heteronuclear dipolar coupling has an intrinsic orientation dependence, and hence the effect from this interaction can be fully removed by MAS.

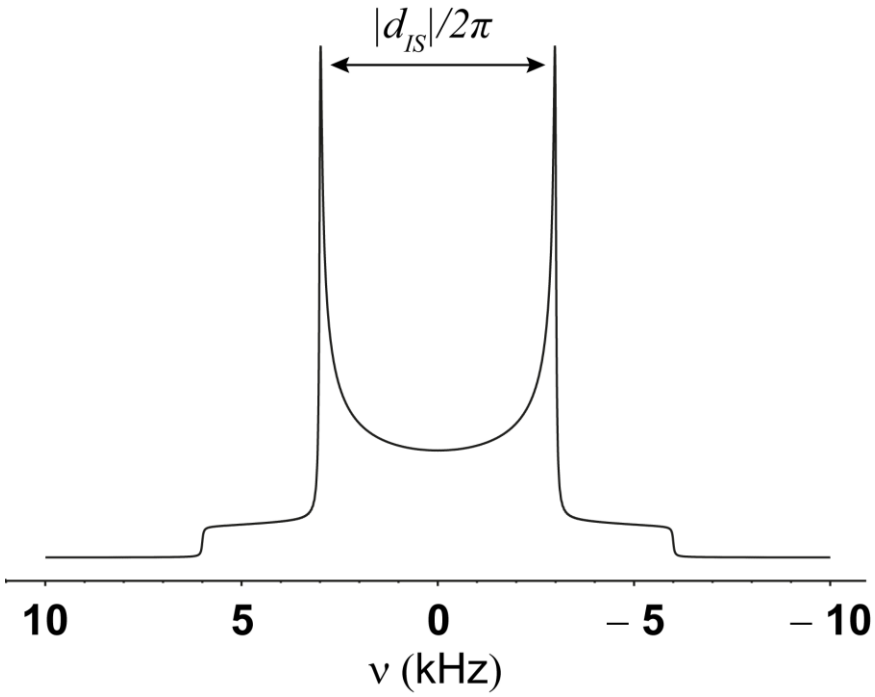

Figure 2.7 Simulated NMR lineshape for a heteronuclear dipolar coupling between two spin – ½ nuclei, in this case $\frac{|d_{IS}|}{2\pi} = 6$ kHz. The above pattern is often referred to as a Pake powder pattern.

Since the majority of the work presented in this thesis concerns itself with homonuclear ^{1}H – ^{1}H dipolar coupling, this more complicated effect must also be considered in some detail. Returning to the homonuclear dipolar Hamiltonian, specifically the matrix representation of the $(\hat{I}_x\hat{S}_x + \hat{I}_y\hat{S}_y)$ spin term, the off-diagonal elements are no longer necessarily non-zero. It is more convenient to express this term as a combination of so-called lowering and raising operators:

$$(\hat{I}_x\hat{S}_x + \hat{I}_y\hat{S}_y) \equiv (\hat{I}_-\hat{S}_+ + \hat{I}_+\hat{S}_-). \tag{2.109}$$

These terms are often referred to as a flip-flop term. Importantly the spin eigenstates for a pair of spin ½ nuclei are no longer simple Zeeman product states but rather a linear combination of Zeeman levels, as presented in Fig 2.8.

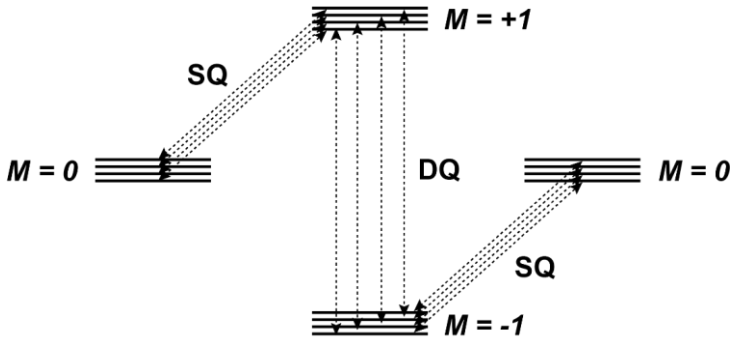

Figure 2.8 Energy level transitions for the homonuclear case (heteronuclear case is different), adapted from Duer.(165)

Therefore, in a real system where one considers a vast network of dipolar coupled protons, a number of degenerate eigenstates exist. This leads to a large range of different transition frequencies in the NMR spectrum, resulting in broadening of individual ^{1}H resonances. In quantum mechanical terms, this means that the dipolar Hamiltonian no longer commutes with itself at different times. Indeed, this phenomenon has the significant consequence that homogeneous line broadening due to a homonuclear dipolar coupled network is only partially removed under magic angle spinning (MAS).

2.4.5 Interactions under magic angle spinning

The principal application of magic angle spinning (MAS) is to remove the effects of the chemical shift anisotropy (CSA) and heteronuclear dipolar coupling (although *rf* decoupling is more effectively employed for this purpose), the magnitudes of which are of the order of ~10 kHz. The technique may also be used to narrow resonances in quadrupolar NMR and, if high spinning frequencies are attainable, can partially remove the line broadening effects of strong homonuclear dipolar couplings.

MAS attempts to achieve the same effect as molecular tumbling in solution i.e. the removal of anisotropic contributions to the line broadening. The orientation dependence of such anisotropic interactions is of the form $3\cos^2\theta - 1$, where θ is the angle which describes the orientation of the spin interaction tensor with respect to the external magnetic field. θ effectively takes all possible values in a powdered sample, since all possible molecular orientations are sampled over the volume of the powder. In experimental terms, MAS pertains to a physical rotation of the sample at a specific angle.

In order to mathematically describe the effects of MAS upon the NMR spectrum, it is necessary to introduce an intermediate rotation between the PAS of the interaction and the laboratory frame (L). Using Euler angles, the rotations are as follows:

PAS – rotor frame: $R(\alpha_{PR}, \beta_{PR}, \gamma_{PR})$,

Rotor frame – laboratory frame: $R(\alpha_{RL}, \beta_{RL}, \gamma_{RL})$.

This is demonstrated in Fig. 2.9. Note also that α_{RL} is subtended by the physical rotation of the rotor, ω_R, thus taking into account the time dependence of the rotation. γ_{RL} defines the rotor phase.

Rotation of the A_{20}^{PAS} term, which for chemical shielding and the dipolar Hamiltonian is non-zero, after the two successive rotations (PAS – rotor, rotor – lab), using the secular approximation, is given by:

$$A_{20}^{L} = A_{20}^{PAS} \sum_{m'=-2}^{2} D_{0m'}^{2}(\alpha_{PR}, \beta_{PR}, \gamma_{PR}) d_{m'0}^{2}(\beta_{RL}) e^{im'\omega_R t}. \qquad (2.110)$$

It follows that, over a complete rotor period (the time taken for one full 360 degree rotation of the rotor), terms with non-zero values of m' will average over that full rotation, to zero:

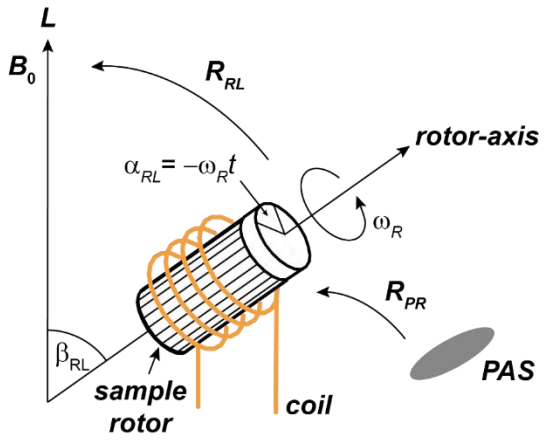

Figure 2.9 Schematic representation of a rotor aligned at β_{RL} relative to the external magnetic field. The time dependence of the rotation is illustrated by α_{RL}, which is a function of the physical spinning frequency, ω_R. The two successive rotations (PAS – rotor, rotor – lab) are presented. The sample coil, in which the nuclear spins create a current resulting ultimately in the NMR signal, is also included for completeness.

$$\int_0^{\tau_R} e^{im'\omega_R t} dt = 0 \qquad if\ m' \neq 0. \tag{2.111}$$

Since the angle $\alpha_{RL} = -\omega_R t$, the interaction Hamiltonian is periodic with a period equal to $\tau_R = 2\pi/\omega_R$. Using average Hamiltonian theory (AHT),(25) the effect of MAS can be described by considering the Hamiltonian only at specific points in time, separated by this periodic time interval. Experimentally, this can be achieved by rotor-synchronised detection/acquisition i.e. detecting the signal only at points separated in time by the rotor period, τ_R. If detection occurs over one complete rotor period, then application of rotation matrices yields:

$$\langle A_{20}^L \rangle = A_{20}^{PAS} d_{00}^2(\beta_{PR}) d_{00}^2(\beta_{RL}) = A_{20}^{PAS} \left[\frac{1}{4}(3\cos^2\beta_{PR} - 1)(3\cos^2\beta_{RL} - 1)\right]. \tag{2.112}$$

It can now be seen that if β_{RL} is set at the so called magic angle of 54.7°, then the anisotropy will reduce to zero over one full rotor period.

Conversely, if the signal is not acquired in a rotor-synchronised fashion, the interaction must be considered over all relevant spatial components i.e. $m' \neq 0$ terms must be considered. The remaining rotation matrices for the MAS condition are:

$$A_{20}^L = A_{20}^{PAS}\left(\frac{1}{2}\sin^2\beta_{PR} cos(2\gamma_{PR} + 2\omega_R t) - \sqrt{2}\sin 2\beta_{PR} cos(\gamma_{PR} + \omega_R t)\right). \tag{2.113}$$

Hence the periodicity of the orientation dependence remains. Experimentally, this effect is seen as manifold spinning sidebands (represented in the above equation by the terms oscillating at ω_R and $2\omega_R$), found at increments of the spinning frequency away from the isotropic resonance. Note that if the dwell time, the time between which data points in the FID are sampled, is set equal to an integer ratio of the rotor period then spinning sidebands are folded back into the spectrum. Spinning sidebands appear when the MAS frequency is smaller than the magnitude of a given internal interaction (the MAS frequency needs to be three to four times greater than the magnitude of the anisotropic interaction in order to reduce the spectrum to a single resonance at the isotropic chemical shift value). Note that for heavier elements such as ^{195}Pt, ^{207}Pb and $^{117,\ 119}$Sn, the magnitude of the CSA is such that even at high spinning frequencies (> 60 kHz) sidebands are still commonly observed. At the time of writing a maximum of 110 kHz MAS is achievable with many laboratories now able to routinely achieve spinning frequencies of up to 60 kHz. At such MAS frequencies, for nuclei such as ^{13}C and ^{15}N, the CSA is fully reduced (sidebands not observed). For ^{1}H experiments, the magnitude of the homonuclear dipolar coupling is such that one still observes broadened lineshapes in a typical organic sample.

2.4.6 Scalar coupling

By some distance the weakest of the internal interactions, with values typically no greater than a few 100 Hz (except for heavy atoms), scalar (*J)* couplings correspond to a through-bond interaction which is mediated by electrons (in comparison to the dipolar coupling which is a through-space interaction). The tensor describing the interaction has both isotropic and anisotropic components.

The magnitude of the anisotropic *J* coupling, when compared to say a typical dipolar coupling strength, is such that, for the purposes of the work presented herein, its influence can be safely ignored. The isotropic component is the scalar average/trace of the interaction tensor (hence the name scalar coupling), such that:

$$J_{iso} = \frac{1}{3}Tr\{J\} = \frac{1}{3}\left(J_{xx} + J_{yy} + J_{zz}\right). \tag{2.114}$$

The magnitude of the isotropic *J* coupling is such that it is often superseded by the intrinsic linewidth and the dominance of the homonuclear ^{1}H dipolar coupling, hence, it is rarely directly observed in the solid state. However, many experiments can be employed which exploit the *J* coupling as a means of polarisation transfer.

The Hamiltonian can be expressed:

$$\hat{H}_J = \sum_{i<j} \hat{I}_i \tilde{J} \hat{S}_j, \tag{2.115}$$

where $\tilde{J}$ is the coupling tensor, and $\hat{I}_i$ and $\hat{S}_j$ correspond to two spins (homo- or heteronuclear) which are connected *via* a chemical bond. Since isotropic *J* couplings have no orientation dependence they are invariant under MAS.

2.4.7 The quadrupolar interaction

For nuclei with spin > 1/2, another form of coupling exists, in addition to the scalar and dipolar coupling discussed above, known as the quadrupolar coupling. This interaction, unlike the dipolar interaction, is an electric rather than magnetic interaction. Spins which fall into this category, accounting for around three quarters of all NMR active nuclei, possess a nuclear electric quadrupole moment (eQ), in addition to a magnetic dipole and electric monopole moment (shown in Fig. 2.10), which interacts with the so-called electric field gradient (EFG) traversing the nucleus. The quadrupole moment (Q) of a given nucleus is a fixed quantity and can take positive (^{27}Al, I = 5/2, Q = 14.66 fm^2) or negative (^{17}O, I = 5/2, Q = −2.558 fm^2) values. These values arise from charge distribution within a given nucleus.

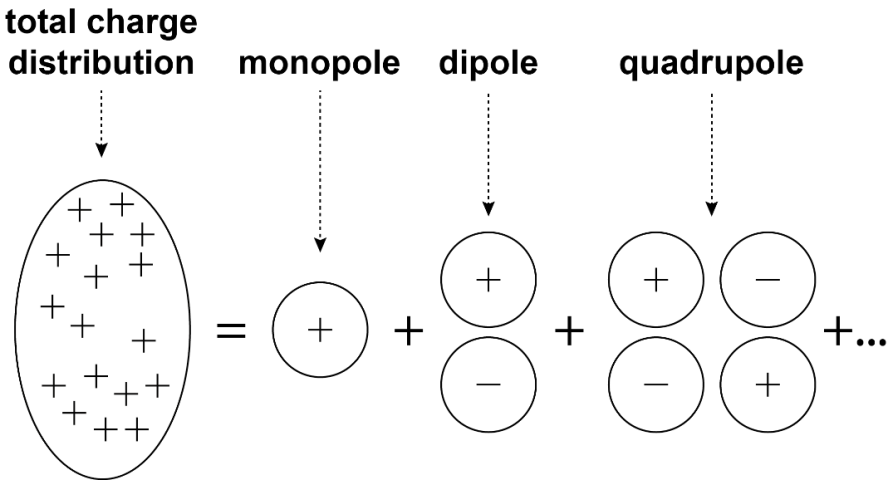

Figure 2.10 Schematic representation of the expansion of charge distribution (say that in a nucleus) as a series of multipoles. Adapted from Duer.(165)

Importantly, the quadrupolar interaction is significantly larger (MHz) than the other internal interactions discussed in this chapter (kHz to Hz). However, the Zeeman interaction is (usually) still approximately ten times greater than the strongest quadrupolar interaction. Hence, the interaction can still be treated as a perturbation of the Zeeman energy. The Hamiltonian, in Cartesian coordinates, can be written as:

$$\widehat{H}_Q = \frac{eQ}{2I(2I-1)\hbar}\hat{I}\tilde{V}\hat{I}, \qquad (2.116)$$

where $\tilde{V}$ is represented by a tensor describing the Cartesian components of the EFG,

$$\tilde{V} = \begin{pmatrix} V_{xx} & V_{xy} & V_{xz} \\ V_{yx} & V_{yy} & V_{yz} \\ V_{zx} & V_{zy} & V_{zz} \end{pmatrix}. \quad (2.117)$$

For a nucleus at a site of cubic symmetry, the EFG is zero. However, local environments in real systems tend to lower the symmetry about a given nucleus. In order to describe the nature of the interaction, it is necessary to describe the anisotropy of the EFG. However, it is more convenient to describe the nuclear quadrupole coupling constant (C_Q), which is proportional to the anisotropy, with a low C_Q value indicative of high symmetry about the nucleus in question. The components of the tensor $\tilde{V}$, in the PAS, are described by the parameters C_Q and η_Q:

$$C_Q = \frac{e^2 qQ}{h} = \frac{eQV_{zz}}{h}, \quad (2.118)$$

and

$$\eta_Q = \frac{V_{xx} - V_{yy}}{V_{zz}}, \quad (2.119)$$

where

$$|V_{xx}| \leq |V_{yy}| \leq |V_{zz}|. \quad (2.120)$$

The asymmetry parameter, η_Q, describes the strength of the field relative to three orthogonal directions, *x*, *y* and *z*. An η_Q of zero represents an EFG that is axially symmetric. A value of one indicates high asymmetry.

The magnitude of the quadrupolar coupling is such that, for systems with small quadrupolar interactions, the interaction may be sufficiently treated as a first-order perturbation to the Zeeman energy. However, when the value of C_Q is large, higher order perturbations, specifically second-order, must be considered. Since, in all practical cases for NMR, the quadrupolar interaction is smaller than the total Zeeman energy, the quadrupolar Hamiltonian must be rotated from its PAS into the laboratory frame. Expressing the Hamiltonian in spherical tensor form, the expression, in the PAS, may be written as:

$$\hat{H}_Q^{PAS} = \frac{2\pi}{2I(2I-1)}\left(A_{20}^{PAS}\hat{T}_{20} - A_{22}^{PAS}\hat{T}_{2-2} - A_{2-2}^{PAS}\hat{T}_{22}\right), \tag{2.121}$$

with the spatial terms defined as:

$$A_{20}^{PAS} = \sqrt{\frac{3}{2}}C_Q, \tag{2.122}$$

$$A_{22}^{PAS} = A_{2-2}^{PAS} = \frac{1}{2}\eta_Q C_Q. \tag{2.123}$$

In the laboratory frame, the Hamiltonian becomes:

$$\hat{H}_Q^L = \frac{2\pi}{2I(2I-1)}\left(A_{20}^L\hat{T}_{20} - A_{21}^L\hat{T}_{2-1} - A_{2-1}^L\hat{T}_{21} + A_{22}^L\hat{T}_{2-2} + A_{2-2}^L\hat{T}_{22}\right). \tag{2.124}$$

Under a first-order perturbation, the secular approximation holds, hence only A_{20}^L terms need to be considered:

$$A_{20}^L = A_{20}^{PAS}D_{00}^2 + A_{22}^{PAS}D_{20}^2 + A_{2-2}^{PAS}D_{-20}^2. \tag{2.125}$$

Applying the relevant rotation matrices yields the following expression for the spatial component of the quadrupolar Hamiltonian in the laboratory frame:

$$A_{20}^L = \sqrt{\frac{3}{2}}\frac{C_Q}{2I(2I-1)}\frac{1}{2}\left[(3\cos^2\beta_{PL} - 1) + \eta_Q \sin^2\beta_{PL}\cos 2\alpha_{PL}\right]. \tag{2.126}$$

Considering spatial and spin components, the first-order quadrupolar Hamiltonian is therefore:

$$A_{20}^L = \sqrt{\frac{3}{2}}\frac{C_Q}{2I(2I-1)}\frac{1}{2}\left[(3\cos^2\beta_{PL} - 1) + \eta_Q \sin^2\beta_{PL}\cos 2\alpha_{PL}\right]\hat{T}_{20}. \tag{2.127}$$

The first-order perturbation of the Zeeman interaction is written as:

$$E_m^{(1)} = \langle m|\hat{H}^1|m\rangle. \tag{2.128}$$

Substitution of the first-order Hamiltonian yields:

$$E_m^{(1)} = \sqrt{\frac{3}{2}}\frac{C_Q}{2I(2I-1)}\frac{1}{2}\left(3m^2 - I(I+1)\right)\left[(3\cos^2\beta_{PL} - 1) + \eta_Q \sin^2\beta_{PL}\cos 2\alpha_{PL}\right]. \tag{2.129}$$

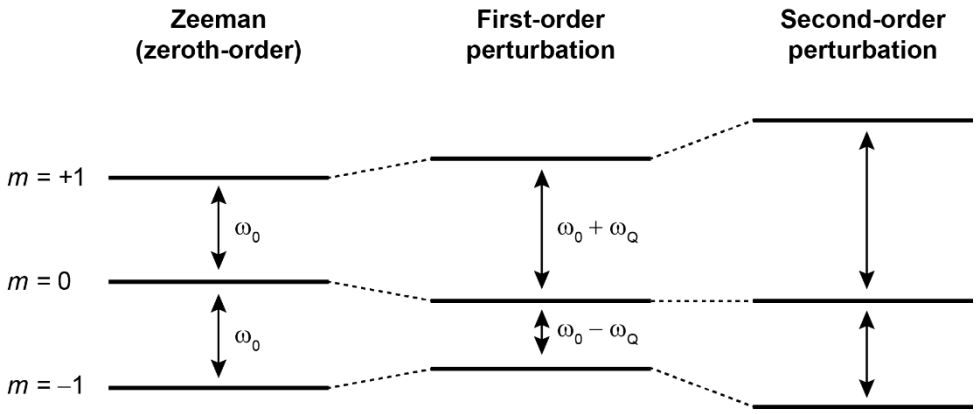

Figure 2.11 Schematic representation of the perturbation to the Zeeman energy levels for a spin-1 nucleus, such as ^{14}N. Both first- and second-order perturbations are considered. Note that the first-order perturbation does not affect the total transition energy (m = −1 ↔ m = 1), however the individual SQ transitions (m = −1 ↔ m = 0, m = 0 ↔ m = 1) have different energies. The second-order perturbation does affect the SQ transition energy. Note that these perturbations are exaggerated to more suitably demonstrate the change to the energy levels.

For ^{14}N, which has spin 1, there are three possible energy levels $(m = -1, 0, 1)$ and hence two possible transitions $(m = -1 \leftrightarrow m = 0, m = 0 \leftrightarrow m = 1)$ as shown in Fig. 2.11. The total transition energy $(m = -1 \leftrightarrow m = 1)$ is unchanged relative to the total Zeeman energy. However, the individual SQ transitions have different energies relative to each other.

For the majority of quadrupolar nuclei, in which the value of C_Q is such that the second-order perturbation to the Zeeman energy must be considered, the energy may be written as:

$$E_m^{(2)} = \sum_{m \neq n} \frac{\langle n|\hat{H}^1|m\rangle\langle m|\hat{H}^1|n\rangle}{E_n^{(0)} - E_m^{(0)}}. \tag{2.130}$$

For second-order perturbations, the secular approximation no longer holds, hence all $A^L_{2-m,\ldots,m}$ terms must be considered. These terms can be calculated in the same manner as for the A^L_{20} terms. Calculation of the second-order perturbation is performed by multiplying A^2_{2m} spatial terms. The multiplication of

$A^2_{2m}.A^2_{2m}$ yields zeroth-, second- and fourth-rank Wigner rotation matrices, which have important implications for the effect of MAS upon quadrupolar lineshapes. Consequently, the second-order perturbation may now be written as:

$$E_m^{(2)} = -\left(\frac{C_Q}{4I(2I-1)}\right)^2 \frac{2}{\omega_0} m \left[\left([I(I+1)-3m^2]D_{00}^{0(Q)}\right) + \left([8I(I+1)-12m^2-3]D_{20}^{2(Q)}\right) + \left([18I(I+1)-34m^2-5]D_{40}^{4(Q)}\right)\right], \quad (2.131)$$

where

$$D_{00}^{0(Q)} = -\frac{1}{5}\left(3+\eta_Q^2\right), \quad (2.132)$$

$$D_{20}^{2(Q)} = \frac{1}{28}\left[\left(\eta_Q^2-3\right)(3\cos^2\beta_{PL}-1) + 6\eta_Q^2\sin^2\beta_{PL}\cos 2\alpha_{PL}\right], \quad (2.133)$$

$$D_{40}^{4(Q)} = \frac{1}{8}\left[\left(\frac{1}{140}\left(18+\eta_Q^2\right)(35\cos^4\beta_{PL}-30\cos^2\beta_{PL}+3)\right) + \left(\frac{3}{7}\eta_Q\sin^2\beta_{PL}(7\cos^2\beta_{PL}-1)\cos 2\alpha_{RL}\right) + \left(\frac{1}{4}\eta_Q^2\sin^4\beta_{PL}\cos 4\alpha_{PL}\right)\right]. \quad (2.134)$$

Under a second-order perturbation, the energy levels presented in Fig. 2.10 are perturbed further, relative to the first-order case. The magnitude of the second-order perturbation is inversely proportional to ω_0, hence experimentally, the effects of the quadrupolar interaction are reduced by moving up in magnetic field strength, e.g., from 14.1 T to 20.0 T.

The zeroth-rank term, being isotropic, adds a second isotropic shift to the spectra of quadrupolar nuclei, alongside the isotropic chemical shift. This so-called isotropic second-order quadrupolar shift, δ_{iso}^{Q}, is defined, in the ppm scale for a $(m \rightarrow m-1)$ transition, as:

$$\delta_{iso}^{Q} = -\left(\frac{3}{40}\right)\left(\frac{P_Q}{\nu_0}\right)^2 \frac{[I(I+1)-9m(m-1)-3]}{[I^2(2I-1)^2]} \times 10^6. \quad (2.135)$$

When $I = 1$ and $m = 0, 1$, the expression is simplified to,

$$\delta_{iso}^{Q} = \left(\frac{3}{40}\right)\left(\frac{P_Q}{\nu_0}\right)^2 \times 10^6, \tag{2.136}$$

where P_Q is defined as:

$$P_Q = C_Q\sqrt{1 + \frac{\eta_Q^2}{3}}, \tag{2.137}$$

and is known as the quadrupolar product.

The second-rank term is anisotropic and hence is removed when the system is under the influence of MAS. Residual broadening due to the quadrupolar interaction is retained however, since the fourth-rank term also has an anisotropic dependence. It is not possible to average both second- and fourth-rank terms simultaneously by rotation about a single angle (i.e. under MAS). It is possible, however, to remove this contribution to the line broadening by spinning the sample at a second angle relative to the magic angle. This concept forms the basis of the double rotation (DOR) method,(168) which is not considered further in this thesis.

Chapter 3 : Experimental methods in solid-state NMR spectroscopy

3.1 One-dimensional lineshapes and phase

In a modern NMR experiment, the time-domain signal (generated by the induction of current in the probehead's coil), is detected *via* quadrature detection (see Fig. 3.1). Experimentally, the two orthogonal components of the magnetisation (*x* and *y*) are measured by mixing the signal from the coil with reference frequencies which are 90° out of phase with respect to one another.

As such, the NMR time-domain signal, with its two orthogonal components, can be considered mathematically as a complex function:

$$s(t) = \cos(\Omega t) + i\sin(\Omega t). \tag{3.01}$$

Note, equation 3.01 only holds if all internal interactions are excluded and only evolution under a resonance offset is considered. However, $s(t)$ is typically a damped oscillation and can hence be written as:

$$s(t) = S_0 \exp(i\Omega t) \exp\left(-\frac{t}{T_2}\right), \tag{3.02}$$

which now accounts for relaxation effects, specifically transverse relaxation, T_2, which describes the loss of coherence order between individual spins in the transverse plane. Since equation 3.02 is sensitive to the sign of the resonance offset (i.e. $\exp(+i\Omega t)$ and $\exp(-i\Omega t)$ are different functions), Fourier transformation of this signal will result in a frequency discriminated spectrum i.e. a peak will appear at $+\Omega$ only. Recording the spectrum in this way is known as quadrature detection.

Fourier transformation of the complex time-domain signal gives a complex frequency-domain signal:

$$S_0 \exp(i\Omega t) \exp(-Rt) \rightarrow \frac{S_0 R}{R^2 + (\omega - \Omega)^2} + i\frac{-S_0(\omega - \Omega)}{R^2 + (\omega - \Omega)^2}, \tag{3.03}$$

where, for simplicity,

$$R = \frac{1}{T_2}. \tag{3.04}$$

The two components of the right hand side of equation 3.03 correspond to the real and imaginary parts of the spectrum respectively. The real part of the spectrum generates a so-called absorption mode Lorentzian lineshape, whereas the imaginary part has a dispersion mode Lorentzian lineshape.

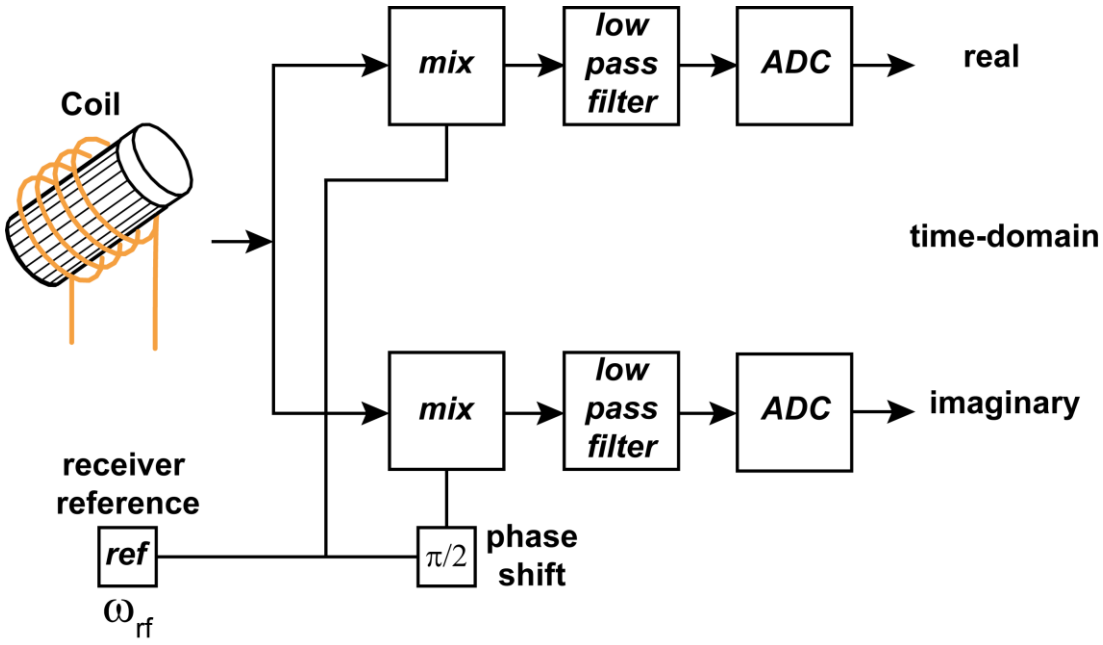

Figure 3.1 Schematic representation of the process of quadrature detection in which two mixers are fed by receiver reference signals, which are phase shifted by 90° with respect to one another. The respective outputs are proportional to the orthogonal components of the magnetisation in the transverse plane. Adapted from Keeler.(166)

The S_0 term in equation 3.03 represents a scaling factor and is usually omitted. Mathematically, the absorption and dispersion modes are represented as:

$$S(\omega) = A(\omega) - iD(\omega), \tag{3.05}$$

$$A(\omega) = \frac{R}{R^2 + (\omega - \Omega)^2} \qquad D(\omega) = \frac{-(\omega - \Omega)}{R^2 + (\omega - \Omega)^2}. \tag{3.06}$$

In the case of absorption mode lineshapes, which are positive and centred at the resonance offset, $\omega = \Omega$, (where $\Omega = \omega_0 - \omega_{rf}$), the transverse relaxation rate therefore affects the linewidth, referred to as half width at half the maximum peak height (HWHMH) in rad s^{-1}:

$$HWHMH = 1/T_2. \tag{3.07}$$

Since $(1/T_2)$ is a decay constant, the observed linewidth depends upon the rate of decay. Hence for systems with short T_2 constants and hence a faster decay, the observed linewidth is broad when compared with a resonance corresponding to a site with a long transverse relaxation delay.

Practically, the time-domain signal has arbitrary phase, ϕ, due to the way the *rf* electronics work in modern NMR spectrometers. The time-domain expression in equation 3.02 can now be re-written to account for this:

$$s(t) = S_0 \exp(i\Omega t) \exp(-Rt) \exp(i\phi). \tag{3.08}$$

Since this phase is constant, Fourier transformation yields:

$$S_0 \exp(i\Omega t) \exp(-Rt) \exp(i\phi) \rightarrow S_0[A(\omega) + iD(\omega)] \exp(i\phi). \tag{3.09}$$

Since only the real part of the frequency domain is displayed, $\exp(i\phi)$ is replaced by $(\cos\phi + i\sin\phi)$:

$$\begin{aligned} S_0[A(\omega) + iD(\omega)] \exp(i\phi) &= S_0[A(\omega) + iD(\omega)][\cos\phi + i\sin\phi] \\ &= S_0[\cos\phi\, A(\omega) - \sin\phi\, D(\omega)] + iS_0[\cos\phi\, D(\omega) + \sin\phi\, A(\omega)]. \end{aligned} \tag{3.10}$$

Hence the real part of the spectrum will contain a mixture of absorption and dispersion lineshapes, depending upon the arbitrary phase. During data processing, a phase correction procedure is employed by multiplying the spectrum by some correcting phase, $\exp(i\phi_{corr})$, as chosen by the spectroscopist.

3.2 Two-dimensional lineshapes

The true power of NMR derives from its ability to exploit multiple dimensions i.e. 1D, 2D, 3D and higher. Since the work in this thesis concerns experiments performed in one and two-dimensions, it is necessary to discuss two-dimensional lineshapes and to describe the generic form two-dimensional experiments take.

A general two-dimensional NMR experiment can be broken down into four time periods: *preparation*, *evolution*, *mixing* and *detection*. The first period, the preparation or excitation period, is necessary to excite the desired nuclear spins and also to generate the required coherence order. Once excited the spins evolve under whatever interactions are permitted by the pulse sequence in question. This evolution period has characteristic time t_1, which is incremented (Δt_1) over the course of the experiment. In order to detect the signal, it is necessary to convert the spin coherence into an observable form (in-phase SQ coherence), which occurs during the mixing period. Finally, and analogously with the one-dimensional

acquisition time, the NMR signal is detected. This detection period has characteristic time t_2. Recording a series of FIDs as a function of t_1 (indirect) and t_2 (direct) results in a two-dimensional NMR dataset.

Under a resonance offset, the general form of a two-dimensional NMR signal can be written:

$$s(t_1, t_2) = \exp(-ip\Omega t_1) \exp\left(-t_1/T_2^{(1)}\right) \exp(i\Omega t_2) \exp\left(-t_2/T_2^{(2)}\right), \tag{3.11}$$

where p indicates the selected coherence order and $T_2^{(1)}$ and $T_2^{(2)}$ correspond to the transverse relaxation or dephasing times in t_1 and t_2, respectively. The concepts of coherence order and phase will be discussed at length later in this chapter. Consider a case in which only $p = +1$ is allowed in t_1, Equation 3.11 can now be written:

$$s_{pm}(t_1, t_2) = \exp(-i\Omega t_1) \exp\left(-t_1/T_2^{(1)}\right) \exp(i\Omega t_2) \exp\left(-t_2/T_2^{(2)}\right), \tag{3.12}$$

where the subscript pm indicates *phase modulation* with respect to Ω_1. Fourier transformation of the signal yields:

$$s_{pm}(\omega_1, \omega_2) = (A_1^- - iD_1^-)(A_2^+ - iD_2^+) = (A_1^- A_2^+ - D_1^- D_2^+) - i(A_1^- D_2^+ - D_1^- A_2^+). \tag{3.13}$$

Equation 3.13 demonstrates that only resonances with negative frequency in the indirect dimension (ω_1) are observed, hence phase modulation allows for sign discrimination in two-dimensional datasets. However, since both the real and imaginary components of Equation 3.13 have both absorptive and dispersive elements, such a FT gives rise to a so-called phase-twist lineshape, which is much broader than a purely absorptive resonance, and is therefore undesirable. In order to remedy this problem, it is necessary to record the NMR experiment in an amplitude-modulated fashion. In such an experiment, during t_1, both positive and negative coherence orders are present i.e. $p = \pm 1, \pm 2, \ldots$ The signal can now be written:

$$\begin{aligned} s_{am}(t_1, t_2) = {} & [\exp(-i\Omega t_1) \\ & + \exp(i\Omega t_1)] \exp\left(-t_1/T_2^{(1)}\right) \exp(i\Omega t_2) \exp\left(-t_2/T_2^{(2)}\right) \\ & = 2\cos(\Omega t_1) \exp\left(-t_1/T_2^{(1)}\right) \exp(i\Omega t_2) \exp\left(-t_2/T_2^{(2)}\right). \end{aligned} \tag{3.14}$$

FT with respect to t_2 yields:

$$s_{am}(t_1, \omega_2) = [\exp(-i\Omega t_1) + \exp(i\Omega t_1)] \exp\left(-t_1/T_2^{(1)}\right) (A_2^+ - iD_2^+). \tag{3.15}$$

FT with respect to t_1, if the real and imaginary components are transformed separately, yields:

$$s_{am}^{Re}(t_1, \omega_2) = [\exp(-i\Omega t_1) + \exp(i\Omega t_1)] \exp\left(-t_1/T_2^{(1)}\right) A_2^+$$

$$s_{am}^{Re}(t_1, \omega_2) = (A_1^- + A_1^+)A_2^+ - i(D_1^- + D_1^+)A_2^+, \tag{3.16}$$

$$s_{am}^{Im}(t_1, \omega_2) = [\exp(-i\Omega t_1) + \exp(i\Omega t_1)] \exp\left(-t_1/T_2^{(1)}\right) D_2^+$$

$$s_{am}^{Im}(\omega_1, \omega_2) = (A_1^+ + A_1^-)D_2^+ - i(D_1^+ + D_1^-)D_2^+. \tag{3.17}$$

The real component of the spectrum now has purely absorptive lineshapes in both dimensions. However, since the resonances are both positive (A_1^+) and negative (A_1^-) in the indirect dimension (corresponding to mirrored peaks in F_1 at $\pm\Omega_1$), it is necessary to employ one of the following methods for sign discrimination in F_1: States, TPPI or States-TPPI, which will be discussed in the next sections.

3.2.1 States, TPPI and States-TPPI acquisition

Recall in section 3.2 that, in two-dimensional NMR, the evolution time, t_1, is incremented over the duration of the experiment. A popular method for achieving sign discrimination in F_1 was proposed in 1982 by States, Haberkorn and Ruben,(169) in which for every value of t_1, two FIDs are recorded in an amplitude-modulated fashion. The difference is that the phase of the preparation pulse for the second FID is increased by $\pi/2|p|$, where $|p|$ represents the desired coherence order that evolves during t_1. Since the first and second signals are 90° out of phase with respect to one another, the signal is said to be sine-modulated such that:

$$\begin{aligned} s_{am,sin}(t_1, t_2) = &\left[\exp(i\Omega t_1) \exp\left(i\frac{\pi}{2}\right)\right. \\ &\left. + \exp(-i\Omega t_1) \exp\left(-i\frac{\pi}{2}\right)\right] \exp\left(-\frac{t_1}{T_2^{(1)}}\right) \exp(i\Omega t_2) \exp\left(-\frac{t_2}{T_2^{(2)}}\right) \\ = &[\exp(i\Omega t_1) \\ &- \exp(-i\Omega t_1)] \exp\left(-t_1/T_2^{(1)}\right) \exp(i\Omega t_2) \exp\left(-t_2/T_2^{(2)}\right) \\ = &\, 2i \sin(\Omega t_1) \exp\left(-t_1/T_2^{(1)}\right) \exp(i\Omega t_2) \exp\left(-t_2/T_2^{(2)}\right). \end{aligned} \tag{3.18}$$

FT with respect to t_1 and then t_2 yields:

$$s^{Re}_{am,sin}(\omega_1, \omega_2) = (A_1^- - A_1^+)A_2^+ - i(D_1^- - D_1^+)A_2^+. \quad (3.19)$$

The difference between the absorptive components of the cosine (Eq. 3.17) and sine (Eq. 3.19) modulated signals produces a purely absorptive resonance at positive offsets only, in t_1 and t_2:

$$(A_1^- + A_1^+)A_2^+ - (A_1^- - A_1^+)A_2^+ = 2A_1^+A_2^+. \quad (3.20)$$

This method is known as the States acquisition method and is commonly employed in the work presented herein.

The TPPI (Two Pulse Phase Incremented) method is an alternative tool for sign discrimination in F_1 in which, rather than record two FIDs for each value of t_1, only one is recorded although the increment is halved to $\Delta t_1 = \frac{1}{2}s\omega_1$, where $s\omega_1$ represents the spectral width (Hz) of the indirect dimension. The phase of the preparation pulse is changed by $\pi/2|p|$ for *each* t_1 increment. This ensures that sign discrimination is achieved by modulating the coherence order by a phase that is dependent upon the specific t_1 increment. However, since TPPI requires that Δt_1 be rotor synchronised, and that the spectral width be halved, in this work the States or combined States-TPPI approach is used, the latter of which incorporates the principles of both methods. Specifically, States-TPPI records two signals for each t_1 value but increments the phase 0, 90, 180, 270 rather than 0, 90, 0, 90 for SQ evolution in t_1.

3.2.2 Coherence transfer pathways and phase cycling

The concept of coherence order was introduced in the last section. Coherence is created as a direct result of an *rf* pulse. Pulse sequences are designed specifically to introduce certain desired coherences, based on the needs of the user. A significant problem therefore arises: how do we selectively create only specific coherences? An *rf* pulse will, if left to itself, create all manner of coherences, desired or otherwise.

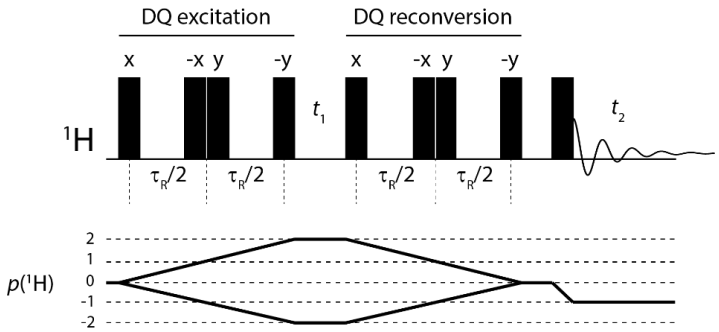

Figure 3.2 Schematic representation of a DQ/SQ MAS pulse sequence, using one rotor period of BABA recoupling for the excitation and reconversion of DQ coherence, and the corresponding coherence transfer pathway diagram. The preparation (or excitation), evolution (t_1), mixing and detection (t_2) periods of a two-dimensional experiment are presented. The purpose of the pulse sequence is to generate double-quantum (DQ, $|p| = 2$) coherence. The data for this specific sequence is amplitude-modulated with respect to t_1.

One method used in solution-state NMR to filter out the unwanted coherences is to use pulse field gradients, in which spatially homogeneous magnetic fields dephase and then rephase only desired coherences.(164) The idea being that the application of a magnetic field along the *z* axis forces a phase shift on all existing coherences, with the shift being proportional to the coherence order. However, a much more commonly executed method, especially in solid-state NMR, where it is technologically demanding to combine gradients with MAS, is the concept of phase cycling which, in modern NMR, is an integral part of any experiment.

Before any specific discussion of phase cycling, it is prudent to introduce the concept of coherence transfer pathways. Such pathways represent a convenient and visual method of observing the specific coherence order at any time of free precession during the experiment. As an example, Fig. 3.2 presents the coherence transfer pathway diagram and pulse sequence for the workhorse double-quantum/single-quantum (DQ/SQ) MAS NMR experiment that, as in this thesis, is often used in work concerning high resolution ^{1}H solid-state NMR. The purpose of the experiment is to excite DQ coherence which then evolves in t_1 before being converted into in-phase SQ coherence. The generation of the desired coherences is presented by the coherence transfer pathway diagram in Fig. 3.2.

The basic concept of phase cycling involves repeating the experiment many times where, for each FID, the phase of the *rf* pulses and the receiver are changed. The principles of phase cycling are enshrined in the two 'Golden' rules:

1. If the phase of a single or group of pulses is changed by $\Delta\phi$, then a coherence undergoing a change in coherence order, Δp, experiences a phase shift equal to $-\Delta\phi\Delta p$.

The significance of the first rule is that pathways with different Δp acquire a different phase, therefore it is possible to differentiate between them. Practically, this is achieved by repeating the experiment several times, each time using a different value of $\Delta\phi$ and combining the results in such a way as to amplify the signals from desired pathways whilst totally suppressing those signals from unwanted pathways. This is achieved by altering the receiver phase. Experimentally, it is important that the receiver phase follows the overall phase acquired by the desired coherence, so that the total signal due to this pathway is amplified over the duration of the phase cycle. All other signals will then cancel. Note that any phase acquired by a particular coherence is carried forward with that coherence until the end of the pulse sequence. This effectively means that any signal arising from that coherence will have the same phase shift.

2. If a phase cycle uses steps of $360°/N$ then, along with desired coherences, Δp, $\Delta p \pm nN$ pathways are also selected, where $n = 1, 2, 3$ ... All other pathways are suppressed.

Phase cycling is therefore used to drive changes in coherence order *via* the use of *rf* pulses *during* the course of the experiment. Note that the coherences at the start (thermal equilibrium) and end of an

experiment are always fixed, at $p = 0$ and $p = -1$, respectively. In order for the phase cycle to achieve its purpose, i.e., the cancellation of signals due to unwanted coherences, the total number of FIDs collected must be equal to an integer multiple of the *N* steps of the phase cycle employed. Only in such a manner will these unwanted coherences cancel completely. Higher order coherences selected automatically as a result of the second rule are normally ignored because the efficiency of exciting a coherence decreases as the order increases and hence the chance of exciting 4, 5, 6Q, ... is negligible.

For complex experiments in which multiple coherence changes occur over the sequence, it is necessary to employ nested phase cycles. In such a cycle, the phases of individual pulses are chosen according to the rules outlined above. Importantly, the overall receiver phase is calculated as the sum of all the individual receiver phases existing for each coherence change, defined by the second rule. Crucially, nested phase cycles allow for the selection of both positive and negative coherence pathways, therefore allowing the data to be acquired in an amplitude-modulated fashion.

3.3 Experimental techniques in solid-state NMR – dipolar decoupling

3.3.1 Dipolar decoupling

Extensive work with ^{1}H in solid-state MAS NMR is a relatively recent phenomenon, especially when compared with ^{1}H detection in solution. The broadening of ^{1}H lineshapes is a direct consequence of the extensive network of homonuclear ^{1}H – ^{1}H dipolar couplings which exist in a typical organic sample. MAS, even at high spinning frequencies of up to and exceeding 60 kHz, is not sufficient to fully average these couplings and hence significant broadening of resonances, especially those relating to aromatic and alkyl environments, persists. It has been shown, for small organic molecules, that combining MAS with high performance decoupling schemes can significantly improve the resolution of ^{1}H lineshapes.(44) The fate of homonuclear dipolar couplings in solid-state NMR and under MAS was discussed in sections 2.4.4 and 2.4.5.

Specifically, decoupling refers to the process of subjecting a given sample to irradiation at a certain frequency in order to eliminate, fully or partially, the effect of a coupling between certain nuclei. Such a process can either be employed in a homonuclear or heteronuclear fashion. Homonuclear decoupling refers to the situation where both the nucleus to be irradiated and observed belongs to the same spin species, i.e., ^{1}H – ^{1}H. For heteronuclear decoupling the opposite is true, i.e., ^{1}H – ^{13}C. Both types of decoupling will be briefly described in the following sections.

3.3.2 Heteronuclear dipolar decoupling

For experiments in which the low natural abundance or ‘dilute’ spin is to be observed, i.e., in a CP MAS experiment (see section 3.4.1 below), it is generally assumed that the X – H heteronuclear dipolar coupling is the most significant internal interaction that needs to be considered. For ^{13}C, for instance, the CSA is typically removed by the sample rotation (provided that the MAS frequency is high enough

so as to avoid spinning sidebands), therefore, in order to obtain clearly resolved lines it is necessary to decouple during acquisition.

Heteronuclear decoupling is typically applied in a continuous manner *via* close-to-resonance high frequency *rf* irradiation to the abundant spin species (usually ^{1}H). The effect of this irradiation is to excite continuous transitions between the α and β states in the ^{1}H spins at a rate determined by the amplitude of the *rf* irradiation. If this frequency is high enough, then these transitions are fast when compared to the magnitude of the heteronuclear dipolar coupling, which is subsequently averaged by such transitions. In order to fully average a coupling, the *rf* nutation frequency must be at least three times higher than the magnitude of the largest X – H heteronuclear dipolar coupling. The nutation frequency is usually set to 100 kHz, which more than satisfies this condition. However, since heteronuclear decoupling is usually applied alongside MAS, the two effects can combine to introduce a periodicity into the dipolar Hamiltonian. This means that at certain ratios of ν_r and ν_1 (irradiation frequency), destructive interference may occur which subsequently negates the averaging effect of the decoupling sequence. In order to correct for this, optimised heteronuclear decoupling sequences consisting of *rf* pulse blocks, in which individual pulses alternate their respective phase, have been developed. Popular examples include the Two Pulse Phase Modulated (TPPM) (170) and SPINAL-64 (171) schemes. TPPM decoupling is continuous and consists of two alternating pulses of flip angle θ_p with phase of ϕ_p and $\phi_p + \Delta\phi_p$ respectively. The values of these phases are determined experimentally, with the optimal values being dependent upon the spinning frequency and the sample under consideration. Other schemes with similar efficiencies were developed in the late 1990s and early 2000s, including FMPM,(172) SPARC,(173) $C12_2^{-1}$,(174), amplitude-modulated TPPM,(175) and methods continue to be developed. (176-178)

3.3.3 Homonuclear dipolar decoupling

The magnitude of ^{1}H – ^{1}H homonuclear dipolar coupling is such that, for an ensemble of spins, MAS alone is insufficient to fully average the line broadening effect, in its current maximum limit. There exist many schemes which are capable of efficiently decoupling this interaction in conjunction with MAS (CRAMPS), such as the popular DUMBO (decoupling under mind-boggling optimisation) scheme,(45,46,179) which works well at moderate MAS frequencies for small organic molecules such as peptides. For the theory and subtleties of the various schemes there are many excellent reviews,(180) an in-depth discussion here is beyond the scope of this thesis. The first homonuclear decoupling sequence, WAHUHA,(25) is very simply a sequence of $\pi/2$ pulses with different phases separated by delays, τ, with the sequence being repeated throughout the acquisition time and FID points being collected at the end of each repetition.

Modern homonuclear decoupling schemes can be applied in a windowed or windowless manner. Early schemes such as Lee-Goldberg were exclusively windowless.(40) Windowed schemes such as

DUMBO-1 allow for periods of free evolution,(45) in which the signal is acquired, alternating with irradiation periods. Windowless decoupling, such as eDUMBO$_{22}$,(46) is applied during t_1 evolution periods in two-dimensional experiments, with the irradiation being constant over the course of the decoupling period.

Homonuclear decoupling sequences use high nutation frequencies and subsequently require short rise times since the duty cycle, which is the decoupling duration as a percentage of the whole pulse sequence duration, needs to be kept short, in order to avoid damage to the sample or the probe head. Homonuclear decoupling is therefore much more complex when compared to its heteronuclear counterpart. As such much effort is spent in devising high performance, robust homonuclear decoupling schemes, which can be employed under various experimental conditions and still achieve efficient line narrowing in one- and two-dimensional ^{1}H spectra.

3.4 Experimental techniques in solid-state NMR – dipolar recoupling

Magic angle spinning (MAS), which was discussed at length in section 2.4.5, is commonly employed in solid-state NMR to attenuate anisotropic broadening which arises from the various internal spin interactions acting upon a given system. Since MAS suppresses the dipolar coupling, vital ^{1}H – ^{1}H distance information is also lost, information which is critical for structural elucidation. Decoupling is a NMR method in which specific interactions i.e. dipole – dipole couplings, may be averaged to zero (in theory). Recoupling, on the other hand, is a technique by which desired interactions may be *selectively* reintroduced in a coherent manner into the system, by means of carefully constructed sequences of *rf* pulses. The work in this thesis includes homonuclear (^{1}H – ^{1}H) and heteronuclear (^{14}N – ^{1}H) recoupling.

Dipolar recoupling is now a central methodology in ^{1}H MAS NMR. A discussion of the number and diversity of recoupling schemes is well beyond the scope of this introduction. The recoupling schemes employed in this thesis will be briefly discussed in the next sections.

Historically, the term ‘recoupling’ was first used in the heteronuclear sense. It was shown that a continuous application of an *rf* field to one spin species can restore the effects of a heteronuclear dipolar coupling, which in turn provides information regarding heteronuclear correlations, to a second spin species in close spatial proximity.(181) The technique was dubbed ‘rotary resonance’ and requires that the *rf* amplitude is selected such that the MAS frequency is an integer multiple of the nutation frequency:

$$\omega_1 = n\omega_r. \tag{3.21}$$

Note that the integer value, *n*, depends (in essence) upon the specific spin interaction to be reintroduced into the system. This pioneering work led to a multitude of other recoupling sequences still in use today, such as: REDOR (rotational echo double resonance),(182) DRAMA (dipolar recoupling at the magic angle) which was the first example of a homonuclear recoupling sequence,(27) RFDR (radio frequency

driven recoupling) which was developed in part to address the low experimental robustness of the DRAMA scheme,(183) and DQ-HORROR (double-quantum homonuclear rotary resonance) which demonstrated for the first time that efficient excitation of DQC is possible in powdered solids.(184) This efficiency derived from a better control of the orientational dependence of the relevant Hamiltonian in a process known as γ-encoding. (γ-encoded sequences have a phase dependence on the third Euler angle which defines the orientation of the spin system with respect to the rotor frame). However, the HORROR sequence is only applicable when recoupling spins which have only a small difference in isotropic chemical shift. The subsequent quest for a more powerful broadband scheme led to the well characterised C7 scheme and its variants,(185) with the POST-C7 (permutationally offset stabilised C7) sequence being employed in CRAMPS based DQ/SQ experiments.(28) The concept of symmetry based sequences was developed in the late 1980s. Recoupling schemes (and decoupling) can be broadly split into two types of symmetry, C and R. The difference between them arises from the specific shift in phase between repeated *rf* cycles.(186) A full review of symmetry based sequences is beyond the scope of this work.

3.4.1 Cross polarisation

In terms of natural abundance (n.a.), ^{1}H is known as an abundant spin species (^{1}H ~ 100% n.a.). Of the other nuclei commonly encountered in organic systems, nitrogen can exist in two isotropic forms, ^{14}N (~ 99.6% n.a.) and ^{15}N (~ 0.4% n.a.) and carbon also in two forms, ^{12}C which has spin = 0 and is hence NMR silent, and ^{13}C which has a natural abundance of ~ 1%. Thus, ^{15}N and ^{13}C are termed ‘dilute’ spin species. In the absence of costly and often synthetically challenging isotropic labelling schemes, the cross polarisation (CP) technique offers an experimental solution to the problems associated with detecting such spins.

Originally developed by Hartman and Hahn,(32) the CP method consists of double-resonance irradiation of a given system such that, *via* the heteronuclear H – X dipolar couplings, magnetisation is transferred from the abundant species (*I*) to the dilute one (*S*), i.e., ^{1}H → ^{13}C/^{15}N. Thus, the observed signal of the dilute spin is enhanced *via* an increase in its bulk magnetisation. In addition to the signal enhancement, the CP method benefits from the fact that the experimental T_1 time is now determined by that of the abundant spin, which is normally much shorter than that of the dilute spin, thereby reducing experimental times. ^{1}H T_1 times are shorter since, compared to a dilute spin system, there exist more strong homonuclear dipolar couplings in the sample, which induce, *via* motional processes, a faster return to equilibrium.

The CP pulse sequence, which is now routinely combined with MAS in the CP MAS experiment,(36) is shown schematically in Fig. 3.3. It consists of an initial π/2 pulse (ν_1 = 100 kHz in this work) on the *I* channel, followed by a contact time in which the magnetisation transfer takes place from *I* to *S*. The duration of this contact time can be varied experimentally, with longer times being selected in order for

non-proton bonded dilute spin environments to be observed (magnetisation transfer takes longer to reach such sites). However, the appropriate contact time (on the order of ms usually) needs to take into account *I* relaxation during the application of *rf* irradiation, referred to as $T_{1\rho}$, since any contact pulse exceeding this time will be inefficient. It is then necessary to acquire the signal whilst heteronuclear decoupling is applied to the abundant spin species.

In order for efficient magnetisation transfer to occur during the contact time, it is necessary to satisfy the so-called Hartman-Hahn matching condition. This means that the amplitude of the B_1 magnetic field for the contact pulses on each channel are optimised so that the nutation frequencies of the two spins coincide which, under static conditions can be written as:

$$\gamma_I B_1(I) = \gamma_S B_1(S). \tag{3.22}$$

If maximum efficiency is assumed, the highest possible signal enhancement for $^1H \rightarrow {}^{13}C$ is ~ 4. Under MAS the condition can be rewritten:

$$\gamma_I B_1(I) = \gamma_S B_1(S) \pm n\omega_r \qquad n = 1, 2, \ldots \tag{3.23}$$

Magnetisation transfer is observed to be less efficient at faster MAS frequencies, although this can be compensated for by applying a ramped contact pulse to one of the channels.(187)

Since the transfer of magnetisation in a CP experiment occurs *via* the heteronuclear dipolar couplings, it is no longer possible to assume that the integrated peak intensity quantitatively correlates with the number of environments of that resonance. Rather the peak intensity becomes an indicator of relative ^1H – X proximities and motional processes within the system.

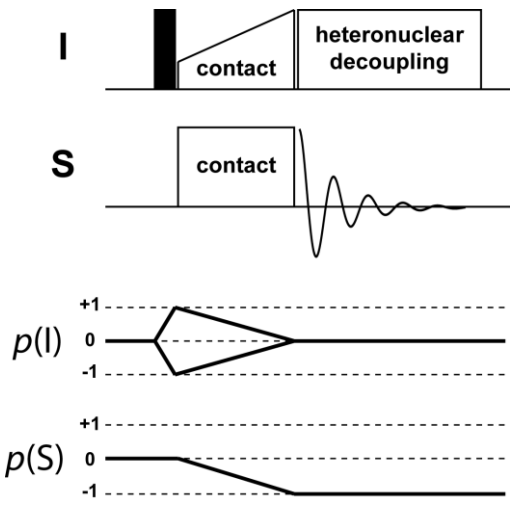

Figure 3.3 Schematic representation of the cross polarisation (CP) pulse sequence alongside coherence transfer pathway diagrams for both the *I* and *S* spins. Note that under MAS, it is usual to apply a ramp to one of the contact times, in this case the *I* channel. Heteronuclear decoupling, usually TPPM or SPINAL-64, is applied during t_2 acquisition in order to remove the influence of strong *I* – *S* heteronuclear dipolar couplings. Note that moderate MAS frequencies (~10 – 20 kHz) are usually sufficient to largely suppress the effect of CSA. At lower frequencies manifold spinning sidebands are observed.

3.4.2 Homonuclear dipolar recoupling: the DQ/SQ MAS experiment

The aptly named BAck-to-BAck (BABA) dipolar recoupling scheme is employed in all double-quantum (DQ)/ single-quantum (SQ) MAS experiments presented herein, where it is used for the excitation and reconversion of double-quantum coherence (DQC). The basic BABA scheme consists of four $\pi/2$ pulses per rotor period (τ_R), as shown in Fig.3.4a. It is possible to repeat the basic BABA cycle over several rotor periods, and hence achieve longer dipolar recoupling times. Another key feature of the scheme is the inherent amplitude dependence upon the rotor phase, hence the BABA scheme is an example of a non-γ encoded DQ recoupling sequence. This means that, in two-dimensional experiments, the data must be collected in a rotor-synchronised fashion, so as to avoid rotor-encoded spinning sidebands in the indirect (DQ) dimension. Rotor synchronisation has two additional benefits, (*i*) reducing experimental times (since the number of t_1 increments required is reduced), and (*ii*) increasing sensitivity (since the sidebands are folded back into the centreband positions).(188) In such an experiment, it is necessary to exploit an MAS frequency which is high enough so as to result in a large enough spectral width in the indirect dimension so as to observe all the DQ peaks, as well as providing enough resolution in the direct dimension so as to assign ^{1}H environments. The technique represents an efficient method for the excitation of DQC and was designed to be simple, robust and insensitive to off-resonance effects, isotropic chemical shifts, and CSA (assuming that strong, short *rf* pulses are employed), and has been experimentally demonstrated for ^{1}H and ^{31}P.

When designing sequences for the efficient excitation of ^{1}H DQC under MAS, it is necessary to carefully consider the possibility of interference with sample rotation, since such schemes are generally employed under a moderate to fast MAS regime. The simple $90 - \tau - 90$ sequence, which is used in multiple quantum solution state experiments, experiences significant limitations under MAS. Specifically, Schnell and Spiess demonstrated that, under MAS, the excitation and reconversion period is limited to $\tau_R/2$, since sample rotation ensures that the second half of the pulse sequence behaves essentially as a time reversal of the first half, meaning that the signal is greatly diminished after one full rotor period. This is demonstrated in Figure 12 of ref. (189) The basic BABA sequence, as demonstrated in Fig. 3.4, consists of a $90_x - \tau - 90_{-x}\ 90_y - \tau - 90_{-y}$ arrangement, which takes place over one full rotor period. The sequence compensates for the aforementioned MAS interference by including two segments per rotor period being 90° out of phase with respect to one another. By negating the spin component of the DQ Hamiltonian, the phase shift compensates the negation of the spatial component of the Hamiltonian caused by the sample rotation.(188-190)

The first experimental application of the BABA scheme, incidentally, was for multiple quantum coherence (MQC) experiments involving ^{13}C and ^{1}H, the results being first published in 1995.(29) Although homonuclear applications of the BABA scheme were initially geared towards its application in ^{31}P NMR,(191,192) the original sequence performs relatively poorly for systems with large offsets

or CSA. Including additional rotor periods into the sequence can have the effect of reducing offset and *rf* pulse imperfections, with modified two- and four-τ_R versions having been previously reported.(193) Other BABA-based schemes have been proposed to compensate for the shortcomings of the original sequences. Based on 'rational design principles', BaBa-xy16 was developed to ensure truly broadband performance.(31) The scheme essentially adds virtual π pulses to the BABA sequence, specifically the xy-16 supercycle. In this thesis, both the traditional BABA and BaBa-xy16 schemes are used. The basic unit of the BABA and BaBa-xy16 schemes are presented in Fig. 3.4a and 3.4b, respectively. Both of these recoupling schemes can be employed in so-called double-quantum (DQ)/single-quantum (SQ) MAS experiments. The pulse sequence, coherence transfer pathway diagram and a schematic representation of a DQ/SQ MAS spectrum for a system with two sites, A and B, are presented in Fig. 3.5 (a), (b) and (c), respectively. Importantly, peaks only appear in such a spectrum if a dipolar coupling exists between two sites, i.e., if the two sites are within a certain distance from one another. Typically, this experiment is sensitive up to approximately 3.5 Å.(189) Note that the appearance of certain cross-peaks is heavily influenced by the presence and magnitude of dipolar truncation present in a given system. By using such an experiment, it is possible to probe ^1H – ^1H internuclear proximities by measuring DQ build-up curves.(194) As was shown in the introductory example, in chapter 1, this experiment has proven itself to be very capable at probing hydrogen bonding motifs in organic systems. As such, this experiment plays a major role in the narrative of this thesis.

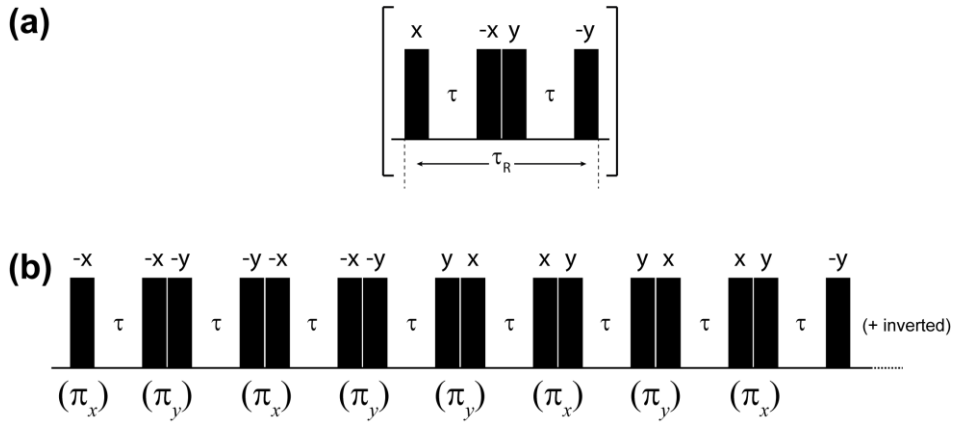

Figure 3.4 Schematic representation of the (a) basic BABA unit and (b) the more sophisticated BaBa-xy16 sequence (figure adapted from reference (31).

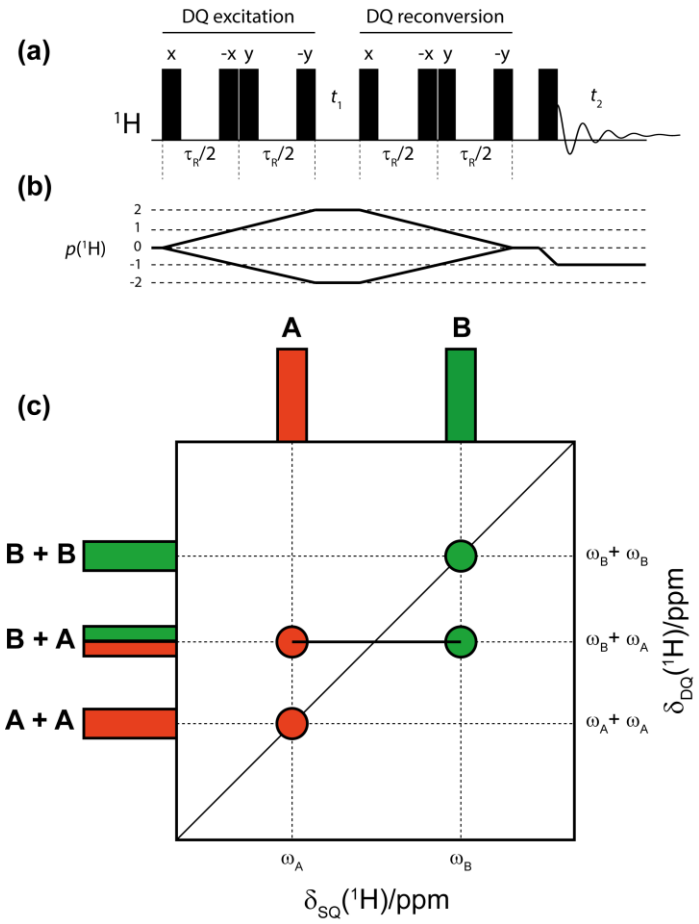

Figure 3.5 Schematic representation of (a) the DQ/SQ pulse sequence, (b) the corresponding coherence transfer pathway diagram, and (c) a general spectrum obtained for a two spin system where site A and site B are dipolar coupled with themselves (auto-peaks on the diagonal) and each other (cross-peaks off the diagonal). Note that this experiment reports only on ^{1}H – ^{1}H proximities, be they intra- or intermolecular, it cannot distinguish between the two.

3.4.3 ^{1}H – ^{1}H spin diffusion experiment

Structural information can also be extracted from a ^{1}H – ^{1}H spin diffusion experiment, in which the transfer of *z* magnetisation *via* ^{1}H – ^{1}H dipolar couplings is probed. Quantum mechanically, it can be shown that, for an ensemble of spins, transfer of such magnetisation is diffusive in nature,(188) and hence it is described as ^{1}H spin diffusion. Note that the same pulse sequence, shown schematically in Fig. 3.6a, is employed in both solution, i.e., in the well-known NOESY experiment in which polarisation transfer is based on the Nuclear Overhauser Effect (NOE) (which occurs *via* incoherent cross relaxation), and in the solid state. Schematic representation of spin diffusion spectrum is presented for a simple two resonance system in Fig. 3.6b. Such experiments are particularly well suited to probing mobility, i.e., to probe magnetisation transfer between two dynamically different components.(188) It can also be used, as it is in this thesis, to determine the number of specific phases present in a sample. For instance, if only one phase is present then all resonances in the spectrum will transfer magnetisation to all other ^{1}H environments, if the mixing time, τ_{mix}, is sufficiently long enough (usually on the order of 10s to 100s of ms).

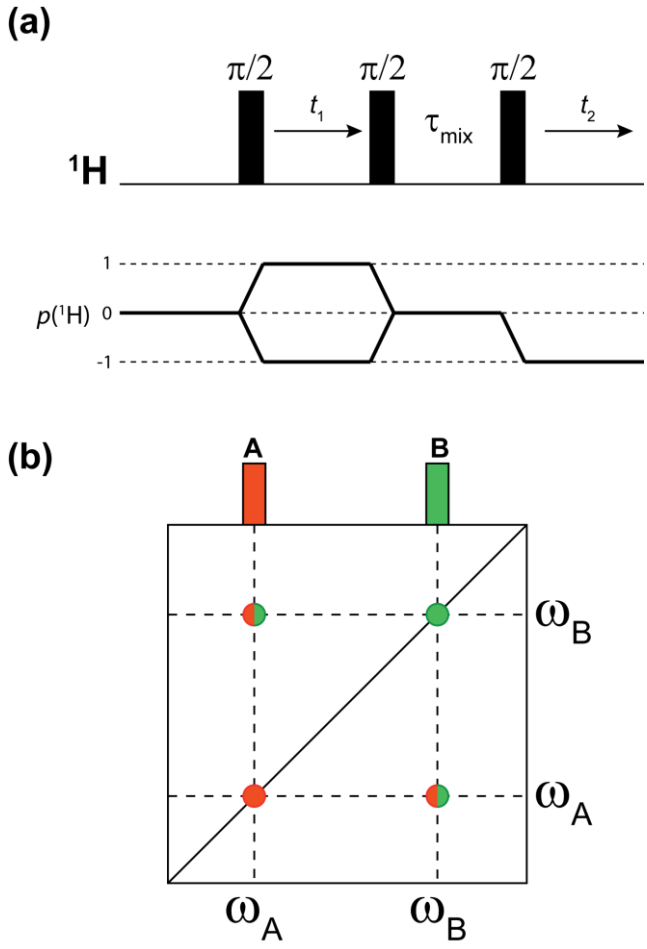

Figure 3.6 Schematic representation of, (a) the pulse sequence employed in a ^{1}H – ^{1}H spin diffusion experiment together with a coherence transfer pathway diagram, (b) a typical spectrum for a two site system.

3.4.4 Refocused INEPT

Scalar couplings can also be employed in order to transfer polarisation between different sites. There are several sequences which can achieve this transfer, however in the context of probing ^{1}H – ^{13}C connectivities in this thesis, the refocused INEPT (Insensitive Nuclei Enhanced by Polarisation Transfer) sequence is employed.(195,196) The experiment employs eDUMBO-1 ^{1}H – ^{1}H dipolar coupling, discussed in section 3.3.3, in order to improve resolution in the ^{1}H dimension, and to increase proton transverse coherence lifetimes.(196) The solid-state NMR pulse sequence was adapted from the original solution-state sequence,(197-199) by including ^{1}H homonuclear decoupling during t_1 and the τ and τ' transfer periods, as shown in Fig. 3.7. Assuming efficient decoupling, MAS is then used to remove contributions to the line broadening from the CSA and heteronuclear dipolar couplings, leaving only scalar couplings and the isotropic chemical shift, the latter of which is refocused by simultaneous π pulses on the ^{1}H and ^{13}C channels. Hence, in this way, only scalar couplings are assumed affect the coherence transfer and evolution during the transfer periods to any great extent, though residual dipolar couplings affect the transverse dephasing.(200)

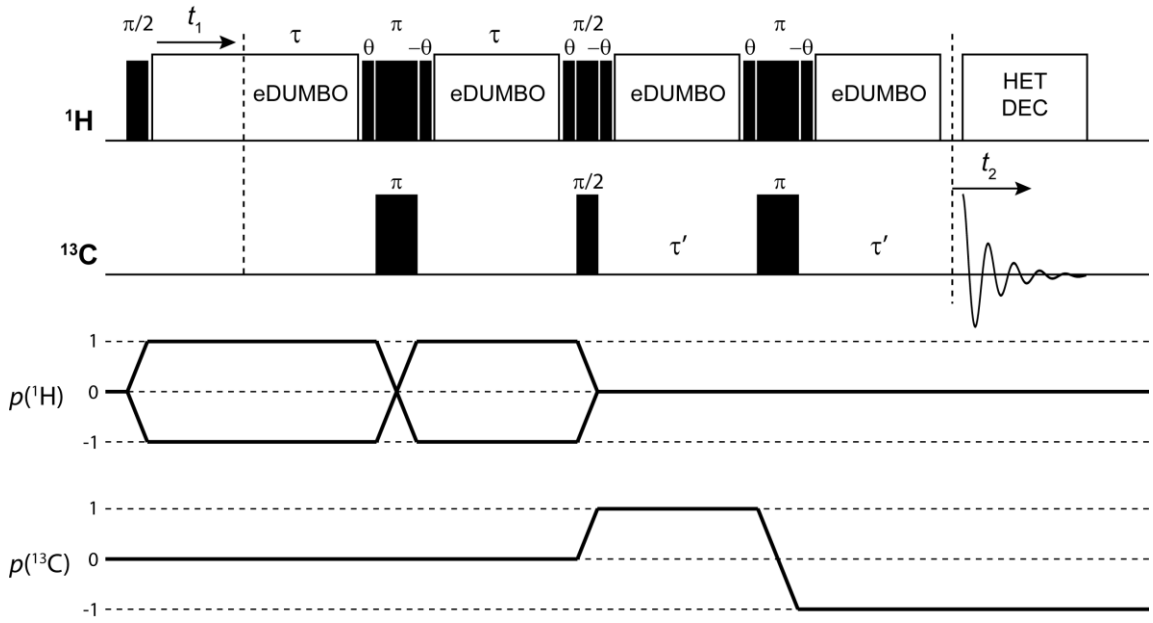

Figure 3.7 Schematic representation of the 2D ^{1}H – ^{13}C INEPT pulse sequence, together with coherence transfer pathway diagrams for the ^{1}H and ^{13}C channels. Figure adapted from reference (196).

3.4.5 Heteronuclear dipolar recoupling: the HMQC MAS experiment

Heteronuclear experiments are often an important tool with which to fully assign ^{1}H chemical shifts since such experiments benefit from the larger chemical shift range in the heteronuclear dimension (i.e. ^{13}C ~ 200 ppm, ^{1}H ~ 20 ppm). ^{13}C – ^{1}H correlations methods are well established,(147) but those experiments which probe nitrogen – proton correlations have only appeared relatively recently (~ last 10 years).

Nitrogen is an incredibly important element in organic and biological chemistry, precisely because of its capacity to participate in a range of hydrogen bonding structures. It can exist in two natural isotopic forms, the spin – ½ ^{15}N species, which has a low natural abundance of less than 0.4% and the more abundant spin – 1 ^{14}N isotope, which accounts for the other ~ 99.6% of naturally occurring nitrogen. Since it is spin – ½, ^{15}N is relatively easy to manipulate in an NMR experiment, but its low abundance presents real problems in the absence of isotopic labelling schemes, which is further confounded by the fact that it has a gyromagnetic ratio of approximately 10% of that for ^{1}H (indeed it is significantly lower than even that for ^{13}C). ^{14}N is therefore potentially more attractive from an NMR perspective despite having a gyromagnetic ratio approximately 7% the size of proton. The quadrupolar nature of ^{14}N is further useful in the sense that it can provide information pertaining to the electric field gradient about the nitrogen, but significant limitations arise due to the interaction leading to significant line broadening which cannot be completely removed under any conceivable MAS frequency due to so-called second order quadrupolar broadening effect (see section 2.4.7 for a broader discussion of quadrupolar coupling under MAS).

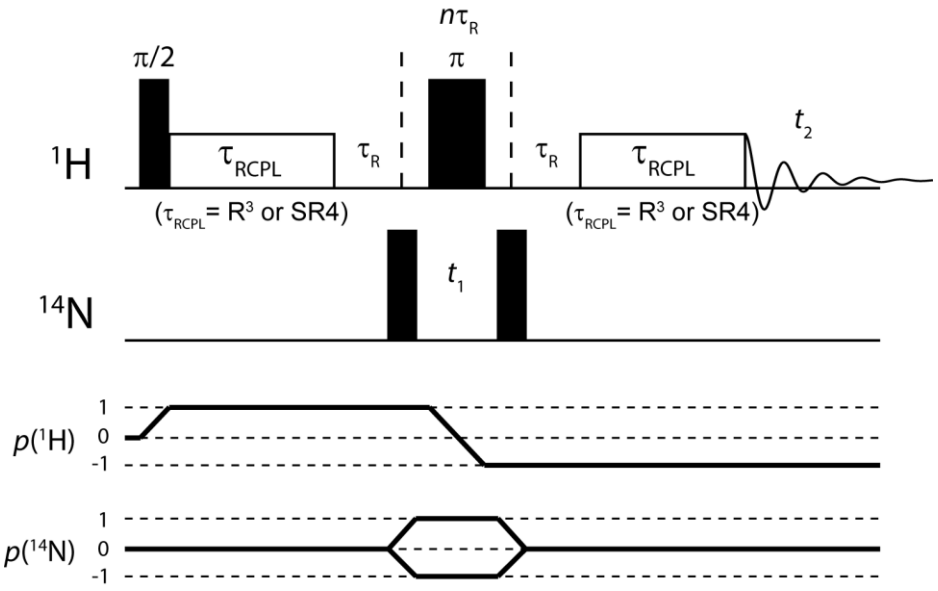

Figure 3.8 Schematic representation of the solid state ^{14}N – ^{1}H HMQC pulse sequence used in this thesis and the corresponding coherence transfer pathway diagrams for ^{1}H and ^{14}N. Note that during the recoupling period, τ_{RCPL}, rotary resonance recoupling (R^3) or SR4 recoupling is used throughout this thesis. In both cases, recoupling at the $n = 2$ condition, i.e., $\nu_1 = 2\nu_r$, recouples both the heteronuclear dipolar couplings and the ^{1}H CSA (the latter of which is refocused by the central π pulse), whilst simultaneously decoupling the ^{1}H – ^{1}H dipolar interaction.

The ^{14}N – ^{1}H heteronuclear multiple quantum correlation (HMQC) experiment is an exquisite probe of hydrogen bonding, with manifold examples being presented in the solid state for small molecules,(201) pharmaceuticals,(202) and nucleic acid derivatives.(100) Originally adapted from the analogous solution experiment, the HMQC experiment can be employed using either *J* couplings or heteronuclear dipolar couplings to achieve efficient magnetisation transfer. As such the experiment uses inverse detection of ^{14}N *via* either ^{13}C,(203) or more commonly, ^{1}H.(204,205) Note that in this thesis, only the dipolar coupling modulated experiment is reported. A schematic representation of the pulse sequence is presented in Fig. 3.8. Note that during the recoupling period, τ_{RCPL}, either rotary resonance recoupling (R^3) or the symmetry based SR4 scheme are employed in this work.

3.4.5.1 Rotary resonance recoupling (R^3)

In the late 1980s it was noted that, for dilute heteronuclear spin – ½ pairs, a recoupling effect was observed whenever the amplitude of the nutation frequency matched a small integer of the spinning frequency (rotary resonance, see equation 3.23).(206)

In the mid-to-late 2000s, when the ^{14}N – ^{1}H HMQC experiment was first exploited in the solid state, it was recognised by Gan, Amoureux and Trébosc,(207) that a sensitivity enhancement could be obtained using rotary resonance at the $n = 2$ condition. Such a condition was shown to efficiently recouple the heteronuclear dipolar couplings (in addition to the CSA) whilst decoupling the strong ^{1}H – ^{1}H

homonuclear dipolar couplings. Note that at n = 1 both heteronuclear and homonuclear dipolar couplings are recoupled as well as the CSA, whilst at the n = ½ condition only the homonuclear couplings are reintroduced (HORROR, see section 3.4). In addition to this recoupling effect, it was shown that utilising such a recoupling method offsets rapid transverse dephasing often associated with networks of strong coupled protons. The subsequent increase in ^{1}H coherence lifetimes helps to minimise signal loss. More broadly, the R^3 sequence satisfies three important criteria,(207) which are essential to designing a successful recoupling scheme for ^{14}N – ^{1}H experiments:

1. The *rf* irradiation is applied only to ^{1}H, since the ^{14}N quadrupolar interaction is too large when compared to the *rf* field to be manipulated in this way.
2. The sequence does not interfere with the averaging effects of MAS, thereby ensuring well resolved ^{1}H lineshapes (provided that the spinning frequency is sufficiently high).
3. Apart for the heteronuclear dipolar coupling, *all other* spin interactions are refocused over the course of the experiment (isotropic chemical shift survives).

3.4.5.2 SR4 recoupling

SR4 recoupling is an example of a symmetry based recoupling sequence which was originally developed in 2006 to reintroduce ^{17}O – ^{1}H heteronuclear dipolar couplings in order to probe hydrogen bonding distances in L-tyrosine.(208) Other examples of its use can be found for the recoupling of ^{14}N – ^{1}H dipolar couplings in simple amino acid systems,(209) and nucleic acid derivatives,(163) and recently for probing ^{35}Cl – ^{1}H correlations.(210)

The $SR4_1^2$ recoupling scheme is a supercycle of the rotor-synchronised $R4_1^2$ sequence:

$$180_{90}180_{-90}180_{90}180_{-90},$$

which spans one full rotor period. The supercycle is constructed by adding a consecutive $R4_1^{-2}$ block:

$$180_{-90}180_{90}180_{-90}180_{90},$$

and repeating this combined $R4_1^2$ $R4_1^{-2}$ sequence three times with overall phase shifts of 0°, 120° and 240°:

$$SR4_1^2 = [R4_1^2\ R4_1^{-2}]_0\ [R4_1^2\ R4_1^{-2}]_{120}\ [R4_1^2\ R4_1^{-2}]_{240}.$$

The $R4_1^2$ scheme belongs to the RN_n^v symmetry class where N, v and n are so-called symmetry numbers. As defined by Levitt, ‘the sample rotates bodily through n full rotations, in the same time that it takes the *rf* phases to advance through v full rotations, in N equal steps’.(186)

3.5 Experimental and computational details

3.5.1 Chemical shift referencing

In solution-state NMR, an internal reference compound can be added to the sample or the residual solvent signal can be used, in order to ascertain the correct value of the chemical shift. However, in solid-state NMR it is often more prudent to use an external reference in order to avoid contamination, or partial solubilisation of the sample under investigation. Since chemical shifts obtained under MAS are independent of the isotropic bulk susceptibility of the sample, referencing in this way is usually quite accurate.(211)

Unless otherwise stated, in all experiments presented in this thesis, ^{1}H and ^{13}C chemical shifts were referenced with respect to neat TMS using L-alanine as a secondary reference (1.3 ppm for CH_3 ^{1}H resonance, corresponding to 1.85 ppm for adamantane,(212) and 20.5 ppm for CH_3 ^{13}C resonance). ^{15}N chemical shifts are references relative to neat liquid CH_3NO_2, using the ^{15}N resonance of labelled glycine at – 347.4 ppm as an external reference. ^{14}N chemical shifts were referenced relative to neat CH_3NO_2 using the ^{14}N resonance of NH_4Cl (powdered solid) at 341.2 ppm as an external reference.(213) To convert to the chemical shift scale frequently used in protein NMR, where the alternative IUPAC reference (see Appendix 1 of ref (214)) is liquid ammonia at 50 °C, it is necessary to add 379.5 ppm to the given values.(215)

3.5.2 Experimental solid-state NMR

Solid-state NMR experiments in this thesis were performed at 20.0 (Bruker Avance III), 16.4 (JEOL ECA700II), 14.1 (Bruker Avance II+) and 11.7 (Bruker Avance III) T, operating at a ^{1}H Larmor frequency of 850, 700, 600 and 500 MHz, respectively. Note that the precise field for each experimental spectrum presented herein is given in the relevant figure legend. Experiments were performed using a 1.0 mm double-resonance Ultrafast MAS probe (JEOL RESONANCE Inc., Tokyo, Japan), a 1.3 mm triple-resonance probe (Bruker, operating in double-resonance mode), a 2.5 mm triple-resonance probe (Bruker, operating in double-resonance mode) and a 4 mm triple-resonance probe (Bruker, operating in double-resonance mode) for experiments performed at MAS frequencies of 70, 50 – 60, 30 and 12.5 kHz, respectively. In *all* cases the ^{1}H $\pi/2$ pulse duration was 2.5 μs. Sign discrimination in the F_1 dimension of 2D experiments was achieved using the States (chapters 4 and 6) or States-TPPI (chapter 5) methods. Note that, in 2D spectra, positive and negative contours are shown in black and red, respectively. Unless otherwise stated, for ^{1}H – ^{1}H DQ/SQ MAS experiments, a 16-step phase cycle was used to select $\Delta p = \pm 2$ on the DQ excitation pulses (4 steps) and $\Delta p = \pm 1$ (4-steps) on the *z*-filter 90° pulse, where p is the coherence order. For ^{14}N – ^{1}H HMQC experiments a 4-step nested phase cycle was used to select changes in coherence order $\Delta p = \pm 1$ (on the first ^{1}H pulse, 2 steps) and $\Delta p = \pm 1$ (on the last ^{14}N pulse, 2 steps).

3.5.3 GIPAW calculations

Calculations in this thesis were performed using the CASTEP code,(159) academic release version 8.0. Geometry optimisations and GIPAW (155,156) calculations of NMR parameters employed the PBE exchange correlation functional (160) with a semi empirical dispersion correction scheme due to Tkatchenko and Sheffler.(216) A plane wave basis set with ultra-soft pseudopotentials with a maximum cut-off energy of 800 eV was used in all cases.(217) Geometry optimisation procedures were performed with the unit cell parameters fixed, starting from a single crystal X-ray structure. For **4-3** (CCDC 930256), Z = 4, space group $P2_1$, Z' = 1. For **5-2** (CCDC 188941), Z = 2, space group P1, Z' = 2. All distances and angles quoted in the respective experimental chapters are extracted from the geometry optimised crystal structures. A plot of experimental chemical shifts against calculated chemical shieldings for ^{1}H is used to extract a chemical shielding reference, σ_{ref}, which is equal to the *y* intercept.(103,157) This value can then be used to produce calculated chemical shift values according to the following equation:

$$\delta_{iso} = \sigma_{ref} - \sigma_{calc} \tag{3.24}$$

Chapter 4 : (a) Investigating the self-assembling properties of guanine-like pterin analogues by ^{1}H MAS NMR, (b) Analysis of complex pterin – deoxycytidine analogues by ^{1}H MAS NMR

4a.1 Introduction

Pterin analogues represent a useful class of heterocyclic compounds which have manifold potential for hydrogen bonding. Pterin chemistry is diverse,(218) and there exist examples of sophisticated self-assembled structures,(120,219) with such systems having been synthesised since the late 1980s.(220-223) In this chapter, the solid-state structures of a range of pterin inspired analogues are discussed. The descriptor pterin inspired is used because, unlike typical pterin compounds which are based directly on the pteridine subunit, the systems discussed here do not contain the N5 nitrogen on the pyrazine ring (thus becoming a pyridine ring), as shown in Fig. 4.1.

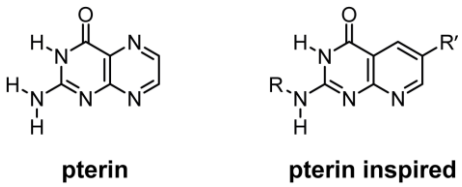

Figure 4.1 Schematic representation of the typical pterin structure and the pterin inspired subunit examined in this chapter.

It will be shown that the self-assembly properties of these pterin inspired compounds depend critically on the chemical nature of the R group attached to the exocyclic amine nitrogen, with the R' group on the 'pyrazine' ring being less important. The structures of the compounds discussed in this chapter are presented in Fig. 4.2 – note that the more complex compounds, **4-6** and **4-7** will be discussed in chapter 4b. With the aid of an NMR crystallographic analysis for compound **4-3** (where there is a single-crystal X-ray structure), it will be shown that ^{1}H MAS NMR techniques are capable of probing the structure of such systems.

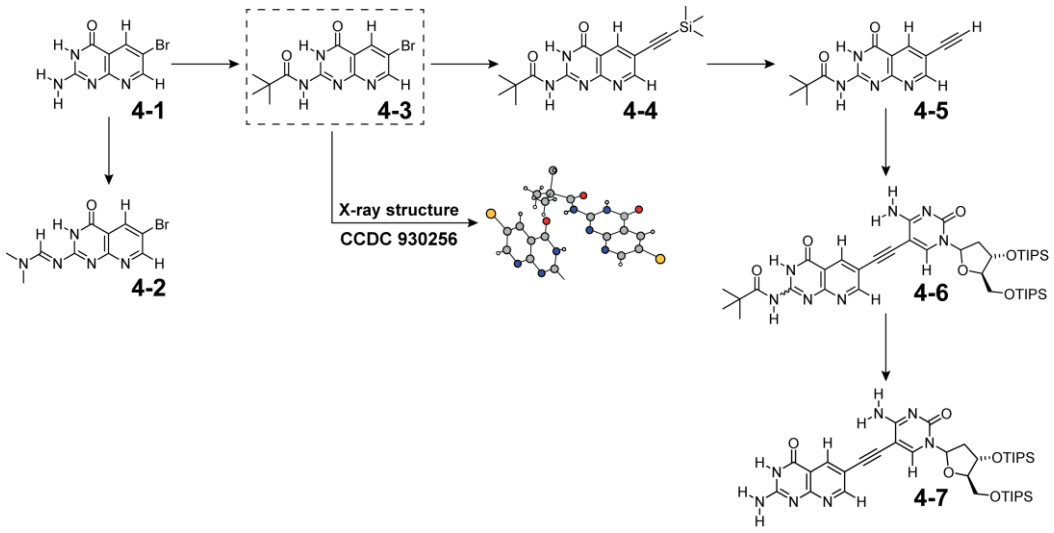

Figure 4.2 Schematic structures of the six compounds discussed in chapters 4a and 4b. Note that for **4-3** an X-ray diffraction structure exists which allows for an NMR crystallographic methodology to be applied to this system.

The chapter begins with an in depth inspection of the NMR data for compound **4-3** and conclusions are presented by comparing this information to that extracted from the single-crystal X-ray data, using the

GIPAW method discussed in chapter 1. Using these conclusions, it is possible to infer some structural characteristics in **4-4** and **4-5** owing to their overall structural and spectral similarity with **4-3**. It will be demonstrated that the pivaloyl (C_4H_9O) amide functionality is the crucial promoter of self-assembly in the solid state. Finally, a discussion of compound **4-2** will illustrate this point by examining the very different nature of its spectra when compared to the ordered spectra of pivaloyl containing systems.

4a.2 Experimental details

4a.2.1 Sample preparation

The guanine base analogues 2N-(N,N-dimethylaminomethylene)-6-bromo-5-deazapterin (**4-2**), 2-pivaloyl-6-bromo-5-deazapterin (**4-3**), 2-pivaloyl-6-(trimethylsilylethynyl)-5-deazapterin (**4-4**) and 2-pivaloyl-6-ethynyl-5-deazapterin (**4-5**) were all resynthesized according to the methods outlined in A Likhutsup's PhD thesis (Department of Chemistry, University of Warwick, 2006, see chapter 5), with all solution state characterisation data being identical to those previously reported. Note that previous discussions of compounds **4-3** and **4-6** have been presented in chapter 4 of John Griffin's thesis (Department of Physics, University of Warwick, 2007).

4a.3 Results

4a.3.1 A NMR crystallographic study of **4-3**

The solid-state packing arrangement of **4-3** as observed in the single crystal X-ray data is presented in Fig. 4.3. In a crystallographic sense, **4-3** has Z' = 1. Specifically, self-assembly into ribbon-like structures *via* two intermolecular hydrogen bonding interactions between H3 and N1 and H11 and O4 is observed. The intramolecular hydrogen bond formed between H3 and O12 is, as will be demonstrated in the rest of this subchapter, critically important to directing the overall self-assembly of **4-3**. As presented in Fig. 4.3b, the aforementioned ribbon is staggered and, as is presented in Fig. 4.3c, the presence of the heterocyclic moiety in **4-3** allows for the close approach and subsequent $\pi - \pi$ stacking interactions between individual molecules, mediated *via* the bromine containing pyridine ring.

The presence of the pivaloyl amide moiety is key to dictating the overall self-assembly of compound **4-3** (and **4-4** and **4-5** as will be demonstrated later). As shown in Fig. 4.4, the two major rotameric forms of **4-3** (**4-3a** and **4-3b**) arise as a result of rotation about the C – N bond. The fundamental difference between the two compounds is the resulting capacity for hydrogen bonding afforded by the conformation of the pivaloyl group. In the case of **4-3a**, the formation of an intramolecular hydrogen bond between H3 and the carbonyl oxygen of the pivaloyl functionality precludes the exposure of the guanine-like interface offered by **4-3b**. In the case of the latter rotamer, the rotation of the pivaloyl amide group would effectively block the approach to the free ring nitrogens in the pterin unit, thereby ensuring that the only effective hydrogen bonding possibilities reside with the guanine-like DDA motif.

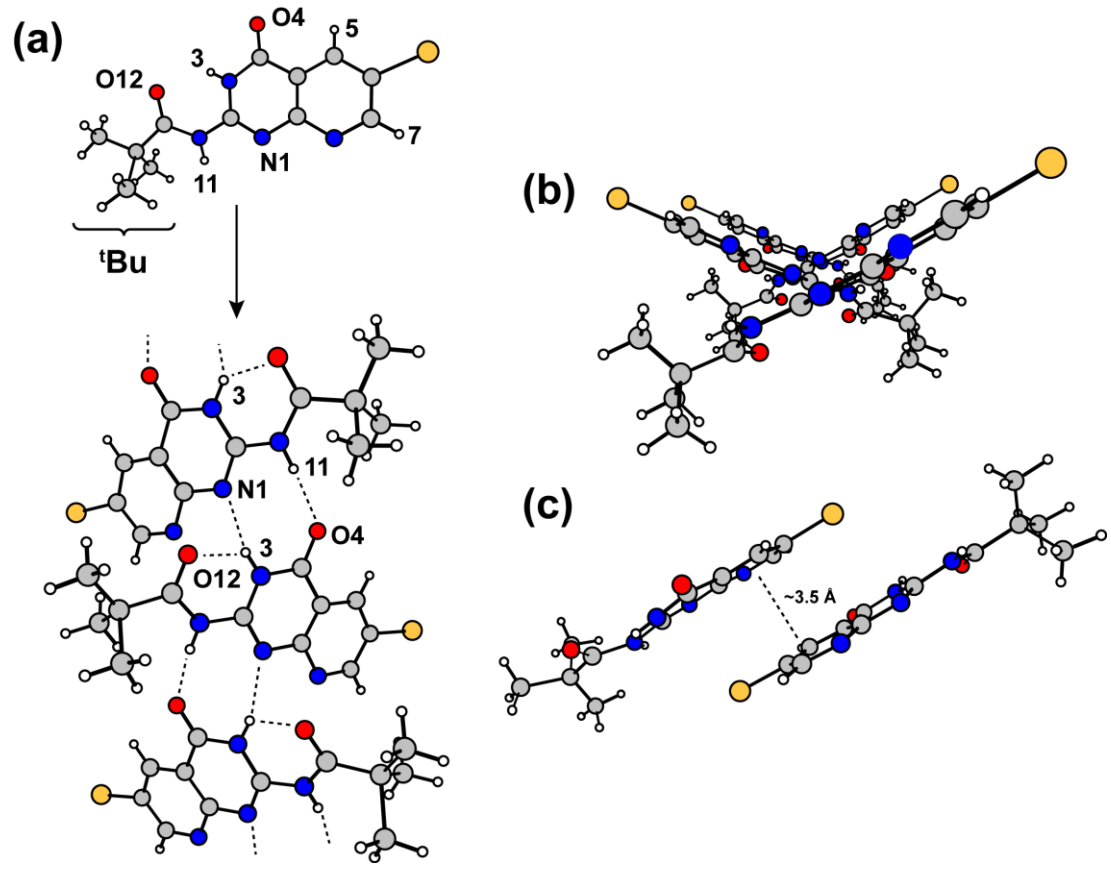

Figure 4.3 Schematic representation of (a) the asymmetric unit cell of **4-3** and its hydrogen bonded ribbon structure, (b) the staggered nature of the hydrogen bonded ribbon, (c) the π – π stacking effects observed for **4-3**. The structural views correspond to the geometry optimised crystal structure of **4-3** (CCDC 930256).

As a result rotamer **4-3b** would be only capable of forming a simple dimeric arrangement. The intramolecular hydrogen bond in **4-3a** is energetically favourable and acts to stabilise the structure. In **4-3b**, the rotation of the pivaloyl amide group about the CN bond results in the carbonyl oxygen being in close spatial proximity with the free pterin nitrogen, N1, as shown in Fig. 4.4. Such a steric clash and the preference for the intramolecular hydrogen bond in the absence of more energetically favourable hydrogen bonding motifs, is likely to drive the observation of **4-3a** only. As a result of its well-ordered structure, **4-3a** (henceforth referred to simply as **4-3**) yields highly resolved ^{1}H MAS NMR data (see below) in both one and two dimensions (even at moderate MAS frequencies). The availability of a single crystal X-ray diffraction structure for compound **4-3** allows for the assignment of experimental ^{1}H and ^{14}N chemical shifts, *via* GIPAW calculations of its NMR shielding parameters, which are presented in Table 4.1 and 4.2 respectively. As a consequence, it is possible to use this data to infer the structures of several related non-crystalline precursors with good confidence, as will be discussed in the preceding sections. It is to be noted that, the intramolecular hydrogen bond observed in **4-3** also occurs in the X-ray diffraction structure of a related pterin compound published by Corbin *et al*. (120)

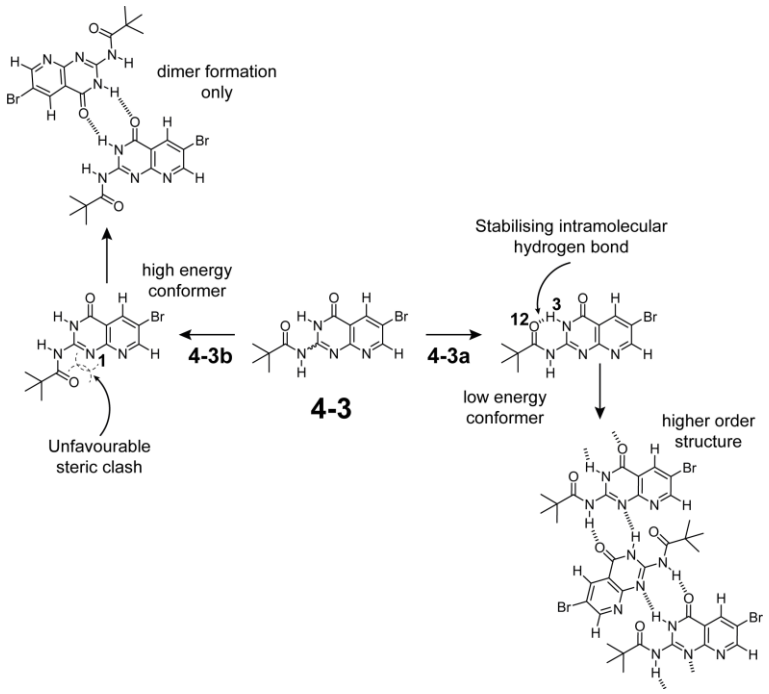

Figure 4.4 Schematic representation of the major rotameric forms of **4-3** (**4-3a** and **4-3b**). The single-crystal X-ray data is consistent with rotamer **4-3a** therefore driving tape-like self-assembly in the solid state.

Table 4.1 ^{1}H NMR parameters for **4-3** calculated using the GIPAW method.

Nucleus	σ_{xx}	σ_{yy}	σ_{zz}	σ_{ISO}	δ_{ISO}(calc)[a]	δ_{ISO}(exp)
CH_3 (a)	28.72	29.08	36.39	31.39	–0.7[b]	0.5
CH_3 (b)	26.88	30.43	36.80	31.37	–0.6[b]	0.5
CH_3 (c)	27.42	29.29	35.48	30.73	0.0[b]	0.5
CH_3 (d)	25.75	29.26	36.62	30.54	0.2[b]	0.5
CH_3 (e)	27.48	28.23	35.73	30.47	0.3[b]	0.5
CH_3 (f)	25.96	29.32	36.08	30.45	0.3[b]	0.5
CH_3 (g)	26.90	28.88	34.74	30.17	0.6[b]	0.5
CH_3 (h)	24.25	29.31	35.96	29.84	0.9[b]	0.5
CH_3 (i)	23.74	29.04	35.53	29.44	1.3[b]	0.5
H7	22.03	22.82	24.57	23.14	7.6	7.9
H5	18.81	22.35	26.46	22.54	8.2	8.5
H11	12.15	18.23	26.97	19.12	11.6	10.9
H3	10.32	16.85	23.39	16.85	13.9	13.8

[a] σ_{ref} = 30.74 ppm, [b] Due to fast rotation of CH_3 groups only one experimental resonance is observed at 0.5 ppm.

Table 4.2 A full list of ^{14}N parameters for **4-3** calculated *via* the GIPAW method.

Nucleus	V_{xx}	V_{yy}	V_{zz}	C_Q/MHz[a]	η_Q[a]	P_Q/MHz[a]	δ^Q_{iso}/ppm[a]
N3	0.06	0.42	-0.49	-2.3	0.7	2.48	122.8
N11	0.16	0.51	-0.66	-3.2	0.5	3.33	221.4
N1	0.20	0.49	-0.70	-3.4	0.4	3.49	243.2
N8	0.34	0.60	-0.95	-4.5	0.3	4.57	416.9

Nucleus	δ_{iso}(calc)/ppm	δ^Q_{iso}/ppm	δ_{iso}(calc) + δ^Q_{iso}	δ_{iso}(exp)/ppm
N3	–228.3	122.8	–105.5	–116.7
N11	–248.0	221.4	–26.6	–43.8
N1	–172.6	243.2	70.6	-
N8	–66.7	416.9	350.2	-

[a] The relevant equations for C_Q (eqn. 2.118), η_Q (eqn. 2.119), P_Q (eqn. 2.137) and δ^Q_{iso} (eqns. 2.135 and 2.136) are provided in section 2.4.7. ν_0 = 850 MHz.

In the following discussion of the ^{1}H MAS NMR data, the ^{1}H – ^{1}H distances quoted are extracted from the geometry optimised single crystal X-ray structure of **4-3**. The distances between the methyl group protons and other proton environments within **4-3** are given as average distances (av) to reflect the mobile nature of these groups. Indeed, despite variations in the calculated ^{1}H shielding parameters for the nine methyl protons in **4-3** (see Table 4.1), experimentally only one resonance is observed at 0.5 ppm, as a result of rapid rotation of these groups in a *t*-butyl moiety over the NMR timescale – note that the average of all 9 calculated ^{1}H chemical shifts is 0.3 ppm.

A ^{1}H – ^{1}H (600 MHz) DQ/SQ MAS (30 kHz) spectrum of **4-3** is presented in Fig. 4.5, alongside a schematic representation of the single crystal X-ray diffraction structure (a full list of DQ correlations is presented in Table 4.3). Since the ^{1}H spectrum is highly resolved at 30 kHz MAS, it is possible to assign, together with the GIPAW calculated chemical shifts (see Table 4.1), each individual ^{1}H environment with high confidence.

The strong auto-peak observed at δ_{DQ} = 0.5 + 0.5 = 1.0 ppm occurs due to the high density of methyl protons in close spatial proximity. This is a common feature of the compounds outlined in this chapter (and indeed others), where the presence of methyl groups in protecting functionalities is synthetically necessary (principally for purposes of solubility in organic solvents). This high abundance of methyl ^{1}H environments results in cross-peaks to three other resonances, δ_{DQ} = 0.5 + 7.9 = 8.4 ppm (CH_3 – H7, 2.82 Å, av), δ_{DQ} = 0.5 + 10.9 = 11.4 ppm (CH_3 – H11, 2.72 Å(av)) and δ_{DQ} = 0.5 + 13.8 = 14.3 ppm

(CH_3 – H3, 3.08 Å(av)). The X-ray crystal structure shows an intermolecular contact involving the two distinct NH protons (2.83 Å) and also between the two aromatic CH protons (2.79 Å). This is consistent with the NMR data which reveals cross-peaks at δ_{DQ} = 10.9 + 13.9 = 24.8 ppm (H11 – H3) and δ_{DQ} = 7.9 + 8.5 = 16.4 ppm (H7 – H5), respectively.

The ^{1}H chemical shifts of the H11 and H3 protons at 10.9 and 13.8 ppm, respectively, are highly indicative of their involvement in hydrogen bonding interactions. Indeed, the 13.8 ppm ^{1}H chemical shift of proton H3 is consistent with the formation of an intramolecular hydrogen bonding arrangement in **4-3** (see the crystal structure representation in Fig. 4.3). Proton H11 is involved in an intermolecular hydrogen bonding interaction (N – H ⋯ O, N to O distance of 2.92 Å, angle 170.6°) with the carbonyl oxygen on the pterin unit (see Fig. 4.3), hence consistent with a ^{1}H chemical shift of 10.9 ppm. Interestingly, proton H3 seemingly forms a second intermolecular hydrogen bonding interaction with nitrogen N1 (N – H ⋯ N, N to N distance of 2.96 Å, angle 149.8°). These interactions lead to **4-3** forming a staggered tape-like or ribbon structure in the solid state, with individual ribbons associating *via* π – π stacking interactions (through the bromine containing pyridine ring).

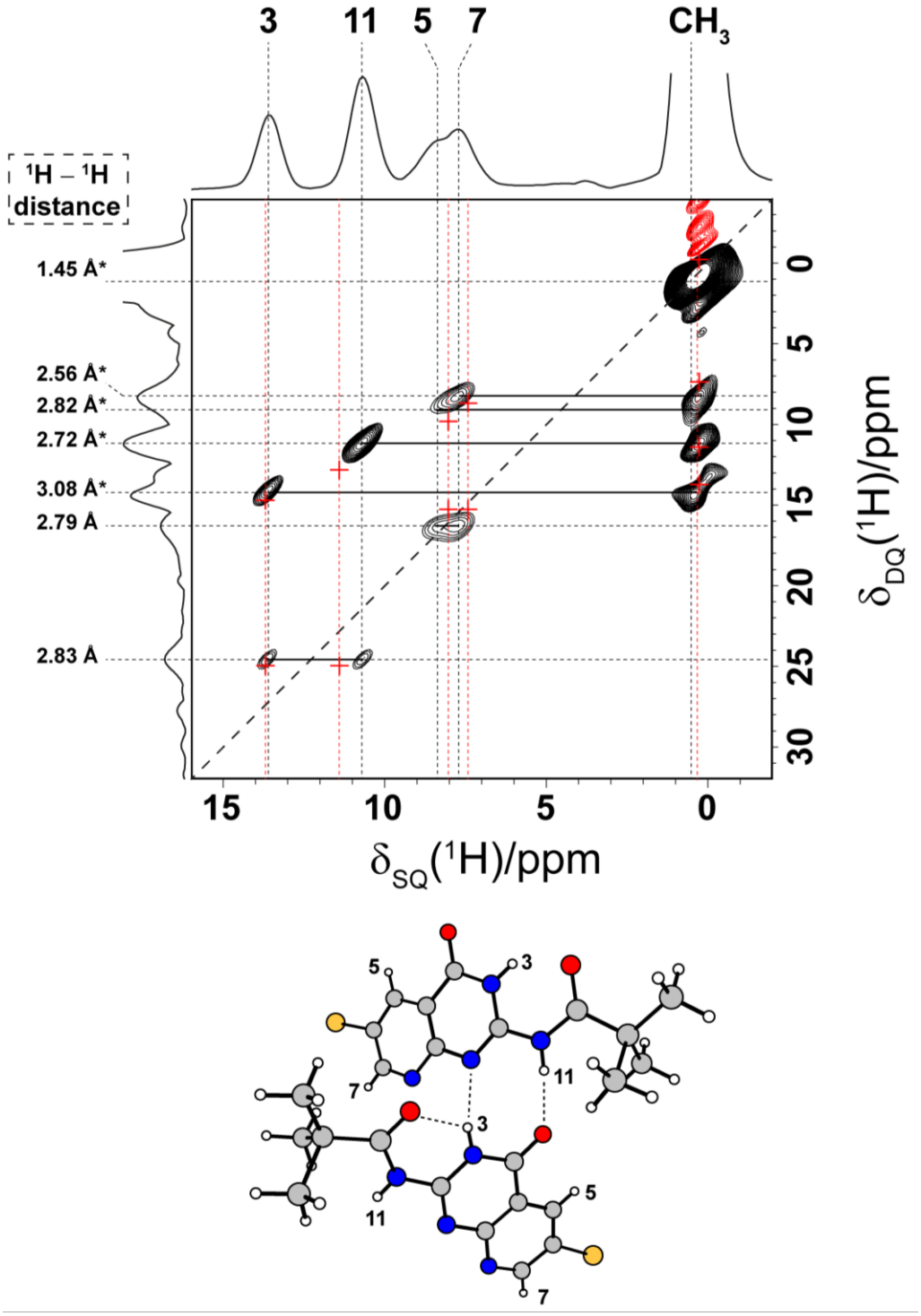

Figure 4.5 A $^{1}H - ^{1}H$ (ω_0 = 600 MHz) DQ/SQ MAS (30 kHz spinning) spectrum of **4-3**, together with skyline projections, GIPAW calculated ^{1}H chemical shifts (red crosses, $^{1}H - ^{1}H$ cut-off is 3.1 Å, for the CH_3 protons an average calculated chemical shift is given for all nine environments), and a schematic representation of the geometry-optimised (CASTEP) crystal structure. One rotor period of BABA recoupling was used for the excitation and reconversion of DQ coherence. For each of 256 t_1 FIDs, 96 transients were coadded with a recycle delay of 3 seconds. The $F_1 = 2F_2$ diagonal is indicated as a dashed black line, with DQ correlations highlighted via solid horizontal lines. The base contour level is shown at 4% of the maximum peak intensity. The observed $^{1}H - ^{1}H$ distances, extracted from the geometry optimised crystal structure, are given alongside the corresponding cross-peak. Note that * indicates an average distance between environments.

Table 4.3 DQ correlations extracted from the $^{1}H - {}^{1}H$ DQ/SQ MAS spectrum of **4-3** in Fig. 4.5

4-3	#	correlation	Sum of SQ freq (ppm)	DQ freq (ppm)	Distance[ǂ] (Å)
	1	$CH_3 - CH_3$	0.5 +0.5	1.0	1.45 (av)
	2	CH_3 – H7	0.5 + 7.9	8.4	2.56 (av)
	3	CH_3 – H5	0.5 + 8.5	9.0	2.82 (av)
	4	CH_3 – H11	0.5 + 10.9	11.4	2.72 (av)
	5	CH_3 – H3	0.5 + 13.9	14.4	3.08 (av)
	6	H7 – H5	7.9 + 8.5	16.4	2.79
	7	H11 – H3	10.9 + 13.9	24.8	2.83

[ǂ] Distances extracted from geometry optimised X-ray single crystal structure. (av) represents an average distance to the three CH_3 protons.

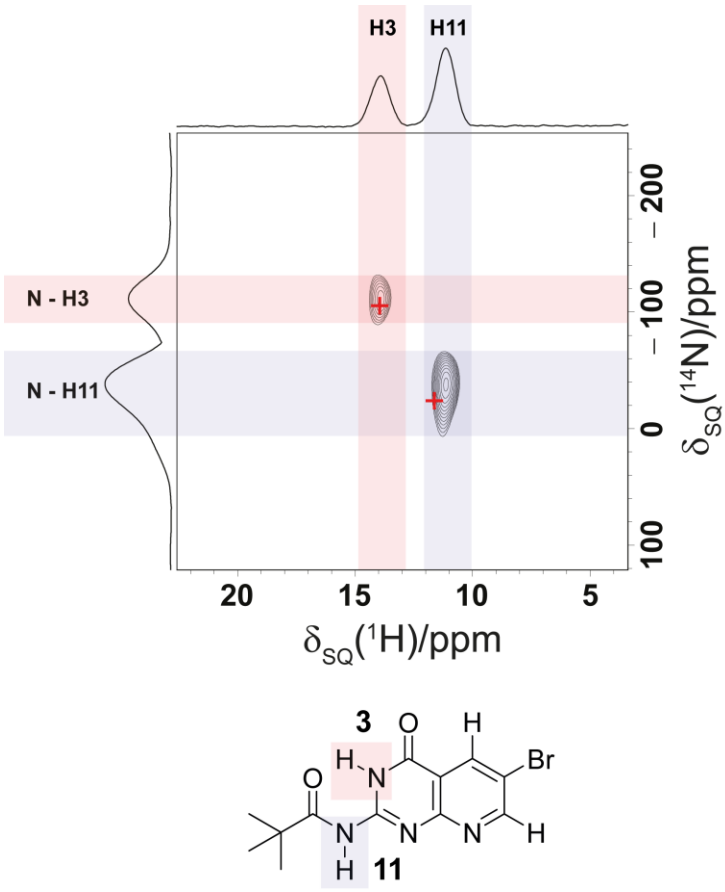

Figure 4.6 A $^{14}N - {}^{1}H$ (ω_0 = 850 MHz) HMQC spectrum of **4-3**, including GIPAW calculated NMR shift parameters in both the ^{1}H and ^{14}N dimensions (given as red crosses). The spectrum was recorded using the R^3 recoupling scheme (for the recoupling of the $^{14}N - {}^{1}H$ heteronuclear dipolar couplings) for a τ_{RCPL} = 107 μs. For each of 48 t_1 FIDs, 320 transients were coadded with a recycle delay of 2 seconds. The base contour level is shown at 68.5% of the maximum peak intensity.

The ^{14}N – ^{1}H HMQC spectrum shown in Fig. 4.6 provides further support for the assignments of the H3 and H11 protons. At the short recoupling time (τ_{RCPL}) employed, only one bond N – H correlations are expected to be observed, hence the two peaks in the spectrum correspond to the only two NH groups in **4-3**. Extending the recoupling time can in principle reveal longer distance correlations, and is therefore particularly useful in probing NH ⋯ N hydrogen bonding motifs. However, if the protons relax during the time required to observe such correlations then the signal is too weak to be properly resolved, or observed at all, as was the case for **4-3**. Nevertheless, the complementary GIPAW ^{14}N parameters remain useful for assignment purposes.

4a.3.2 The packing of **4-4** and **4-5** in the solid state

The molecular structures of **4-3**, **4-4** and **4-5**, are differentiated by the nature of the chemical functionality at the 6-position on the pyridine ring of the pterin-inspired heterocycle. As was discussed in section 4a.3.1, the pivaloyl amide moiety is key to directing the self-assembly of **4-3**, with the bromine atom being less significant. Replacing this halogen atom with the bulkier trimethylsilyl(TMS)ethynyl (**4-4**) and ethynyl (**4-5**) groups may be expected to have some additional effect on the overall structures of these analogues in the solid state, given that these moieties are larger than the aforementioned halogen, but as shown in this section, the high-ppm ^{1}H chemical shifts are similar, indicating that the same intermolecular hydrogen bonding is observed in **4-3**, **4-4** and **4-5**.

A ^{1}H – ^{1}H (600 MHz) DQ/SQ MAS (30 kHz) spectrum of **4-4** is presented in Fig. 4.7 (DQ correlations are listed in Table 4.4), together with (at the bottom of Fig. 4.7) the spectrum of **4-3** that was presented in Fig. 4.5. As can be seen from this direct comparison, the ^{1}H chemical shifts of each individual proton environment and the overall 'spectral pattern', is almost identical in **4-3** and **4-4**, thereby suggesting a common mode of assembly in the solid state. The major difference between these two compounds relates to the extra methyl protons contained, in the case of **4-4**, within the trimethylsilyl group, and hence two distinct methyl resonances are observed. These protons generate additional cross-peaks that are observed in the DQ spectrum of **4-4**, with proton H5 now within close contact of the TMS methyl protons (δ_{DQ} = – 0.3 + 8.6 = 8.3 ppm). The nitrogen bound H11 and H3 protons also experience dipolar couplings with these methyl environments, as evidenced by the appearance of cross-peaks at δ_{DQ} = – 0.3 + 11.0 = 10.7 ppm and δ_{DQ} = – 0.3 + 13.7 = 13.4 ppm, respectively. The resolution of the spectrum is marginally better across the whole ^{1}H chemical shift range for **4-4**, when compared to **4-3**, but significantly more so in the aromatic region (δ_{SQ} 8.0 – 9.0 ppm), in which it is possible to clearly resolve each of the two separate aromatic protons, H7 and H5, in **4-4**. Note that these two ^{1}H environments overlapped significantly in **4-3**, as was observed in Fig. 4.5. Despite this minor resolution difference, based on the similarity of the ^{1}H chemical shifts and overall spectrum, the TMSethynyl group seemingly has little effect on the self-assembling properties of **4-4**, suggesting that association is driven by the conformation of the pivaloyl amide group with respect to the pterin moiety, as was the case for **4-3**.

In the case of **4-5**, in which the trimethylsilyl moiety has been removed to yield the ethynyl functionality, the spectrum is somewhat different when compared to the corresponding spectra of **4-3** and **4-4**. A $^{1}H - ^{1}H$ (500 MHz) DQ/SQ MAS (30 kHz) spectrum of **4-5** is presented in Fig. 4.8, together with the spectra of **4-3** and **4-4** (presented at the bottom of Fig. 4.8), originally presented in Figs. 4.5 and 4.7, respectively. A full list of DQ correlations for **4-5** is presented in Table 4.5.

Several observations can be made upon inspection of the DQ spectrum of **4-5**. The first thing to note is that the ^{1}H chemical shift positions are similar to those observed in the corresponding spectra of the previous two compounds including, importantly, the H3 chemical shift (H3 resonates at approximately 14 ppm in **4-3**, **4-4** and **4-5**). This is demonstrated by the comparison of ^{1}H MAS one-pulse spectra presented in Fig. 4.9. This evidence alone is highly suggestive of a retention of the intramolecular hydrogen bond and hence retention of the conformation of the pivaloyl functionality about the CN bond. This is logical since the presence of the ethynyl moiety alone offers no obvious additional hydrogen bonding pathways, except those already open to both **4-3** and **4-4**. However, this being said, the spectrum is much broader than for its two precursors, perhaps suggesting some additional disorder in the solid-state packing. In addition, several extra cross-peaks are also revealed and, interestingly, the appearance of a H3 – H3 auto-peak at $\delta_{DQ} = 14.2 + 14.2 = 28.4$ ppm, is observed (this peak is observed in the column extracted at $\delta_{SQ} = 14.2$ ppm, in Fig. 4.8). It should be noted that no evidence was found for the existence of such an auto-contact in the spectra of either **4-3** or **4-4**, which may suggest a number of things but, given the high likelihood of the intramolecular hydrogen bond being retained, is most likely due to some closer packing of individual tapes. Given that in the crystal structure of **4-3** no close approach of two H3 protons is observed (closest distance is 5.1 Å), this auto-peak perhaps suggests a different crystal packing, a different π stacking arrangement or some other phenomenon, although this is purely speculation based on this data. **4-5** therefore epitomises a disadvantage of solid-state NMR when compared to single crystal diffraction techniques. Although it is possible to extract distance constraints and probe other local atomic phenomenon, it is not possible to elucidate the complete three-dimensional packing for the system in question based on the solid-state NMR data alone.

Cross-peaks between the nitrogen bound H11 and H3 protons and the aromatic protons are also now observed at $\delta_{DQ} = 8.2 + 11.1 = 19.3$ ppm and $\delta_{DQ} = 8.2 + 14.2 = 22.4$ ppm, respectively, for **4-5**. However, the broadened lineshapes now make it impossible to distinguish between the two aromatic protons, which was possible in the case of **4-4**. Multiple cross-peaks are also observed between NH and aromatic protons and the alkynyl proton at approximately 4.0 ppm. Despite these additional contacts, the similar spectral pattern and ^{1}H chemical shifts are indicative of a retention of the intramolecular hydrogen bond and thus persistence of the ribbon assembly in all three analogues: **4-3**, **4-4** and **4-5**.

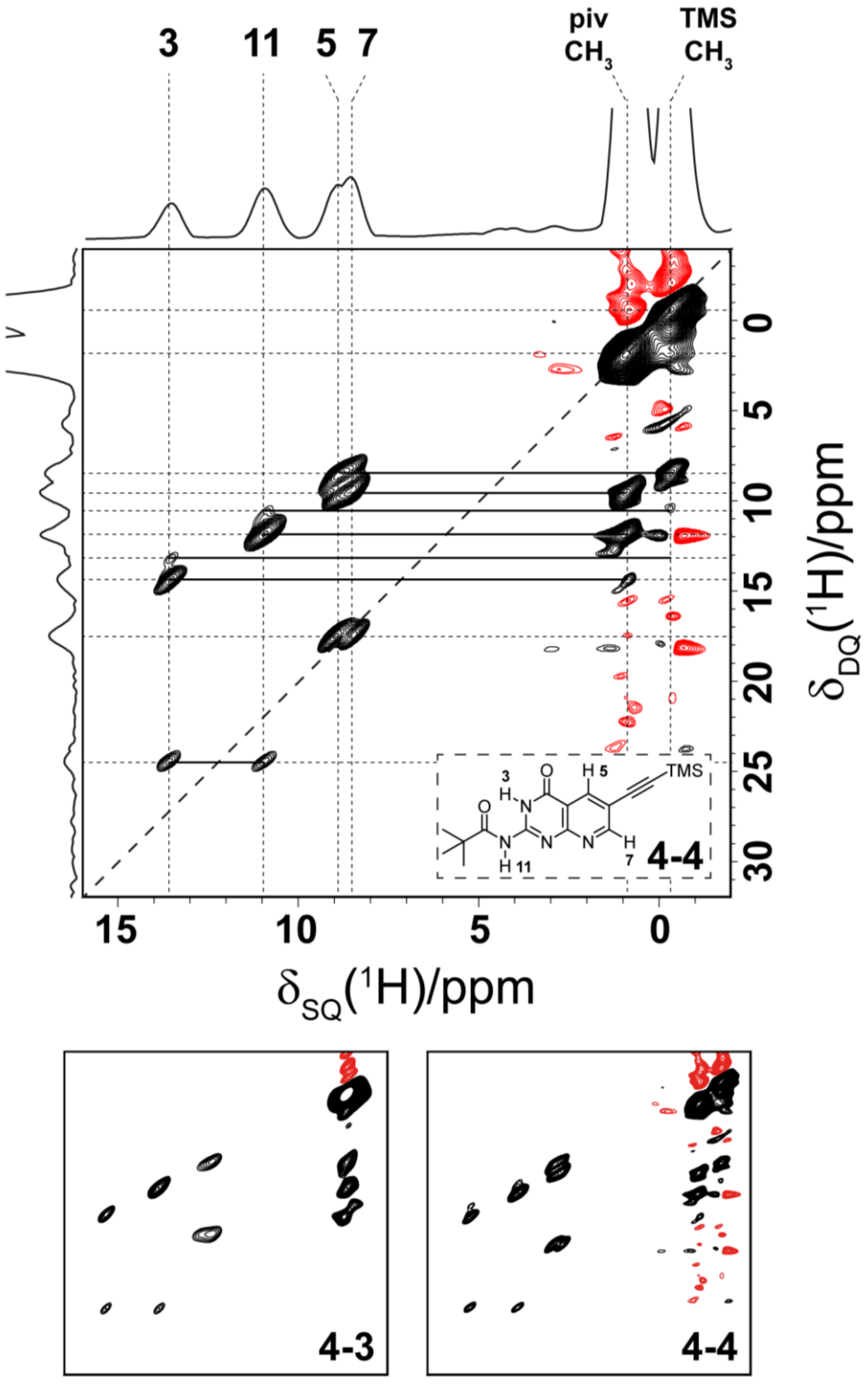

Figure 4.7 A ^{1}H – ^{1}H (ω_0 = 600 MHz) DQ/SQ MAS (30 kHz spinning) spectrum of **4-4** together with skyline projections and assignments of the separate ^{1}H environments. One rotor period of BABA recoupling was used for the excitation and reconversion of DQ coherence. For each of 128 t_1 FIDs, 16 transients were coadded with a recycle delay of 3 seconds. The $F_1 = 2F_2$ diagonal is given as a dashed black line, with DQ correlations highlighted via solid horizontal lines. The base contour level is shown at 5% of the maximum peak intensity. The DQ spectrum of **4-3**, given in Fig. 4.5, is presented for comparison.

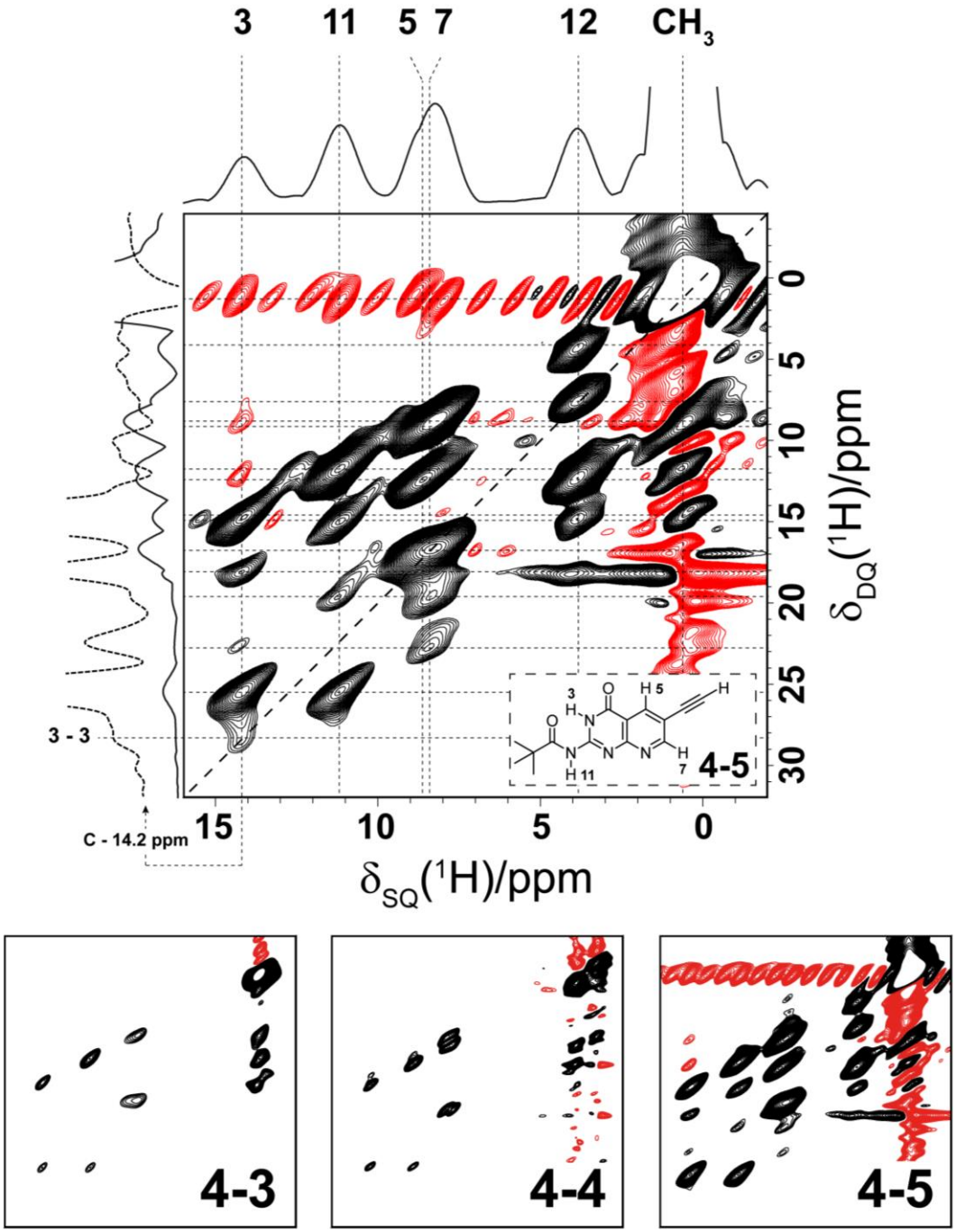

Figure 4.8 A ^{1}H – ^{1}H (ω_0 = 500 MHz) DQ/SQ MAS (30 kHz spinning) spectrum of **4-5** together with skyline projections and assignments of the separate ^{1}H environments. One rotor period of BABA recoupling was used for the excitation and reconversion of DQ coherence. For each of 256 t_1 FIDs, 64 transients were coadded with a recycle delay of 3 seconds. The $F_1 = 2F_2$ diagonal is given as a dashed black line, with DQ correlations highlighted via solid horizontal lines. The base contour level is shown at 1% of the maximum peak intensity. The DQ spectrum of **4-3**, given in Fig. 4.5, and **4-4**, given in Fig. 4.7, are also presented for comparison. The dashed lineshape in F_1 represents the column extracted at 14.2 ppm (SQ), which indicates that the weak H3 – H3 auto-peak is real and above the noise.

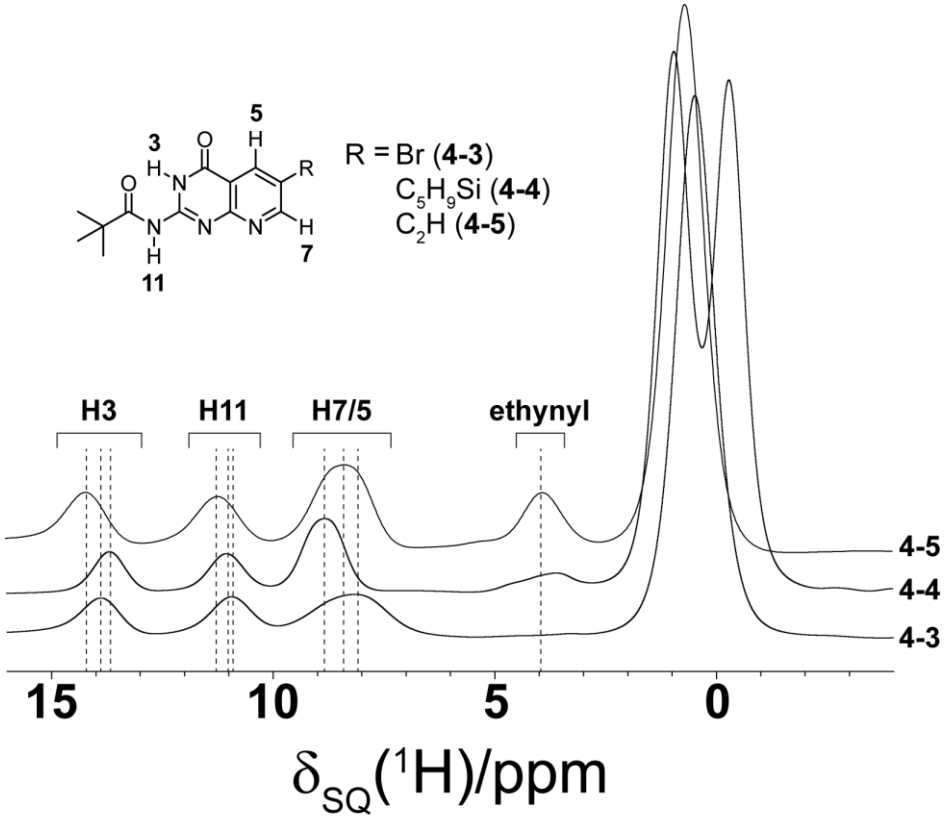

Figure 4.9 Comparison of ^{1}H (ω_0 = 600 MHz, **4-3**, **4-4**, 500 MHz, **4-5**) MAS (30 kHz spinning) one-pulse spectra of **4-3**, **4-4** and **4-5**, with assignments of the various ^{1}H chemical shifts. In each case, 8 (**4-3**, **4-4**) and 4 (**4-5**) transients were coadded with a recycle delay of 3 seconds.

Consider the self-assembly possibilities for **4-5**. The appearance of the H3 auto-peak can in theory be explained by a dimeric hydrogen bonded motif, as shown in Fig. 4.10, where the intramolecular hydrogen bond is retained and the H3 proton forms an intermolecular contact with itself across the hydrogen bond interface. This arrangement, however, does not account for many of the other cross-peaks observed in the DQ spectrum presented in Fig. 4.7, most notably the strong H11 – H3 peak at δ_{DQ} = 11.1 + 14.2 = 25.3 ppm. As was discussed in section 4a.3.1, this particular compound has no other routes to self-assembly even if the CN bond rotates (recall Fig. 4.3), making ribbon/tape formation the only realistic option if dimer formation is excluded. Likewise, if possible prototropic tautomers involving the H3 proton are considered (Fig. 4.10), it is not feasible to envisage any other structure which can account for all the observed peaks. In addition, it is unlikely that any tautomerism occurs, since no evidence for this phenomenon was observed with **4-3** and **4-4**. Based on this evidence it is assumed that **4-5** adopts an identical conformation as observed for **4-3** and **4-4**, and therefore exhibits the same hydrogen bonding properties, with perhaps some variable packing arrangement being suggested by the additional cross-peaks, in particular the H3 – H3 contact.

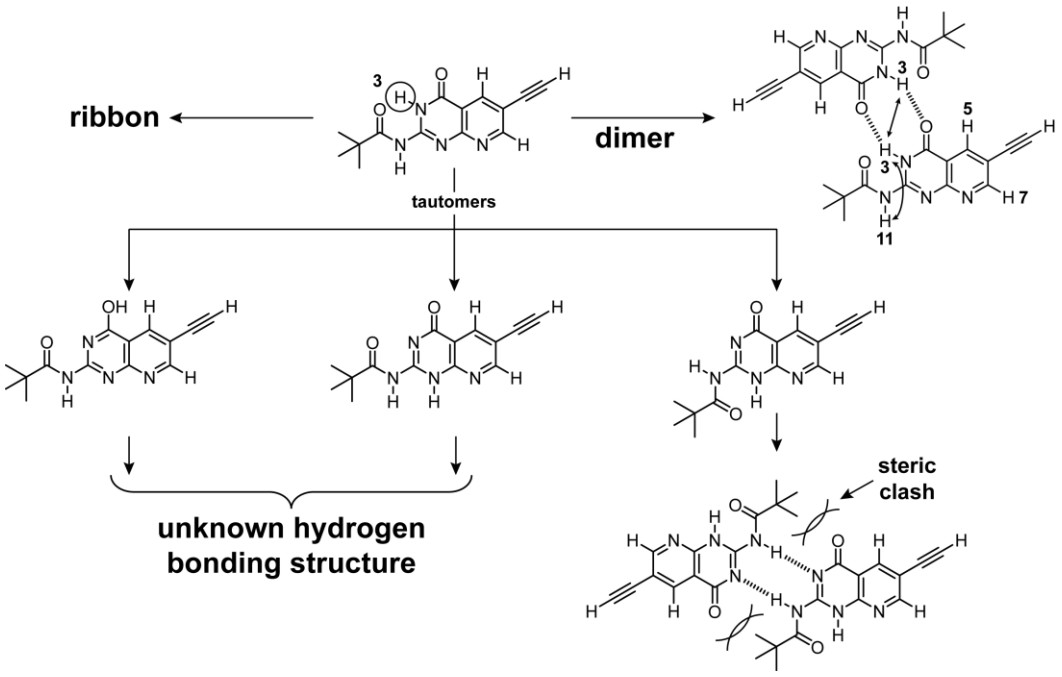

Figure 4.10 Schematic representation of some possible prototropic tautomers of **4-5** involving *only* the H3 proton. Note that no concieved structure can account for the observed cross-peaks, in particular the strong H11 – H3 contact other than the tape/ribbon like structure observed for **4-3** and **4-4**.

Table 4.4 DQ correlations extracted from the $^{1}H - ^{1}H$ DQ/SQ MAS spectrum of **4-4** (see Fig. 4.7)

4-4	#	Correlation	Sum of SQ freq / ppm	DQ freq / ppm
	1	CH_3 (TMS, auto)	– 0.3 + –0.3	– 0.6
	2	CH_3 (^{t}Bu, auto)	0.9 + 0.9	1.8
	3	CH_3 (TMS) – H5	– 0.3 + 8.6	8.3
	4	CH_3 (TMS) – H7	– 0.3 + 9.0	8.7
	5	CH_3 (^{t}Bu) – H5	0.9 + 8.6	9.5
	6	CH_3 (^{t}Bu) – H7	0.9 + 9.0	9.9
	7	CH_3 (TMS) – H11	– 0.3 + 11.0	10.7
	8	CH_3 (^{t}Bu) – H11	0.9 + 11.0	11.9
	9	CH_3 (TMS) – H3	– 0.3 + 13.7	13.4
	10	CH_3 (^{t}Bu) – H3	0.9 + 13.7	14.6
	11	H5 – H7	8.6 + 9.0	17.6
	12	H11 – H3	11.0 + 13.7	24.7

Table 4.5 DQ correlations extracted from the $^{1}H - ^{1}H$ DQ/SQ MAS spectrum of **4-5** (see Fig. 4.8)

4-5	#	Correlation	Sum of SQ freq / ppm	DQ freq / ppm
	1	CH_3 (auto)	0.7 + 0.7	1.4
	2	CH_3 – H12	0.7 + 3.9	4.6
	3	H12 – H12	3.9 + 3.9	7.8
	4	CH_3 – H5	0.7 + 8.2	8.9
	5	CH_3 – H7	0.7 + 8.6	9.3
	6	CH_3 – H11	0.7 + 11.2	11.9
	7	H12 – H7	3.9 + 8.6	12.5
	8	CH_3 – H3	0.7 + 14.2	14.9
	9	H12 – H11	3.9 + 11.2	15.1
	10	H5 – H7	8.2 + 8.6	16.8
	11	H12 – H3	3.9 + 14.2	18.1
	12	H5 – H11	8.2 + 11.1	19.3
	13	H5 – H3	8.2 + 14.2	22.4
	14	H11 – H3	11.2 + 14.2	25.4
	15	H3 – H3	14.2 + 14.2	28.4

4a.3.3 The importance of the pivaloylamide group

The hydrogen bonding, and thus self-assembling properties of the pivaloylamide functionality, and the intramolecular hydrogen bond the carbonyl oxygen forms with the H3 proton, have been discussed at some length in sections 4a.3.1 and 4a.3.2. In compound **4-2**, the pivaloyl amide moiety is replaced with a dimethylaminomethylene group, thereby removing any possibility for intramolecular hydrogen bond formation with proton H3. As will be demonstrated in this section, the absence of the pivaloyl amide functionality has important consequences for the self-assembling options of the pterin unit. A $^{1}H - ^{1}H$ (600 MHz) DQ/SQ MAS (60 kHz) spectrum of **4-2** is presented in Fig. 4.11 alongside the DQ spectrum of **4-3** (Fig. 4.5), for comparison. A full list of DQ correlations for **4-2** is presented in Table 4.6.

The conformation of the dimethylaminomethylene group is the key consideration in determining the overall self-assembly properties of **4-2**. However, in this case, the question of supramolecular structure is made easier in that the structure of **4-2** may permit only dimer formation, considering its available

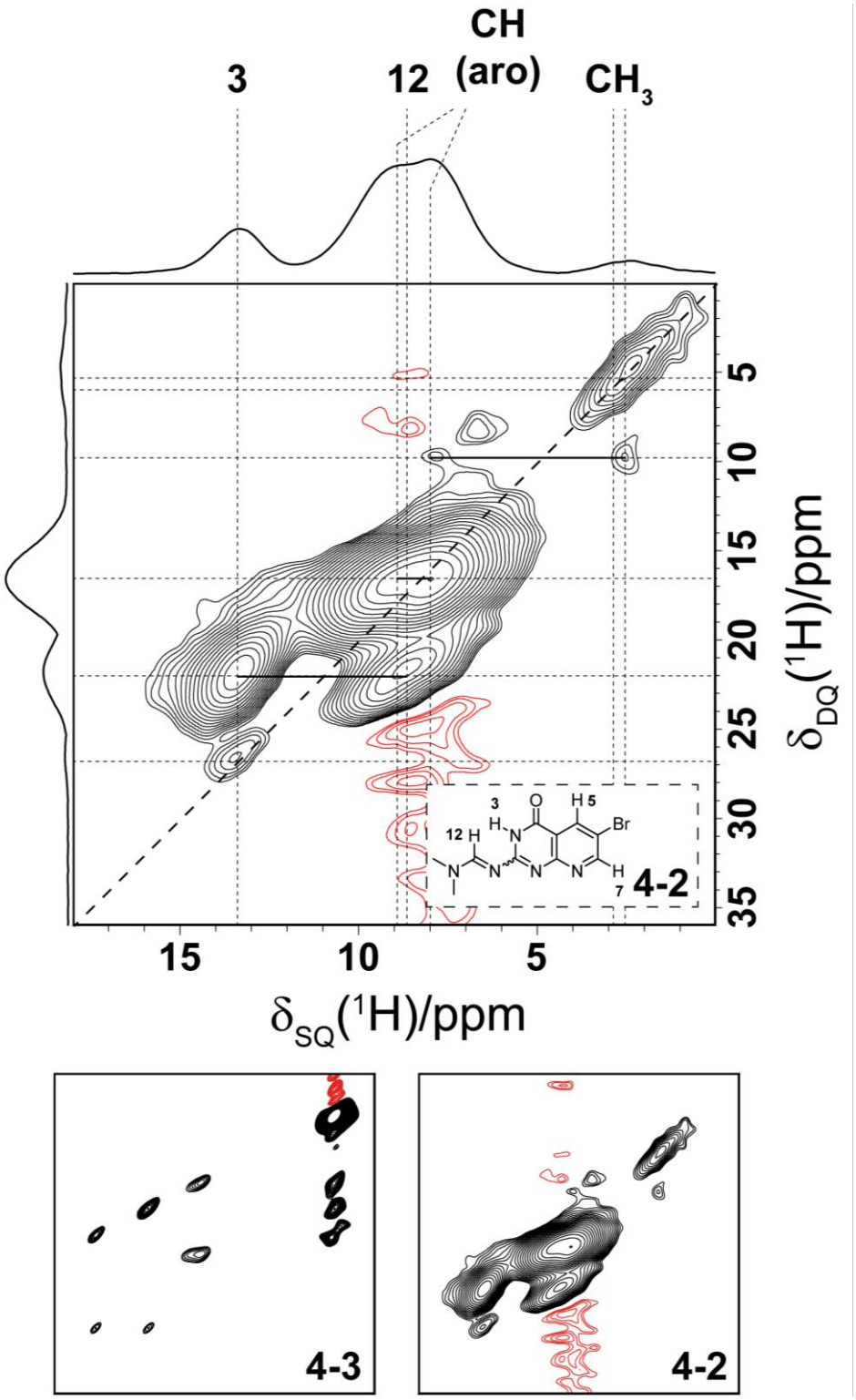

Figure 4.11 A ^{1}H – ^{1}H (ω_0 = 600 MHz) DQ/SQ MAS (60 kHz spinning) of **4-2** together with skyline projections and assignments of the separate ^{1}H environments. One rotor period of BABA recoupling was used for the excitation and reconversion of DQ coherence. For each of 128 t_1 FIDs, 16 transients were coadded with a recycle delay of 3 seconds. The $F_1 = 2F_2$ diagonal is given as a dashed black line, with DQ correlations highlighted via solid horizontal lines. The base contour level is shown at 1% of the maximum peak intensity. The DQ spectrum of **4-3**, given in Fig. 4.5, is presented for comparison.

hydrogen bonding donor and acceptor capabilities, regardless of the conformation about the CN bond. This explains the broad nature of the ^{1}H DQ spectrum when compared to that of **4-3**, since higher order structures (ribbons etc.) are not possible in **4-2**, hence the packing is likely to be more disordered.

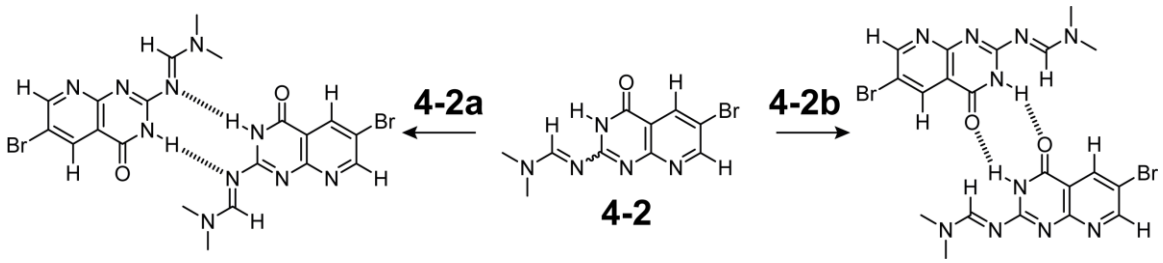

Figure 4.12 Schematic representation of the possible dimeric arrangments of **4-2** depending on the orientation of the CN bond.

Two different hydrogen bonding arrangements are possible in this compound, both of which lead to dimer formation, as shown in Fig. 4.12. Based on the DQ spectrum and, in particular, the strong cross-peak at δ_{DQ} = 8.7 + 13.4 = 22.1 ppm, only dimer **4-2b** is observed, given that this cross-peak is consistent with a strong intramolecular H12 – H3 coupling. The H3 – H3 auto-peak at δ_{DQ} = 13.4 + 13.4 = 26.8 ppm corresponds to the contact across the hydrogen bonding face. Note that rotamer **4-2a** would give rise to a H3 auto-peak (again consistent with a contact across the hydrogen bonding face), but cannot account for the intense H12 – H3 cross-peak, given the conformation of the dimethylaminomethylene group, assuming that the assignment of the H12 proton is correct.

Table 4.6 DQ correlations extracted from a ^{1}H – ^{1}H DQ/SQ MAS spectrum of **4-2** (see Fig. 4.11)

4-2	#	Correlation	Sum of SQ freq / ppm	DQ freq / ppm
	1	CH_3 (auto)	2.6 + 2.6	5.2
	2	CH_3 (auto)	2.8 + 2.8	5.6
	3	CH_3 – aro	2.6 + 8.0	10.6
	4	aro - aro	8.0 + 8.9	16.9
	5	H12 – H3	8.7 + 13.4	22.1
	6	H3 – H3	13.4 + 13.4	26.8

Two ^{14}N – ^{1}H (600 MHz) HMQC spectra of **4-2** are presented in Fig. 4.13, alongside the DQ spectrum presented in Fig. 4.11 (Fig. 4.13a), with different recoupling times (τ_{RCPL}), corresponding to 107 (Fig. 4.13b) and 666 μs (Fig. 4.13c) respectively. At the short recoupling time, a strong N3 – H3 peak is observed, as expected, corresponding to the fact that these environments constitute a directly bonded pair.

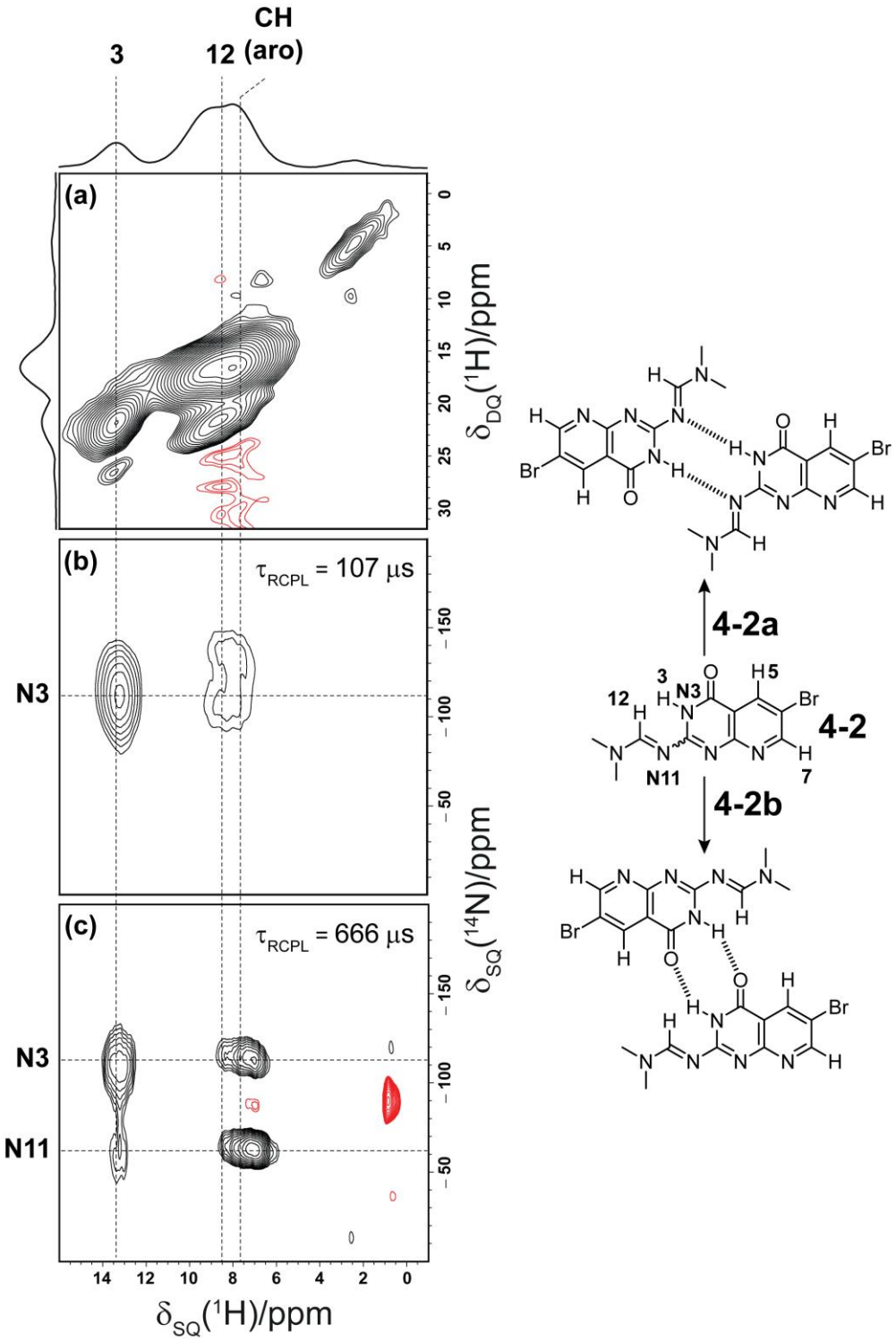

Figure 4.13 Spectra for **4-2** (structures of **4-2a** and **4-2b** shown on the left), measured at 600 MHz and 60 kHz MAS: (a) a ^{1}H – ^{1}H DQ/SQ MAS spectrum (reproduced from Fig. 4.11) and (b, c) ^{14}N – ^{1}H HMQC spectra recorded using the R^3 recoupling scheme (recoupling of the ^{14}N – ^{1}H heteronuclear dipolar couplings) for a τ_{RCPL} time of (b) 107 μs and (c) 666 μs. For the HMQC spectra, for each of 64 t_1 FIDs, 16 transients were coadded with a recycle delay of 3 seconds. The base contour level for each spectrum is shown at (b) 50% and (c) 60% of the maximum peak intensity.

A very low intensity peak is also observed in this spectrum, consistent with the H12 proton. Assuming this assignment is correct (the exact centre of the peak in the HMQC spectrum is somewhat ambiguous), it gives further credence to the **4-2b** rotamer discussed in Fig. 4.12, given that in this system the H12 and N3 environments sit in close spatial proximity. At longer recoupling times (τ_{RCPL} = 666 μs), a strong peak is observed at approximately 8.0 ppm in the ^{1}H dimension and −60 ppm in the ^{14}N dimension. Further peaks are observed at ~ 13.0 ppm in the ^{1}H dimension and −60 and −110 ppm in the ^{14}N dimension, which is expected since at longer recoupling times polarisation transfer between the H3, H12, N3 and N11 environments will all take place.

4a.4 Summary

In this subchapter, it has been shown, using NMR crystallographic approaches (for **4-3**) and high resolution ^{1}H MAS NMR data, that for the simple pterin unit alone to self-assemble into higher order aggregates, the nature of the chemical moiety bonded to the exocyclic N11 nitrogen is critically important, with other chemical features being less significant (but still worthy of consideration). In chapter 4b, two important compounds will be discussed at length, **4-6** and **4-7** (see Fig. 4.2) in which the functionality at the 6-position on the pyrazine ring, contains not only a simple halogen or triple bond, but instead a deoxycytidine group which is capable of hydrogen bonding and self-assembly in its own right (see also chapter 5). As will be demonstrated, the addition of this group dramatically influences the hydrogen bonding properties of the pterin unit (in a way that was not observed for **4-3**, **4-4** and **4-5**) and, in the case of **4-6**, the conformation of the pivaloyl amide group, rotation of which now affords a DDA/AAD hydrogen bonding motif between the pterin and deoxycytidine components of the molecule.

4b.1 Introduction

Complex synthetic molecules, based on the hydrogen bonding motifs of the guanine and cytosine base units, offer an attractive route for synthetic supramolecular chemists in the quest for new materials with useful properties. The compounds described in this subchapter build upon the molecules introduced previously in chapter 4a. The versatile pterin unit which, as was demonstrated in chapter 4a, has its own unique capacity for self-assembly, is now combined with the well-known deoxycytidine moiety. In particular, compound **4-7** was originally designed to self-assemble into higher order structures in solution. The DDA and AAD hydrogen bonding motifs of the pterin and cytidine units, respectively, allow for this possibility. Indeed, this molecule forms structures consistent with a cyclic trimer in solution based on DOSY NMR, gel permeation chromatography (GPC) and circular dichroism (CD) measurements (A Likhutsup thesis 2006).

Previous solution data for **4-6** shows that it also exhibits significant self-assembly. The solid-state NMR data, as will be shown in this chapter, also indicates a high level of structural order based on the highly resolved nature of the two-dimensional ^{1}H DQ spectrum. The higher chemical complexity in these molecules leads to a more sophisticated ^{1}H chemical shift signature and makes effective assignment of the various proton environments more difficult.

As will be demonstrated in this chapter, the capabilities of high-resolution ^{1}H solid-state NMR are truly tested for non-crystalline, high molecular weight compounds containing several possible outlets for self-assembly *via* hydrogen bonding and $\pi - \pi$ stacking interactions. In particular, compounds designed to associate through certain hydrogen bonding motifs but which, *via* e.g. bond rotations/tautomerism, can form multiple possible supramolecular structures (i.e. trimers, helices, ribbons, stacked nanotubes), still present a significant challenge, and as such there is still a paucity of data in the literature regarding the solid-state aggregation of such materials. The data presented herein is capable of elucidating the likely hydrogen bonding structure; however, as will be discussed, it is not possible to extract information concerning the specific *mode* of higher-order self-assembly on this data alone. This is because these molecules, whilst exhibiting identical hydrogen bonding arrangements, may form multiple different assemblies which are difficult to probe by means of NMR (e.g. the same hydrogen bonding arrangement would be observed for trimers and ribbons for instance). In any case, in the absence of suitable single crystal formation for these compounds, solid-state NMR is the only high-resolution technique which has the potential to provide answers. Attempts at single crystal diffraction were made for **4-6**, which is observed to form a 'micro-crystalline' solid, however the material is non-crystalline and glassy in nature upon closer inspection (hence single crystal diffraction was not possible). The chemical structures of compounds **4-6** and **4-7** are presented in Fig. 4.14, alongside the structure of the triisopropylsilyl (TIPS) protecting group.

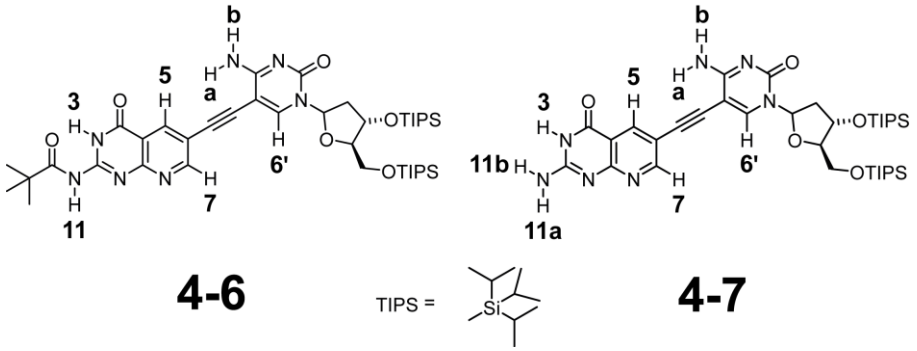

Figure 4.14 Schematic representation of compounds **4-6** and **4-7** with the chemical structure of the triisopropylsilyl (TIPS) protecting groups also shown. The atom numbers of the 'important' ^{1}H environments are also provided.

4b.2 Experimental details

4b.2.1 Sample preparation

The guanine/cytidine analogues 2-pivaloyl-6-[2'-deoxy-3',5'-di(triisopropylsilyl)cytidine-5-ethynyl]-5-deazapterin (**4-6**) and 6-[2'-deoxy-3',5'-di(triisopropylsilyl)cytidine-5-ethynyl]-5-deazapterin (**4-7**) were resynthesised according to the methods outlined in A. Likhitsup's PhD thesis.

4b.3 Results

4b.3.1 One-pulse ^{1}H MAS NMR results

The only structural difference between compounds **4-6** and **4-7** is the chemical nature of the functional group bonded to the exocyclic N11 nitrogen on the pterin unit. In chapter 4a, the conformation of the pivaloyl amide group was discussed at length. In every compound containing this unit so far, an intramolecular hydrogen bond was observed between the pivaloyl carbonyl oxygen and the H3 proton.

For compounds **4-3**, **4-4** and **4-5**, the H3 proton was observed with a ^{1}H chemical shift in the 13.7 – 14.0 ppm range. The ^{1}H isotropic chemical shift is an extremely sensitive probe of local electronic environment such that, given the total shift range is typically 20 ppm, any significant change in environment results in a significant change in chemical shift. One-pulse ^{1}H MAS NMR spectra of **4-6** and **4-7** are presented in Fig. 4.15. Since **4-6** shares a common structural motif with **4-3**, a one-pulse ^{1}H spectrum of this compound is also included in Fig. 4.15 for comparison. The most important feature of the spectrum of **4-6** is the chemical shift value of the proton at the highest frequency, which on inspection resonates at approximately 11.0 – 12.0 ppm. The change of ~2 ppm represents an important change in the local environment of the H3 proton (assigned at 11.3 ppm), potentially resulting from a rotation of the pivaloyl amide functionality. Indeed, the energetic barrier to CN bond rotation could be overcome if there is a real possibility of self-assembly upon revealing the DDA face of the pterin unit. This rotation is shown schematically in Fig. 4.16.

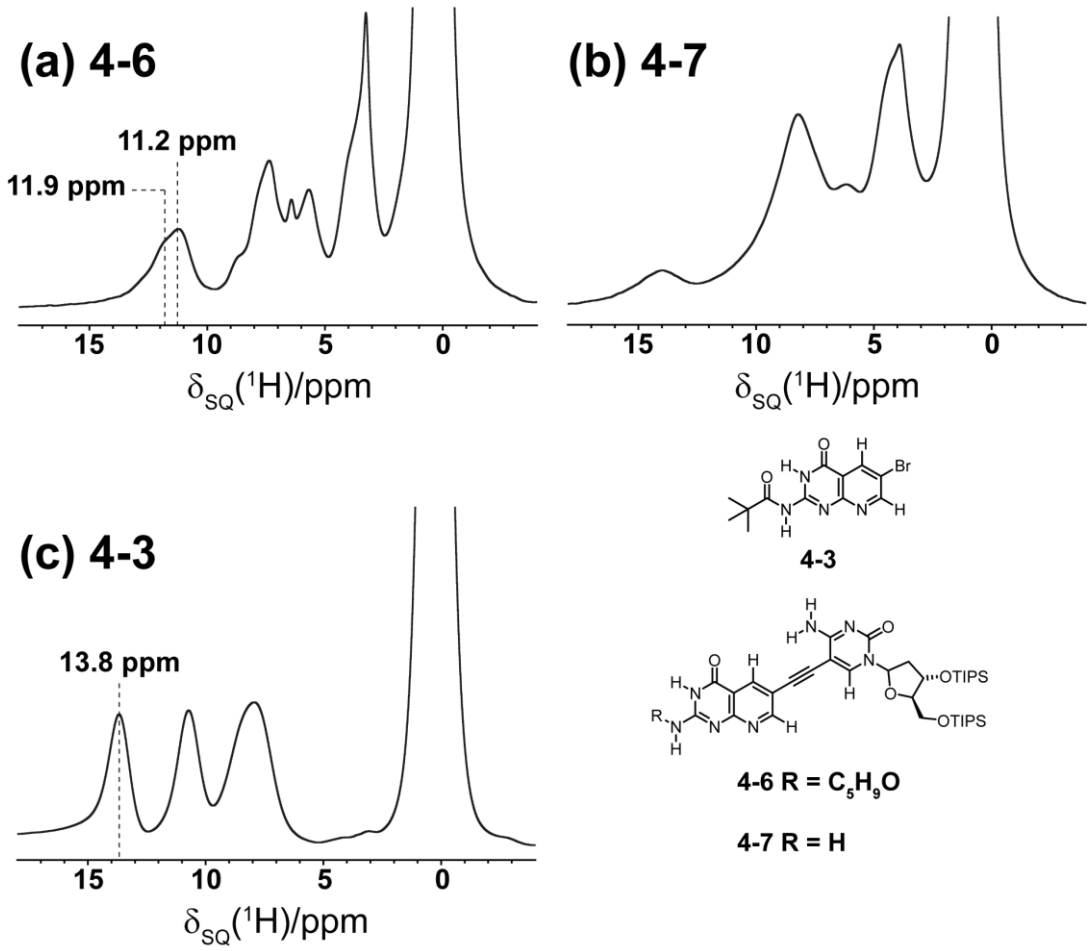

Figure 4.15 One-pulse ^{1}H (ω_0 = 600 MHz) MAS NMR spectra of (a) **4-6** (60 kHz), (b) **4-7** (55 kHz), and (c) **4-3** (30 kHz), alongside schematic representation of the corresponding chemical structures. 64 (**4-6**), 128 (**4-7**) and 8 (**4-3**) transients were coadded with a recycle delay of 2 (**4-7**) and 3 seconds (**4-3**, **4-6**). In each plot, the intense methyl peak has been truncated at approximately 8% (**4-6**, **4-7**) and 17% (**4-3**) of its full height. Note the significant chemical shift difference of the highest resonating peak in the spectra of **4-6** (11.9 ppm) and **4-3** (13.8 ppm), respectively.

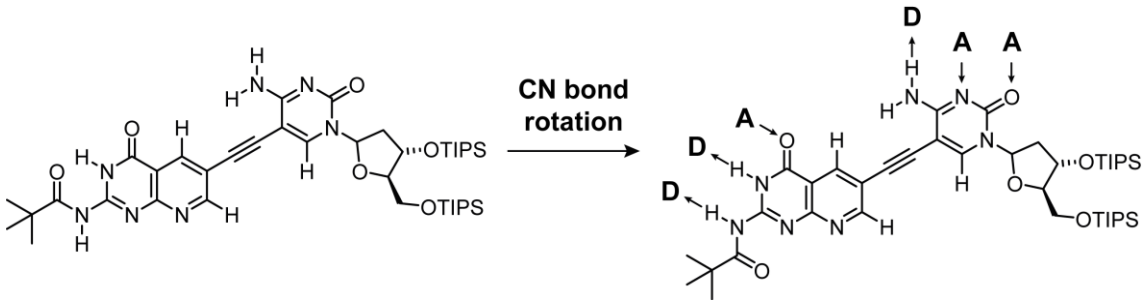

Figure 4.16 Schematic representation of the CN bond rotation in **4-6**.

Although this conformation brings the carbonyl oxygen into an unfavourable steric contact with the N1 nitrogen on the pterin-like moiety, this unfavourable clash may potentially be overcome if the pivaloyl group lies somewhat out of the plane of the molecule. The DDA face on the pterin now complements the AAD motif on the cytidine moiety, such that **4-6** can associate primarily *via* hydrogen bonding

interactions into higher order structures. **4-6** will now be considered to adopt this conformation throughout the remainder of the subchapter.

The ^{1}H one-pulse spectrum of **4-7**, presented in Fig. 4.15b, is considerably broader than that of **4-6** and, as a result, it is difficult to assign the ^{1}H resonances accurately on this evidence alone. One notable feature however is that the resonance at the highest frequency now appears at approximately 14.0 ppm. Given that the pivaloyl group has been deprotected in the conversion of **4-6** to **4-7**, accounting for this change in shift is non-trivial, but will discussed in more detail later. Note that **4-7** is designed specifically to self-assembly *via* the pterin DDA and cytidine AAD motifs. Given that the one-pulse spectrum is significantly broadened when compared to **4-6**, it is perhaps likely that there is some additional disorder in the solid-state structure. In order to further investigate the solid-state structures of **4-6** and **4-7**, it is necessary to analyse two-dimensional ^{1}H MAS data recorded for these compounds.

4b.3.2 Two-dimensional ^{1}H MAS NMR data for **4-6**

Compound **4-6** is a large organic molecule ($C_{41}H_{66}N_7O_6Si_2$, MW = 809.17 g/mol) and, since it contains a large number of protons, it has a complex ^{1}H chemical shift signiture. Of the 66 protons in this molecule, 42 (36 CH_3 and 6 CH) are contained within the triisopropylsilyl (TIPS) protecting groups on the cytidine unit and 9 within the *t*-butyl group on the pivaloyl amide functionality. Such a high abundance of methyl protons leads to an extremely intense peak centred at approximately 0.9 ppm (this was observed in the one-pulse spectrum in Fig. 4.15a). In addition to these 45 methyl protons, 7 reside in the ribose sugar moiety, which leads to a broadened resonance at 3.7 ppm and a H1' peak at 5.8 ppm. The existence of these environments, in particular the pentasaccharide protons, results in broad features in the ^{1}H – ^{1}H (600 MHz) DQ/SQ MAS (60 kHz) spectrum of **4-6**, presented in Fig. 4.17, in the lower frequency range of the plot (< 5.0 ppm). A list of DQ correlations for **4-6** is presented in Table 4.7.

Inspection of the ^{1}H DQ spectrum in Fig. 4.17a reveals several important features, the most important of which correspond to the nitrogen bound protons. Resonances are observed at 7.5, 9.0, 11.3 and 12.0 ppm which are herein assigned to the Ha, H11, H3 and Hb protons, respectively. Cross-peaks are observed at δ_{DQ} = 7.5 + 12.0 = 19.5 ppm and δ_{DQ} = 9.0 + 11.3 = 20.3 ppm, corresponding to the intense intramolecular Ha – Hb (NH_2) and H11 – H3 contacts, respectively; the appearance of the latter is consistent with the conformation wherein the CN bond rotates to afford the DDA hydrogen bonding face (Fig. 4.16). Furthermore, inspection of the columns and rows extracted from the DQ spectrum in Fig. 4.17b reveals a weak auto-peak at δ_{DQ} = 11.3 + 11.3 = 22.6 ppm, corresponding to a H3 – H3 intermolecular contact, and a H3 – Hb intermolecular contact across the hydrogen bonding interface, corresponding to δ_{DQ} = 11.3 + 12.0 = 23.3 ppm. These weak peaks are around 60 – 80% less intense than the aforementioned intramolecular contacts, which is attributed to dipolar truncation in the presence of stronger intramolecular couplings (Ha – Hb, H11 – H3) (see section 1.4). In addition, the H11 proton interacts with the CH_3 methyl protons contained within the tertiary butyl groups on the

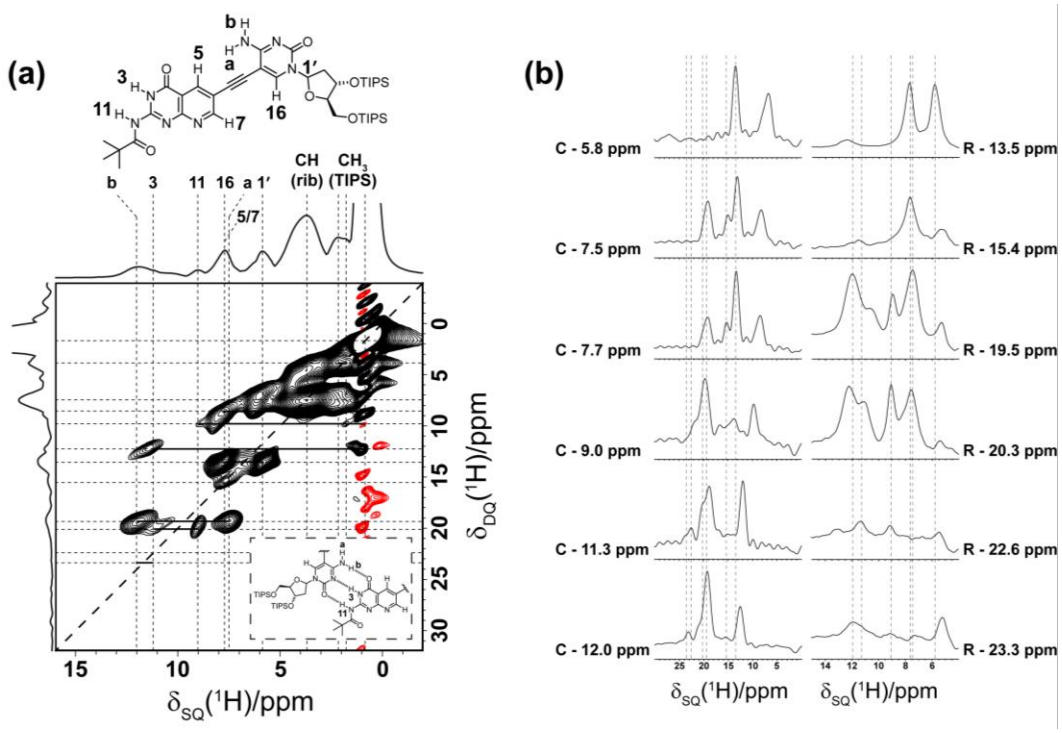

Figure 4.17 (a) ^{1}H – ^{1}H (ω_0 = 600 MHz) DQ/SQ MAS (60 kHz spinning) spectrum of **4-6**. The $F_1 = 2F_2$ diagonal is given as a dashed black line. DQ cross-peaks are shown as solid horizontal black lines. For each of 256 t_1 FIDs, 64 transients were coadded with a recycle delay of 3 seconds. The base contour level is shown at 0.5% of the maximum intensity. (b) columns (C) and rows (R) extracted at specific ^{1}H DQ and SQ chemical shifts, respectively, from the ^{1}H – ^{1}H DQ/SQ MAS spectra of **4-6** in (a). Columns are extracted for all proton peaks resonating above 5.0 ppm, the rows are taken through the cross-peaks. Note that the rows taken through 22.6 and 23.3 ppm correspond to weak auto/cross-peaks, respectively, that are not evident for the contour levels shown in the DQ spectrum. The columns at 11.3 and 12.0 ppm reveal weak peaks in the 22.0 – 24.0 ppm range, corresponding to a H3 – H3 auto-peak (δ_{DQ} = 11.3 + 11.3 = 22.6 ppm) and a H3 – Ha cross-peak (δ_{DQ} = 11.3 + 12.0 = 23.3 ppm), respectively.

pivaloyl unit, at δ_{DQ} = 0.9 + 9.0 = 9.9 ppm, as expected from the structure. Likewise the H3 proton forms a cross-peak with methyl protons at δ_{DQ} = 0.9 + 11.3 = 20.3 ppm. An intense set of cross-peaks is observed at δ_{DQ} = 5.8 + 7.7 = 13.5 ppm that is assigned to the contact between the aromatic H16 proton on the cytidine moiety and the H1' proton on the ribose unit, which are locked within a close spatial proximity. In the same region of the spectrum, an auto-peak is observed at δ_{DQ} = 7.7 + 7.7 = 15.4 ppm; this is assigned to the H5/7 aromatic peaks on the pterin unit, which fall into this general chemical shift region in the spectra of **4-3**, **4-4** and **4-5**. Importantly, these assignments (of the NH protons in particular) are consistent with the DDA – AAD pterin – cytidine hydrogen bonding motif which in turn affords multiple pathways to self-assembly, as presented in Fig. 4.18.

Additional ^{1}H – ^{1}H two-dimensional experiments can provide further structural insights into **4-6**. By employing a ^{1}H – ^{1}H spin-diffusion experiment, it is possible to estimate the number of distinct phases in **4-6**, i.e., distinct self-assembled architectures.

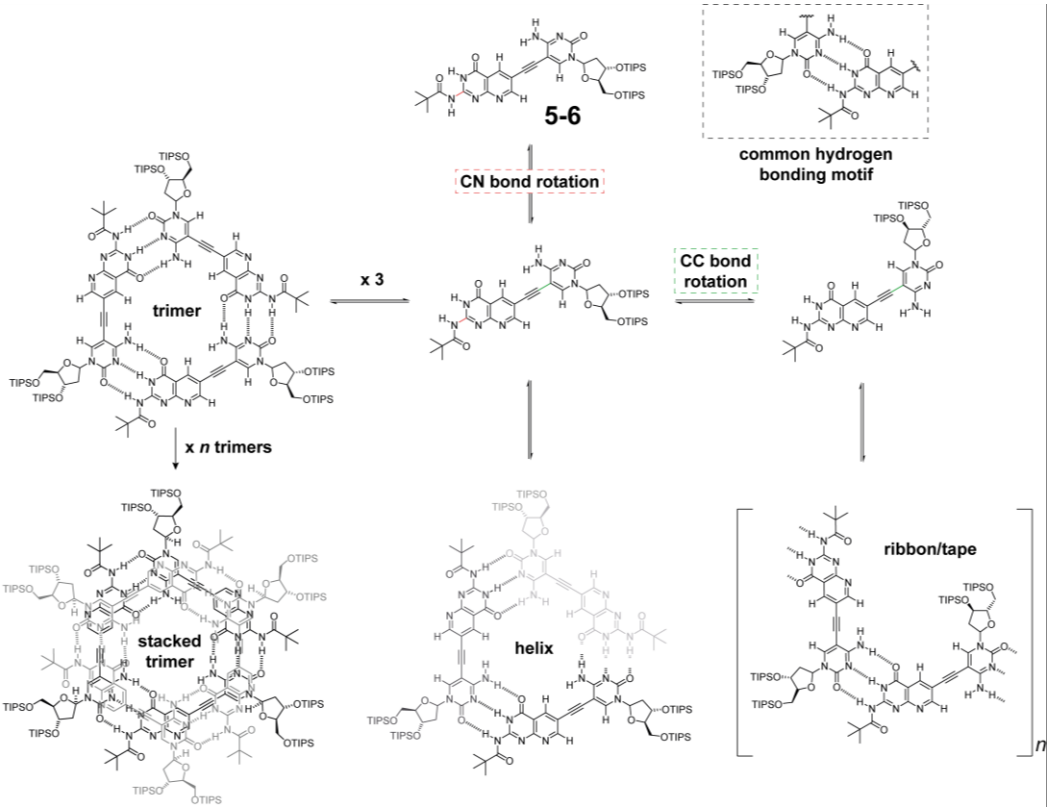

Figure 4.18 Schematic representation of the hydrogen bonding structure of **4-6** suggested by the $^{1}H - {}^{1}H$ DQ/SQ MAS spectrum, alongside potential higher order assemblies afforded by such a motif.

Table 4.7 DQ correlations extracted from the $^{1}H - {}^{1}H$ DQ/SQ MAS spectrum of **4-6** in Fig. 4.17.

4-6	#	Correlation	Sum of SQ freq / ppm	DQ freq / ppm
	1	CH_3 (auto)	0.9 + 0.9	1.8
	2	CH – CH (TIPS)	1.8 + 2.2	4.0
	3	CH_3 – H1'	0.9 + 5.8	6.7
	4	CH (rib, auto)	3.7 + 3.7	7.4
	5	CH_3 – H16	0.9 + 7.7	8.6
	6	CH_3 – H11	0.9 + 9.0	9.9
	7	CH_3 – H3	0.9 + 11.3	12.2
	8	H1' – H16	5.8 + 7.7	13.5
	9	CH (aro, auto)	7.7 + 7.7	15.4
	10	Ha – Hb	7.5 + 12.0	19.5
	11	H11 – H3	9.0 + 11.3	20.3
	12	H3 (auto, weak)	11.3 + 11.3	22.6
	13	H3 – Hb (weak)	11.3 + 12.0	23.3

Specifically, $^{1}H - {}^{1}H$ spin-diffusion experiments under the moderate to fast MAS regime are particularly useful in terms of improving ^{1}H resolution, thereby making effective analysis of weak cross-peaks easier. A $^{1}H - {}^{1}H$ spin diffusion spectrum of **4-6** at an intermediate mixing time (τ_{mix}) of 100 ms is presented in Fig. 4.19. In such an experiment, if only one phase exists, then it is expected that all ^{1}H environments in the molecule will experience polarisation transfer from and to all other sites. In other words, cross-peaks are expected between all resonances in the spectrum. This phenomenon is clearly observed in Fig. 4.19, with broad intense peaks indicating, in this particular case, a high degree of *z* magnetisation transfer between all individual ^{1}H environments in the molecule.

This evidence, when considered alongside the highly resolved nature of the $^{1}H - {}^{1}H$ DQ/SQ MAS spectrum presented in Fig. 4.17a, is consistent with the existence of one specific self-assembled architecture persisting in the solid state.

However, in spite of this evidence, it is non-trivial to ascertain the precise mode of self-assembly in this system. This difficulty is compounded by the fact that, for the hydrogen bonding motif discussed above, there can in theory exist multiple different possibilities for higher order aggregation, i.e., trimeric, helical, ribbon etc. as was illustrated schematically in Fig. 4.18. The $^{1}H - {}^{1}H$ DQ/SQ MAS and spin diffusion data is consistent with the existence of only one of these possible structures, thus the existence of different self-assembled forms coexisting in the solid state can be excluded. Importantly, the weak H3 – H3 auto-peak that was observed in Fig. 4.17, at a $\delta_{DQ} = 11.3 + 11.3 = 22.6$ ppm, may offer some clues. Such low intensity auto-peaks (this particular peak is very weak) are often associated with intermolecular couplings between discrete layers, as was observed by Peters *et al*,(102) in which the presence of a weak auto-peak was consistent with the stacking of individual G-quartets in hydrogel systems. The observation of this weak H3 – H3 auto-peak makes stacked trimeric and ribbon-type assembly the most obvious candidates, as a helical assembly would not bring two individual H3 protons into close enough proximity and hence cannot therefore account for the observed peak.

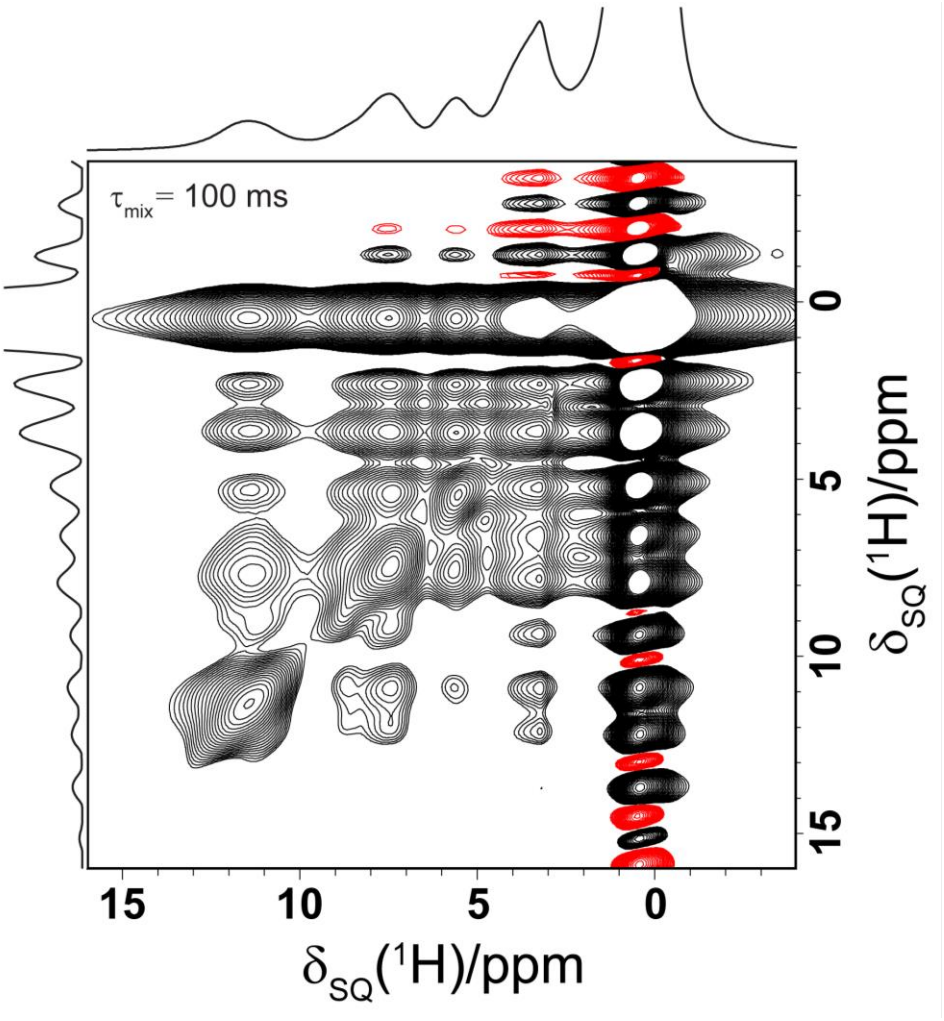

Figure 4.19 A $^{1}H - ^{1}H$ (ω_0 = 600 MHz) spin diffusion spectrum of **4-6**, recorded at 60 kHz MAS with a τ_{mix} = 100 ms. For each of 128 t_1 FIDs, 16 transients were coadded with a recycle delay of 2 seconds. The base contour level is shown at 0.1% of the maximum peak height.

4b.3.3 A $^{1}H - ^{13}C$ CP MAS spectrum of **4-6**

As can be seen from the spectrum presented in Fig. 4.20, the ^{13}C chemical shift signiture for **4-6** is broad and complex,(224) likely as a result of a distribution of ^{13}C chemical shifts due to higher order aggregation, and significant disorder in the TIPS groups. The spectrum was recorded using 30720 transients, in order to obtain a sufficient signal-to-noise ratio, particularly for the ^{13}C resonances in the higher ppm region of the spectrum. This is a common phenomenon in the higher molecular weight analogues presented in this work. The subsequent requirement for long experimental times precludes the employment of useful experiments such as INEPT based correlation methods, due to practical considerations (time). This is disappointing since the precise assignment of, say, the aromatic $^{1}H - ^{13}C$ correlations would have been beneficial in the assignment of the other ^{1}H spectra presented for **4-6** in this subchapter. Although it is difficult to assign the majority of ^{13}C resonances in Fig. 4.20 with much accuracy, it is possible to make some tentative assumptions based on typical chemical shift ranges observed in organic molecules.

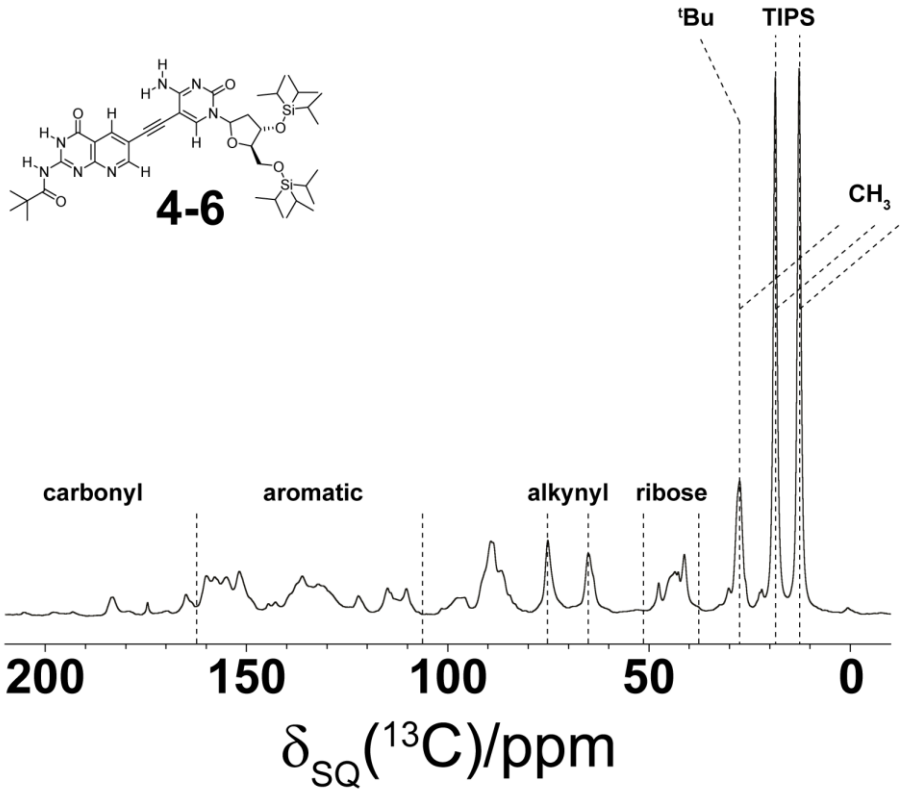

Figure 4.20 A ^{1}H (ω_0 = 600 MHz) – ^{13}C CP MAS (12.345 kHz spinning) spectrum of **4-6** alongside tentative assignments.

4b.3.4 Two-dimensional ^{1}H MAS NMR data for **4-7**

The overall resolution and appearance of the ^{1}H – ^{1}H DQ/SQ MAS spectrum of **4-7** presented in Fig. 4.21 (DQ correlations are provided in Table 4.8), is dominated by the presence of two distinct and strongly coupled NH_2 environments on the pterin unit and the cytosine moiety, respectively. Since intramolecular ^{1}H amine dipolar couplings are strong given their close spatial proximity, these environments give rise to intense cross-peaks in two-dimensional DQ spectra. As such, given that these two NH_2 moieties have similar chemical shifts, it is unsuprising that these overlapping environments lead to a significantly broadened group of resonances in the ($\delta_{SQ}(^{1}H)$) 5.0 – 10.0 ppm range. In addition to these amine resonances, the situation is complicated further by the presence of overlapping aromatic signals within this same chemical shift range. These factors alone make analysis non-trivial. Despite such difficulties, several important assignments can be made, from which it is possible to elucidate the likely hydrogen bonding structure. Such elucidation is aided significantly by the fact that **4-7** is designed specifically so as to interact *via* the DDA face on the pterin, which in turn associates with the AAD face on the deoxycytidine unit. Fortunately, there is no ambiguity in this case, unlike in **4-6**, since the pivaloyl functionality has been synthetically removed (thereby removing any conformational uncertainty). In addition, the DDA/AAD motifs represent the only real outlets for hydrogen bonding interactions in **4-7**, if the absence of prototropic tautomers is assumed (which is a sound assumption since no evidence of this phenomenon was observed in any of the precursor compounds). The ribose

and alkyl regions of the spectrum of **4-7** in Fig. 4.21 are broadly similar to those of **4-6** presented in Fig. 4.17a. These similarities were observed in the respective ^{1}H MAS NMR spectra presented in Fig. 4.15a (**4-6**) and Fig. 4.15b (**4-7**). Such similarities are expected since, other than the additional methyl environments in **4-6**, both **4-6** and **4-7** contain identical TIPS protected ribose units.

It is important to note at this stage that the assignments discussed in this section are tentative given the difficulty in finding the exact centres of such broad resonances. However, the assigned cross-peaks in the 'NH' region of the spectrum (δ_{DQ} > 15.0 ppm) are consistent with the DDA – AAD hydrogen bonding motif indicated in Fig. 4.21. Evidence in the solution state (see A. Likhitsup's 2006 thesis for details) points to assembly *via* this hydrogen bonding motif. In the absence of impurities, which the relevant solution data is consistent with, this molecule can only interact *via* the outlets highlighted in Fig. 4.21. This region (for δ_{DQ} > 15 ppm) is broad due to the high number of protons in such environments which sit in close spatial proximity, thereby resulting in strong dipolar couplings which serve to broaden the observed lineshapes and hence the observed cross-peaks.

The exact assignment of the individual NH_2 protons is of less significance given that the hydrogen bonding arrangement is essentially symmetric about the H3 proton (see Fig. 4.21). The fact that the H3 environment appears to form contacts with two overlapping resonances at approximately 8.9 and 9.4 ppm (SQ frequency) is sufficient to assume couplings between both hydrogen bonding NH_2 protons, across the hydrogen bonding interface. However, this assignment is made on the basis that the H11b – H3 intramolecular contact may be expected to experience a stronger dipolar coupling than the intermolecular Hb – H3 contact across the hydrogen bond, since the former protons are fixed into close spatial proximity *via* covalent bonds, whilst the latter experience a dipolar coupling only if the postulated hydrogen bonding structure occurs. This can be seen by comparing the two cross-peaks at δ_{DQ} = 8.9 + 13.8 = 22.7 ppm and δ_{DQ} = 9.4 + 13.8 = 23.2 ppm, consistent with the H11b – H3 and Hb – H3 contacts, respectively. As can be seen upon inspection of the DQ spectrum in Fig. 4.21, the resonance at δ_{SQ} = 9.4 ppm, presents as a shoulder peak on the seemingly more intense peak at δ_{SQ} = 8.9 ppm. However, the key word here is *consistent*, since it is difficult based only upon the ^{1}H data to make definitive conclusions in cases where significant peak overlap is observed.

As was seen for **4-6**, two-dimensional ^{1}H – ^{1}H spin-diffusion spectra can be used to determine the number of distinct phases present within this sample, as was discussed in section 3.4.3. Such a spectrum is presented in Fig. 4.22. At an intermediate mixing time, τ_{mix}, of 100 ms, it is clearly observed that all protons within this sample experience polarisation transfer to and from all other proton environments, thereby confirming the presence of only one phase in the solid state. This evidence alone gives further credence to the hypothesis that the broadened lineshapes observed for **4-7** are as a result of strong dipolar couplings among, principally, NH_2 environments and alkyl protons. Thus, the data contradicts alternative explanations for the appearance of the DQ spectrum, such as a possibility of several self-

assembled structures coexisting in the solid state, since such a phenomenon would lead to the observation of several distinct phases in the spin-diffusion spectrum. Such a situation would be expected to give rise to broadened lineshapes since the major self-assembled architectures which can be conceived of for **4-7** would involve the same DDA/AAD hydrogen bonding motif, effectively meaning that the NH ^{1}H chemical shifts would be similar in each case, which could explain the broadened resonances. For similar architectures such as cyclic trimers or potential helical structures, this problem would be particularly acute, since the conformation of the molecule is identical in each case, meaning similar ^{1}H chemical shifts across the entire range (see Fig. 4.18 for schematic representation of similar architectures for **4-6**). Ribbon assembly would be expected to be different since such assembly requires a rotation of the deoxycytidine unit about the acetylenic axis. **4-7** therefore represents a significant challenge in terms of solid-state characterisation methods, given its non-crystalline nature and broadened ^{1}H DQ spectrum. However, the ^{1}H solid-state NMR data presented in this section provides some indication of the hydrogen bonding motif, which is more likely given the lack of alternative donor and acceptor groups.

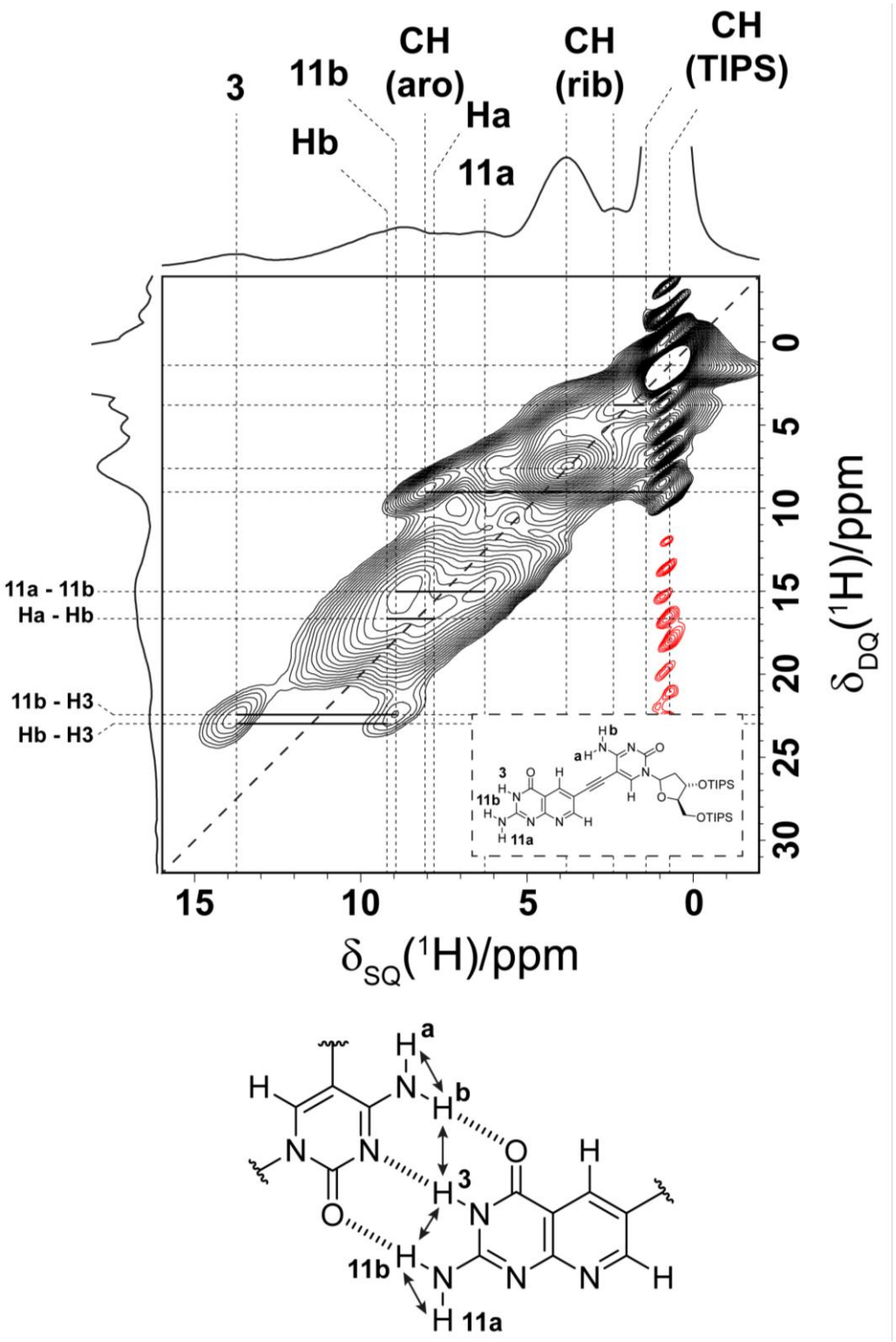

Figure 4.21 A $^{1}H - {}^{1}H$ (ω_0 = 600 MHz) DQ/SQ MAS (55 kHz spinning) spectrum of **4-7** with skyline projections and a schematic representation of the hypothesised hydrogen bonding structure between the DDA pterin and AAD cytosine interfaces. The labels of the important nitrogen bound protons are given and four important cross-peaks consistent with the hydrogen bonding structure are indicated in the DQ spectrum. The $F_1 = 2F_2$ diagonal is given as a dashed black line. DQ cross-peaks are shown as solid horizontal black lines. For each of 256 t_1 FIDs, 128 transients were coadded with a recycle delay of 2 seconds. The base contour level is shown at 1.4% of the maximum intensity.

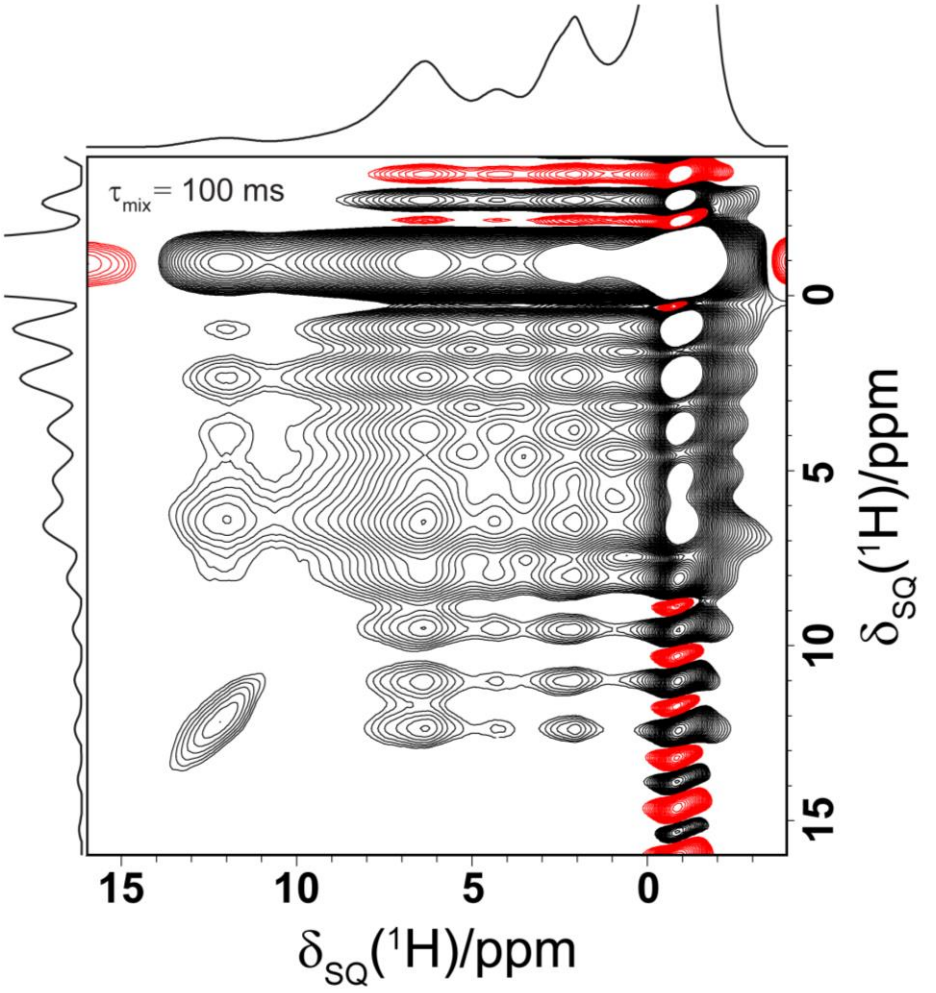

Figure 4.22 A $^{1}H - ^{1}H$ (ω_0 = 600 MHz) spin-diffusion spectrum of **4-7**, recorded at 60 kHz MAS with a τ_{mix} = 100 ms. For each of 128 t_1 FIDs, 16 transients were coadded with a recycle delay of 2 seconds. The base contour level is shown at 0.05% of the maximum peak height.

Table 4.8 DQ correlations extracted from a $^{1}H - ^{1}H$ DQ/SQ MAS spectrum of **4-7** (see Fig. 4.21)

4-7	#	Correlation	Sum of SQ freq / ppm	DQ freq / ppm
	1	CH_3 (auto)	0.8 + 0.8	1.6
	2	CH – CH (TIPS)	1.7 + 2.4	4.1
	3	CH (rib, auto)	3.8 + 3.8	7.6
	4	CH_3 – aro	0.8 + 8.1	8.9
	5	11a – 11b	6.4 + 8.9	15.3
	6	Ha - Hb	8.2 + 9.4	17.6
	7	11b – H3	8.9 + 13.8	22.7
	8	Hb – H3	9.4 + 13.8	23.2

4b.3.5 A $^{1}H - ^{13}C$ CP MAS spectrum of **4-7**

A $^{1}H - ^{13}C$ CPMAS spectrum of **4-7**, presented in Fig. 4.23, is broad and disordered as was the case for **4-6** in Fig. 4.20. The spectrum required in excess of 30720 scans to achieve the presented signal to noise ratio, hence precluding the use of techniques such as INEPT, which would have been useful in terms of assignments, particularly in the aromatic region of the DQ spectrum which is hidden amongst the strong NH_2 peaks. For comparison, a CPMAS spectrum recorded with 2048 scans is also included in Fig. 4.23.

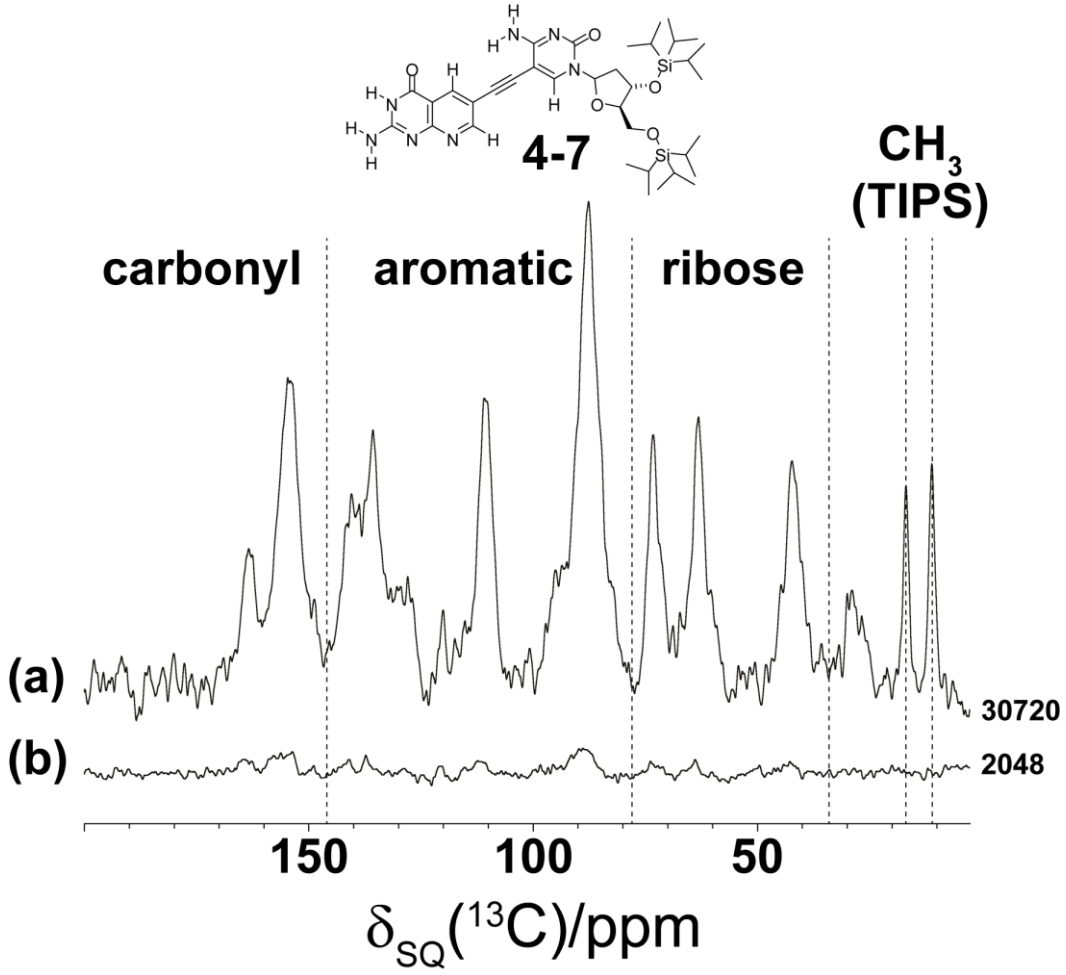

Figure 4.23 ^{1}H (ω_0 = 600 MHz) – ^{13}C CP MAS (12.5 kHz spinning) spectra of **4-7** alongside tentative general assignments recorded with (a) 30720 and (b) 2048 transients, the recycle delay in each case was 2 seconds.

4b.3.6 Summary

As demonstrated in this subchapter, compounds **4-6** and **4-7** are extremely challenging from a characterisation standpoint, especially in the solid state given their non-crystalline nature (**4-6** is a glassy solid whilst **4-7** is a powder). In terms of high-resolution solid-state characterisation, ^{1}H MAS NMR is the only feasible option capable of achieving atomic resolution for key hydrogen-bonded protons. In particular, it was shown in this subchapter that two-dimensional fast MAS $^{1}H - ^{1}H$ DQ/SQ experiments

are a powerful probe of proton proximities which, when combined with the sensitivity of the ^{1}H chemical shift to hydrogen bonding phenomenon, provides insight regarding the likely hydrogen bonding motifs which drive self-assembly processes. The difficulty in acquiring two-dimensional heteronuclear experiments, such as the $^{1}H - ^{13}C$ INEPT experiment (not possible due to the time required to obtain sufficient signal-to-noise) and the $^{14}N - ^{1}H$ HMQC experiment (which was attempted multiple times for both **4-6** and **4-7** with no success), effectively preclude making definitive assignments. As such, it is only possible to make assignments which are consistent with the structures postulated in this subchapter.

Chapter 5 : A study of the self-assembling properties of deoxycytidine analogues by ^{1}H and ^{14}N fast 2D MAS NMR

The work outlined in this chapter relates to the solid-state characterisation of three cytidine analogues first introduced by Marsh *et al*.(225)

5.1 Introduction

The concept of molecular self-assembly was introduced in some detail in section 1.3, and several important examples were discussed in section 1.3.1. Through the exploitation of non-covalent interactions, most significantly hydrogen bonding,(132) and $\pi - \pi$ stacking interactions,(137) it is possible to envisage many systems with many potential applications. Of all the self-assembled systems imaginable, perhaps the most impressive and certainly the most ubiquitous in nature is the helix,(226) with such structures being prevalent in biological systems ranging from DNA, to the substructure of proteins and several important polysaccharides as well as playing an important role in the external structure of virus membranes.(227-229) Synthetic helical structures can be created from organic, biological and inorganic materials with manifold recent examples in aqueous solution,(108,109,230-244) and as hydrogels.(245-247) In particular, synthetic DNA-based analogues offer attractive potential for self-assembly given the natural propensity of nucleobases to form hydrogen bonded structures, as well as their inherent potential for $\pi - \pi$ stacking interactions.(248) Characterisation of such systems is of fundamental importance however, as with many of these type of systems, there exists a paucity of such characterisation data for the solid state. In chapter 4 it was shown that high-resolution ^{1}H MAS NMR methods were capable of providing site-specific detail for a range of self-assembling pterin analogues, with such techniques being exquisitely sensitive to hydrogen bonding interactions *via* the sensitivity of the ^{1}H chemical shift.

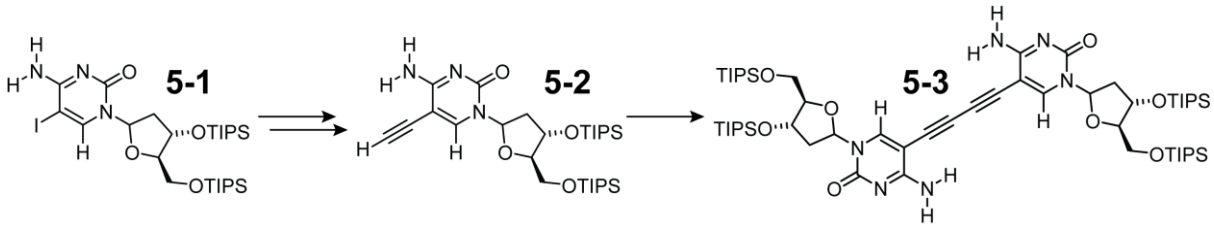

Figure 5.1 Schematic representation of the structures of **5-1**, **5-2** and **5-3**.

This chapter discusses the solid-state packing arrangement of the synthetic nucleoside 5-(2',4'-butadiynyl 2''-deoxy-3'',5''-di(triisopropylsilyl)cytidinyl)(2'-deoxy-3',5'-di(triisopropylsilyl)cytidine, **5-3**, which is shown to form helical arrays in the solid state. An NMR crystallographic study of precursor 5-ethynyl-2'-deoxy-3',5'-di(triisopropylsilyl)cytidine, **5-2** as an isopropanol solvate, is also presented which allows structural insight into precursor 5-iodo-2'-deoxy-3',5'-di(triisopropylsilyl)cytidine **5-1** *via* comparison of their respective ^{1}H – ^{1}H DQ/SQ MAS and ^{14}N – ^{1}H HMQC spectra. Furthermore it will be shown that all three compounds interact through a common hydrogen bonding motif, and that the highly resolved ^{1}H MAS NMR spectra allow for extraction of the number of crystallographically

distinct molecules in the asymmetric unit cell. Note that **5-3** also has a published crystal structure (CCDC 188942), however disorder within the unit cell has to date precluded a GIPAW calculation of its NMR parameters. The structures of **5-1**, **5-2** and **5-3** are presented schematically in Fig. 5.1.

5.2 Experimental details

5.2.1 Sample preparation

The three cytidine analogues discussed in this chapter, **5-1**, **5-2** and **5-3**, were prepared according to the methods outlined by Marsh *et al*. (225) Note that **5-2** and **5-3** were prepared by Azawin Likhitsup. All solution-state characterisation data was consistent with those published.

5.3 Results

5.3.1 An NMR crystallographic study of **5-2**

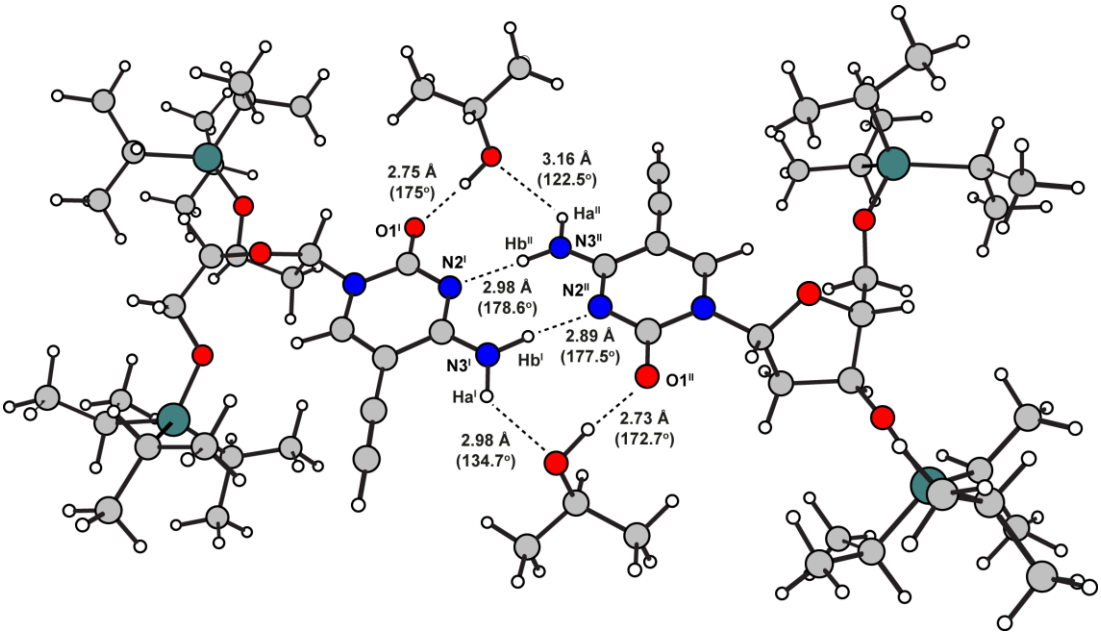

Figure 5.2 Schematic representation of the single crystal structure for **5-2** as an isopropanol solvate; hydrogen bond distances and angles extracted from the geometry optimised structure are labelled. The distances quoted correspond to X ⋯ Y distances where X and Y correspond to the donor and acceptor species, respectively.

Inspection of the crystal structure of **5-2** (CCDC 188941) in Fig. 5.2 reveals a dimeric hydrogen bonded arrangement consistent with Z' = 2, i.e., two crystallographically distinct molecules of **5-2** in the asymmetric unit cell (in addition to two molecules of isopropanol solvent). The compound is observed, in the single crystal X-ray diffraction data, to form two NH ⋯ N hydrogen bonding interactions across the cytosine interface (these protons are labelled NHb^{I} and NHb^{II}, respectively, with $N3^{I/II}$ – $N2^{II/I}$ distances of 2.89 (I ⋯ II) and 2.98 Å (II ⋯ I)). In addition, two molecules of propan-2-ol (isopropanol) are incorporated into the structure, with the alcohol oxygen sitting within hydrogen bonding distance

of the other NH_2 protons, labelled NHa^{I} and NHa^{II}. The two solvent OH protons are orientated towards the carbonyl oxygens on the cytosine heterocycle ($O1^{I/II}$, see Fig. 5.2), corresponding to hydrogen bonds with O ⋯ O distances of 2.73 and 2.75 Å. Table 5.1 and Table 5.2 present a list of ^{1}H and ^{14}N NMR parameters calculated using the GIPAW method. For simplicity, the 84 protons contained within the TIPS groups in this system are omitted.

Table 5.1 ^{1}H NMR parameters for **5-2** calculated using the GIPAW method.

Nucleus	σxx	σyy	σzz	σiso	δiso(calc)[a]	δiso(exp)
OH^{I}	14.10	17.87	41.02	24.3	5.6	–
OH^{II}	14,35	18.75	41.44	24.9	5.1	–
$H2'(a)^{I}$	25.33	27.29	33.11	28.6	1.4	1.7
$H2'(a)^{II}$	23.39	26.48	34.97	28.3	1.7	1.7
$H2'(b)^{I}$	25.98	26.89	32.39	28.4	1.5	1.7
$H2'(b)^{II}$	24.72	27.66	32.40	28.3	1.7	1.7
ethynyl H^{I}	22.40	23.17	33.12	26.2	3.7	3.9
ethynyl H^{II}	22.81	24.24	32.54	26.5	3.4	3.5
$H3''^{I}$	29.41	26.49	19.50	25.1	4.8	4.5
$H3''^{II}$	29.35	26.68	20.49	25.5	4.4	4.5
$H4''^{I}$	22.53	24.34	30.63	25.8	4.1	4.1
$H4''^{II}$	23.91	25.04	29.24	26.1	3.9	4.1
$H1^{I}$	19.57	22.81	29.07	23.8	6.1	6.2
$H1^{II}$	20.96	21.75	28.60	23.8	6.2	6.3
$H6^{I}$	19.55	20.62	25.61	21.9	8.0	8.0
$H6^{II}$	18.98	21.08	26.88	22.3	7.6	7.9
NHa^{I}	17.47	21.58	30.60	23.2	6.7	5.3
NHa^{II}	19.80	22.93	28.4	23.7	6.2	6.0
NHb^{II}	11.74	16.60	31.00	19.8	10.2	10.5
NHb^{I}	9.36	15.17	31.69	18.7	11.2	11.0

[a] $\delta_{iso} = -[\sigma_{iso} - \sigma_{ref}]$, where $\sigma_{ref} = 29.93$ ppm for ^{1}H.

Table 5.2 A full list of ^{14}N parameters calculated *via* the GIPAW method, for **5-2**.

Nucleus	V_{xx}	V_{yy}	V_{zz}	C_Q/MHz[a]	η_Q[a]	P_Q/MHz[a]	δ^Q_{iso}/ppm[a]
$N1^I$	0.82	0.43	–0.38	–2.9	0.10	2.9	169.0
$N2^I$	0.43	–0.01	0.90	–3.0	0.74	3.3	218.7
$N3^I$	0.79	–0.36	–0.50	–2.6	0.53	2.7	146.6
$N1^{II}$	0.86	0.28	0.43	–2.9	0.08	2.9	164.4
$N2^{II}$	0.46	0.06	0.89	–3.0	0.76	3.3	220.0
$N3^{II}$	0.84	–0.33	–0.42	–2.8	0.44	2.9	162.1

[a] The relevant equations for C_Q (eqn. 2.118), η_Q (eqn. 2.119), P_Q (eqn. 2.137) and δ^Q_{iso} (eqns. 2.135 and 2.136) are provided in section 2.4.7. ν_0 = 850 MHz.

Nucleus	δ_{iso}(calc)/ppm	δ^Q_{iso}/ppm	δ_{iso}(calc) + δ^Q_{iso}	δ_{iso}(exp)/ppm
$N1^I$	–217.1	169.0	–56.5	–60
$N2^I$	–186.2	218.7	21.5	–
$N3^I$	–282.4	146.6	–143.2	–145
$N1^{II}$	–213.5	164.4	–57.3	–60
$N2^{II}$	–188.8	220.0	20.2	–
$N3^{II}$	–282.9	162.1	–128.9	–140

The presence of four crystallographically distinct NH protons is consistent with four NH peaks observed in the ^{1}H MAS NMR data: Fig. 5.3a presents a ^{1}H MAS one-pulse spectrum of **5-2**, in which these four distinct NH environments are assigned. The resolution in this case is aided by fast MAS (60 kHz) and a high magnetic field strength (850 MHz). This high resolution also leads to an observed splitting of aromatic H6 and anomeric (ribose bound) H1' proton environments. The broad peak at 7.3 ppm does not correspond to any proton environment within **5-2**, which is verified by the GIPAW results which will be discussed subsequently (i.e., there is no calculated chemical shift within that range). The environment leads to an auto-peak in the DQ MAS data (see below discussion of Fig. 5.5) but the absence of any cross-peaks to other proton environments in the spectrum means that this resonance is likely due to some impurity. Moreover, this impurity does not transfer polarisation to any other proton environment in **5-2**, as observed by the absence of peaks in the ^{1}H – ^{1}H (600 MHz) spin diffusion data presented in Fig. 5.3b. Since this impurity does not influence the structure of **5-2** it will not be considered further.

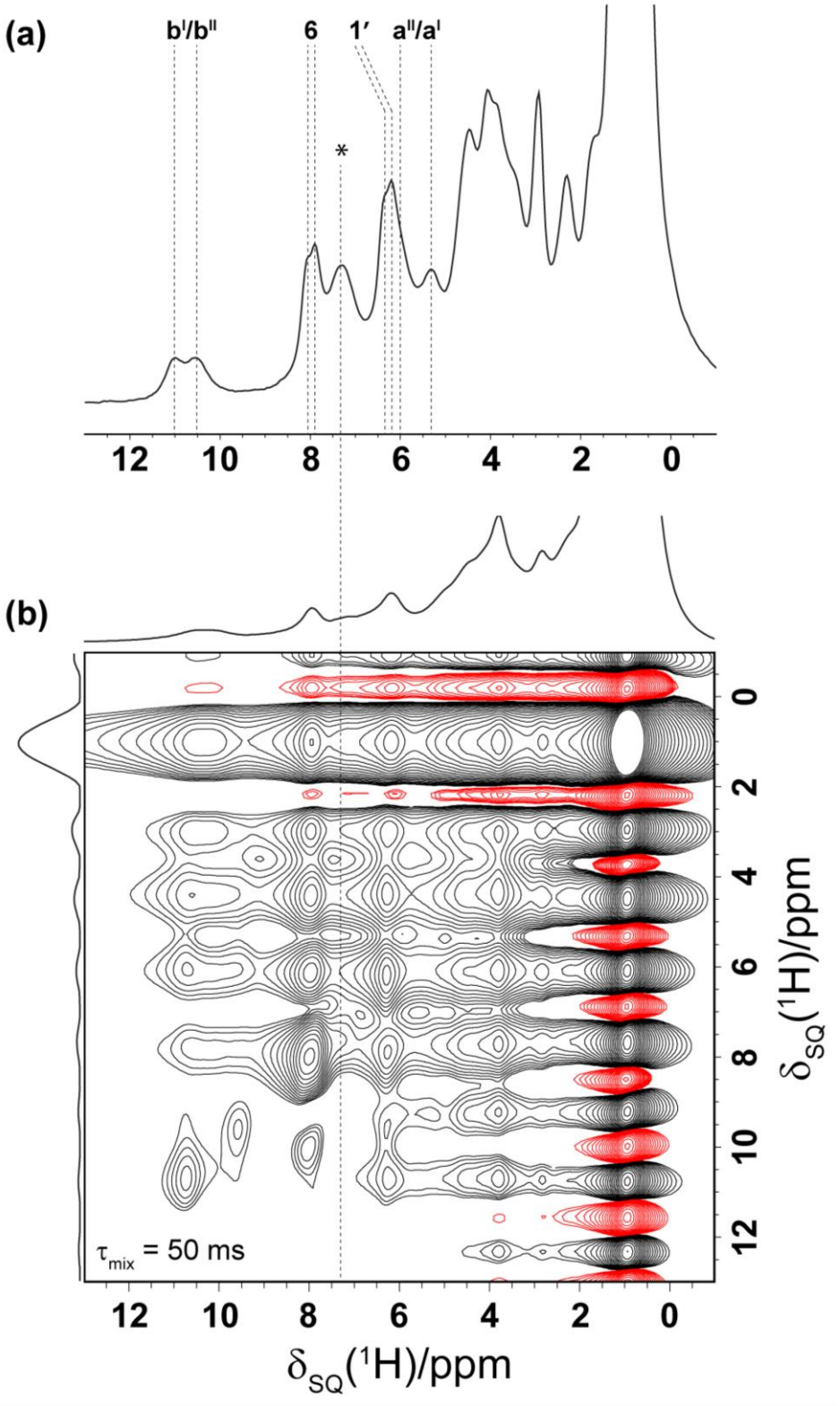

Figure 5.3 (a) A ^{1}H (ω_0 = 850 MHz) MAS (60 kHz spinning) one-pulse spectrum of **5-2**. A clear splitting of the NH, aromatic H6 and anomeric ribose H1' environments can clearly be seen. 16 transients were coadded, with a recycle delay of 2 seconds. (b) A ^{1}H – ^{1}H (600 MHz) spin diffusion spectrum of **5-2** recorded at 60 kHz MAS with a mixing time, τ_{mix}, of 50 ms. For each of 128 t_1 FIDs, 16 transients were coadded with a recycle delay of 2 seconds. The * in (a) indicates the position of an impurity resonance.

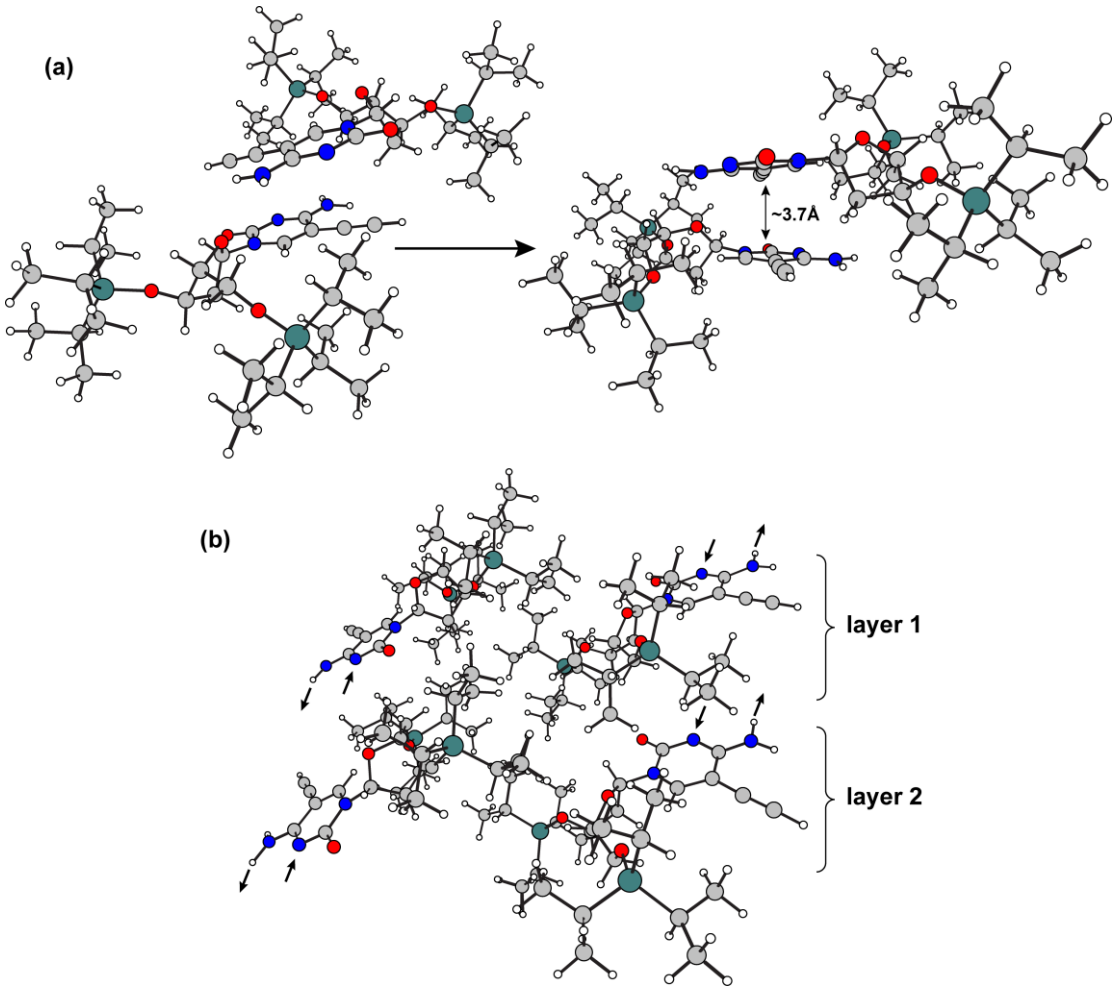

Figure 5.4 (a) Stacking of individual molecules of **5-2** with the separation between individual layers being approximately 3.7 Å, (b) individual dimers are shielded by TIPS protecting groups on the ribose moiety, the arrows represent the hydrogen bonding interactions between dimers (only one molecule of the dimer shown in each case).

The individual cytosine moieties stack with the ethynyl moiety sitting directly under the cytosine ring, as presented in Fig. 5.4a, with the distance between layers being approximately 3.7 Å. The triisopropylsilyl (TIPS) groups in **5-2** reside upon the edge of the dimeric structure and act to shield individual dimers from each other in the xy plane, as shown in Fig. 5.4b (two layers are extracted with the solvent molecules omitted for simplicity). As for other TIPS containing compounds reported in this thesis, this high abundance of methyl protons leads to an intense auto-peak in the DQ MAS data (Fig. 5.5), whilst ensuring that polarisation transfer between these environments and all other non-methyl proton environments in **5-2** occurs rapidly, as revealed by the spin diffusion data presented in Fig. 5.3b.

A ^{1}H – ^{1}H (850 MHz) DQ/SQ MAS (60 kHz) spectrum of **5-2** is presented in Fig. 5.5, with GIPAW calculated ^{1}H chemical shifts of the NH bound protons indicated by red crosses (for a full list of non-methyl calculated ^{1}H shielding parameters see Table 5.1, whilst experimental DQ shifts are reported in Table 5.3).

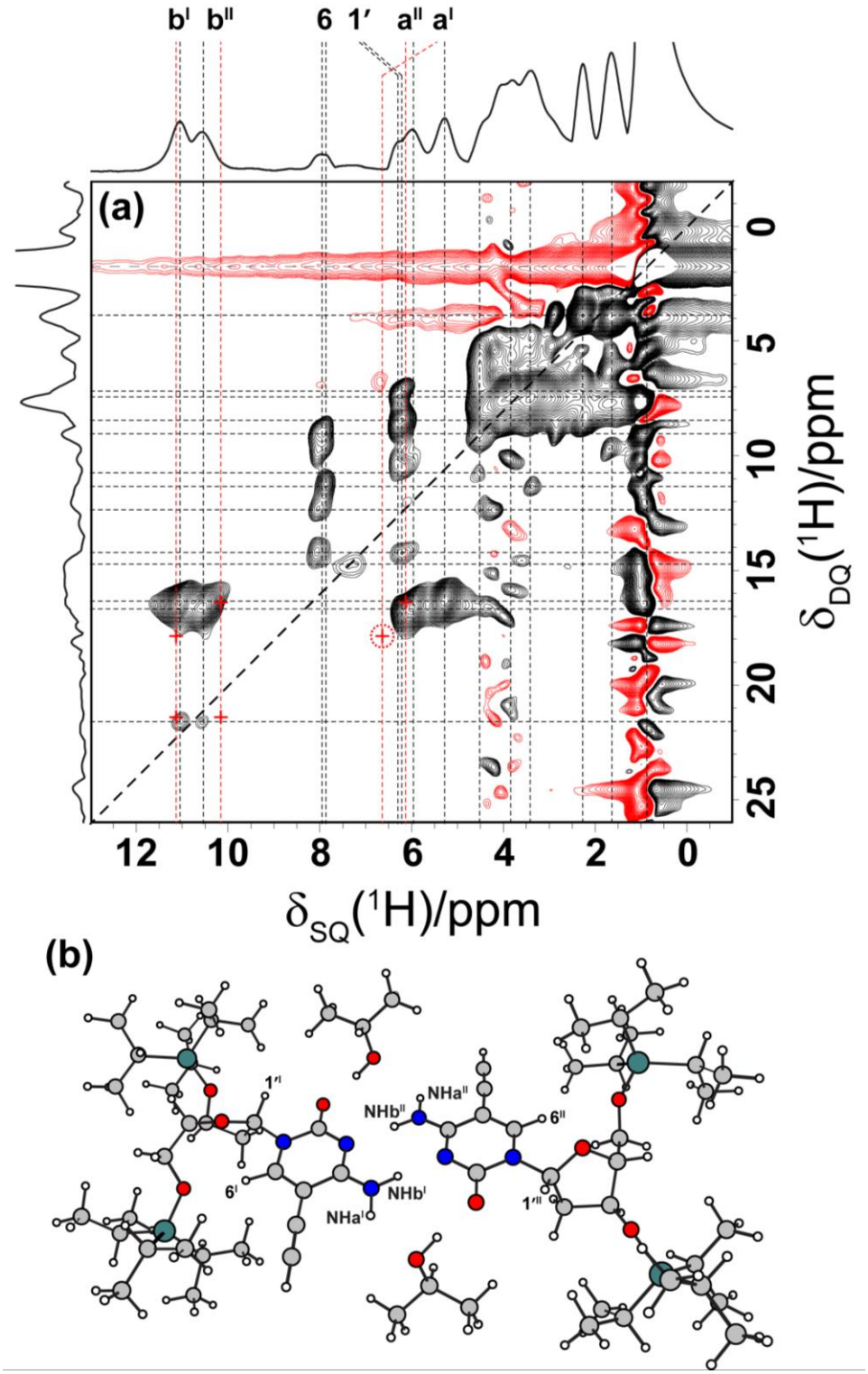

Figure 5.5 (a) A ^{1}H – ^{1}H (ω_0 = 850 MHz) DQ/SQ MAS (60 kHz spinning) spectrum of **5-2**, together with skyline projections and (b) a schematic representation of the published crystal structure. The positions of the GIPAW calculated ^{1}H chemical shifts of the NH bound protons are presented as red crosses, whilst the calculated SQ positions are shown as red dashed vertical lines for comparison to the experimental SQ shifts (black dashed line). The red dotted circle highlights the anomaly for the GIPAW calculated ^{1}H chemical shift for a^{I}. One rotor period of BABA recoupling was used for the excitation and reconversion of DQ coherence. For each of 128 t_1 FIDs, 16 transients were coadded with a recycle delay of 3 seconds. The $F_1 = 2F_2$ diagonal is given as a dashed black line.

For the majority of ^{1}H environments, the calculated chemical shifts are in good agreement with experimental shifts. However, there is one anomaly for one of the Ha protons (Ha^{I}), as can be seen in Fig. 5.5, in which there is a significant difference of 1.4 ppm between calculated and experimental chemical shifts. This result accounts for the observation of the inconsistent calculated cross-peak pattern as compared to experiment for the intramolecular NH_2 contacts: observed experimentally at δ_{DQ} = 5.3 + 11.0 = 16.3 ppm and δ_{DQ} = 6.0 + 10.5 = 16.5 ppm, corresponding to the a^{I} - b^{I} and a^{II} - b^{II} amine dipolar interactions, respectively, while GIPAW calculated ^{1}H data gives δ_{DQ} = 6.7 + 11.2 = 17.9 ppm and δ_{DQ} = 6.2 + 10.2 = 16.4 ppm, respectively. This anomaly is difficult to account for since the other Ha proton has good agreement between calculated and experimental shifts. Both Ha environments sit in close spatial proximity to both the ethynyl moiety and a molecule of isopropanol, which sits within hydrogen bonding distance (HO ⋯ HN) although with different O ⋯ N distances (see Fig. 5.2). Any disorder (mobility) in the solvent molecule position may account for the overestimated calculated chemical shift for NHa^{I}.

Experimentally, the DQ MAS spectrum of **5-2**, presented in Fig. 5.5, is sufficiently resolved such that four distinct NH environments are clearly observed. It is also possible to observe a doubling of resonances corresponding to the aromatic H6 and H1' sugar environments at δ_{SQ} = 7.9/8.0 ppm and δ_{SQ} = 6.1/6.2 ppm, respectively. These results are consistent with Z' =2, which is indicated by the single crystal data (Fig. 5.2.). Interestingly, this MAS frequency and field strength are sufficient to resolve some individual peaks in the broad region of the spectrum at δ_{DQ} ~ 5.0 – 10.0 ppm, which corresponds to the CH protons contained within the ribose sugar moiety. However, it is not possible to distinguish between these environments and the ethynyl proton, whose resonances fall within the same general region (according to the GIPAW results ~ 4 ppm). These environments have a minimal role in the dimeric arrangement which is observed for **5-2**, and hence it is of lesser importance that precise assignment be made.

The key cross-peak is observed at δ_{DQ} = 10.5 + 11.0 = 21.5 ppm, which is consistent with a truncated intermolecular dipolar interaction across the hydrogen bonding interface, i.e., a b^{II} – b^{I} contact. This evidence alone, in conjunction with the single crystal data, is consistent with the proposed dimeric structure. Additionally, the well resolved nature of **5-2**'s ^{1}H MAS data makes this compound a good example of how solid-state NMR can be exploited to yield crystallographic information (in the absence of such ^{1}H resolution, CP MAS spectra are usually required to observe a doubling of resonances) which, as will be observed in the next section, is particularly useful for non-crystalline materials.

In order to provide further confirmation of chemical shift assignments, Fig. 5.6 presents ^{14}N – ^{1}H (850 MHz) HMQC spectra of **5-2** (alongside a zoomed in region of the ^{1}H DQ MAS spectrum presented in Fig. 5.5) at recoupling times, τ_{RCPL}, of 130 μs (Fig. 5.6e) and 400 μs (Fig. 5.6f). From this data it can be clearly observed that the ^{1}H chemical shifts at δ_{SQ} = 5.3, 6.0, 10.5 and 11.0 ppm correspond to the

NHa^{I}, NHa^{II}, NHb^{II} and NHb^{I} environments, respectively. Unfortunately, no peaks are observed in the N2 region of the HMQC spectrum in Fig. 5.6f (GIPAW calculated position is given as a dashed green horizontal line). Given the likely hydrogen bonding structure, correlations between these nitrogen environments and the NHb protons are expected, since these atoms are locked within close spatial proximity in the proposed hydrogen bonding structure. Given the strong evidence for this structure already discussed in this chapter, it is unclear as to why such correlations are not observed, especially given that at a τ_{RCPL} duration of 400 μs (Fig. 5.6f), correlations between the N1 nitrogen and the H6 and H1' protons are clearly observed.

Table 5.3 DQ correlations extracted from a $^{1}H - {}^{1}H$ DQ/SQ MAS spectrum of **5-2** (see Fig. 5.5)

5-2	#	Correlation	$\delta_{SQ}^{(1)} + \delta_{SQ}^{(2)}$ / ppm	δ_{DQ} / ppm
	1	$CH_3 - CH_3$	0.8 + 0.8	1.6
	2	CH – CH	1.6 + 2.2	3.8
	3	CH_3 – 1'	0.8 + 6.2	7.0
	4	rib – rib	3.4 + 3.8	7.2
	5	CH_3 – 1'	2.2 + 6.3	8.5
	6	CH_3 – 6	0.9 + 7.9	8.8
	7	rib – 1'	4.4 + 6.2	10.6
	8	rib – 6	3.4 + 7.9	11.3
	9	rib – 6	4.4 + 8.0	12.4
	10	1' – 6	6.3 + 8.0	14.3
	11	a^{I} - b^{I}	5.3 + 11.0	16.3
	12	a^{II} - b^{II}	6.0 + 10.5	16.5
	13	b^{II} - b^{I}	10.5 + 11.0	21.5

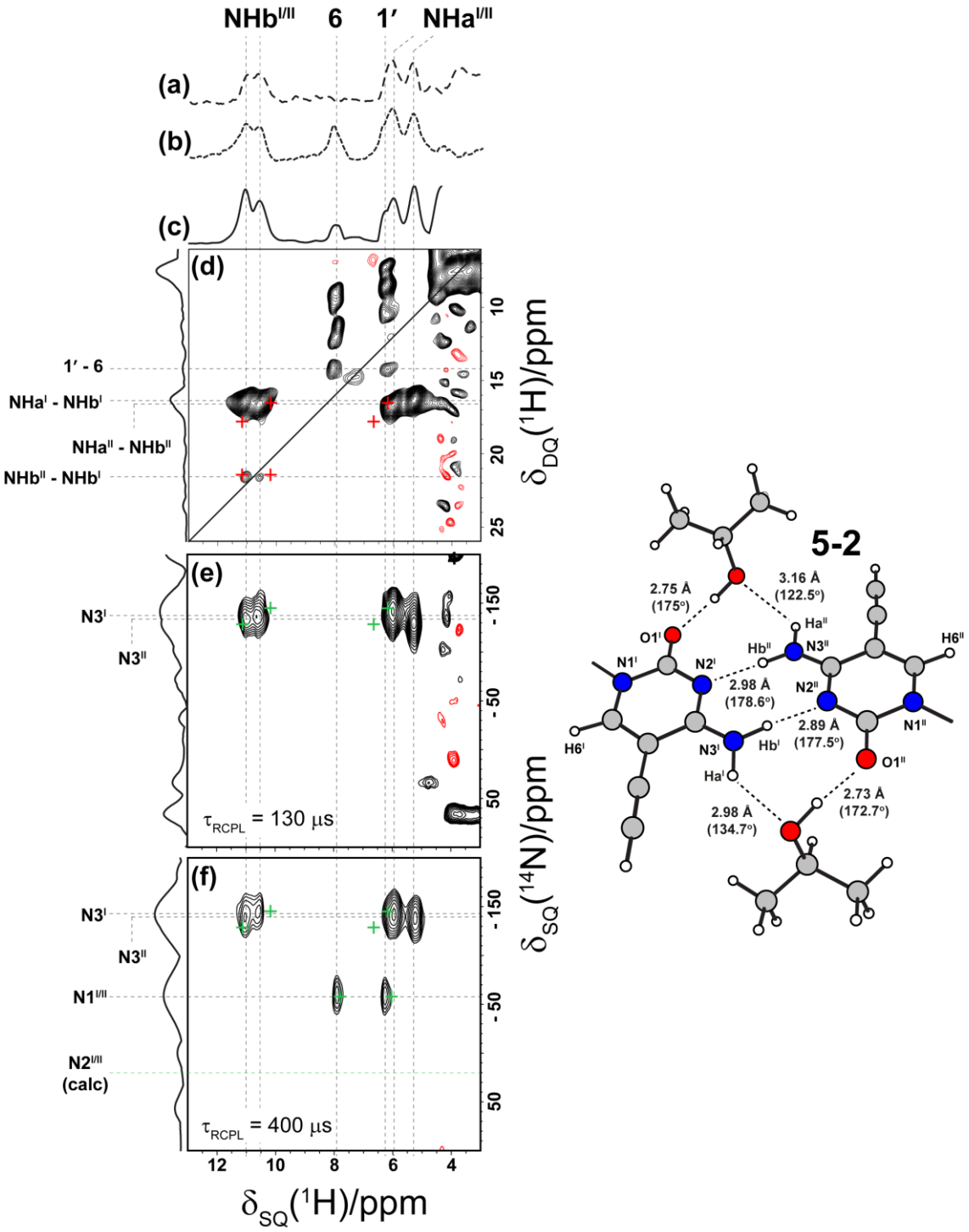

Figure 5.6 For **5-2**, (a, b) 1D HMQC filtered (t_1 = 0) spectra, for (a) τ_{RCPL} = 130 μs and (b) τ_{RCPL} = 400 μs; (c) a 1D DQ-filtered spectrum, and (d) the NH region of the ^{1}H – ^{1}H DQ/SQ MAS spectrum from Fig. 5.5; (e, f) 2D ^{14}N – ^{1}H HMQC spectra with R^3 recoupling of the ^{14}N – ^{1}H heteronuclear dipolar couplings for (e) τ_{RCPL} = 130 μs and (f) τ_{RCPL} = 400 μs. GIPAW calculated chemical shift positions for the ^{1}H – ^{1}H and ^{14}N – ^{1}H correlation spectra are indicated by red and green crosses, respectively. A schematic representation of the dimer based on the single crystal structure is also provided. (e) 124 and (f) 96 transients were recorded for each of 64 t_1 FIDs. The recycle delay was 3 seconds in both cases. The base contour level is at (e) 73% and (f) 68% of the maximum peak height in each spectrum, with negative contours shown in red.

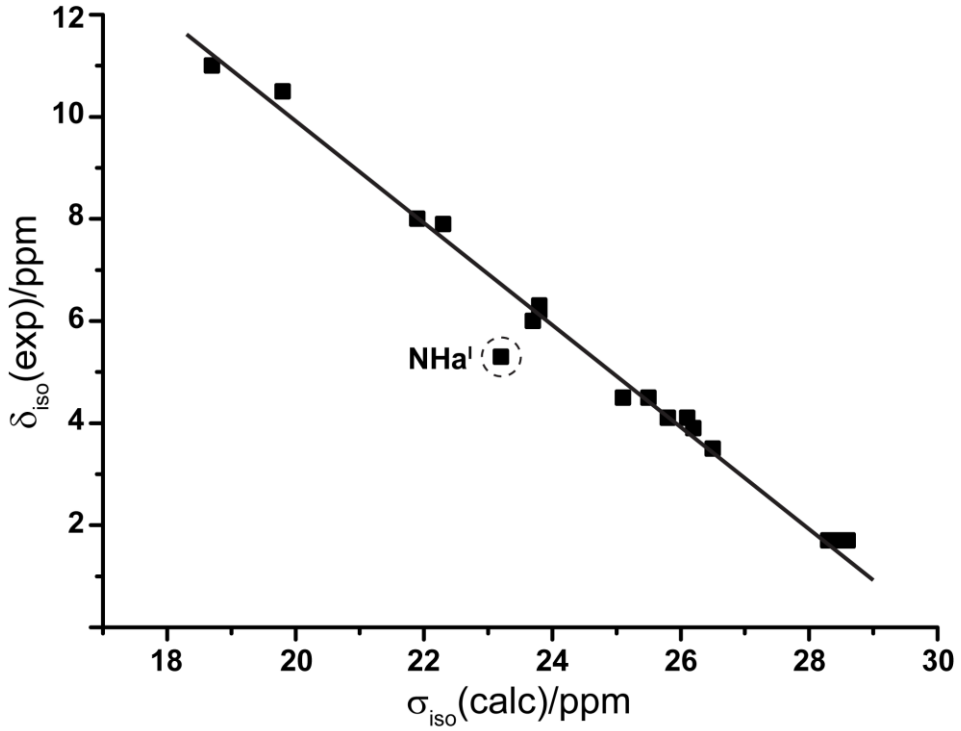

Figure 5.7 Plot of calculated (GIPAW, see Table 5.1) σ_{iso}(calc) against ^{1}H δ_{iso}(exp) values for **5-2**. The anomalous NHa^{I} calculated shift, as discussed in the main text, is highlighted.

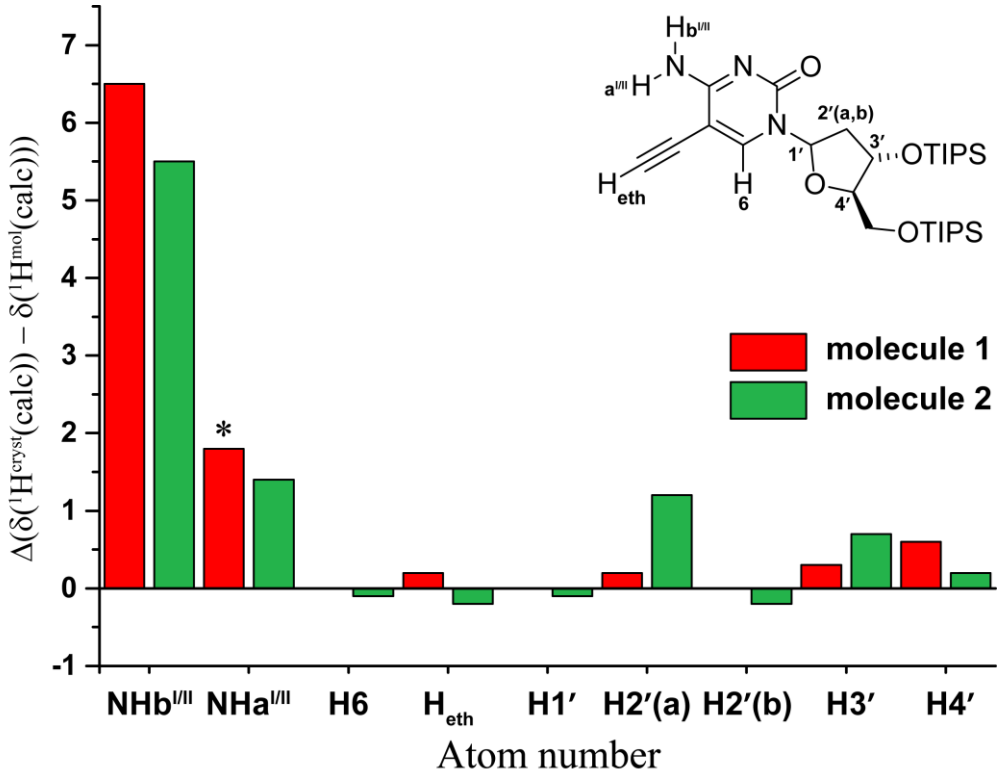

Figure 5.8 Plot of the difference in ^{1}H δ_{iso}(calc) values between the full crystal and individual **5-2** molecules. A large difference of values indicates that that particular atom is heavily influenced by non-covalent interactions in this case hydrogen bonding. The * indicates the anomalous a^{I} proton.

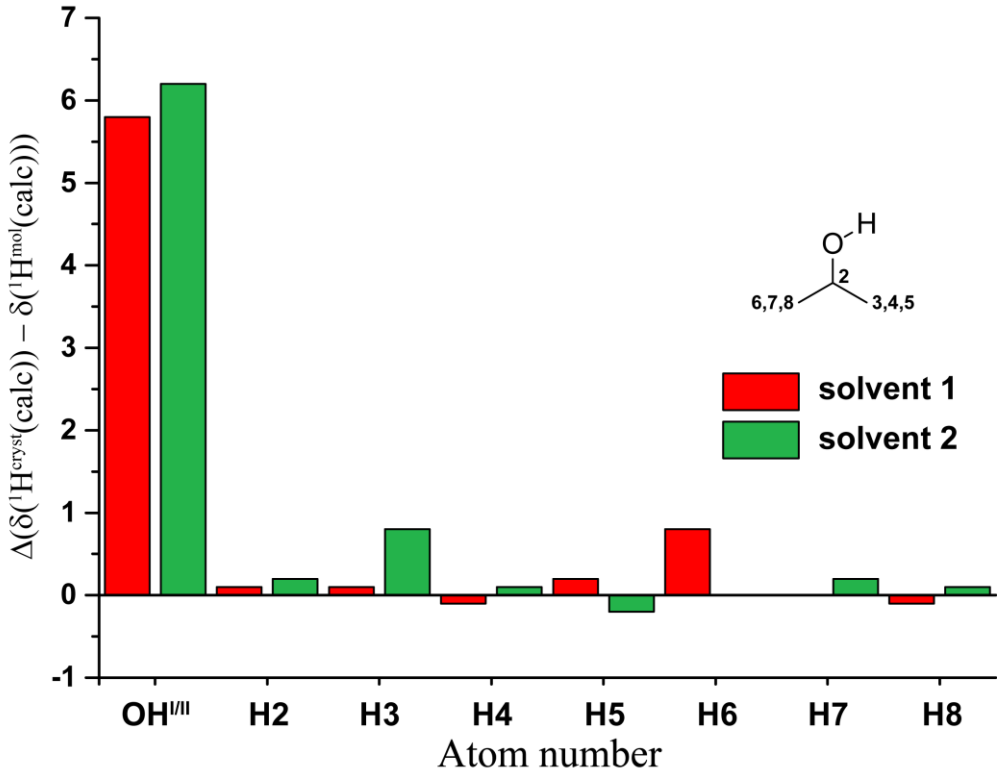

Figure 5.9 Plot of the difference in ^{1}H δ_{iso}(calc) values between the full crystal and individual isopropanol solvent molecules.

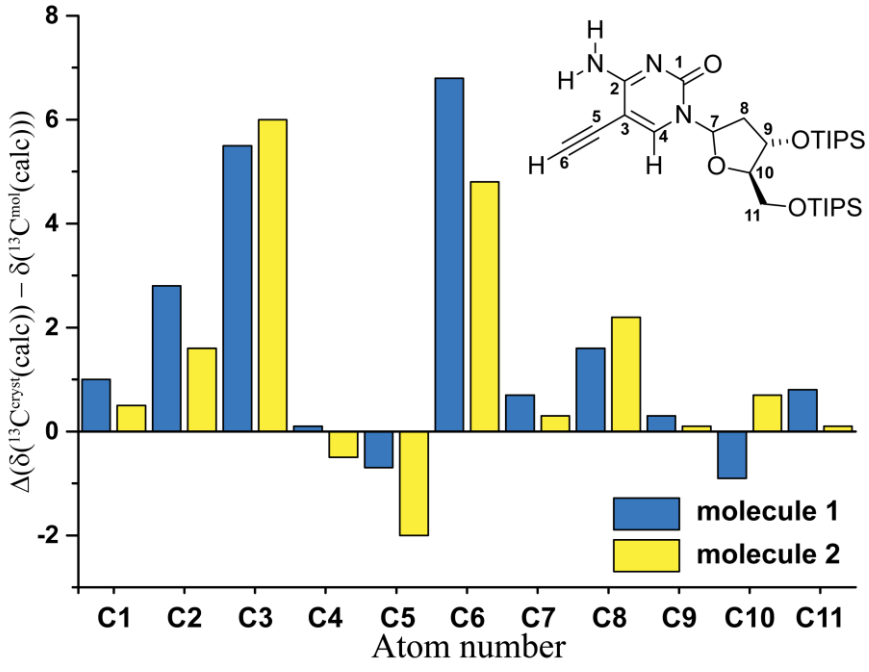

Figure 5.10 Plot of the difference in ^{13}C δ_{iso}(calc) values between the full crystal and individual **5-2** molecules.

A plot of calculated σ_{iso}(calc) against δ_{iso}(exp) is presented in Fig. 5.7. From this data, the anomalous NHa^{I} calculated chemical shift can clearly be seen. All other calculated shifts agree relatively well with

experimental values, and as such these data points form the expected linear trend. Such a plot allows for the extraction of the σ_{ref} value used in Table 5.1.

By comparing the results of GIPAW calculations of the NMR chemical shifts for the full crystal (all intermolecular interactions present) and the individual extracted single molecules (no intermolecular interactions present), it is possible to use NMR crystallographic approaches to investigate the role of non-covalent forces at play in a given system, thereby complementing single crystal data. Large, positive differences between the full crystal and isolated molecule calculated chemical shift values for a given atom indicate that that environment (^{1}H in this case) is strongly influenced by non-covalent interactions. Positive differences are indicative of hydrogen bonding interactions, whilst negative differences indicate π - type influence (i.e., the site is more shielded).

Examination of the plots presented in Fig. 5.8 (isolated molecules of **5-2**) and Fig. 5.9 (isolated isopropanol solvent molecules), reveals significant changes in the NH (H1 = $Hb^{I/II}$, H2 = $Ha^{I/II}$) and OH proton environments, respectively, consistent with significant hydrogen bonding interactions. For **5-2** (Fig. 5.6), the NHb protons (labelled as H1 in Fig. 5.8) experience the largest difference of ~ 6 ppm, when the isolated molecules are extracted from the full crystal structure. This phenomenon is consistent with these protons being involved in a hydrogen bonded dimer (see Fig. 5.2). The NHa protons (labelled H2 in Fig. 5.8) experience a smaller molecule to crystal change of ~ 1.5 – 2.0 ppm, consistent with a weaker hydrogen-bonding interaction between these protons and the alcoholic oxygen on the isopropanol. In a study by Reddy *et al*,(104) it was also noted that NH ⋯ O hydrogen bonding interactions are generally weaker than NH ⋯ N hydrogen bonds, which is consistent with the data presented herein. Interestingly, a significant difference in ^{1}H chemical shift between isolated molecule and full crystal is also observed for the OH protons in the isopropanol molecules (labelled H1 in Fig. 5.9) of between 5.5 – 6.5 ppm, corresponding to a strong hydrogen bonding interaction between these environments and the carbonyl oxygen ($O1^{I/II}$) on the cytidine units (see Fig. 5.2).

In addition, Fig. 5.10 presents the difference in ^{13}C δ_{iso}(calc) for the full crystal and isolated molecules for **5-2**. Significant differences are observed for C3 and C6, which pertain to those carbons contained within the ethynyl moiety. As was discussed in Fig. 5.4, this triple bond sits directly below a cytosine moiety in the crystal packing structure. These differences are consistent with the significant non-covalent forces expected to influence these carbons in the solid state as a result of this packing. A sizable change in the ^{13}C calculated chemical shift of C2 is also observed (~ 2 ppm), which may suggest that the hydrogen bonding activity of the directly bonded NH_2 has some influence on this carbon environment

5.3.2 Solid-state structure of related precursor **5-1**

In the absence of crystallographic data for **5-1** (note that efforts to obtain a single-crystal X-ray diffraction structure are ongoing), in which the ethynyl moiety in **5-2** is replaced by an iodine atom, the ^{1}H MAS NMR data presented in this section is sufficient to determine the packing arrangement. The detailed structural analysis offered by the NMR crystallographic approach applied to **5-2** in section 5.3.1 can be used to infer the structure of the related precursor **5-1**, given the high overall similarity of their molecular structure and, as is demonstrated herein, their respective ^{1}H MAS spectra.

The **5-1** molecule interacts *via* an identical hydrogen bonding motif as was observed for **5-2**, this being the only viable hydrogen bonding structure open to the two compounds. Further evidence of this identical dimeric hydrogen bonded structure can be seen in the ^{1}H – ^{1}H (850 MHz) DQ/SQ MAS (60 kHz) spectrum of **5-1** which is presented in Fig. 5.11, with the same cross-peaks being observed for both **5-1** and **5-2** (see Fig. 5.5, also included in Fig. 5.11 for comparison). A list of DQ correlations for **5-1** is provided in Table 5.4. The general dimeric structure common to both **5-1** and **5-2** is also presented in Fig. 5.11, which highlights the four distinct NH protons observed in both spectra. For **5-1**, two crystallographically distinct molecules are expected in the asymmetric unit cell, based on these four environments (i.e., 2 x NH_2).

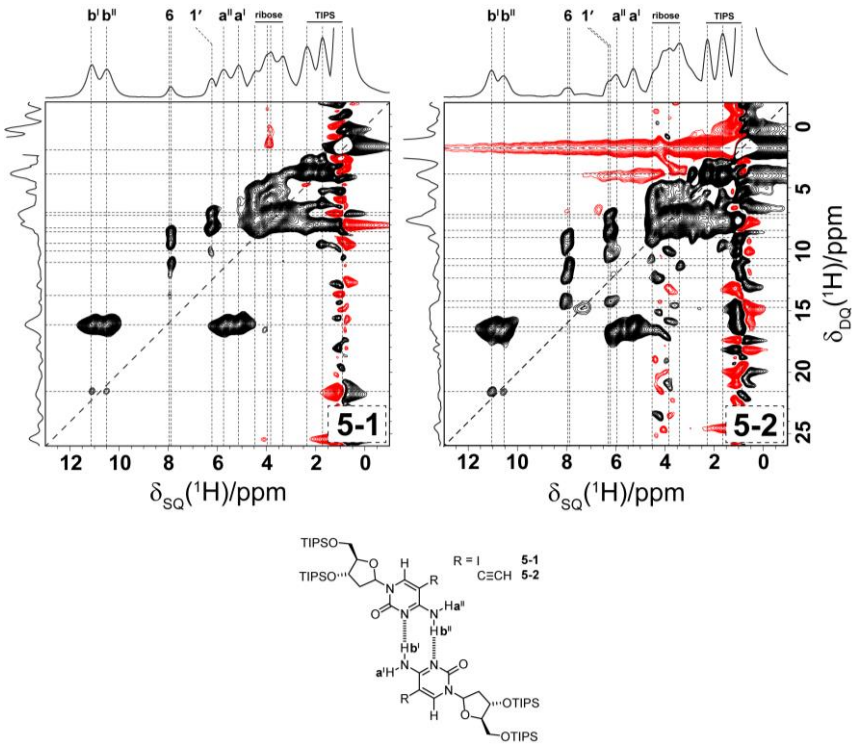

Figure 5.11 Comparison of ^{1}H – ^{1}H (ω_0 = 850 MHz) DQ/SQ MAS (60 kHz spinning) spectra of **5-1** (left) and **5-2** (right, see Fig. 5.5), alongside skyline projections and a schematic representation of the shared structural motif. One rotor period of BABA recoupling was used for the excitation and reconversion of DQ coherence. In both cases, for each of 128 t_1 FIDs, 16 transients were coadded with a recycle delay of 3 seconds. The $F_1 = 2F_2$ diagonal is given as a dashed black line. The base contour level is at 1% of the maximum peak height.

This assumption is well founded since the single crystal data for **5-2** revealed a Z' value of 2, in addition to the observation of four distinct NH environments being observed in its respective DQ MAS spectrum.

In addition to the similar $^{1}H - {}^{1}H$ correlations observed in Fig. 5.11, the $^{14}N - {}^{1}H$ (850 MHz) HMQC spectra of **5-1** presented in Fig. 5.12 and recorded with a τ_{RCPL} duration of 130 (Fig. 5.12e) and 400 μs (Fig. 5.12f), reveal the same correlations as were observed for **5-2** in Fig. 5.6. These data are therefore consistent with a retention of the dimeric structure in both **5-1** and **5-2**. Analogously with **5-2**, correlations in the N2 region of the ^{14}N dimension are not observed at these recoupling durations.

Table 5.4 DQ correlations extracted from a $^{1}H - {}^{1}H$ DQ/SQ MAS spectrum of **5-1** (see Fig. 5.11)

5-1	#	Correlation	Sum of SQ freq / ppm	DQ freq / ppm
	1	$CH_3 - CH_3$	0.9 + 0.9	1.8
	2	CH – CH	1.7 + 2.4	4.1
	3	CH_3 – 1'	0.9 + 6.2	7.1
	4	rib – rib	3.4 + 3.8	7.2
	5	CH – 1'	2.4 + 6.2	8.6
	6	CH_3 – 6	0.9 + 7.9	8.8
	7	CH – 6	1.7 + 7.9	9.6
	8	rib – 6	3.4 + 7.9	11.3
	9	1' – 6	6.2 + 7.9	14.1
	10	a^{I} - b^{I}	5.1 + 11.1	16.2
	11	a^{II} - b^{II}	5.8 + 10.5	16.3
	12	b^{II} - b^{I}	10.5 + 11.1	21.6

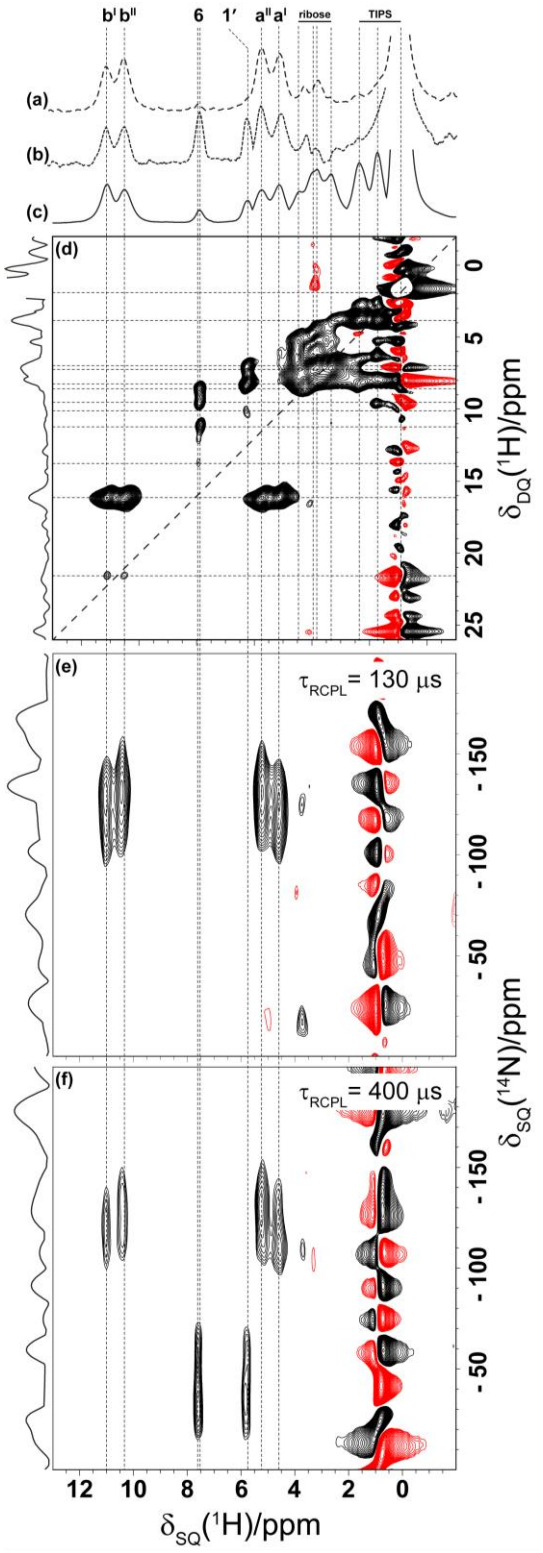

Figure 5.12 For **5-1**, (a, b) 1D HMQC filtered (t_1 = 0) spectrum, for (a) τ_{RCPL} = 130 μs and (b) τ_{RCPL} = 400 μs; (c) a 1D DQ-filtered spectrum and (d) ^{1}H – ^{1}H (850 MHz) DQ/SQ MAS (60 kHz) spectrum from Fig. 5.3; (e, f) 2D ^{14}N – ^{1}H (850 MHz) HMQC spectra recorded using R^3 recoupling of the ^{14}N – ^{1}H heteronuclear dipolar couplings for (e) τ_{RCPL} = 130 μs and (f) τ_{RCPL} = 400 μs. (e and f) 124 transients were recorded for each of 64 t_1 FIDs. The recycle delay was 3 seconds in both cases. The base contour level is at (e) 72% and (f) 68% of the maximum peak height in each spectrum, with negative contours shown in red.

5.3.3 The helical assembly of **5-3**

In a crystallographic sense, **5-3** differs from **5-2** (and **5-1**) in that only one molecule exists in the asymmetric unit cell (i.e. Z' = 1, Fig. 5.13a). Despite this difference, **5-3** is expected to associate with itself *via* the same hydrogen bonding motif as was observed in the two precursor compounds. The acetylenic axis in **5-3** allows for rotation (Fig. 5.13a) which, as is observed in the single crystal structure of **5-3**, allows for a helical assembly in the solid state (Fig. 5.14). Since this helical assembly requires that the two individual cytosine moieties in one molecule of **5-3** sit out of plane with respect to one another, four distinct NH peaks are observed in the $^{1}H - {}^{1}H$ (600 MHz) DQ/SQ MAS (60 kHz) spectrum of **5-3**, presented in Fig. 5.15 (a list of DQ correlations for **5-3** is provided in Table 5.5).

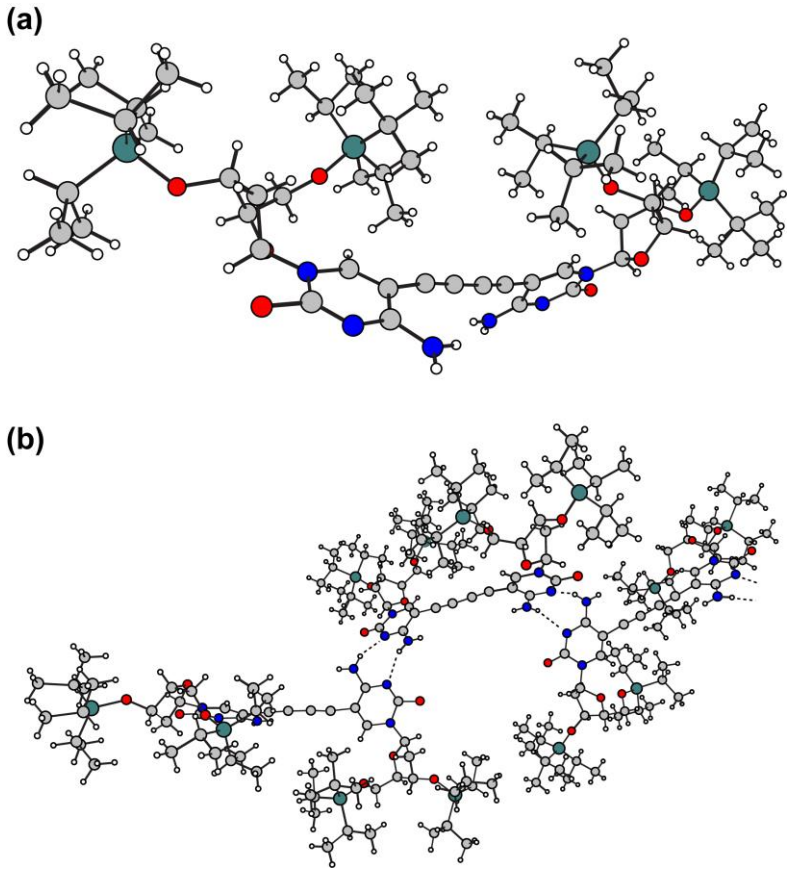

Figure 5.13 (a) The asymmetric unit cell of **5-3** demonstrating the staggered nature of the individual cytosine moieties, (b) the hydrogen bonding structure of **5-3** as extracted from the single crystal X-ray diffraction data.

Significant solvent molecule (isopropanol) disorder is observed in the single crystal structure which, alongside the large number of molecules in the unit cell (Z = 4), have so far precluded the calculation of NMR shielding parameters for **5-3**. Despite this, the resolution of the ^{1}H DQ MAS data (Fig. 5.15) at 60 kHz is sufficient so as to resolve three important sets of cross-peaks, observed at δ_{DQ} = 5.5 + 10.6 = 16.1 ppm, 7.5 + 9.9 = 17.4 ppm and 9.9 + 10.6 = 20.5 ppm, corresponding to dipolar couplings between $NHa^{I} - NHb^{I}$, $NHa^{II} - NHb^{II}$ and $NHb^{II} - NHb^{I}$ environments, respectively.

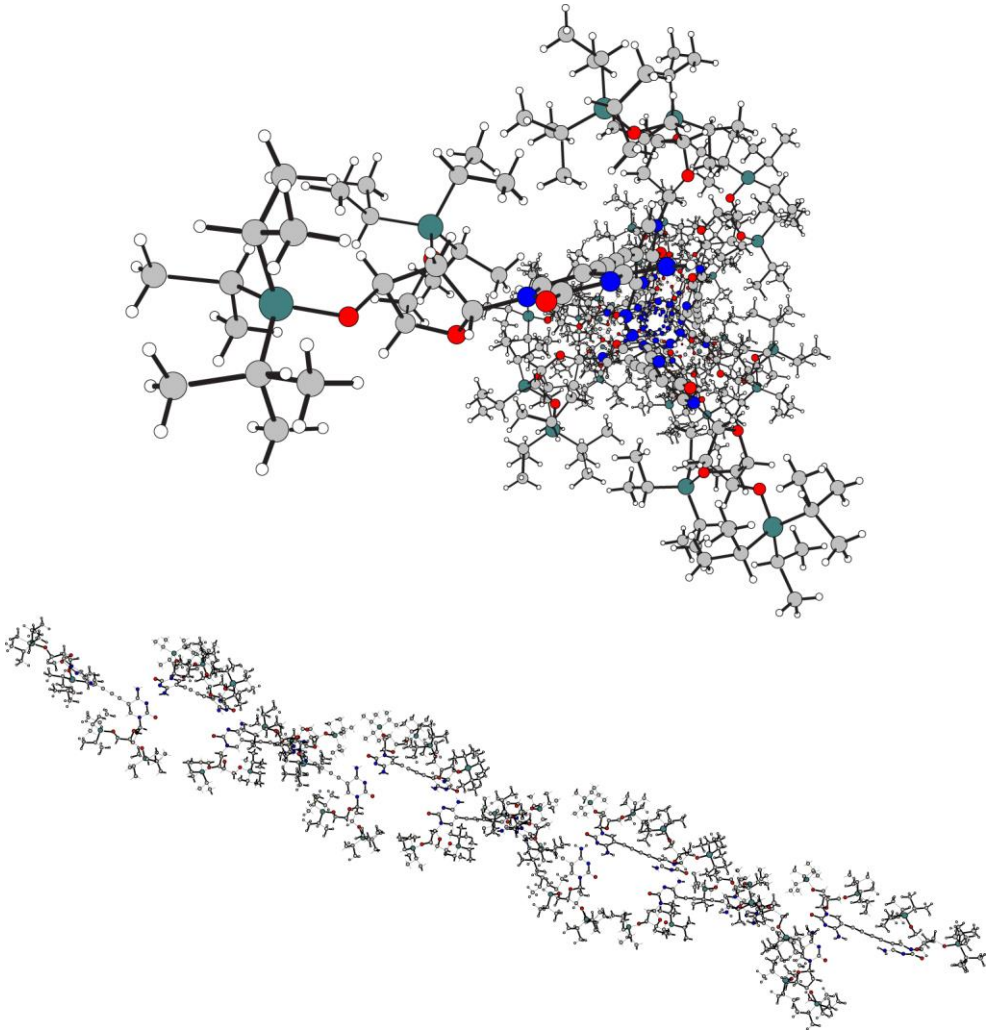

Figure 5.14 Schematic representation of the helical assembly of **5-3**, extracted from the single crystal structure, (top) looking down through the helix, (bottom) sidelong view of the helix.

As was the case for **5-1** and **5-2**, the weak cross-peak corresponding to a NHb^{II} – NHb^{I} contact is the most significant, since it corresponds to the truncated dipolar coupling across the hydrogen bonding motif, with this cross-peak being common in all three compounds (see Fig. 5.11/ 5.15). In addition, the well-resolved nature of the ^{1}H – ^{1}H DQ/SQ MAS spectrum is indicative of a high degree of periodic order in the solid-state which is expected given the helical nature of **5-3**.

Despite dramatic differences in the crystal packing arrangements of **5-3** and **5-2** (and by extension **5-1**), i.e., the former self-assembles into helical arrays whilst the latter exists in a dimeric form, the ^{1}H – ^{1}H DQ/SQ MAS spectra for the respective compounds share common spectral features and ^{1}H chemical shifts, since both compounds interact with themselves through the same cytosine hydrogen bonding motif. The alkyl and ribose regions are highly similar, as expected upon inspection of the relative molecular structures (Fig. 5.1), leading to similar spectral patterns. Interestingly, the same sets of cross-peaks relating to the NH protons are observed in the spectra of **5-1**, **5-2** and **5-3**, albeit at different chemical shifts (resulting from different crystal packing arrangements).

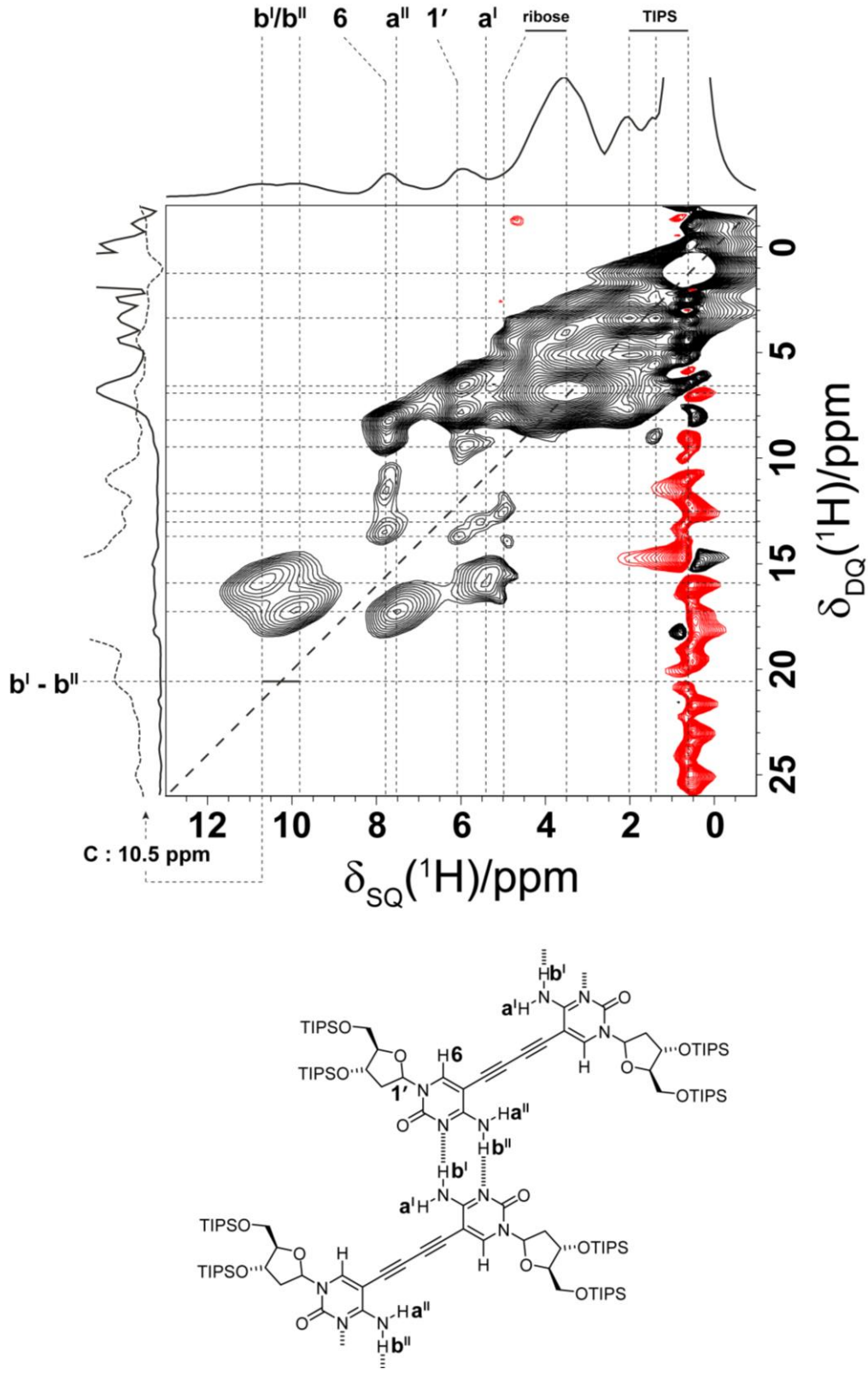

Figure 5.15 A ^{1}H – ^{1}H (ω_0 = 600 MHz) DQ/SQ MAS (60 kHz spinning) spectrum of **5-3**, alongside skyline projections and a schematic representation of its hydrogen bonding structure. The column extracted at δ_{SQ} = 10.5 ppm is consistent with a weak b^{I} – b^{II} cross-peak. One rotor period of BABA recoupling was used for the excitation and reconversion of DQ coherence. For each of 200 t_1 FIDs, 48 transients were coadded with a recycle delay of 3 seconds. The $F_1 = 2F_2$ diagonal is given as a dashed black line. The base contour level is at 0.2% of the maximum peak height.

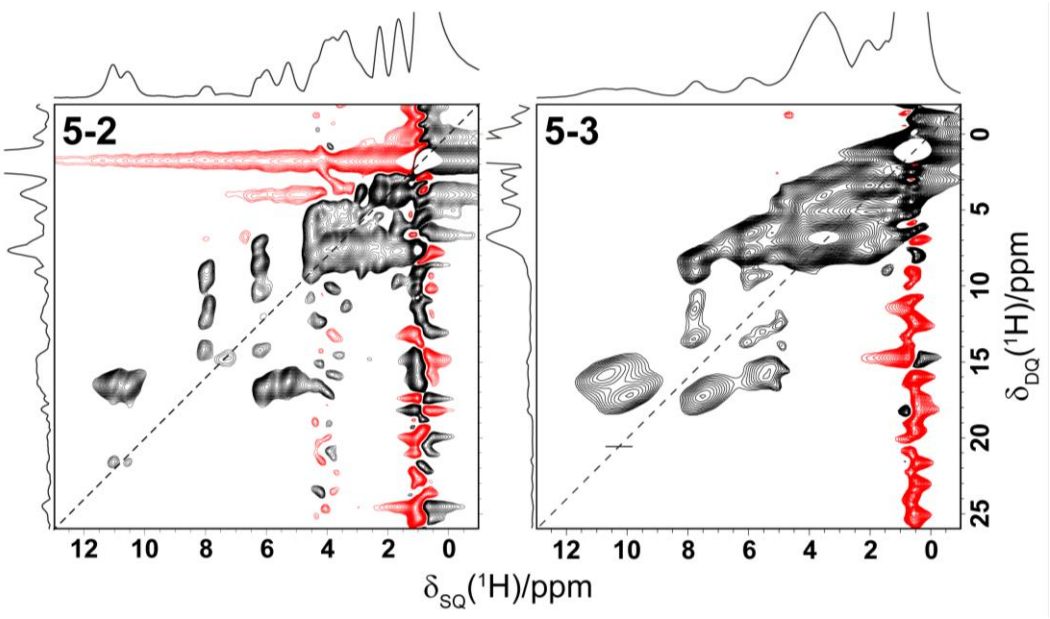

Figure 5.16 Comparison of $^{1}H - ^{1}H$ DQ/SQ MAS spectra of **5-2** (Fig. 5.5) and **5-3** (Fig. 5.15) demonstrating the similar overall spectral pattern and chemical shifts.

Table 5.5 DQ correlations extracted from a $^{1}H - ^{1}H$ DQ/SQ MAS spectrum of **5-3** (see Fig. 5.15)

5-3	#	Correlation	Sum of SQ freq / ppm	DQ freq / ppm
	1	$CH_3 - CH_3$	0.6 + 0.6	1.2
	2	CH – CH	1.4 + 2.0	3.4
	3	CH_3 – rib	0.6 + 3.5	4.1
	4	CH_3 – 1'	0.6 + 5.9	6.5
	5	rib – rib	3.5 + 3.5	7.0
	6	CH – 1'	2.0 + 5.9	7.9
	7	CH_3 – 6	0.6 + 7.7	8.3
	8	CH – 6	1.4 + 7.7	9.1
	9	rib – 1'	3.5 + 5.9	9.4
	10	rib – 6	3.5 + 7.7	11.2
	11	rib – 6	4.9 + 7.7	12.6
	12	1' – 6	5.9 + 7.7	13.6
	13	$a^{I} - b^{I}$	5.5 + 10.6	16.1
	14	a^{II} - b^{II}	7.5 + 9.9	17.4
	15	$b^{II} - b^{I}$	9.9 + 10.6	20.5

The significant difference in the NHa^{II} ^{1}H chemical shift, observed at δ_{SQ} = 7.5 ppm for **5-3** (5.8 ppm in **5-1**, 6.0 ppm in **5-2**), is probably due to the distorted nature of the hydrogen bonding interface in **5-3** (see Fig. 5.12b), when compared to the more planar motif observed in the crystal structure of **5-2** (Fig. 5.2). In the single-crystal X-ray structure of **5-3**, protons $NHa^{I/II}$ do not form hydrogen bonding interactions – this likely shows the deficiency of the crystal structure in locating the isopropanol molecules. A comparison of ^{1}H – ^{1}H DQ/SQ MAS spectra for **5-2** and **5-3** is presented in Fig. 5.16. The observed resolution in the spectrum of **5-3** (600 MHz) is lower than in the corresponding spectrum of **5-2** (850 MHz) due primarily to differences in applied field strength. Based on this data, it is plausible to conceptualise **5-3** as a linear arrangement of dimeric structures (analogous to **5-2**) separated by the acetylenic axis, which is presented schematically in Fig. 5.17. When isolated in this sense, it becomes apparent that the respective spectra should display a degree of similarity since **5-3** is, essentially, a pair of molecules of **5-2** connected by a motif of triple C – C bonds, sitting in a similar local environment. In addition, the TIPS groups on the periphery of individual helices insulate the central cytosine moieties from adjacent helices, giving further credence to the consideration of the structure as isolated dimers.

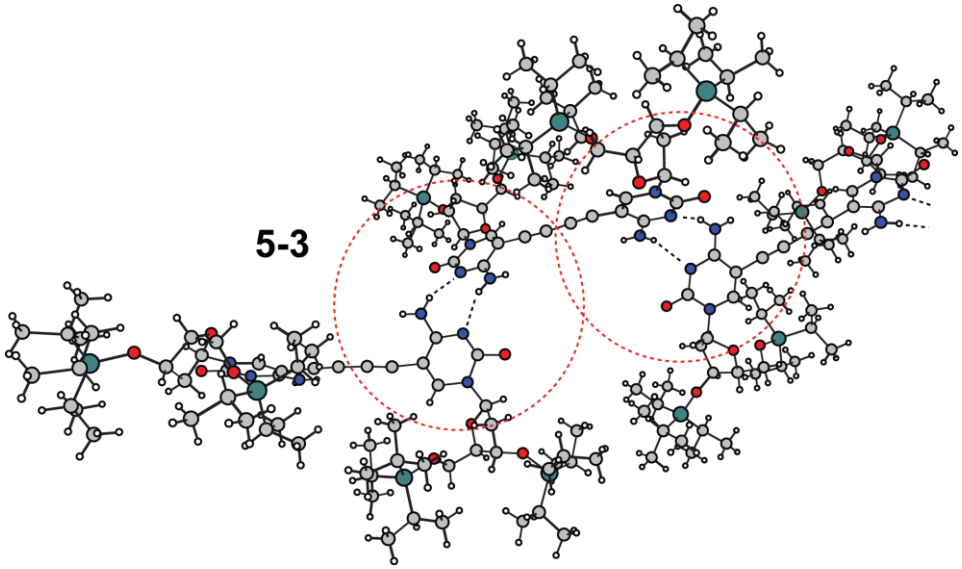

Figure 5.17 Schematic representation of the hydrogen bonding structure of **5-3**, as shown in Fig. 5.13, with the red circles indicating the cytosine dimers isolated from one another *via* the acetylenic axis. When viewed in this sense it is not surprising that the respective ^{1}H – ^{1}H DQ/SQ MAS spectra of **5-2** (dimeric assembly) and **5-3** (helical assembly) share common spectral features.

The ^{14}N – ^{1}H (600 MHz) HMQC spectrum of **5-3** is complex, unlike the corresponding HMQC spectra of **5-1** (Fig. 5.12) and **5-2** (Fig. 5.6), and difficult to interpret, likely due to the differences in the number of crystallographically distinct molecules in the asymmetric unit cells of the respective compounds. A ^{14}N – ^{1}H HMQC spectrum for **5-3** is presented in Fig. 5.18, alongside tentative assignments. The descriptor 'tentative' is used since, in the absence of GIPAW data, precise assignment of i) ^{14}N chemical shifts and, ii) the exact ^{14}N – ^{1}H correlations is difficult, particularly in the latter case where broadened lineshapes prevent accurate analysis.

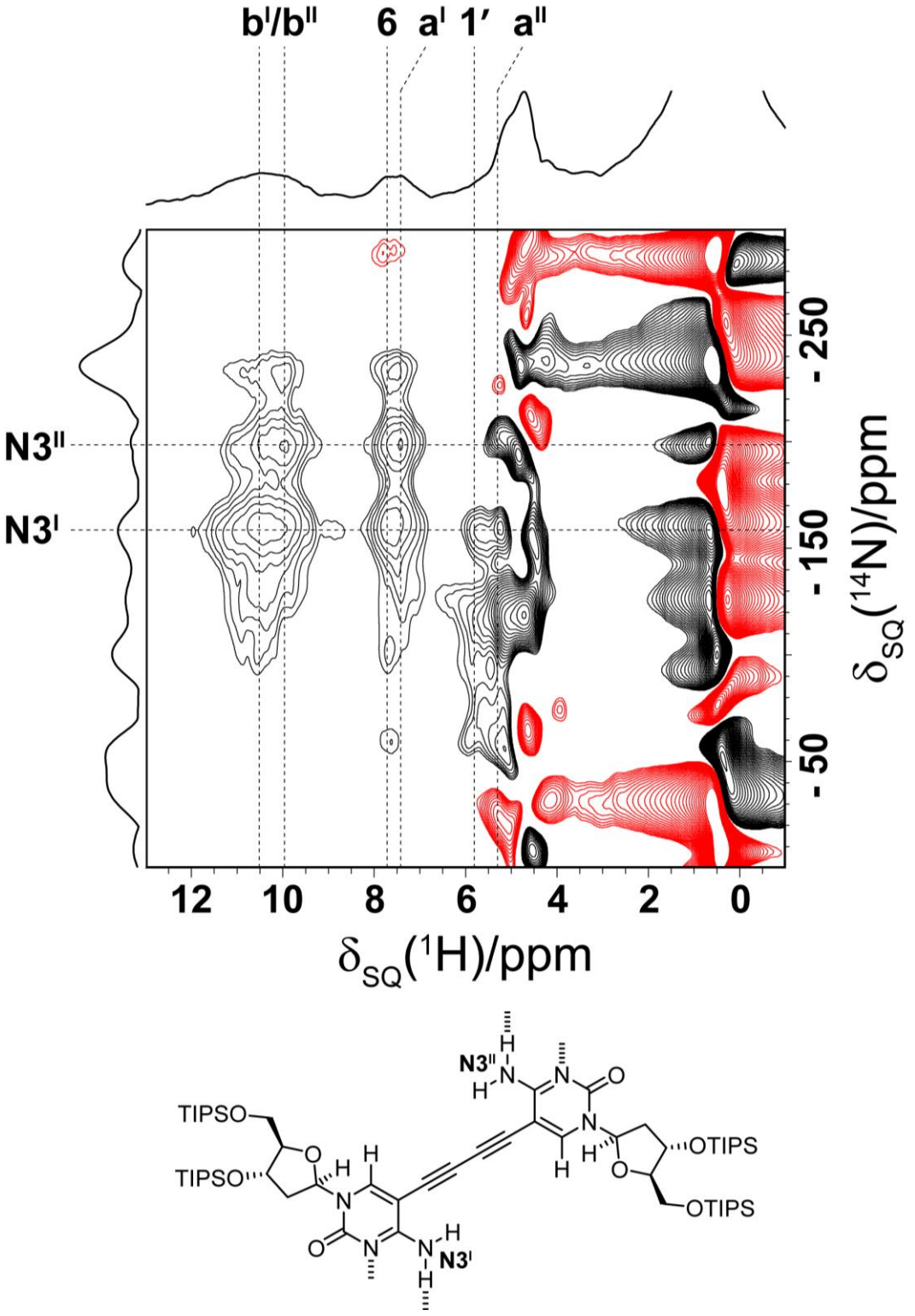

Figure 5.18 A $^{14}N - {}^{1}H$ (ω_0 = 600 MHz) HMQC spectrum of **5-3**, alongside skyline projections and a schematic representation of the molecular structure, with the two distinct N3 nitrogen labelled. The spectrum was recorded using the R^3 recoupling scheme (for the recoupling of the $^{14}N - {}^{1}H$ heteronuclear dipolar couplings) for a τ_{RCPL} = 200 μs. For each of 80 t_1 FIDs, 160 transients were coadded with a recycle delay of 2 seconds. The base contour level is shown at 85% of the maximum peak height.

5.4 Summary

In a similar way to chapter 4 (a and b), the work presented herein has demonstrated the ability of high-resolution ^{1}H MAS NMR techniques to elucidate the mode of assembly of complex organic molecules in the solid state. With the aid of NMR crystallographic techniques, it has been possible to confirm chemical shift assignments for **5-2**, the results of which allowed the structure of **5-1** to be inferred, based on the similarity of the ^{1}H – ^{1}H DQ/SQ MAS NMR data. In addition to chemical shift assignments, GIPAW calculations for the isolated molecules (both **5-2** and the isopropanol solvent) complements the single crystal X-ray diffraction data for **5-2** by providing data on the strength of the various hydrogen bonding interactions, based on the observed differences in ^{1}H chemical shift between the full crystal and the isolated species, whilst also revealing that the influence of $\pi - \pi$ type interactions is minimal on the rest of the protons in the structure.

For **5-3**, the presented ^{1}H MAS NMR data was consistent with the deposited crystal structure in that it suggested Z' = 1, based on the number of distinct NH resonances. Unfortunately, the absence of GIPAW calculations for **5-3** mean that it is not possible to make definitive assignments of the various ^{1}H environments. However, by comparing the DQ MAS spectrum of **5-3** with that of **5-2** it is possible to speculate with high confidence that both compounds (and **5-1**) share a common hydrogen bonding motif. If this assumption holds true then, after inspection of the molecular structure, it is possible to argue that the NMR data is consistent with the helical assembly suggested by the single crystal X-ray structure, despite some significant disorder and deficiencies in the latter data in terms of the positions of the solvent molecules.

Characterisation of such materials, particularly in the case of **5-3**, is incredibly valuable due to the high potential for future materials applications inherent in these systems. Helical assemblies remain an active area of research and, as this chapter has demonstrated, high-resolution ^{1}H MAS NMR is a useful tool with which to probe the solid-state packing arrangement in the absence of 'clean' X-ray diffraction structures.

Chapter 6 : A study of the hydrogen bonding propensity of pyrimidine-based systems

6.1 Introduction

The pyrimidine ring, which is the foundational chemical moiety of cytosine, thymine and uracil, and the related purine heterocycle, and which forms the structural backbone of adenine and guanine, is one of the most widely occurring nitrogen-based heterocycles in nature. As such, synthetic analogues and derivatives of such heterocycles exhibit a diverse range of pharmacological properties. As a consequence of these properties, there exist many examples of such compounds being used for the purposes of drug development and medicinal chemistry.(249-253) In particular pyrimidine-based structures have shown good efficacy in anti-cancer studies. For example in the period 2009 – 2014, 59 patents were published for pyrimidine-based anti-cancer agents, with over half of these patents having been published from 2012 onwards,(254) thereby indicating that the field remains highly active. A similar activity is observed for related quinazoline derivatives.(255)

In addition to these medicinal applications, this class of compounds demonstrates a high capacity for molecular self-assembly. In particular, guanine – cytosine hybrids or so-called 'Janus' molecules, in which the G and C hydrogen bonding faces are contained within the same molecule at 60° with respect to one another, have a tendency to form self-assembled hexameric rosette structures in solution,(113) which can then further aggregate into nanotube-like structures.(108,109,111,114,256) This chapter describes the solid-state characterisation of a series of heterocyclic precursor Janus-type molecules (**6-1** – **6-6**, see Fig. 6.1) and some of the synthetic challenges presented with the later intermediates. Solution-state data for these compounds was published by Marsh, Silvestri and Lehn.(105)

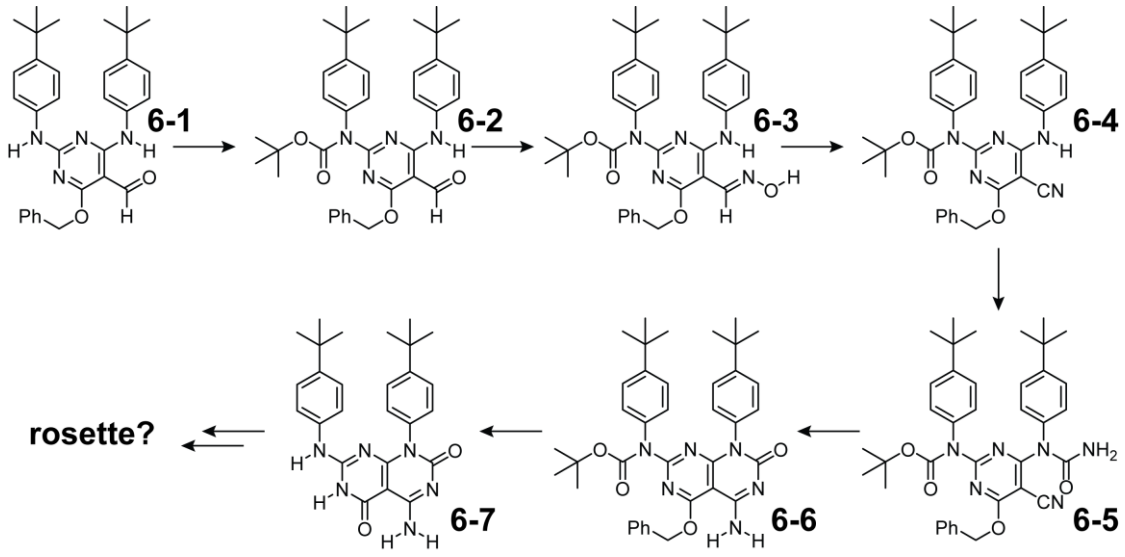

Figure 6.1 Schematic representation of the series of pyrimidine derivatives discussed in this chapter. ^{1}H MAS NMR data is presented for compounds **6-1** – **6-6**.

Despite the absence of solid-state NMR data for **6-7** at the time of writing, the precursor compounds exhibit interesting NMR properties. There is also a paucity of ^{1}H solid-state NMR characterisation for

aldehyde (**6-1/2**) and oxime (**6-3a/b**) containing compounds in the literature. This study is therefore of wider interest for application to this important range of organic molecules and functional groups.

The reagents involved in the later stages of the synthetic pathway, particularly chlorosulfonyl isocyanate in the conversion of **6-4** to **6-5**, are highly toxic, harmful, cause severe burns and react violently with water (and moisture), and decompose into hazardous materials, thereby necessitating the need to develop alternative procedures. For safety reasons it was therefore not possible to synthesis **6-7** prior to submission of this thesis. Some alternative procedures are discussed in section 6.3.5.

6.2 Experimental details

6.2.1 Sample preparation

The samples analysed in this chapter were synthesised by Andrew Marsh according to the methods outlined in reference (105). Several compounds were resynthesized for the purposes of this work, with characterisation of all products being consistent with the aforementioned work.

6.3 Results

6.3.1 Aldehyde containing compounds: **6-1** and **6-2**

In solution-state NMR, aldehyde protons are typically observed in the 9.0 – 10.0 ppm range. In the absence of substantive literature precedence for such moieties in the solid state, ^{1}H – ^{13}C INEPT based methods can be exploited to ascertain the chemical shift of the CHO proton. The CP MAS data for **6-1** (Fig. 6.2) reveals that the ^{13}C aldehyde environment is observed at 186.7 ppm, analysis of which is made easier by the absence of any other carbonyl groups in this molecule. However, in terms of ^{1}H chemical shifts, the situation is complicated for **6-1** in that the NHa and NHb protons, which are postulated to form hydrogen bonding interactions, are observed in the same chemical shift region as the aldehyde, thereby complicating analysis. This is indeed observed in the ^{1}H – ^{1}H (600 MHz) DQ/SQ MAS (60 kHz) spectrum of **6-1** presented in Fig. 6.3d (DQ correlations are listed in Table 6.1), which exhibits broad spectral features due to two simultaneous effects: the presence of typically strong aromatic dipolar coupling interactions and the overlapping aldehyde and amine resonances. Fig. 6.3e presents a ^{14}N – ^{1}H (600 MHz) HMQC spectrum of **6-1**, recorded at a short recoupling duration of 130 μs, in which only one-bond NH proximities are expected to be observed. Despite the high abundance of nitrogens in this molecule sitting in close spatial proximity to several aromatic sites (accounting for the correlations observed between 6.0 and 9.0 ppm in the ^{1}H dimension), two clear, strong correlations are observed at overlapping ^{14}N chemical shifts of ~ –30 ppm and ^{1}H chemical shifts of 11.0 and 9.7 ppm. The ^{1}H – ^{13}C INEPT spectrum presented in Fig. 6.3f, confirms that the resonance at a ^{1}H chemical shift of 9.9 ppm does indeed correspond to the aldehyde proton, since this environment experiences a clear correlation with the aforementioned aldehyde C=O ^{13}C chemical shift at 186.7 ppm.

These data allow for a description of the solid-state packing arrangement for **6-1**. In the ^{1}H DQ MAS data, in Fig. 6.3d, the auto-peak observed at δ_{DQ} = 9.7 + 9.7 = 19.4 ppm is, in light of the HMQC data presented in Fig. 6.3e, assigned as an NHb – NHb contact across the hydrogen bonding face (presented in Fig. 6.4). The resonance observed at 11.0 ppm is therefore assigned as the NHa environment which undergoes an intramolecular hydrogen bonding interaction with the aldehyde carbonyl oxygen (see Fig. 6.4). Interestingly, a cross-peak is observed at δ_{DQ} = 9.9 + 11.0 = 20.9 ppm, assigned herein as a close spatial proximity between the aldehyde proton and the intramolecularly hydrogen bonded NHa proton environments. This interaction may be explained as a close approach of individual dimers or some form of weakly associated linear assembly: putative structural arrangements are presented in Fig. 6.4.

From a self-assembly standpoint, both of the structures presented in Fig. 6.4 are feasible. With the linear arrangement, a cross-peak between the nearby aromatic proton and the aldehyde proton would be expected given their proximity. Unfortunately due to the close NHa and aldehyde chemical shifts, it is not possible to distinguish such a cross-peak at δ_{DQ} = 7.1 + 9.9 = 17.0 ppm in the ^{1}H DQ MAS spectrum (Fig. 6.3d). The number of aromatic moieties in **6-1** mean that a $\pi - \pi$ stacking of individual linear 'tapes' would be expected.

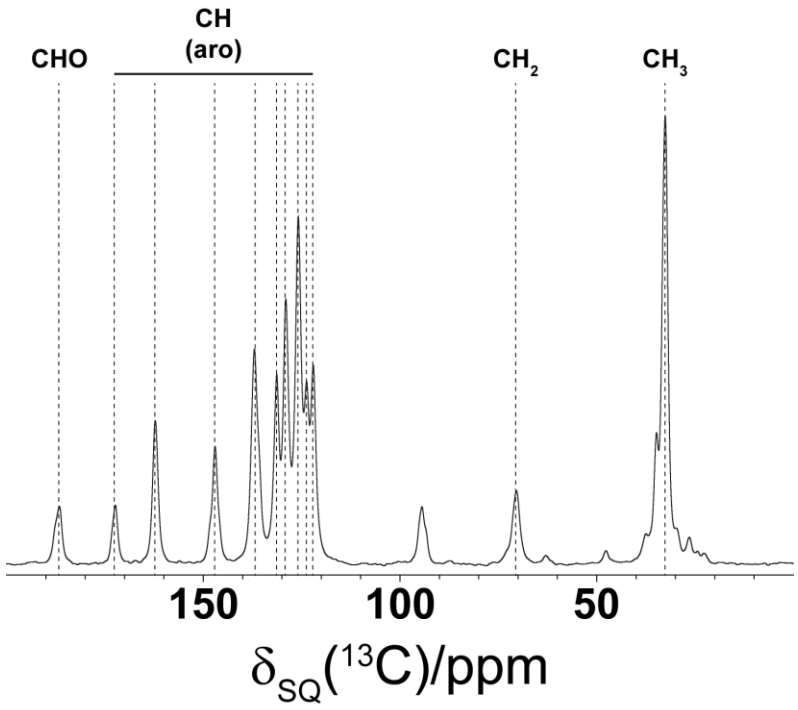

Figure 6.2 ^{1}H (ω_0 = 500 MHz) – ^{13}C CP MAS (12.5 kHz spinning) spectrum of **6-1**, recorded with 1024 transients and a recycle delay of 2 seconds.

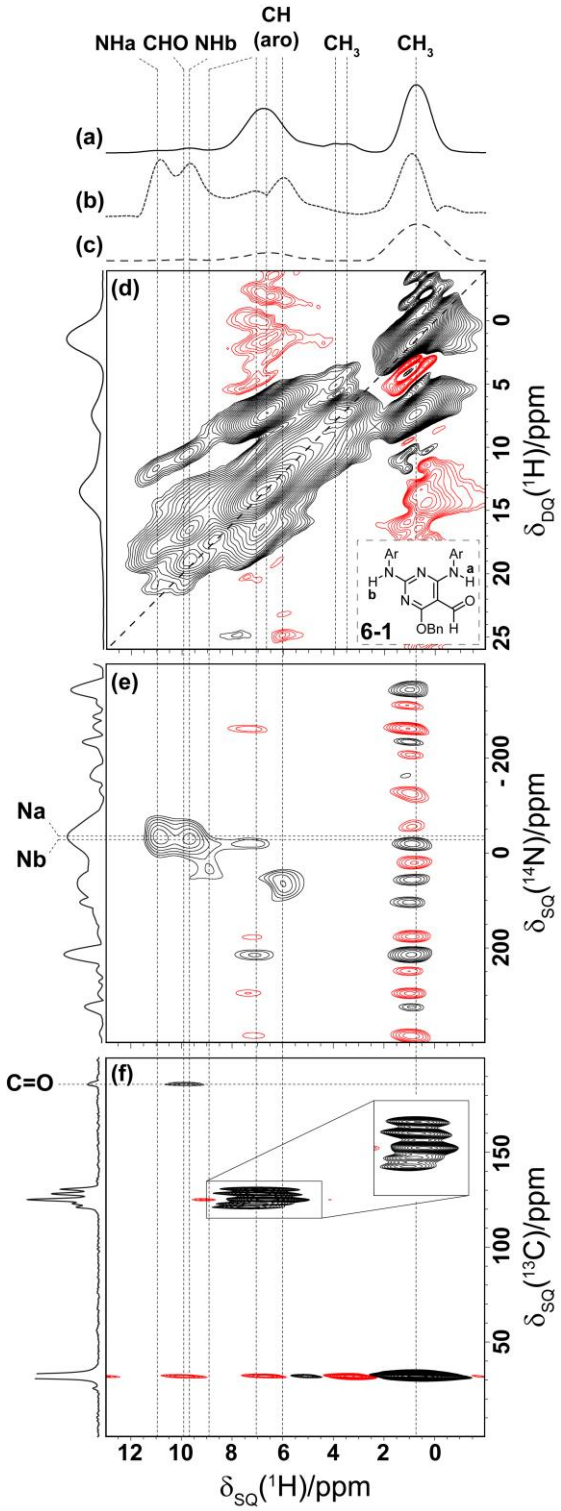

Figure 6.3 For **6-1**, (a, d) 1D ^{1}H (ω_0 = 600 MHz) DQ-filtered, i.e., t_1 = 0, and 2D ^{1}H – ^{1}H (ω_0 = 600 MHz) DQ/SQ MAS spectra, (b, e) 1D HMQC filtered and 2D ^{14}N – ^{1}H (ω_0 = 600 MHz) HMQC spectra, using R^3 recoupling of the ^{14}N – ^{1}H heteronuclear dipolar couplings, with a τ_{RCPL} = 130 μs (c, f) ^{1}H (ω_0 = 500 MHz) – ^{13}C INEPT filtered INEPT spectra, recorded at (a, b, d, e) 60 and (c, f) 12.5 kHz MAS. For (d), 16 transients were recorded for each of 128 t_1 FIDs. For (e), 32 transients were recorded for each of 64 t_1 FIDs. For (f), 256 transients were recorded for each of 32 t_1 FIDs. The recycle delay was 3 (a, b, d, e) and 2 seconds (c, f). The 1D spectra correspond to the first row of the respective 2D spectra. The base contour level is at (d) 1, (e) 41, and (f) 3% of the maximum peak height.

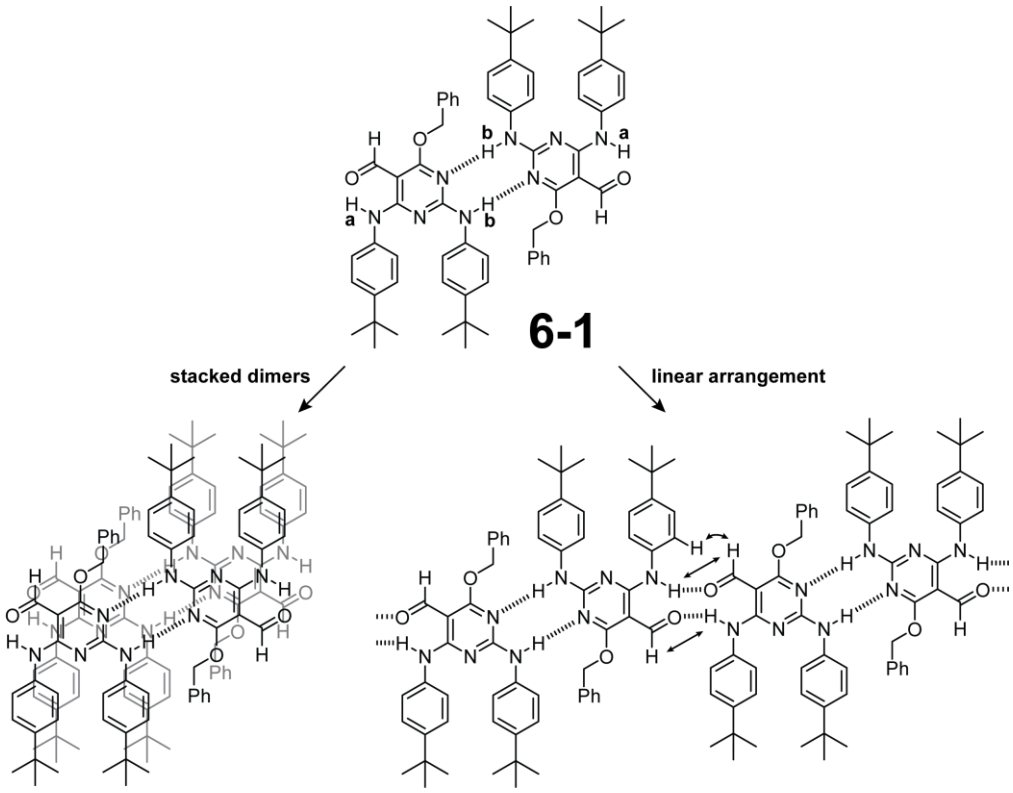

Figure 6.4 Schematic representation of expected hydrogen bonding exhibited by **6-1**. The weak NH – HCO cross-peak, observed in Fig. 6.3d (straight arrows) can be explained by a stacked dimer or linear arrangement. With the linear arrangement, a cross-peak between aromatic and aldehyde protons, as indicated by the curved arrow, is expected.

A ^{1}H – ^{1}H (600 MHz) DQ/SQ MAS (60 kHz) spectrum of **6-2**, presented in Fig. 6.5c (DQ correlations are presented in Table 6.2), is easier to interpret compared to the corresponding spectrum of **6-1**. This is due to the absence of the NHb proton, which in **6-1** was postulated to form a dimeric hydrogen bonded structure (see Fig. 6.4), but which in **6-2** has been protected at this position with a *t*-butyloxycarbonyl (BOC) group. The resulting hydrogen bonding capacity of **6-2** is subsequently reduced, although the intramolecular NHa ⋯ O=C hydrogen bond is retained. This therefore leaves a weakly associated dimer as the only viable structural possibility, as shown in Fig 6.6. The appearance of a cross-peak in the ^{1}H – ^{1}H DQ/SQ MAS spectrum of **6-2** at δ_{DQ} = 7.2 + 9.5 = 16.7 ppm, is consistent with an aldehyde proton – aromatic proton spatial proximity. However, given that the NH amine group forms a cross-peak at δ_{DQ} = 6.6 + 10.3 = 16.9 ppm, with what is likely an aromatic proton in the nearby aryl moiety, it is perhaps more likely that the former cross-peak is explained by some spatial arrangement whereby the benzyl aromatic functionality is close in space with the aldehyde proton environment (intermolecular).

A short recoupling time (τ_{RCPL} = 130 μs) ^{14}N – ^{1}H (600 MHz) HMQC spectrum of **6-2** is presented in Fig. 6.5d. Analysis of the observed correlations reveals a strong peak at ~ –140 ppm and 10.2 ppm in the ^{14}N and ^{1}H dimension, respectively. Weaker correlations due to close spatial proximities of this same nitrogen and the nearby aromatic protons are also clearly observed for this recoupling time.

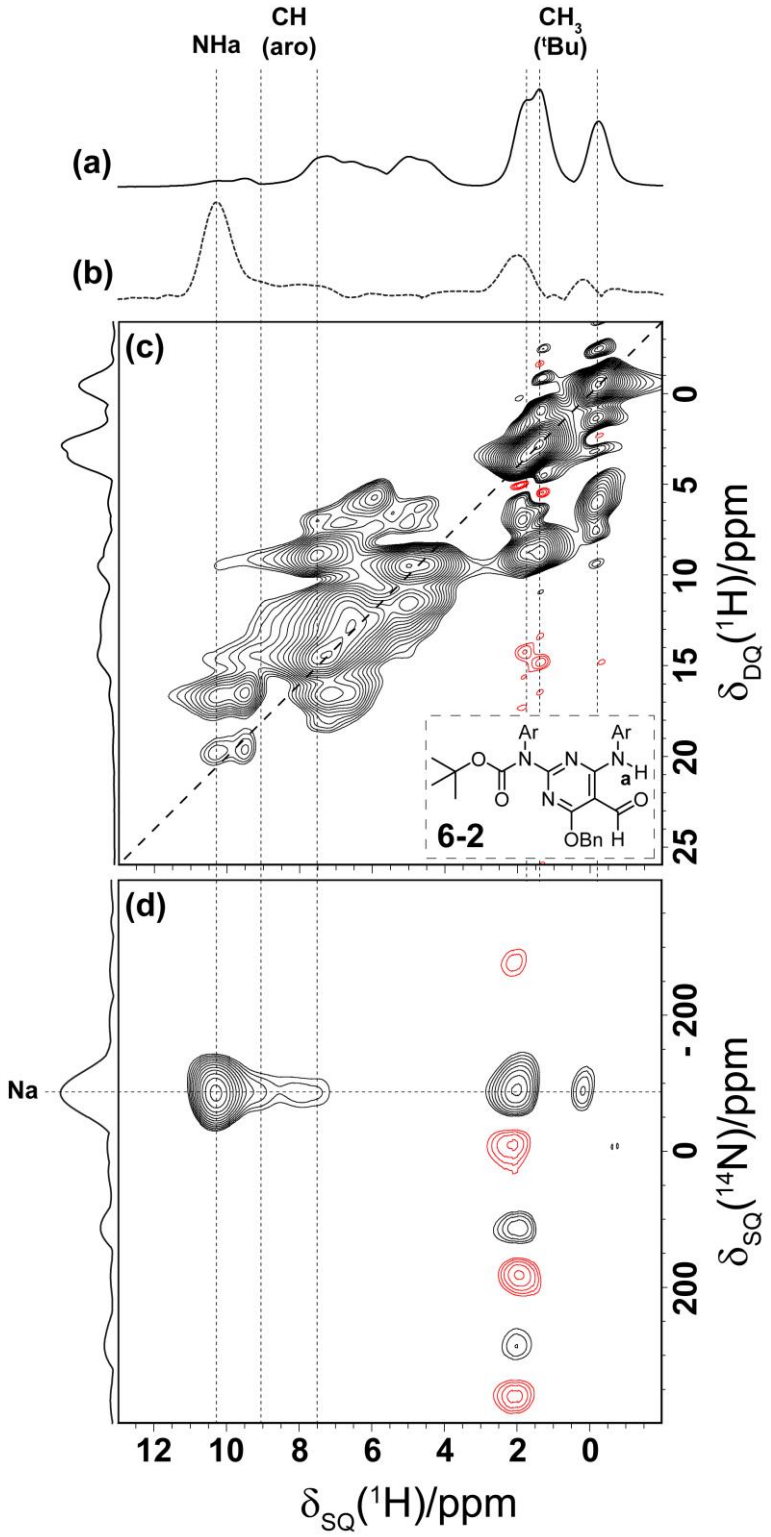

Figure 6.5 (a, c) 1D ^{1}H (ω_0 = 600 MHz) DQ-filtered, i.e., t_1 = 0, and 2D ^{1}H – ^{1}H (ω_0 = 600 MHz) DQ/SQ MAS spectra, (b, d) 1D HMQC filtered and 2D ^{14}N – ^{1}H (ω_0 = 600 MHz) HMQC spectra, using R^3 recoupling of the ^{14}N – ^{1}H heteronuclear dipolar couplings, with a τ_{RCPL} = 130 μs of **6-2**, recorded in all cases at 60 kHz MAS. For (c), 16 transients were recorded for each of 128 t_1 FIDs. For (d), 16 transients were recorded for each of 32 t_1 FIDs. In each case, the recycle delay was 3 seconds. The 1D spectra correspond to the first row of the respective 2D spectra. The base contour level is at (c) 2, and (d) 17% of the maximum peak height.

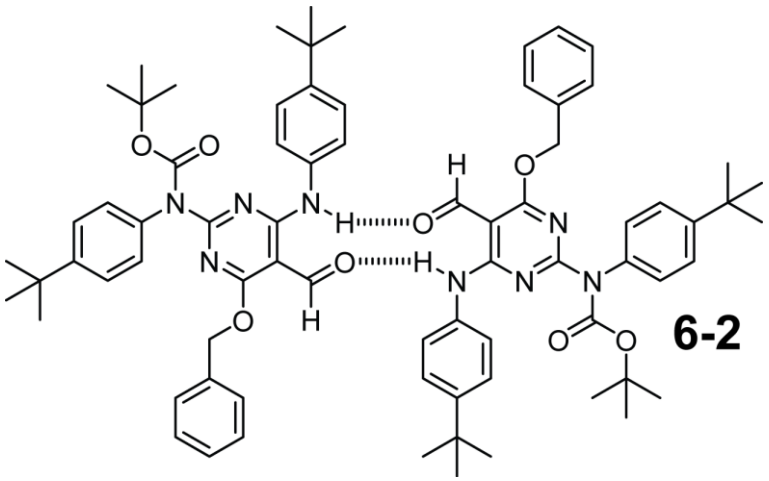

Figure 6.6 Schematic representation of a possible weakly associated dimer for **6-2**.

Three distinct resonances corresponding to three different methyl group environments are clearly observed in the ^{1}H DQ MAS spectrum in Fig. 6.5c which result in three auto-peaks at δ_{DQ} = –0.2 + –0.2 = –0.4, 1.4 + 1.4 = 2.8, and 1.8 + 1.8 = 3.6 ppm, respectively. These three peaks correspond to the three methyl group environments in **6-2**: the two *t*-butyl groups directly bonded to the aromatic moieties and the *t*-butyl group contained within the BOC protecting group. Given that in precursor **6-1** (no BOC group) the two former *t*-butyl groups resulted in one broad resonance at δ_{SQ} = 0.8 ppm, this observed splitting of the methyl signal is perhaps consistent with a rotation of a CN bond as presented in Fig. 6.7. This potential bond rotation would relieve the steric tension between the two aromatic rings. In **6-1**, this rotation is not expected to occur due to the hydrogen bonding capacity offered by the unprotected NHb proton (see Fig. 6.4). This hypothesis is consistent with the observed cross-peaks in the DQ spectrum of **6-1**, presented in Fig. 6.3d, specifically the auto-peak at δ_{DQ} = 9.7 + 9.7 = 19.4 ppm, which is consistent with an intermolecular dipolar coupling of this NH proton with itself across a hydrogen bonding interface (see Fig. 6.4).

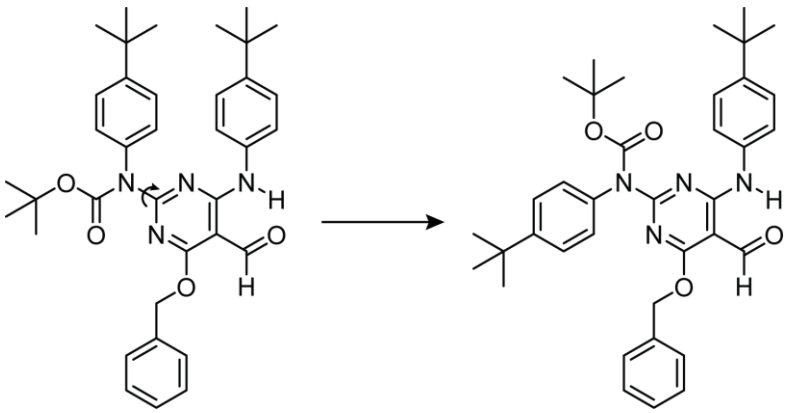

Figure 6.7 Schematic representation of a possible CN bond rotation. Such a rotation could potentially explain the appearance of three distinct methyl group peaks in the DQ MAS spectrum of **6-2** presented in Fig. 6.5c.

Table 6.1 DQ correlations extracted from the $^{1}H - {}^{1}H$ DQ/SQ MAS spectrum of **6-1** in Fig. 6.3d.

6-1	#	Correlation	$\delta_{SQ}(1) + \delta_{SQ}(2)$ / ppm	δ_{DQ} / ppm
	1	$CH_3 - CH_3$	0.7 + 0.7	1.4
	2	$CH_3 - CH_2$	0.7 + 4.0	4.7
	3	CH_3 – CH (aro)	0.7 + 6.6	7.3
	4	$CH_2 - CH_2$	3.5 + 4.0	7.5
	5	CH_3 – NHb	0.7 + 9.7	10.4
	6	CH_3 – CHO	0.7 + 9.9	10.6
	7	CH_3 – NHa	0.7 + 11.1	11.8
	8	CH (aro) – CH (aro)	6.8 + 6.8	13.6
	9	CH (aro) – NHb	6.8 + 9.7	16.5
	10	CH (aro) – NHa	7.5 + 11.1	18.6
	11	NHb – NHb	9.7 + 9.7	19.4
	12	CHO – NHa	9.9 + 11.1	21.0

Table 6.2 DQ correlations extracted from the $^{1}H - {}^{1}H$ DQ/SQ MAS spectrum of **6-2** in Fig. 6.5c.

6-2	#	Correlation	$\delta_{SQ}(1) + \delta_{SQ}(2)$ / ppm	δ_{DQ} / ppm
	1	$CH_3 - CH_3$	−0.2 −0.2	−0.4
	2	$CH_3 - CH_3$	−0.2 + 1.3	1.1
	3	$CH_3 - CH_3$	1.3 + 1.3	2.6
	4	$CH_3 - CH_3$	1.8 + 1.8	3.6
	5	CH_3 – CH (aro)	−0.2 + 6.0	5.8
	6	$CH_3 - CH_2$	1.8 + 4.6	6.4
	7	$CH_3 - CH_2$	1.8 + 5.0	6.8
	8	CH_3 – CH (aro)	1.3 + 7.5	8.8
	9	$CH_2 - CH_2$	4.6 + 5.0	9.6
	10	CH_2 – CH (aro)	5.0 + 6.7	11.7
	11	CH (aro) – CH (aro)	6.7 + 6.7	13.4
	12	CH (aro) – CH (aro)	7.1 + 7.1	14.2

13	CH (aro) – CHO	7.1 + 9.5	16.6
14	CH (aro) – NHa	6.7 + 10.3	17.0
15	CHO – NHa	9.5 + 10.3	19.8

6.3.2 BOC protected and non-protected oxime precursors: **6-3a/6-3b**

t – butyloxycarbonyl (BOC) moieties are a useful, versatile and commonly employed protecting group in synthetic organic chemistry, with particular use in modifying amine functional groups for further reactions. Unfortunately, the group tends to be rather labile in the presence of strong acids, therefore requiring careful reaction setups and purification techniques to be applied. As such, samples of the BOC protected (**6-3a**) and unprotected (**6-3b**) oxime intermediates were isolated, and are investigated in this section. The structures of **6-3a** and **6-3b** are presented in Fig. 6.8.

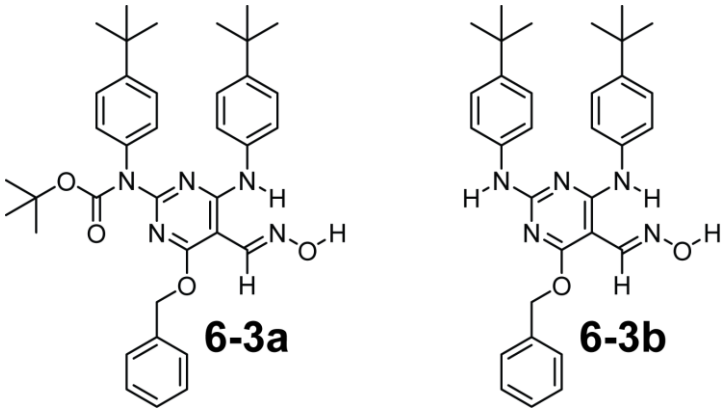

Figure 6.8 Structures of BOC protected (**6-3a**) and unprotected (**6-3b**) oxime intermediates, with formation of a NH ⋯ N intramolecular hydrogen bond.

Oximes (in the case of **6-3a/b**, specifically aromatic aldoximes, $R^1HC{=}NOH$) are a subclass of the more widely known imine functional group. Specifically, they contain an unusual N – OH moiety. Given their unusual nature, there exists a paucity of solid-state NMR characterisation regarding oximes, with only some limited $^{15}N/^{13}C$ CP MAS studies of Beckmann rearrangements (oxime to amide conversion) on solid-state catalysts having been reported.(257,258) To the best of my knowledge, there are currently no published reports utilising fast spinning ^1H – ^1H DQ/SQ MAS methods for oxime containing compounds. The work presented in this section is therefore novel in this respect.

From the structures presented in Fig. 6.8, it is obvious that these two compounds have different hydrogen bonding capacities. As such, it may be expected that their respective ^1H DQ/SQ MAS spectra will reveal significant differences. Figs. 6.9 and 6.10 present ^1H – ^1H DQ/SQ MAS and ^{14}N – ^1H HMQC spectra for **6-3a** and **6-3b**, respectively (observed DQ correlations are listed in Table 6.3 and 6.4, respectively).

Despite the broad nature of the ^1H – ^1H DQ/SQ MAS spectrum of **6-3a**, presented in Fig. 6.9c, it is still possible to resolve several cross-peaks and with the aid of the ^{14}N – ^1H HMQC spectrum, presented in

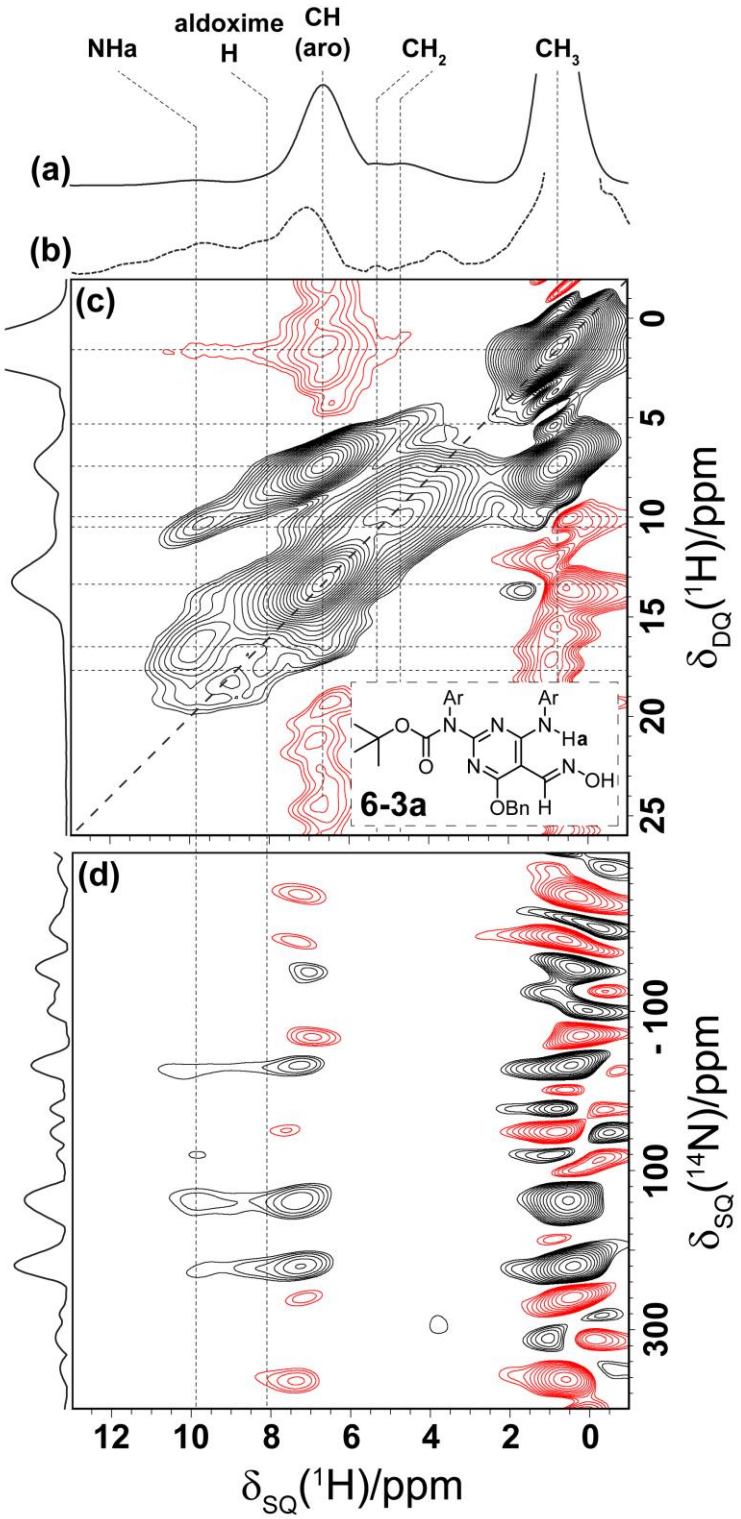

Figure 6.9 For **6.3a**, (a, c) 1D ^{1}H (ω_0 = 600 MHz) DQ-filtered, i.e., t_1 = 0, and 2D ^{1}H – ^{1}H (ω_0 = 600 MHz) DQ/SQ MAS spectra, (b, d) 1D HMQC filtered and 2D ^{14}N – ^{1}H (ω_0 = 600 MHz) HMQC spectra, using R^3 recoupling of the ^{14}N – ^{1}H heteronuclear dipolar couplings, with a τ_{RCPL} = 130 μs. All experiments were recorded at 60 kHz MAS. For (c), 32 transients were recorded for each of 128 t_1 FIDs. For (d), 32 transients were recorded for each of 80 t_1 FIDs. In each case, the recycle delay was 2 seconds. The 1D spectra correspond to the first row of the respective 2D spectra. The base contour level is at (c) 1 and (d) 75% of the maximum peak height.

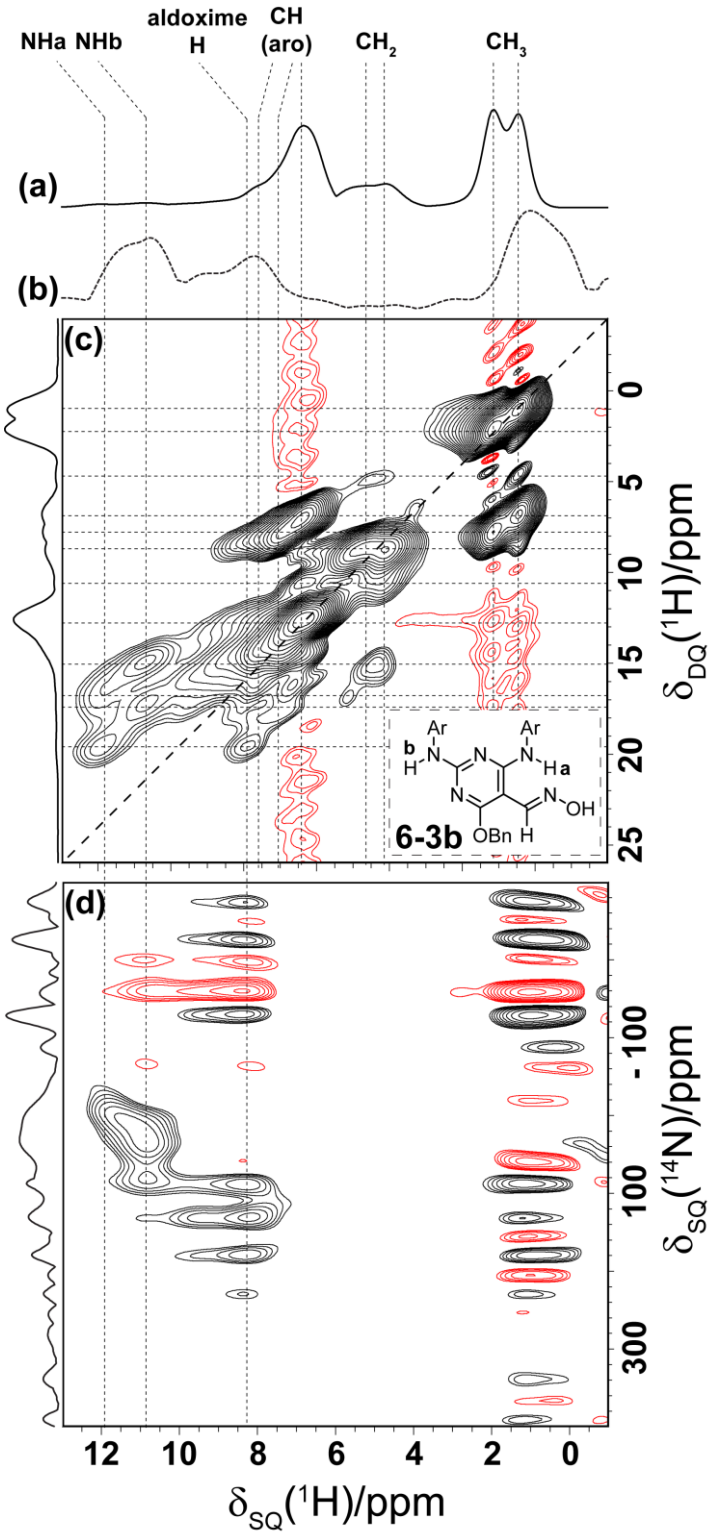

Figure 6.10 For **6-3b**, (a, c) 1D ^{1}H (ω_0 = 600 MHz) DQ-filtered, i.e., t_1 = 0, and 2D ^{1}H – ^{1}H (ω_0 = 600 MHz) DQ/SQ MAS spectra, (b, d) 1D HMQC filtered and 2D ^{14}N – ^{1}H (ω_0 = 600 MHz) HMQC spectra, using R^3 recoupling of the ^{14}N – ^{1}H heteronuclear dipolar couplings, with a τ_{RCPL} = 130 μs. All experiments were recorded at 60 kHz MAS. For (c), 16 transients were recorded for each of 128 t_1 FIDs. For (d), 16 transients were recorded for each of 64 t_1 FIDs. In each case, the recycle delay was 12 seconds. The 1D spectra correspond to the first row of the respective 2D spectra. The base contour level is at (c) 3.5 and (d) 62% of the maximum peak height.

Fig. 6.9d, assign the NHa and vinylic aldoxime proton at δ_{SQ} = 9.7 and 8.0 ppm, respectively. As was seen for the aldehyde derivatives **6-1** and **6-2**, in section 6.3.1, a cross-peak is observed at δ_{DQ} = 8.0 + 9.7 = 17.7 ppm for **6-3a**, consistent with a dipolar coupling between the NHa and oxime protons.

These peaks are consistent with a dimeric arrangement similar to that postulated for **6-2** in Fig. 6.6, meaning that the NH – oxime ^{1}H DQ cross-peaks result from an intermolecular proximity. This is a sound hypothesis if it is assumed that the NH proton forms an intramolecular hydrogen bond with the nitrogen atom contained within the oxime functionality (similar to the one formed between the NHa proton and the aldehyde carbonyl oxygen for **6-1** and **6-2**). The rest of the spectrum is unremarkable and pertains to aromatic, benzylic and methyl group proton environments.

However, comparison of, in particular, the ^{1}H chemical shift position of the NHa proton (9.7 ppm for **6-3a**) with the corresponding environment in **6-3b**, and indeed **6-1**, in which this resonance is observed at δ_{SQ} = 11.9 and 11.1 ppm, respectively, is suggestive of a change in the environment about this proton. When the NHa shift for **6-3a** is compared to that of **6-2**, both of which are BOC protected, the difference is not as acute, δ_{SQ} = 9.7 and 10.3 ppm for **6-3a** and **6-2**, respectively. This suggests that the BOC group has some influence on the strength of the intramolecular NHa – oxime (or aldehyde for **6-2**) hydrogen bond, which is to be expected since this protecting group removes the possibility of the hydrogen bonded dimer interface presented schematically in Fig. 6.4. Hence, the removal of two intermolecular NHb hydrogen bonding interactions evidently has a significant influence upon the solid-state packing arrangement for **6-3a** (and **6-2**).

In the case of **6-3b**, a ^{1}H – ^{1}H DQ/SQ MAS spectrum (presented in Fig. 6.10c) reveals several important features. The first is the absence of an auto-peak at δ_{DQ} = 10.7 + 10.7 = 21.3 ppm, with such a peak being indicative of an intermolecular contact across the dimeric hydrogen bonding interface. This potentially suggests a different mode of self-assembly. However, this would be surprising since other conceivable hydrogen bonding arrangements are likely prohibited by the three aromatic moieties in **6-3b**. However, this being said the observed splitting of the methyl resonance (δ_{SQ} = 0.5 and 1.2 ppm) perhaps points to a different spatial arrangement of the *t*-butyl groups bonded to the aromatic moieties, i.e., a potential bond rotation such as was postulated for **6-2** (Fig. 6.7). Alternatively, it could indicate Z' being equal to two. However, since no splitting was observed in any other compound reported in this chapter, and assuming **6-3b** shares a common mode of assembly with aldehyde dimer **6-1**, this is probably unlikely. Finally, this enhanced resolution in the methyl resonances could indicate a higher level of periodicity in the packing arrangement of **6-3b**. In the absence of any crystallographic data for this series of compounds it is difficult to arrive at firm conclusions.

The ^{1}H chemical shift of the oxime OH proton in both **6-3a** and **6-3b** is expected to overlap with the aromatic signals, based upon the assigned ^{1}H solution-state spectra, presented in Fig. 6.11. This indicates that the OH proton is not involved in hydrogen bonding interactions in either compound,

which is expected on the basis that alternative (i.e., those not already discussed) hydrogen bond acceptors are not expected to be available due to the steric considerations of the various aromatic groups within these systems. Given that, in the case of **6-3a**, the solid-state and solution-state ^{1}H chemical shifts show relatively good agreement, particularly for the NHa and vinylic oxime proton environments, it is likely that **6-3a** exists in solution as an isolated molecule (with the NH forming an intramolecular hydrogen bond with the oxime nitrogen) and in the solid state as a weakly associated dimer (analogous to **6-2** in Fig. 6.6) since crystal packing forces individual molecules into close spatial proximity in the solid phase. For **6-3b**, there is a significant disparity between the solution and solid-state ^{1}H chemical shifts of the NHb proton (the proton postulated to form an intermolecular NH ⋯ N hydrogen bond in the solid state, as was the case for **6-1** in Fig. 6.4), which appears at δ_{SQ} = 6.8 ppm and δ_{SQ} = 10.7 ppm in the solution and solid-state ^{1}H NMR spectra, respectively (see Fig. 6.12). This is expected on the basis that this weak intermolecular hydrogen bonded dimer is not expected to form in solution. In addition, for the intramolecular hydrogen bonded NHa, a difference between solution and solid-state chemical shifts is also observed for **6-3b**, δ_{SQ} = 9.9 ppm and δ_{SQ} = 11.8 ppm, respectively, as a further result of intermolecular interactions in the solid state. The fact that a change between solution and solid-state chemical shifts for this proton environment was observed in **6-3b** and not **6-3a** is, in addition to the dramatic differences observed for these two compounds in the respective ^{1}H DQ MAS spectra, indicative of a significant difference in the solid-state packing engendered by the presence of the BOC protecting group in these systems.

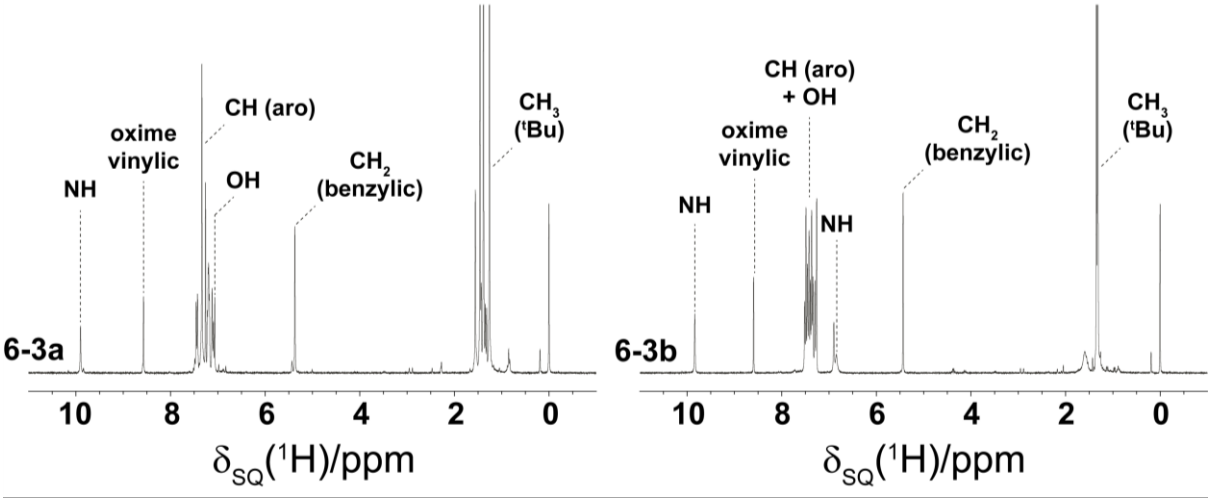

Figure 6.11 ^{1}H (ω_0 = 300 MHz) one-pulse solution-state ($CDCl_3$) spectra for **6-3a** (left) and **6-3b** (right), respectively. General assignments are provided: note that for **6-3b**, which is not BOC protected, an extra NH signal is observed at δ_{SQ} = 6.85 ppm, whilst only two methyl signals are observed (three observed for **6-3a**). 16 transients were coadded with a recycle delay of 1 second in each case. In each spectrum, the methyl signals are truncated at approximately 36% of their maximum height.

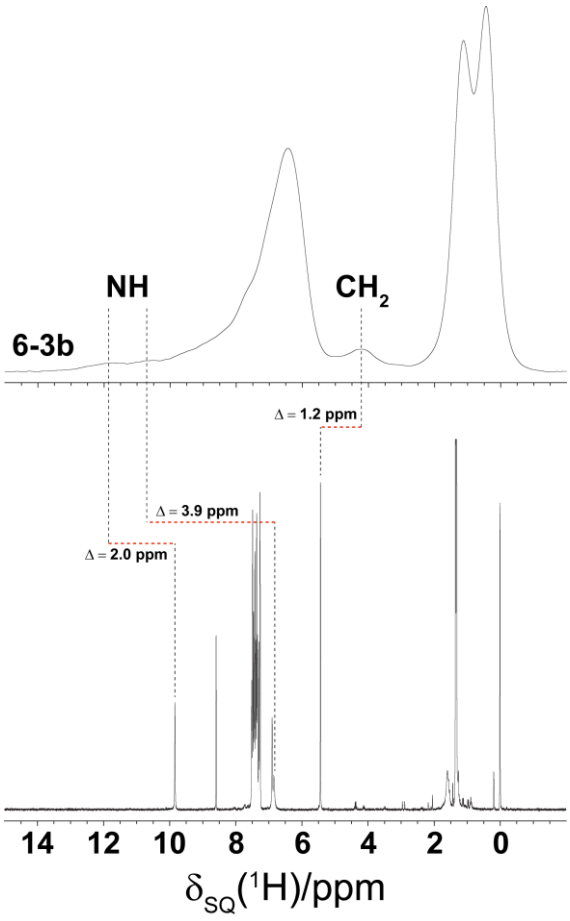

Figure 6.12 Comparison of (top) solid-state (60 kHz MAS), and (bottom) solution-state ^{1}H (ω_0 = 600 and 300 MHz, respectively) one-pulse spectra of **6-3b**. Significant differences in ^{1}H chemical shift (dashed red line) are observed in the two phases, particularly for the two NH protons and the benzylic CH_2 environments, as a result of intermolecular interactions and crystal packing in the solid state. Note that for **6-3a**, there is little variation between solid and solution-state chemical shifts for all proton environments.

Table 6.3 DQ correlations extracted from the ^{1}H – ^{1}H DQ/SQ MAS spectrum of **6-3a** in Fig. 6.9c.

6-3a	#	Correlation	$\delta_{SQ}(1) + \delta_{SQ}(2)$ / ppm	δ_{DQ} / ppm
	1	$CH_3 – CH_3$	0.7 + 0.7	1.4
	2	$CH_3 – CH_2$	0.7 + 4.6	5.3
	3	CH_3 – CH (aro)	0.7 + 6.6	7.3
	4	$CH_2 – CH_2$	4.6 + 5.2	9.8
	5	CH_3 – NHa	0.7 + 9.6	10.3
	6	CH (aro) – CH (aro)	6.6 + 6.6	13.2
	7	CH (aro) – NHa	6.6 + 9.6	16.2
	8	aldoxime H – NHa	8.0 + 9.6	17.2

Table 6.4 DQ correlations extracted from the $^{1}H - {}^{1}H$ DQ/SQ MAS spectrum of **6-3b** in Fig. 6.10c.

6-3b	#	Correlation	$\delta_{SQ}(1) + \delta_{SQ}(2)$ / ppm	δ_{DQ} / ppm
	1	$CH_3 - CH_3$	0.5 + 0.5	1.0
	2	$CH_3 - CH_3$	1.1 + 1.1	2.2
	3	$CH_3 - CH_2$	0.5 + 4.1	4.6
	4	CH_3 – CH (aro)	0.5 + 6.3	6.8
	5	CH_3 – CH (aro)	1.1 + 6.9	8.0
	6	$CH_2 - CH_2$	4.1 + 4.9	9.0
	7	CH_2 – CH (aro)	4.1 + 6.3	10.4
	8	CH (aro) – CH (aro)	6.3 + 6.3	12.6
	9	CH_2 – NHb	4.1 + 10.7	14.8
	10	CH_2 – NHa	4.9 + 11.9	16.8
	11	CH (aro) – NHb	7.0 + 10.7	17.7
	12	aldoxime H – NHa	8.0 + 11.9	19.9

6.3.3 Nitrile precursors: **6-4** and **6-5**

For compounds **6-1**, **6-2** (section 6.3.1) and **6-3a**, **6-3b** (section 6.3.2), an intramolecular hydrogen bond is expected to form, on the basis of the ^{1}H chemical shifts, between the NHa proton and the aldehyde oxygen (**6-1**, **6-2**) and oxime nitrogen (**6-3a**, **6-3b**), respectively. In compound **6-4**, in which the oxime is converted into the nitrile (the NHa proton and the nitrile nitrogen do not sit within hydrogen bonding distance, given the expected linear nature of the nitrile functionality), and in **6-5** where the NHa proton is replaced by an amide functional group (in preparation for the ring closure reaction, **6-5** to **6-6**), this intramolecular interaction is no longer a possibility. As a result, the observed $^{1}H - {}^{1}H$ (600 MHz) DQ/SQ MAS spectra of **6-4** and **6-5**, presented in Fig. 6.13 and 6.14, respectively, are markedly different when compared to the DQ spectra already presented in this chapter. Specifically, these differences are manifested as changes in the respective ^{1}H chemical shifts which are observed at ~8.0 ppm and below, for **6-4** and **6-5**, reflecting the reduced capacity of these molecules to form strong hydrogen bonding interactions.

In the case of both **6-4** and **6-5**, assignment of the various ^{1}H chemical shifts of the NH protons is only possible by means of the respective $^{14}N - {}^{1}H$ HMQC spectra, recorded at a short recoupling time (τ_{RCPL} = 130 μs) and presented in Figs. 6.13d and 6.14d for **6-4** and **6-5**, respectively. This is due to the fact that, in the absence of strong hydrogen bonding interactions, such protons are observed in the aromatic

region of the spectrum, hence making accurate assignment based only upon the $^{1}H - {}^{1}H$ DQ spectra alone impossible.

Interestingly, for **6-4**, the ^{14}N shift of the Na nitrogen, i.e., the nitrogen directly bonded to the NHa proton (see Fig. 6.13d), is revealing if it is compared to the ^{14}N shift of this same nitrogen environment in **6-2** (Fig. 6.5d). In **6-2** this nitrogen is observed at approximately −90 ppm, whereas for **6-4** it is observed at 55 ppm. This is a large difference in shift (~ 150 ppm) and is indicative of a significant change in environment for this nitrogen site, i.e., loss of an intramolecular hydrogen bonding interaction in **6-4**, when compared to **6-2**.

For **6-5**, the presence of the amide moiety bonded to this same Na nitrogen complicates analysis for this molecule. By analysing the $^{1}H - {}^{1}H$ DQ/SQ MAS (Fig. 6.14c) and $^{14}N - {}^{1}H$ HMQC (Fig. 6.14d) spectra together, it can be seen that the two NH_2 protons are observed at ^{1}H chemical shifts of δ_{SQ} = 3.7 and 8.1 ppm. This difference in ^{1}H chemical shift between the two NH protons leads to the suggestion of a weakly hydrogen bonded dimer interacting *via* the amide moiety, as presented in Fig. 6.15a. However, the absence of an NH – NH auto-peak (expected at δ_{DQ} = 8.1 + 8.1 = 16.2 ppm) seems to speak against such a dimeric arrangement. Since such an arrangement in the same plane would likely bring the amide oxygen lone pair into close spatial proximity with the nitrile CN triple bond, it is likely that such an arrangement would cause a rotation of the N(a) – C bond (see Fig. 6.15a), thus forcing the amide moiety out of the plane of the molecule. However, an alternative explanation for the observed NH_2 ^{1}H chemical shifts could be an intramolecularly hydrogen bonded species, as presented in Fig. 6.15b. However, it is not clear whether or not the bulky aromatic and nitrile moieties could sit in such close spatial proximity. It would however explain why no cross-peak is observed between the NH proton (3.7 ppm) and a nearby aromatic proton in the $^{1}H - {}^{1}H$ DQ/SQ MAS spectra of **6-5** (see Fig. 6.14c). Note that the intramolecular species presented in Fig. 6.15b requires that the amide carbonyl C – N bond be rotated, thus explaining the absence of the aforementioned aromatic CH – HN cross-peak in the $^{1}H - {}^{1}H$ DQ/SQ MAS spectrum of **6-5**, presented in Fig. 6.14c.

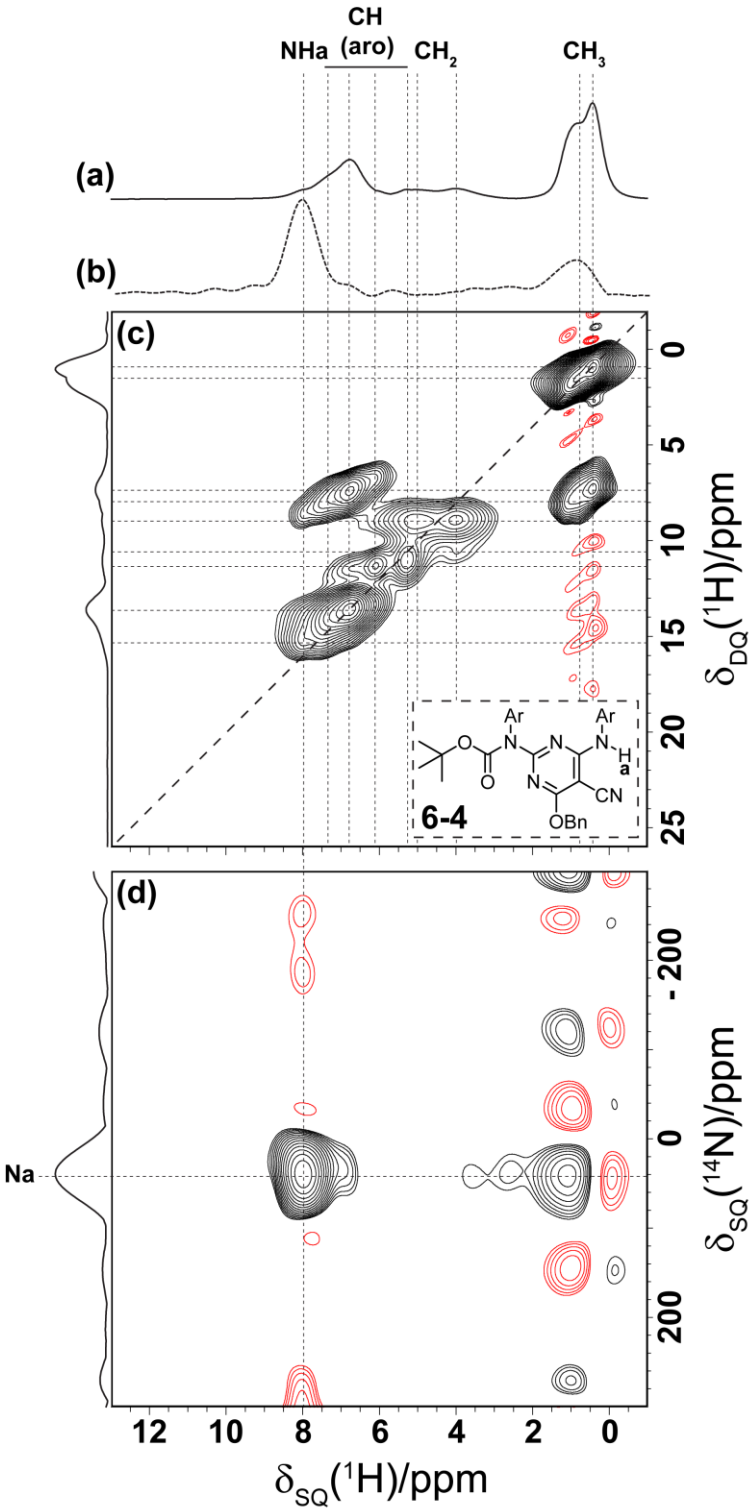

Figure 6.13 For **6-4** (a, c) 1D ^{1}H (ω_0 = 600 MHz) DQ-filtered, i.e., t_1 = 0, and 2D ^{1}H – ^{1}H (ω_0 = 600 MHz) spectra, (b, d) 1D HMQC filtered and 2D ^{14}N – ^{1}H (ω_0 = 600 MHz) HMQC spectra, using R^3 recoupling of the ^{14}N – ^{1}H heteronuclear dipolar couplings, with a τ_{RCPL} = 130 μs. All experiments were recorded at 60 kHz MAS. For (c), 16 transients were recorded for each of 128 t_1 FIDs. For (d), 16 transients were recorded for each of 32 t_1 FIDs. In each case, the recycle delay was 2 seconds. The 1D spectra correspond to the first row of the respective 2D spectra. The base contour level is at (c) 9, and (d) 39% of the maximum peak height.

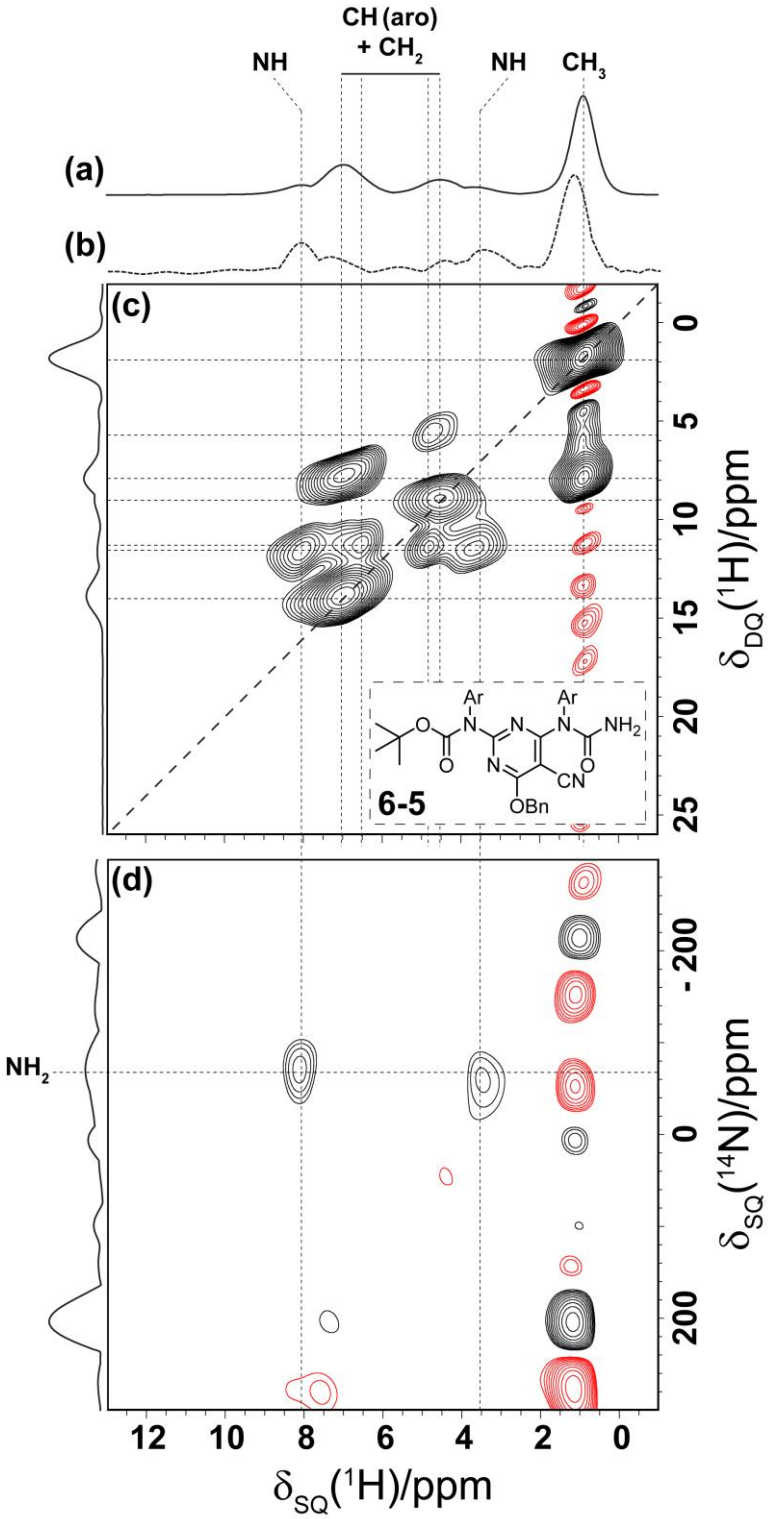

Figure 6.14 For **6-5** (a, c) 1D ^{1}H (ω_0 = 600 MHz) DQ-filtered, i.e., t_1 = 0, and 2D ^{1}H – ^{1}H (ω_0 = 600 MHz) spectra, (b, d) 1D HMQC filtered and 2D ^{14}N – ^{1}H (ω_0 = 600 MHz) HMQC spectra, using R^3 recoupling of the ^{14}N – ^{1}H heteronuclear dipolar couplings, with a τ_{RCPL} = 130 μs. All experiments were recorded at 60 kHz MAS. For (c), 16 transients were recorded for each of 128 t_1 FIDs. For (d), 16 transients were recorded for each of 32 t_1 FIDs. In each case, the recycle delay was 2 seconds. The 1D spectra correspond to the first row of the respective 2D spectra. The base contour level is at (c) 5, and (d) 80% of the maximum peak height.

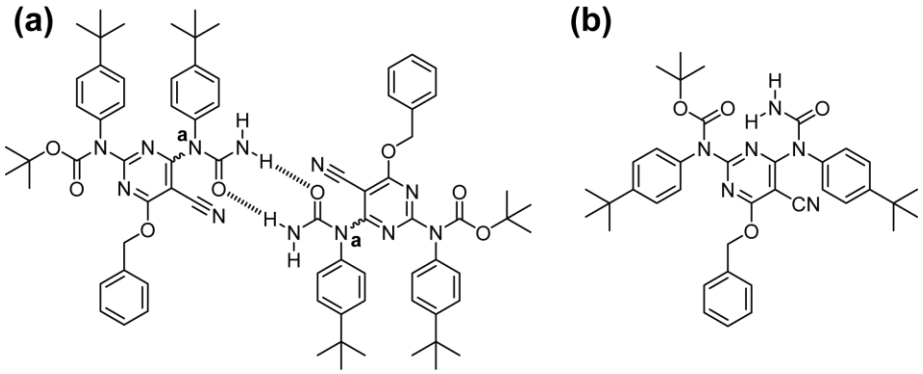

Figure 6.15 Schematic representation of: (a) a hypothesised weak hydrogen bonded dimer for **6-5** interacting *via* the amide and (b) a potential intramolecularly bonded species. The wiggly lines in (a) indicate a potential CN bond rotation. Note that in (b) the other aryl moiety may also rotate to avoid unfavourable steric interference.

Table 6.5 DQ correlations extracted from the $^{1}H - {}^{1}H$ DQ/SQ MAS spectrum of **6-4** in Fig. 6.13c.

6-4	#	Correlation	$\delta_{SQ}(1) + \delta_{SQ}(2)$ / ppm	δ_{DQ} / ppm
	1	$CH_3 - CH_3$	0.4 + 0.4	0.8
	2	$CH_3 - CH_3$	0.7 + 0.7	1.4
	3	CH_3 – CH (aro)	0.4 + 6.8	7.2
	4	CH_3 – CH (aro)	0.7 + 7.3	8.0
	5	$CH_2 - CH_2$	4.0 + 5.0	9.0
	6	CH_2 – CH (aro)	4.0 + 6.8	10.8
	7	CH_2 – CH (aro)	5.0 + 6.1	11.1
	8	CH (aro) – CH (aro)	6.8 + 6.8	13.6
	9	CH (aro) – NHa	7.3 + 8.0	15.2

Table 6.6 DQ correlations extracted from the $^{1}H - {}^{1}H$ DQ/SQ MAS spectrum of **6-5** in Fig. 6.14c.

6-5	#	Correlation	$\delta_{SQ}(1) + \delta_{SQ}(2)$ / ppm	δ_{DQ} / ppm
	1	$CH_3 - CH_3$	0.9 + 0.9	1.8
	2	$CH_3 - CH_2$	0.9 + 4.8	5.7
	3	CH_3 – CH (aro)	0.9 + 7.0	7.9
	4	$CH_2 - CH_2$	4.3 + 4.8	9.1
	5	CH_2 – CH (aro)	4.8 + 6.5	11.3
	6	NH – NH	3.7 + 8.1	11.8
	7	CH (aro) – CH (aro)	7.0 + 7.0	14.0

6.3.4 $^{1}H - {}^{1}H$ DQ/SQ MAS spectrum of **6-6**

The ring closure reaction (**6-5** to **6-6**) yields a cytosine-like hydrogen bond motif (AAD), as presented in Fig. 6.16. Due to a lack of alternative donor/acceptor groups in **6-6**, a dimeric arrangement is expected with two molecules of **6-6** interacting through this AAD interface (see Fig. 6.16). The observed cross-peaks in the $^{1}H - {}^{1}H$ (600 MHz) DQ/SQ MAS (55 kHz) spectrum of **6-6**, presented in Fig. 6.17, are consistent with such a self-assembled structure.

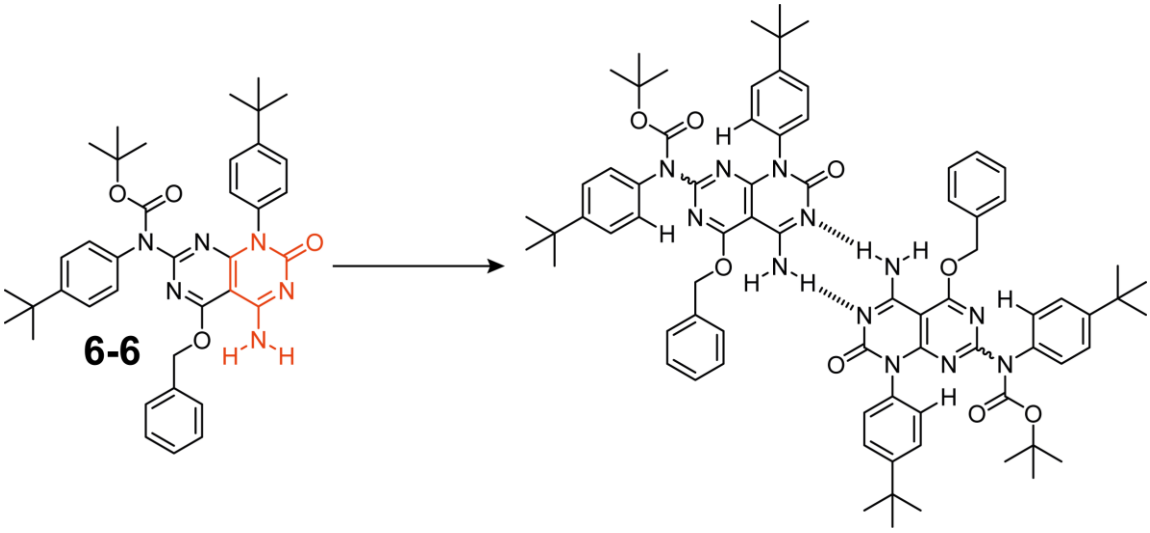

Figure 6.16 Schematic representation of the proposed hydrogen bonded dimer for **6-6**. The cytosine-like moiety is highlighted in red. The wiggly lines represent a possible CN bond rotation.

The high abundance of methyl group protons in **6-6** leads to the appearance of three distinct auto-peaks in the ^{1}H DQ MAS spectrum (Fig. 6.17), at δ_{DQ} = 0.7 + 0.7 = 1.4, 1.3 + 1.3 = 2.6, and 1.8 + 1.8 = 3.6 ppm, respectively. The appearance of these peaks is consistent with a rotation about the CN bond highlighted in Fig. 6.16 (wiggly lines), in which the bulky aromatic groups are rotated away from one another to reduce steric tension in **6-6** (as shown in Fig. 6.16). Indeed, this is a common feature in all BOC protected compounds reported thus far in this chapter. It is perhaps possible that such a rotation allows for a weak C=O ⋯ H – C interaction to occur, between the carbonyl oxygen on the BOC group and the adjacent aromatic moiety, in addition to a N ⋯ H – C interaction (see Fig. 6.16), which may act to stabilise such a conformation, in addition to moving the carbonyl oxygen on the BOC group away from the electron lone pair on the nearby heterocyclic nitrogen. Such a conformation is consistent with three distinct methyl environments observed in the ^{1}H MAS NMR data.

Such a high abundance of methyl groups in **6-6** leads to cross-peaks with the nearby aromatic protons, with cross-peaks being observed at δ_{DQ} = 0.7 + 6.4 = 7.1, 1.3 + 7.1 = 8.4, and 1.8 + 7.5 = 9.3 ppm. These interactions are expected based upon the molecular structure, since these environments are locked in close spatial proximity *via* covalent bonds. Interestingly, a proximity between methyl protons and

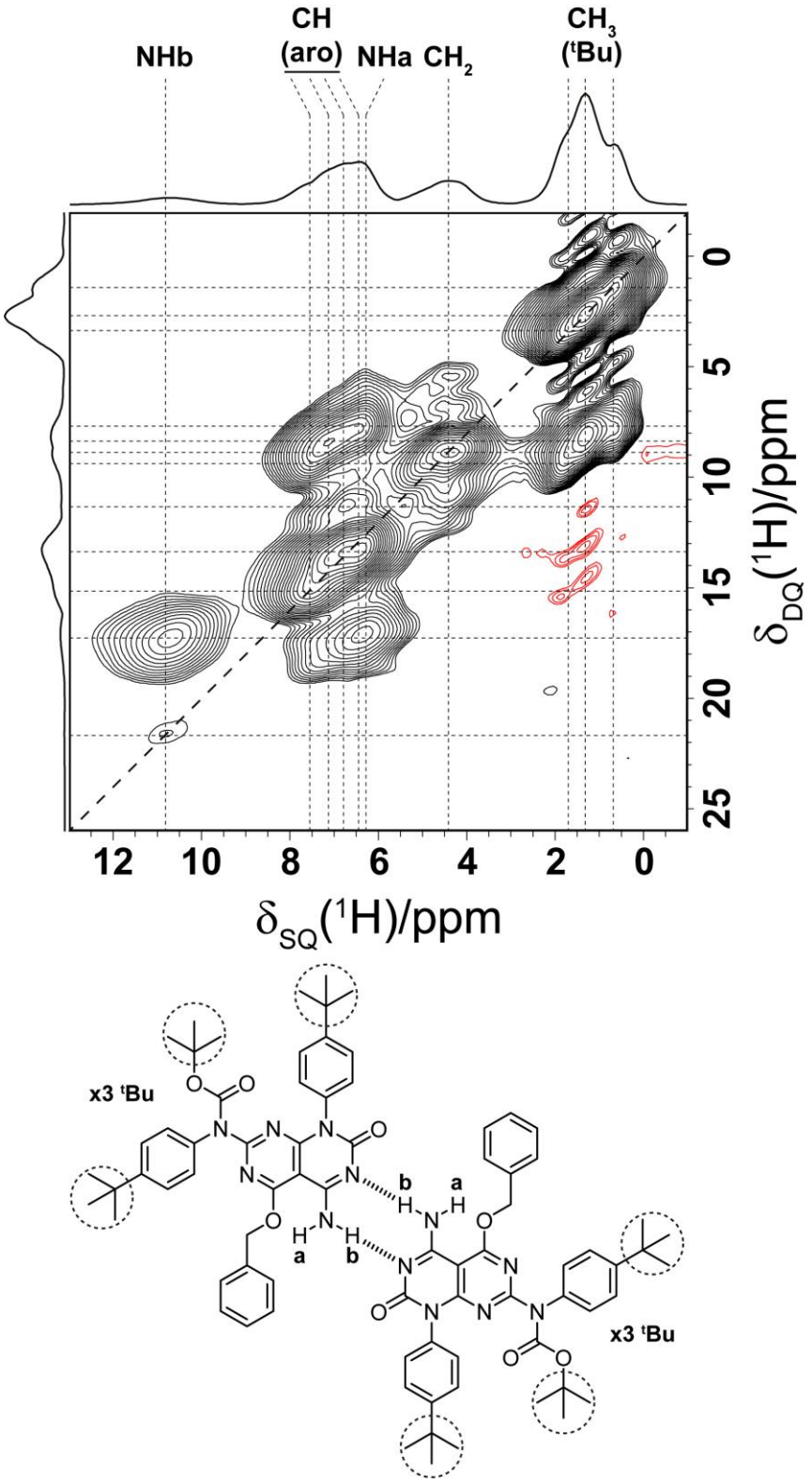

Figure 6.17 $^{1}H - {}^{1}H$ (ω_0 = 600 MHz) DQ/SQ MAS (55 kHz) spectrum of **6-6**, alongside skyline projections and a schematic representation of the proposed hydrogen bonded dimer. One rotor period of BABA recoupling was used for the excitation and reconversion of DQ coherence. For each of 256 t_1 FIDs, 64 transients were coadded with a recycle delay of 3 seconds. The $F_1 = 2F_2$ diagonal is indicated as a dashed black line, with DQ correlations highlighted via solid horizontal lines. The base contour level is shown at 1% of the maximum peak intensity.

benzylic CH_2 protons is also apparent, as evidenced by an observed cross-peak at $\delta_{DQ} = 0.7 + 4.4 = 5.1$ ppm. Such a proximity between these proton environments is not possible within an individual molecule of **6-6** and so must indicate an intermolecular interaction, that is consistent with a packing arrangement of dimers in the solid state. However, based on the data presented in Fig. 6.17, it is impossible to speculate further on the form this packing takes.

The presence of an NH_2 moiety in **6-6** leads to a strong cross-peak at $\delta_{DQ} = 6.3 + 10.8 = 17.1$ ppm, with such interactions leading to intense peaks due to the close spatial proximity (typically ~ 1.5 Å). The NHb proton (10.8 ppm) interacts with itself, as evidenced by a weak auto-peak observed at $\delta_{DQ} = 10.8 + 10.8 = 21.6$ ppm. This is consistent with an intermolecular dipolar coupling across the dimeric hydrogen bonding interface (see the hydrogen bonding structure in Fig. 6.17). As was observed in previous chapters, the dipolar coupling associated with this intermolecular interaction is truncated by the strong NH_2 intramolecular interaction. Based upon the structure of **6-6**, NHa (6.3 ppm) is expected to form an intramolecular hydrogen bonding arrangement with the benzylic oxygen. However, this interaction is expected to be weak (as expected from the low observed ^1H chemical shift of NHa) since aryl ethers are typically poor hydrogen bond acceptors.(259)

Table 6.7 DQ correlations extracted from the $^1H - ^1H$ DQ/SQ MAS spectrum of **6-6** in Fig. 6.17.

6-6	#	Correlation	$\delta_{SQ}(1) + \delta_{SQ}(2)$ / ppm	δ_{DQ} / ppm
	1	$CH_3 - CH_3$	0.7 + 0.7	1.4
	2	$CH_3 - CH_3$	1.3 + 1.3	2.6
	3	$CH_3 - CH_3$	1.8 + 1.8	3.6
	4	$CH_3 - CH_2$	0.7 + 4.4	5.1
	5	CH_3 – CH (aro)	0.7 + 6.5	7.2
	6	CH_3 – CH (aro)	1.3 + 7.1	8.4
	7	$CH_2 - CH_2$	4.4 + 4.4	8.8
	8	CH_3 – CH (aro)	1.8 + 7.6	9.4
	9	CH_2 – CH (aro)	4.4 + 6.7	11.1
	10	CH (aro) – CH (aro)	6.5 + 6.7	13.2
	11	CH (aro) – CH (aro)	7.5 + 7.5	15.0
	12	NHa – NHb	6.4 + 10.8	17.2
	13	NHb – NHb	10.8 + 10.8	21.6

6.3.5 Synthetic challenges and compound **6-7**

Resynthesis of the amide compound **6-5** (i.e., the conversion of **6-4** to **6-5**) proved to be a significant challenge. The original reaction procedure is simple and requires that a solution of chlorocarbonyl isocyanate is added to **6-4** in dichloromethane under an atmosphere of nitrogen. However, since chlorocarbonyl isocyanate has been discontinued, the use of a related reagent, chlorosulfonyl isocyanate, was investigated. Both of these compounds are incredibly dangerous to use, noting in particular the violent reaction that ensues on contact with water. In addition, both compounds are toxic and corrosive and require storage in polyethylene bottles. After consideration, it was decided that it was not possible to complete the reaction under such conditions. As such, it was not possible to resynthesize **6-5** (and subsequently **6-6**) in sufficient quantities so as to complete the synthetic pathway outlined in Fig. 6.1, i.e., synthesis of **6-7** was not possible prior to completion of this thesis. Alternative synthetic methods must therefore be investigated.

All isocyanates are highly toxic in addition to being sensitizers. Chlorosulfonyl isocyanate is particularly hazardous since it is synthesised by bubbling sulfur trioxide through cyanogen chloride as follows:

$$SO_3 + CNCl \rightarrow CNClO_3S$$

Hence any purchased solution of chlorosulfonyl isocyanate is expected to contain trace amounts of both of these reagents. Sulfur trioxide is corrosive and reacts violently with water to produce sulfuric acid. However, cyanogen chloride represents the biggest hazard, since it is a highly toxic blood agent with potential chemical warfare applications. Importantly, cyanogen chloride is thought to be capable of passing through the filters on commercially available gas masks. However, other related isocyanates, whilst also toxic, are easier to handle since they are not manufactured from, or expected to decompose into, cyanogen chloride. Hence other groups have used trichloroacetyl isocyanate to perform this reaction.(260) Trichloroacetyl isocyanate is expected to have a similar reactivity to both chlorocarbonyl and chlorosulfonyl isocyanate. There are several related isocyanates which may also be investigated moving forward.

In recent work published by Fenniri *et al*. (260) an alternative synthetic procedure was performed for the ring closure reaction (**6-5** to **6-6**), in which 7N NH_3/MeOH was used to good effect as opposed to the use of trimethylsilyl trifluoromethanesulfonate and dichloromethane. The latter reagents require that the reaction be performed at – 78°C, hence the use of the 7N NH_3/MeOH is also worth investigating.

Compound **6-7** is an interesting molecule, since it is thought to form hexameric rosette type structures in solution.(105) However, the solid-state aggregation of such molecules is largely unknown with the aforementioned work by Fenniri and co-workers one of only a select few reports in the literature, and the only high-resolution ^{1}H MAS NMR study to date. The situation is particularly complex since fully resolved crystal structures of such materials are rare, owing to the inherent disorder present in the

alkyl/aryl sidechains of these compounds. Therefore, looking forward, synthesis and analysis of this compound is important.

6.4 Summary

This chapter has demonstrated that, in the absence of single crystal X-ray diffraction data, conclusions regarding the solid-state packing can still be made using high-resolution ^{1}H MAS NMR techniques. Combining the ^{1}H – ^{1}H DQ/SQ MAS experiment, which has an excellent ability to elucidate hydrogen bonding motifs in small organic molecules, with heteronuclear methods such as the ^{14}N – ^{1}H HMQC (and ^{1}H – ^{13}C INEPT experiment for **6-1**), allows for a robust assignment of ^{1}H chemical shifts. This was shown to be particularly useful in the case of compounds **6-4** and **6-5** which lacked the high ppm resonances often associated with hydrogen bonded protons (i.e., the NH environments that were observed at or above 10 ppm in **6-1**, **6-2**, **6-3a/b** and **6-6**), with the NH resonances being observed in the aromatic region of the spectrum. In addition, this chapter represents one of only a handful of solid-state NMR characterisation studies of aldehyde containing molecules, and the first such characterisation of aldoxime containing materials. Expanding the database of characterised organic functional groups by solid-state NMR is highly valuable, and may serve to make such techniques more amenable to the larger synthetic field in the future.

Some of the challenges involved in the later stages of the synthetic pathway were also discussed. Moving forward, the use of less hazardous isocyanate compounds needs to be investigated thereby allowing for the synthesis of sufficient quantities of **6-7** for ^{1}H MAS NMR analysis.

Chapter 7 : The use of a selective saturation pulse to suppress t_1 noise in two-dimensional ^{1}H fast MAS solid-state NMR spectroscopy

7.1 Introduction

A common structural theme in the compounds discussed in this thesis is the high abundance of methyl and alkyl protons contained within individual molecules. In two-dimensional ^{1}H MAS spectra, such proton environments generate strong NMR signals and as a result can lead to excessive t_1 noise in the indirect dimension of a given spectrum. This noise manifests itself as long trails emanating from the resonance in question and, in some cases, considerably detracts from the appearance and viewability of such spectra. This phenomenon has also previously been observed for nucleic acid derivatives studied by Webber *et al*.(100) The work in this chapter is adapted from a 2015 publication by Robertson *et al*.(163) Note that a comprehensive discussion of the solid-state packing of **7-1** was presented in chapter 5 (where the molecule is denoted **5-1**).

Problems arising from t_1 noise are frequently encountered in solution-state NMR, often as a result of residual proton signal from deuterated solvents where it is known that the t_1 noise is proportional to the signal strength.(261) Several processing algorithms for the removal of this noise have been presented, such as Reference Deconvolution,(262) the Cadzow procedure,(263) and Correlated Trace Denoising.(264) From an experimental perspective, long, weak *rf* pulses, or selective pulse schemes such as DANTE,(265,266) can be applied to saturate the offending alkyl signals,(267) often in combination with pulsed field gradients (PFG), e.g. WATERGATE (WATER suppression by GrAdient-Tailored Excitation).(268) In solid-state NMR, related methods have been presented for the suppression of the water peak in ^{1}H MAS NMR of biological solids.(269-272)

Consider the challenge of suppressing t_1 noise due to alkyl side chain resonances, i.e., the case where the nuclear spins that are to be saturated are contained within the same spin system as those that are of interest. Fischbach *et al*. using a specially adapted PFG MAS probe head, demonstrated the applicability of the WATERGATE and DANTE based sequences for selectively exciting and suppressing alkyl side chain resonances, applying these techniques to the ^{1}H – ^{1}H DQ/SQ MAS experiment.(273) However, the requirement for specially adapted probe heads means that there has been a low uptake of this method; hence there is a motivation to develop alternatives applicable with a standard MAS probe head. In the work that follows, it will be shown that a combination of slower ^{1}H spin diffusion and enhanced resolution at fast MAS frequencies allows for the use of a selective saturation pulse to suppress intense and unwanted signals, whilst having a minimal effect on the remaining resonances in the spectrum, specifically those of interest, i.e., those NH resonances which are essential for the hydrogen bonding structure of nucleobase analogues.

In this chapter, it will be demonstrated that by employing a simple selective pulse prior to the main pulse sequence, and in combination with fast MAS frequencies (> 60 kHz), it is possible to dramatically improve the appearance of two-dimensional homo- and heteronuclear experiments in the solid state by essentially eliminating or severely reducing the intensity of a strong perturbing signal and thus

minimising t_1 noise. The effectiveness of this method is demonstrated using the DNA base analogue 5-iodo-2'-deoxy-3',5'-di(triisopropylsilyl(TIPS))cytidine,(225) henceforth referred to as compound **7-1** ($C_{27}H_{52}IN_3O_4Si_2$); such pyrimidine (and purine) derivatives have manifold applications in the evolving area of molecular self-assembly.(226,274-282) The structure and one-pulse ^{1}H (700 MHz) MAS (70 kHz) spectrum of **7-1** is presented in Fig. 7.1, demonstrating the intensity of the methyl peak relative to the other resonances in the spectrum. Note the difference in intensity between the methyl peak at 1.1 ppm and the $NHb^{I/II}$ peaks at 10.7 and 11.3 ppm, respectively.

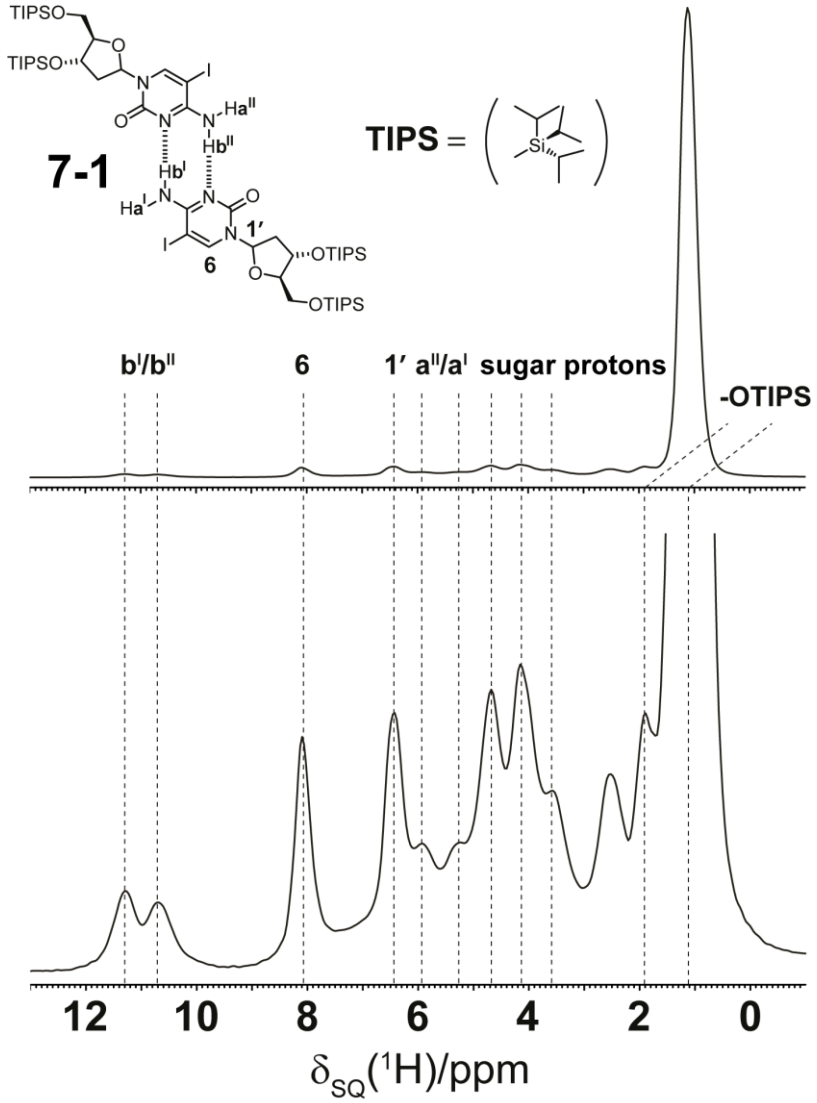

Figure 7.1 A ^{1}H (ω_0 = 700 MHz) MAS (70 kHz spinning) one-pulse spectrum of **7-1**. 4 transients were coadded with a recycle delay of 3 seconds. In the lower plot, the intense TIPS methyl resonance at 1.1 ppm has been truncated at approximately 8% of its full height. The spectrum is assigned according to the atomic labels given in the proposed structure.

Although there is no published crystal structure available for compound **7-1**, related structures are known to form hydrogen bonded dimers (see discussion of compound **5-2** in chapter 5). The existence of two crystallographically distinct molecules in the asymmetric unit cell (Z' = 2) is evidenced by the observation in the ^{1}H MAS NMR spectrum presented in Fig. 7.1 of four distinct resonances at 5.2, 5.9,

10.7 and 11.3 ppm corresponding to four distinct NH environments, NHa^{I}, NHa^{II}, NHb^{II} and NHb^{I} respectively. For **7-1**, the ^{1}H resonance corresponding to the methyl group protons at 1.1 ppm is approximately 36 times more intense (in terms of simple peak height) than the next most intense signal, namely that of the ribose sugar group protons at approximately 4.0 ppm. The key resonances, NHa^{I}/a^{II} and NHb^{I}/b^{II}, are over 100 times less intense when compared to the methyl peak height. In terms of integrated intensity, the combined NHb^{I}/b^{II} peak is 54 times weaker than the methyl resonance – note that the expected ratio is 42:1 given the relative numbers of protons in each environment. This deviation arises from the difficulty in assigning integrated intensity for overlapping ^{1}H resonances as well as the difference in T_1 relaxation times. The measured T_1 values, determined from a saturation recovery experiment, for the nitrogen bound protons and the methyl protons show a clear difference: 2.46 and 2.19 s for the NHb^{I} and NHb^{II} protons, respectively, and 0.93 s for the CH_3 resonance. In this context, it is noted that differences in hydrogen T_1 relaxation times under MAS have previously been observed in ^{2}H and ^{1}H studies.(283,284)

7.2 Experimental details

7.2.1 Sample preparation

The DNA base analogue 5-iodo-2'-deoxy-3',5'-di(triisopropylsilyl)cytidine **7-1** was prepared according to the methods outlined by Marsh *et al*. (225) **7-1** was packed into a 1 mm rotor.

7.2.2 Solid-state NMR experimental details

Solid-state NMR experiments were performed at 16.4 T on a JEOL solid-state NMR spectrometer (JEOL ECA700II) operating at a ^{1}H Larmor frequency of 700 MHz, equipped with a 1.0 mm double-resonance Ultrafast MAS probe (JEOL RESONANCE Inc., Tokyo, Japan). The rotor volume is ~ 0.8 μL corresponding to approximately 0.8 mg of **7-1**. Except for selective pulses, the ^{1}H $\pi/2$ pulse duration was 0.9 μs. Unless otherwise stated, selective pulses were of duration 30 ms with a nutation frequency of 725 Hz. A recycle delay of 3 s was used in all experiments. In all two-dimensional experiments, the States-TPPI method was used to achieve sign discrimination in F_1.

7.2.2.1 ^{1}H – ^{1}H DQ/SQ MAS experiments

Eight rotor periods of the BaBa-xy16 recoupling sequence ($90 - \tau - 90\ 90 - \tau - 90$, where $\tau = \tau_R/2 - 2 * (90°)_{\text{pulse length}}$) were used for the excitation and reconversion of DQ coherence. A four-step nested phase cycle [16(0), 16(180), 16(90), 16(270)] can be applied to the selective saturation pulse (there is no change in receiver phase given that the selective pulse is a saturation pulse and not an excitation pulse). A 16-step phase cycle was used to select $\Delta p = \pm 2$ (4-steps) [0, 90, 180, 270] on the BaBa-xy16 excitation block and $\Delta p = -1$ (4-steps) [4(0), 4(180), 4(90), 4(270)] on the *z*-filter $\pi/2$, where *p* is the coherence order. The receiver phase was [2(0, 180), 2(180, 0), 2(90, 270), 2(270, 90)]. For each

of 64 t_1 FIDs with a rotor-synchronised t_1 increment of 29 μs, 16 transients were coadded, corresponding to a total experimental time of 100 min.

7.2.2.2 ^{1}H – ^{1}H spin diffusion experiments

For each of 64 t_1 FIDs with a rotor synchronised t_1 increment of 29 μs, 2 transients were coadded, corresponding to a total experimental time of 12 min. A [0, 180] phase cycle was used to select a change in coherence order $\Delta p = \pm 1$ on the second π/2 pulse, with the receiver phase following, i.e., [0, 180].

7.2.2.3 ^{14}N – ^{1}H HMQC experiments

SR4 recoupling was used to reintroduce the heteronuclear ^{14}N – ^{1}H dipolar couplings, using a duration τ_{RCPL} = 171 μs. The ^{14}N pulse duration was 20 μs. A four-step nested phase cycle [8(0), 8(180), 8(90), 8(270)] was applied to the selective saturation pulse. For the ^{14}N excitation pulse, a two-step phase cycle [0, 180] was employed to select changes in coherence order $\Delta p = \pm 1$. For the ^{1}H π/2 pulse, the four-step phase cycle [2(0), 2(180), 2(90), 2(270)] was employed. The receiver phase was [0, 2(180), 0, 270, 2(90), 270].

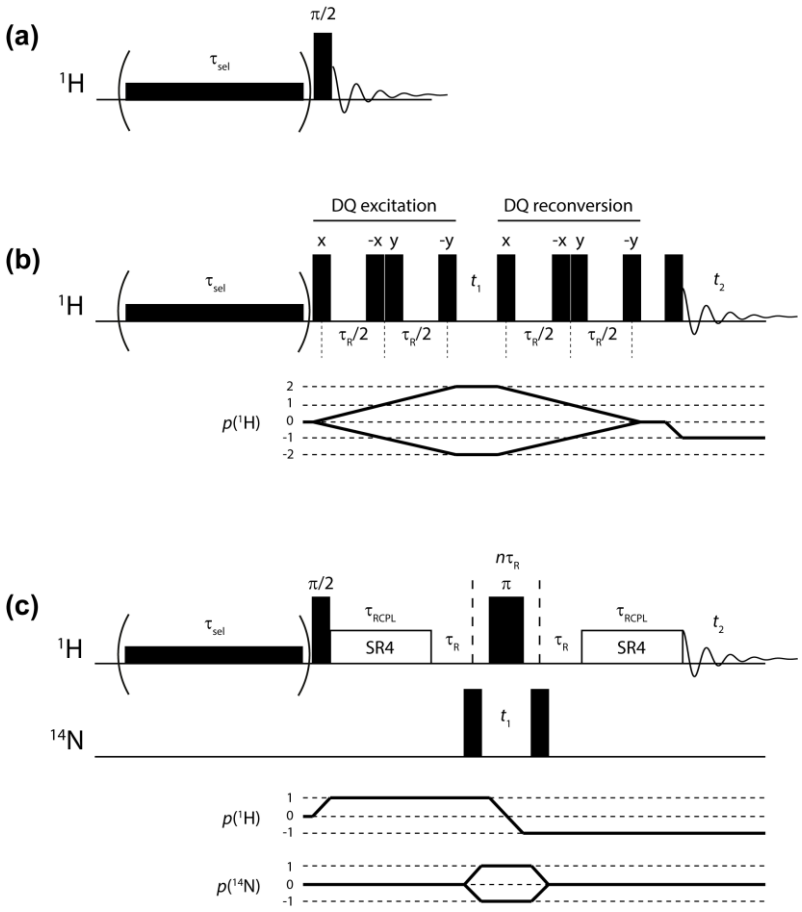

Figure 7.2 Schematic representation of the pulse sequences with/without selective saturation pulses together with coherence transfer pathways for ^{1}H and ^{14}N for (a) 1D ^{1}H MAS, (b) 2D ^{1}H – ^{1}H DQ/SQ MAS (with BABA recoupling) and (c) ^{14}N – ^{1}H HMQC (with SR4 recoupling) experiments.

7.3 Results

7.3.1 One-dimensional ^{1}H MAS NMR spectra under a selective pulse

The effectiveness of a selective pulse at reducing the signal intensity of a methyl resonance at different MAS frequencies is demonstrated in Fig. 7.3, for **7-1**. It is evident from the spectra that ^{1}H resolution improves with increasing MAS frequency. A comparison of the simple one-pulse ^{1}H MAS spectra (dashed line in Fig. 7.3) and the spectra recorded with a selective saturation pulse of nutation frequency 725 Hz and duration 30 ms (solid line in Fig. 7.3) demonstrates the importance of utilising a fast MAS frequency when employing such methodologies. It is observed that the key high ppm resonances corresponding to the hydrogen bonding protons, NHb^I/b^{II}, are largely unaffected by the use of the selective saturation pulse at all MAS frequencies tested here. By comparison, the signal intensity of the nitrogen bound NHa^I/a^{II} protons (5.3 and 5.9 ppm) are increasingly suppressed at lower spinning frequencies. This observation, importantly, highlights the improved effectiveness of the selective saturation pulse at higher MAS frequencies, specifically those above 60 kHz. Note that even at 70 kHz MAS, significant loss of signal intensity is observed in the spectral region between 2.0 and 4.0 ppm, resonances which correspond to methylene and ribose sugar group protons. This is however, in the case of this system, not a significant drawback since the resonances of interest are the cytosine protons (> 5.0 ppm), whilst the ribose and alkyl protons reside on the periphery of the dimer and are therefore of minimal importance to the hydrogen bonding structure.

For the ^{1}H MAS spectra presented in Fig. 7.3, the loss of signal intensity when the selective pulse is turned on as a percentage of the total signal intensity ($\Delta I/I$ (non sel)), is plotted against MAS frequency in Fig. 7.4 for six resonances: H6, H1', NHa^{II}, NHa^I, H^i_{sacc} and H^{ii}_{sacc}. The increased loss in intensity at lower MAS frequencies is clearly demonstrated for all six peaks. Note that, due to the reduction in resolution at lower MAS frequencies, it was not possible to resolve either the NHa^{II} or NHa^I resonances at 30, 40 and 50 kHz, nor the H^i_{sacc} and H^{ii}_{sacc} resonances at 30 kHz MAS, and hence these data are omitted from the plot.

Fig. 7.4 reveals the extent to which signal intensities in the ^{1}H spectra are reduced at lower MAS frequencies when the selective saturation pulse is employed, corresponding to the increased efficiency of ^{1}H spin diffusion at lower spinning frequencies. The signal intensity of the ribose bound protons H^i_{sacc} and H^{ii}_{sacc} are reduced significantly even at the upper limits of fast MAS frequencies (60, 70 kHz). There is also a sizable reduction in intensity for the nitrogen bound NHa^{II} and NHa^I protons, however the reduction is less than 20% and hence these signals are still clearly evident at this spinning frequency (70 kHz) when the selective pulse is applied. Figures 7.3 and 7.4 clearly demonstrate that MAS frequencies of < 60 kHz are required in order to extract the full benefits of utilising such a pulse. In this context, it is also to be remembered that resolution becomes worse as the MAS frequency is reduced. Thus, two factors, i.e. reduced resolution coupled with the significant reduction in signal intensity for

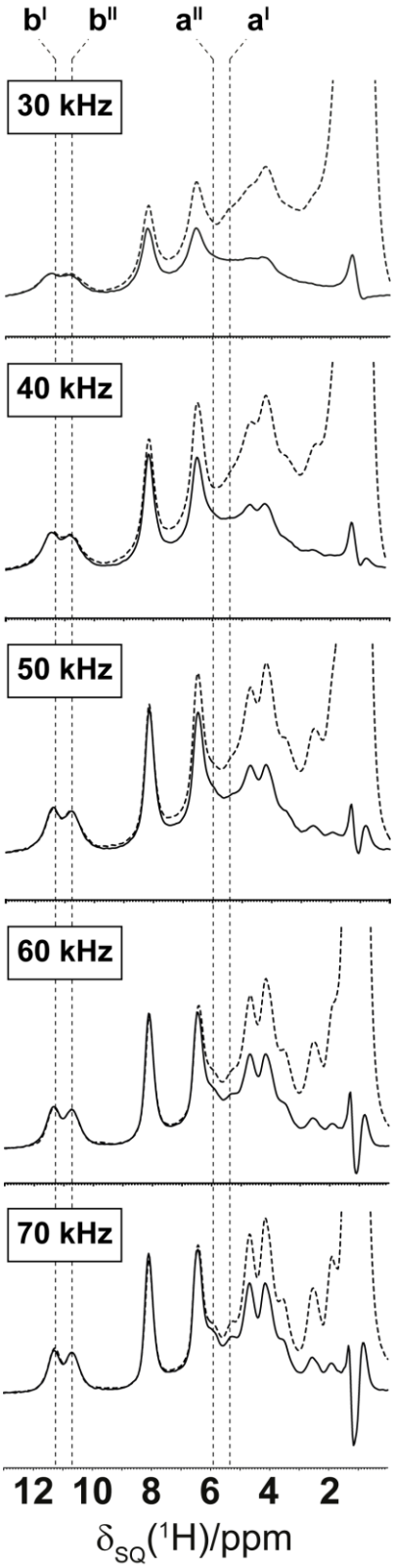

Figure 7.3 Comparison of ^{1}H (ω_0 = 700 MHz) MAS spectra of **7-1** obtained at different MAS frequencies. For each spinning frequency, two spectra are shown corresponding to (dashed line) a standard one-pulse ^{1}H MAS spectrum and (solid line) a ^{1}H MAS spectrum acquired utilising a selective saturation pulse (τ_{sel} = 30 ms, with a nutation frequency of 725 Hz). In all cases, 4 transients were coadded with a recycle delay of 3 seconds.

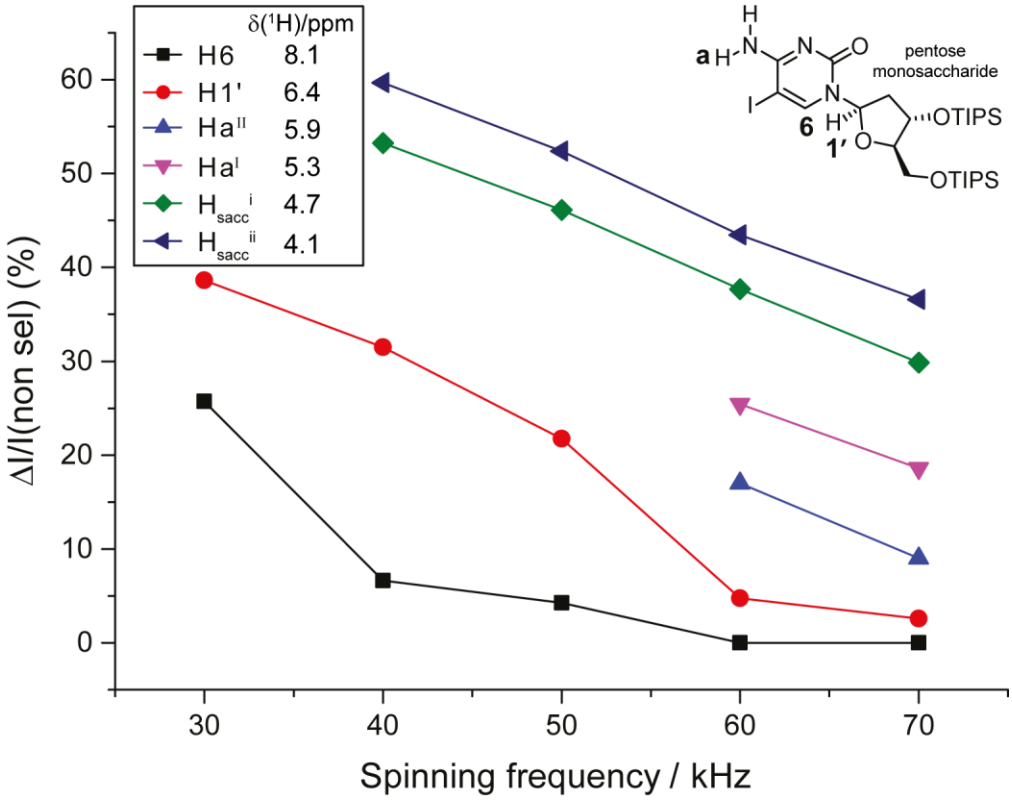

Figure 7.4 The signal intensity loss in a ^{1}H MAS one-pulse spectrum of **7-1** (see Fig. 7.3) when applying a selective saturation pulse (τ_{sel} = 30 ms, with a nutation frequency of 725 Hz), as a percentage of the total signal intensity as compared to the case without the selective pulse is shown for six resonances: H6, H1', NHa^{II}, NHa^{I}, H$^{i}_{sacc}$ and H$^{ii}_{sacc}$, with corresponding ^{1}H chemical shift values stated in the accompanying box. Note that due to insufficient resolution at lower MAS frequencies, some points are omitted from the analysis. Error bars are smaller than the size of the symbols.

the peaks of interest in the cytosine region of the spectrum effectively preclude the use of this technique at slow to moderate MAS frequencies. In summary, the resolution benefits of fast MAS frequencies, the sensitivity enhancements at higher magnetic fields (700 MHz in this case) and the t_1 noise suppression abilities of the selective saturation pulse combine to render this an attractive technique for multidimensional solid-state NMR experiments, as will be demonstrated in sections 7.3.3 and 7.3.4.

The choice of a nutation frequency of 725 Hz and a duration of 30 ms for the selective saturation pulse is an experimental compromise between maximising the degree of saturation of the unwanted signal and minimising the loss of signal intensity for other nearby (in ppm) ^{1}H resonances. This is illustrated in Fig. 7.5a, which shows the effect of changing the nutation frequency for a fixed duration of 30 ms at MAS frequencies of 40, 50, 60 and 70 kHz. For the intense alkyl resonance, increasing the nutation frequency reduces the signal intensity, with a partial signal inversion and an out-of-phase lineshape being observed at faster spinning frequencies for the highest nutation frequencies. For the other resonances below 9.0 ppm, at all MAS frequencies, there is a progressive decrease in intensity upon

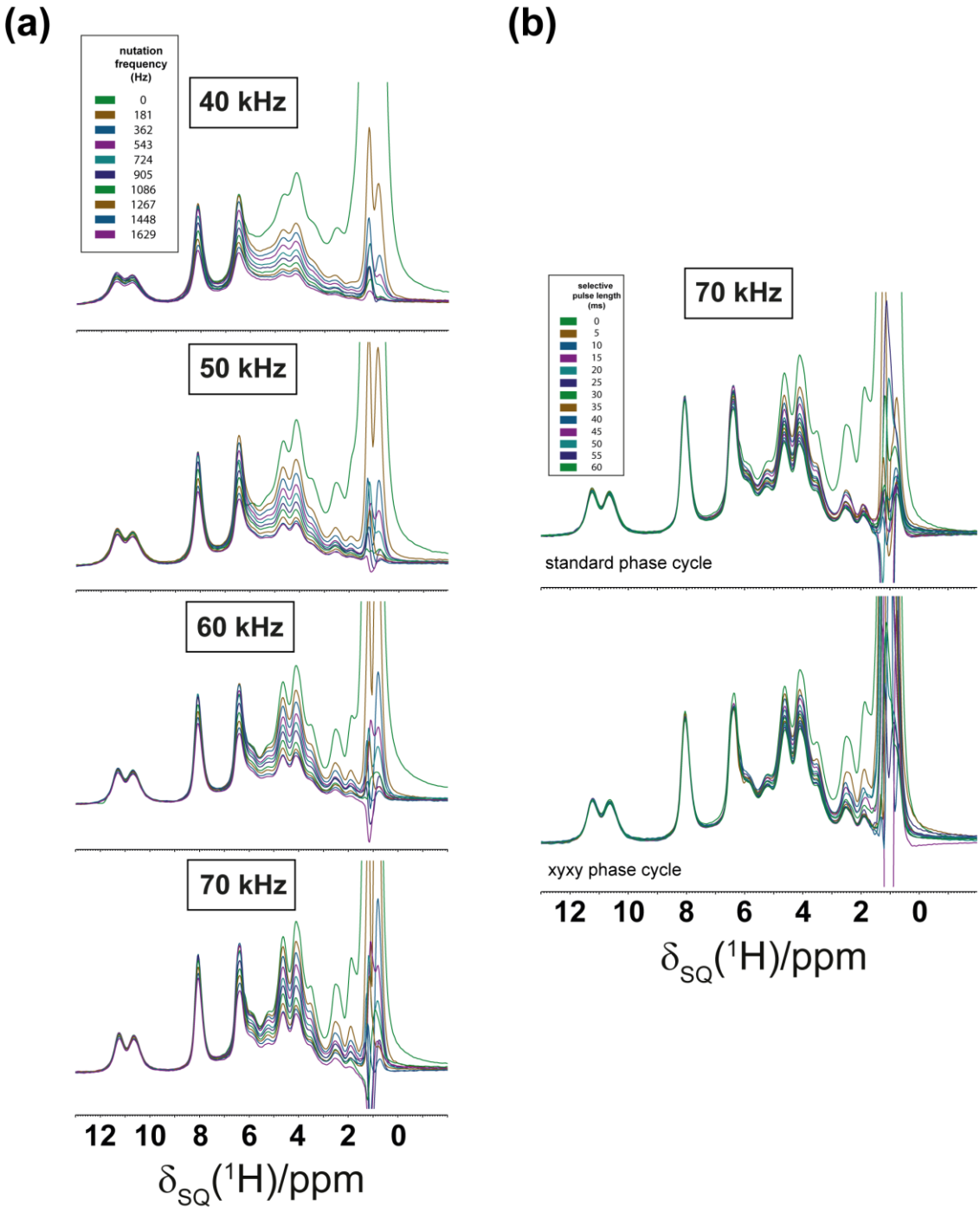

Figure 7.5 (a) Comparison of ^{1}H (ω_0 = 700 MHz) MAS spectra of **7-1** obtained at different MAS frequencies. For each spinning frequency, the spectrum obtained using a standard one-pulse ^{1}H MAS experiment (light green line) is compared to spectra acquired using a saturation pulse of duration τ_{sel} = 30 ms, but with a varying nutation frequency, as indicated in the inset, (b) comparison of ^{1}H (700 MHz) MAS (70 kHz) spectra of **7-1**. A spectrum obtained using a standard one-pulse experiment (light green line) is compared to spectra acquired utilising a saturation pulse of nutation frequency 725 Hz and varying duration, as indicated in the inset. For the bottom plot, a XYXY phase modulation was applied to the selective saturation pulse. In all cases, 4 transients were coadded with a recycle delay of 3 seconds. Note that the data in (b) was recorded by Manoj Pandey (JEOL Tokyo).

increasing the nutation frequency, with this observation having been made in the above discussions of Figures 7.3 and 7.4 above. This phenomenon is a consequence of spin diffusion being reduced at higher spinning frequencies, resulting in a smaller relative reduction of signal intensity for, e.g., the 8.0 ppm resonance. The two highest ppm resonances, those corresponding to the NHb^{I}/b^{II} hydrogen bonding protons, show only a small decrease in intensity across the whole spinning frequency range. This, as will be demonstrated later, is useful for the two-dimensional $^{1}H - {}^{1}H$ data in which cross-peaks pertaining to an intermolecular dipolar coupling across the hydrogen bonding interface are often of low intensity, due to the presence of stronger nearby couplings (NH_2 intramolecular coupling in this case). Fig. 7.5b considers the case of a fixed spinning frequency (70 kHz) and a fixed nutation frequency of 725 Hz, but allowing for the duration of the selective saturation pulse to increase. Moreover, the top and bottom plots in Fig. 7.5b compare the case of a saturation pulse with fixed phase and XYXY phase modulation,(285) respectively. The same trend is observed as for the case in Fig. 7.5a; increasing the saturation pulse duration results in a progressive decrease in the signal intensity of resonances below 9.0 ppm. The two high ppm resonances again show only minimal decreases in signal intensity. Qualitatively, the same trends are observed between the cases of fixed phase and XYXY phase modulation, though the optimum total pulse duration is different in each case.

7.3.2 $^{1}H - {}^{1}H$ spin-diffusion MAS NMR spectra

So far in this chapter, it has been demonstrated that enhanced performance of the saturation pulse in terms of reduced reduction of intensity for nearby (in ppm) ^{1}H resonances is observed at higher MAS frequencies, specifically those above 60 kHz (in the case of **7-1**). In section 7.3.1, this phenomenon was explained in terms of reduced efficiency of ^{1}H spin diffusion upon increasing MAS frequency. In order to further explore this phenomenon, Fig. 7.6 presents a series of $^{1}H - {}^{1}H$ spin diffusion spectra of **7-1** recorded with a τ_{mix} = 30 ms at spinning frequencies of 30, 40, 50, 60 and 70 kHz. It is evident, from inspection of the various spectra, that cross-peak intensity (relative to the auto-peaks) is reduced at faster MAS frequencies. Specifically, Table 7.1 presents an analysis of peak intensity for the rows at frequencies of 11.3, 10.7, 8.2 and 6.4 ppm, i.e., corresponding to the NHb^{I}, NHb^{II}, H6 and H1' resonances, respectively. It is evident that some cross-peaks that are clearly visible at 30 kHz are at or below the noise level at 70 kHz, for example, cross-peaks between NHb^{I} and NHb^{II}. This observation is consistent with the Liouville space simulations of ^{1}H spin diffusion at different MAS frequencies as presented in work by Dumez, Butler and Emsley.(286) It is important to note in this context that whilst spin diffusion in this sense is not the same as what happens during the course of *rf* irradiation, such an experiment does appear to act as a good indicator to account for the signal loss observed during a selective saturation pulse experiment. It should be noted that, unlike the two-dimensional spectra presented below, the intense alkyl peak has less of a perturbing effect on the appearance of the $^{1}H - {}^{1}H$ spin diffusion spectrum; this is presumably a consequence of the reduced relative intensity of the other cross-peaks in the $^{1}H - {}^{1}H$ DQ/SQ and $^{14}N - {}^{1}H$ HMQC spectra outlined in sections 7.3.3 and 7.3.4.

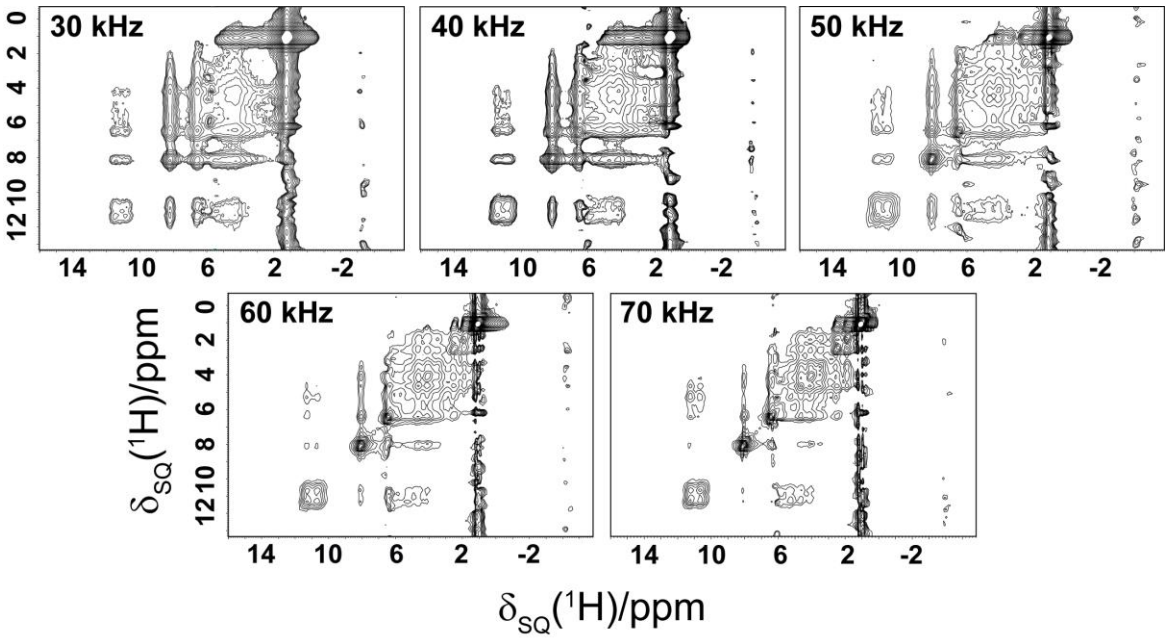

Figure 7.6 $^{1}H - {}^{1}H$ (ω_0 = 700 MHz) spin diffusion spectra of **7-1** recorded using a mixing time equal to 30 ms at MAS frequencies of 30, 40, 50, 60 and 70 kHz. The base contour level is at 0.05% (30 kHz), 0.03% (40 kHz) and 0.02% (50, 60, 70 kHz) of the maximum peak height.

Table 7.1 Peak intensities[a] extracted from rows taken from the $^{1}H - {}^{1}H$ spin diffusion spectra in Fig.7.6.

	NHb^{I}	NHb^{II}	H6	H1'
30 kHz MAS				
NHb^{I} (11.3 ppm)	**0.25**	0.14	0.63	0.27
NHb^{II} (10.7 ppm)	0.19	**0.09**	0.56	0.29
H6 (8.2 ppm)	0.23	0.14	**2.59**	0.92
H1' (6.4 ppm)	0.16	0.07	1.33	**0.82**
40 kHz MAS				
NHb^{I} (11.3 ppm)	**0.50**	0.18	0.62	0.09
NHb^{II} (10.7 ppm)	0.36	**0.23**	0.53	0.29
H6 (8.2 ppm)	0.15	0.10	**5.45**	1.23
H1' (6.4 ppm)	0.23	0.13	1.86	**2.60**
50 kHz MAS				
NHb^{I} (11.3 ppm)	**0.58**	0.43	0.42	0.12
NHb^{II} (10.7 ppm)	0.41	**0.44**	0.39	0.15
H6 (8.2 ppm)	0.21	0.11	**7.45**	0.38
H1' (6.4 ppm)	0.24	0.08	1.36	**4.62**
60 kHz MAS				
NHb^{I} (11.3 ppm)	**0.82**	0.48	0.28	0.34
NHb^{II} (10.7 ppm)	0.33	**0.74**	0.58	0.33
H6 (8.2 ppm)	0.12	0.08	**7.85**	0.43
H1' (6.4 ppm)	0.16	0.05	0.93	**6.79**
70 kHz MAS				
NHb^{I} (11.3 ppm)	**0.61**	0.45	0.17	0.17
NHb^{II} (10.7 ppm)	0.21	**1.00**	0.16	-
H6 (8.2 ppm)	0.13	0.09	**13.10**	0.47
H1' (6.4 ppm)	0.11	-	0.57	**9.19**

[a]Intensities are expressed as percentages of the highest peak in that spectrum. Integration is performed over the following ranges: NHb^{I}: 12.0 – 11.0 ppm, NHb^{II}: 11.0 – 10.0 ppm, H6: 8.7 – 7.6 ppm, H1': 6.9 – 6.1 ppm. Note that bold numbers indicate the integrated intensity of diagonal peaks.

7.3.3 $^{1}H - {}^{1}H$ DQ/SQ MAS NMR spectra

In the absence of a selective saturation pulse, the $^{1}H - {}^{1}H$ DQ/SQ MAS spectrum of **7-1** presented in Fig. 7.7b proves difficult to interpret, given the magnitude of the t_1 noise in the spectrum. A remarkable improvement is observed when, as in Fig. 7.7c, a selective saturation pulse is employed prior to the main pulse sequence. One-dimensional ^{1}H DQ-filtered spectra ($t_1 = 0$) of **7-1** obtained without (dashed line) and with (solid line) the selective saturation pulse are presented in Fig. 7.7a. In the selective pulse spectrum, although some signals corresponding to the CH_2 moieties (~ 2.0 – 3.0 ppm) are severely diminished due to the aforementioned spin diffusion effects, the resonances above 5.0 ppm can now be clearly observed and it is possible to pick out several important cross-peaks, the most significant of which are shown in Fig. 7.7c.

To quantify this improvement, for the row extracted at a DQ frequency of 22.0 ppm, the integrated intensity of the NHb^{II} peak at 10.7 ppm as a percentage of integrated t_1 noise (in magnitude mode) at the methyl resonance changes from 14% in Fig. 7.7b (no selective pulse) to 38% in Fig. 7.7c (with selective pulse). The improvements made by employing the selective saturation pulse means that the benefits of a high magnetic field (700 MHz) and a fast MAS frequency (70 kHz) can now be clearly observed, now that the t_1 noise has largely been suppressed in the indirect dimension.

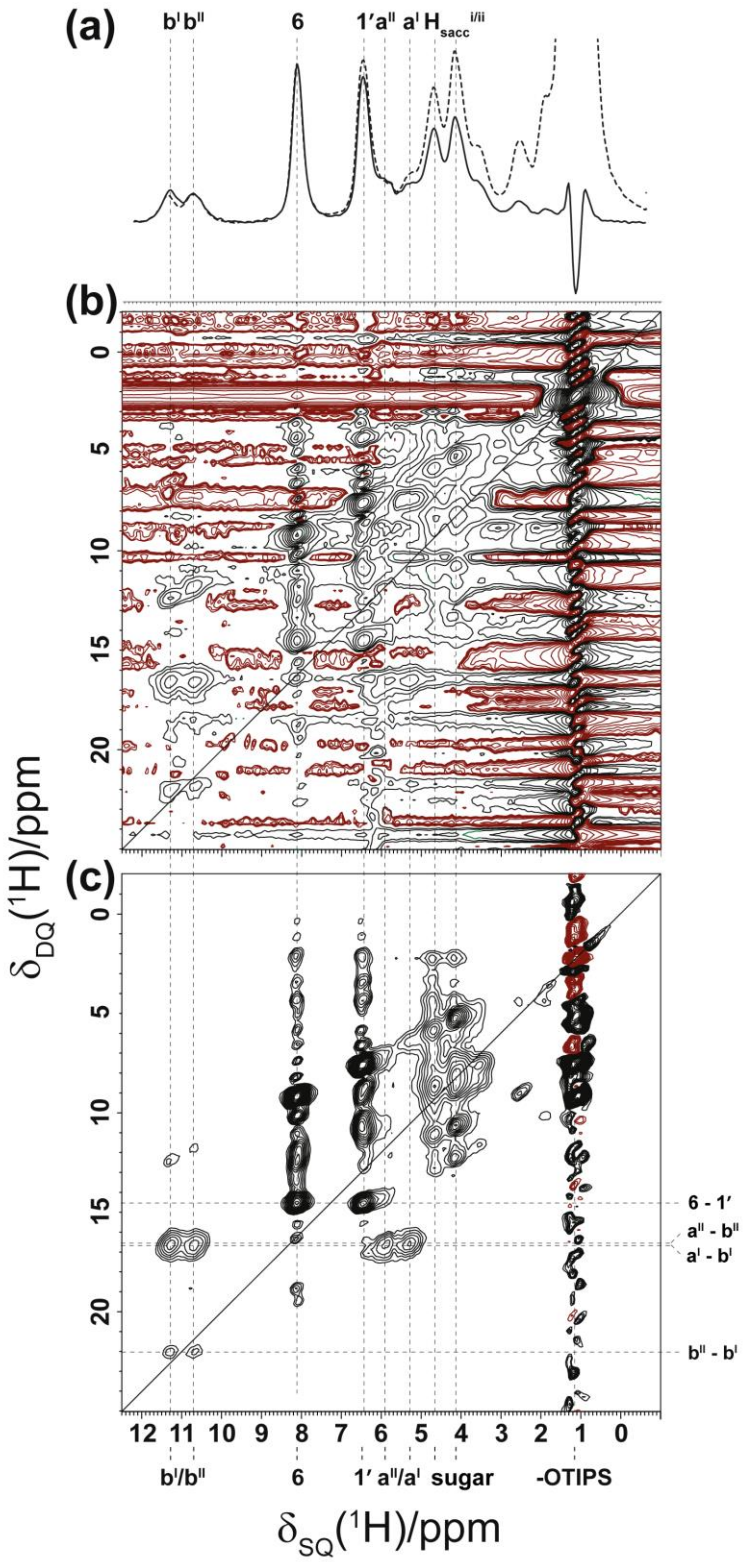

Figure 7.7 A comparison of $^{1}H - ^{1}H$ (ω_0 = 700 MHz) DQ/SQ MAS (70 kHz spinning) spectra of **7-1** obtained using the pulse sequence shown in Fig. 7.2b: (a) 1D (DQ-filtered, i.e., $t_1 = 0$) spectra without a selective pulse (dashed line) and with a selective pulse of nutation frequency 725 Hz and duration, τ_{sel} = 30 ms (solid line), (b and c) 2D spectra obtained (b) without and (c) with a selective saturation pulse of nutation frequency 725 Hz and duration, τ_{sel} = 30 ms. In both cases, eight rotor periods of BABA-xy16 recoupling were used for the excitation and reconversion of DQ coherence. The base contour level is at (b) 22% and (c) 3% of the maximum peak height in each spectrum, with negative contours shown in red.

7.3.4 ^{14}N – ^{1}H HMQC MAS NMR spectra

The efficacy of the selective pulse at reducing t_1 noise is also evident for heteronuclear correlation experiments, such as the ^{14}N – ^{1}H HMQC solid-state NMR experiment. In this experiment, it is often useful to observe ^{14}N lineshapes and hence the removal of t_1 noise from the indirect dimension is of considerable importance. One- and two-dimensional ^{14}N – ^{1}H spectra of **7-1** obtained with and without the use of a selective pulse are shown in Fig. 7.8.

Inspection of the two 1D ^{14}N – ^{1}H HMQC filtered (t_1 = 0) spectra of **7-1** in Fig. 7.8a reveals a sizeable reduction in the intensity of the methyl resonance when the selective pulse is turned on (solid line) as compared to when it is turned off (dashed line). This reduction in intensity is achieved with minimal loss of intensity for the NH bound protons (and H6 and H1' resonances) and leads to a significant improvement in the appearance of the two-dimensional ^{14}N – ^{1}H HMQC spectrum presented in Fig. 7.8c. By contrast, in Fig. 7.8b (standard experiment), it is difficult to differentiate between 'real' signals and signals arising from the t_1 noise. Application of the selective pulse (Fig. 7.8c) allows for the clear observation of distinct resonances in the two-dimensional spectrum, including weaker signals corresponding to the aromatic H6 environment and the H1' proton contained within the pentose monosaccharide. To quantify the improvement, for the row taken at a ^{14}N chemical shift of 100 ppm, the integrated intensity of the NHb^{II} peak at 10.7 ppm (^{1}H shift) as a percentage of integrated t_1 noise (in magnitude mode) at the methyl resonance changes from 5% (no selective pulse) to 20% (with selective pulse), which represents a significant improvement.

In previous work published by Tatton *et al*. (201) it has been demonstrated that the performance of the ^{14}N – ^{1}H HMQC experiment has an intrinsic dependence on the MAS frequency. In this study it was shown using the β-AspAla dipeptide that good experimental performance is achieved only at frequecies above 45 kHz. Specifically, in addition to improved line narrowing, an increase in ^{1}H coherence lifetimes was also observed (as an increase in integrated signal intensity) upon doubling the MAS frequency from 30 to 60 kHz. Whilst in this study rotary resonance recoupling (R^3) at the n = 2 condition was employed,(207) Nishiyama and co-workers showed that the same extension of ^{1}H coherence lifetimes can also be achieved using the SR4 recoupling sequence,(209) which was employed in the work presented in this chapter. It is noted that, as in Fig. 7.3, it is only at higher spinning frequencies that the employment of the selective saturation pulse becomes truly feasible for this experiment.

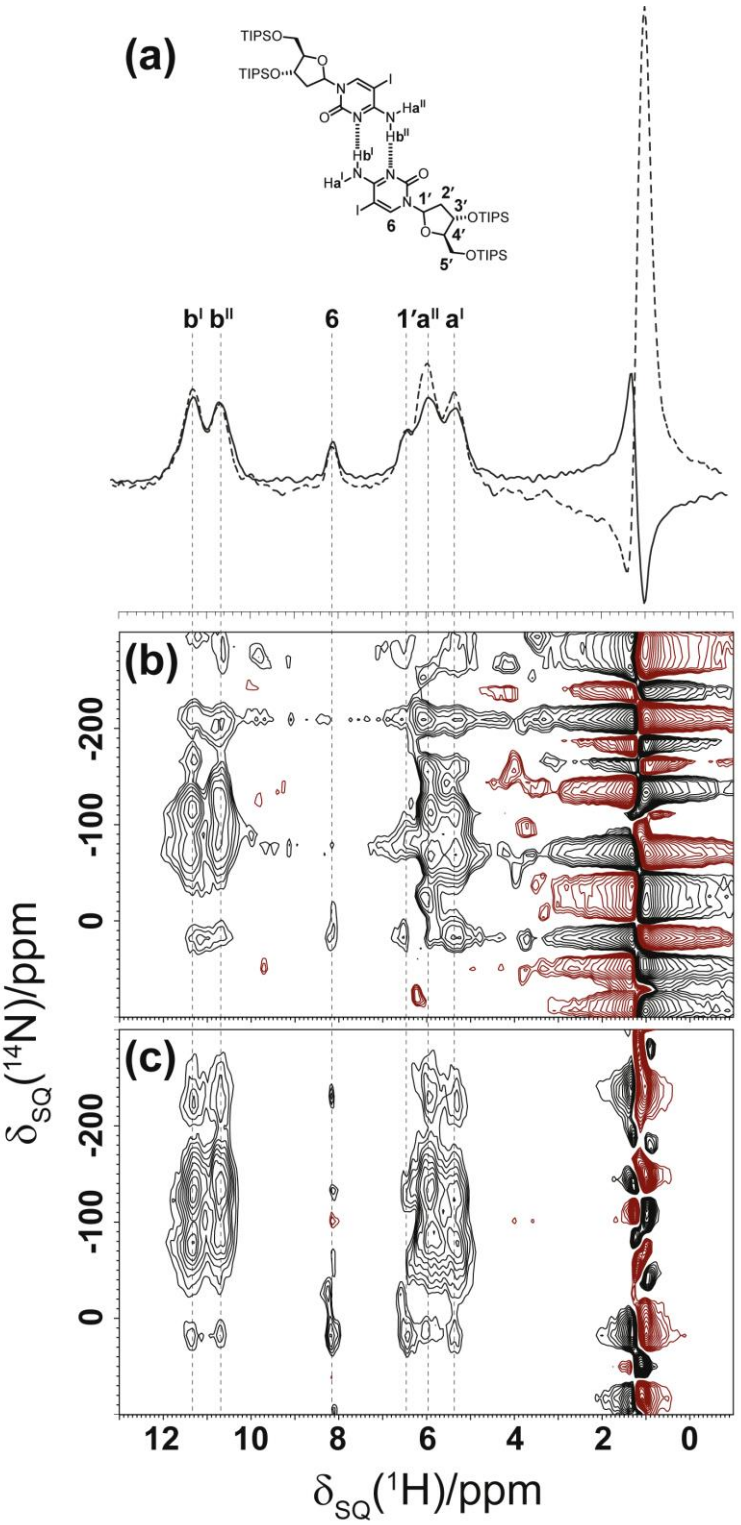

Figure 7.8 A comparison of $^{14}N - ^{1}H$ (ω_0 = 700 MHz) HMQC spectra of **7-1** obtained at 70 kHz MAS: (a) 1D (HMQC filtered, i.e., t_1 = 0) spectra with (solid line) and without (dashed line) a selective saturation pulse of nutation frequency 725 Hz and τ_{sel} = 30 ms, (b and c) 2D spectra, (b) without, and (c) with the use of a selective saturation pulse of nutation frequency 725 Hz and τ_{sel} = 30 ms. (b) 128 or (c) 224 transients were recorded for each of 32 t_1 FIDs. All spectra were recorded using the SR4 recoupling of the $^{14}N - ^{1}H$ heteronuclear dipolar couplings for a τ_{RCPL} = 171 μs. The base contour level is at (b) 42% and (c) 38% of the maximum peak height in each spectrum, with negative contours shown in red.

7.4 Summary

The results in this chapter have demonstrated that a single, long, low amplitude selective saturation pulse can be applied effectively to reduce the magnitude of t_1 noise from the indirect dimension of two-dimensional solid-state NMR experiments. Crucially, it was shown that such a method is only applicable at fast MAS frequencies, specifically those above 60 kHz. However, whilst the selective pulse represents a fast, efficient and user friendly method for reducing the intensity of unwanted signals, there are several important considerations which must be taken into account. In section 7.3.2, it was demonstrated that the extent of $^1H - ^1H$ spin diffusion over the duration of the selective pulse must be taken into account on a sample by sample basis and, if and when, polarisation transfer becomes apparent between various ^1H sites, the choice of whether or not to proceed is determined by the spectroscopist. It is therefore useful to have some basic knowledge or model for the molecular structure, so as to identify valuable resonances (such as the hydrogen bonding ones discussed in this work). If these 'resonances of interest' are largely unaffected by polarisation transfer from the proton signal to be saturated, over the same timescale of the pulse, then this method has been demonstrated herein to be an effective method for the improvement of presentation and readability of important ^1H two-dimensional experiments. This in turn can aid the spectral assignment of specfic peaks, which is the ultimate aim of NMR spectroscopy.

The second consideration, which is of equal importance, is the ready availability of fast MAS probes and, to a lesser extent, access to high magnetic fields (for sensitivity and resolution enhancements). Fast MAS frequencies have been shown in this work to have a marked influence on the spin dynamics of the system, leading to an effective suppression of magnetisation transfer between different proton environments, especially those in the higher ppm range of the spectrum. This has the effect of reducing loss of signal intensity for all non-intentionally suppressed proton environments, which is critically important for the successful implementation of this technique. In principle, the approach could be extended to incorporate the application of a doubly-selective pulse, as achieved using a cosine-modulated Gaussian pulse.(287-290)

Moving forward, it may be prudent to experiment with shaped pulses as opposed to the soft rectangular selective pulses employed in this study. The soft selective pulse is of longer duration than a typical hard rectangular pulse, using a weak *rf* field which therefore selects a narrower range of frequencies, i.e., it allows for the selective saturation the methyl resonance, with adequate accuracy. However, as was demonstrated in this work, suppression of the methyl peak *via* this technique also leads to some undesired suppression of nearby (in ppm) resonances corresponding to methylene and ribose protons. The use of a shaped selective pulse, in which the *rf* amplitude varies over the duration of the saturation pulse, may in theory allow for even more precise saturation of a certain frequency, i.e., a undesired alkyl resonance. A potential downside to the use of a shaped pulse is the loss in sensitivity when

compared to a rectangular constant amplitude pulse. It is worthwhile investigating this idea further in the future, in order to ascertain whether or not more precise saturation can be achieved.

In summary, the efficacy of a selective saturation pulse, applied prior to the main pulse sequence, at reducing t_1 noise generated by an intense alkyl signal has been clearly demonstrated. The method has been shown to lead to a dramatic improvement in the appearance of two-dimensional ^{1}H MAS experiments, in this case the ^{1}H DQ/SQ and ^{14}N – ^{1}H HMQC experiments. Crucially, the technique outlined herein requires no specialised apparatus beyond a fast spinning probe, which are becoming routine in solid-state NMR labs, and therefore represents a simple and accessible tool for the removal of t_1 noise in solid-state NMR spectra.

Chapter 8 : Thesis Summary

8.1 Thesis summary

The work presented in this thesis has demonstrated the power of multinuclear fast MAS solid-state NMR experiments to elucidate hydrogen bonding arrangements in synthetic nucleoside analogues, which self-assemble in the solid state. Specifically, $^{1}H - {}^{1}H$ DQ/SQ MAS, $^{14}N - {}^{1}H$ HMQC and ^{13}C-based methods have been presented for a range of complex systems, the data for which is consistent with aggregation into a range of self-assembled architectures, from ribbons to helices. In addition, for systems with single crystal X-ray data, the power of an NMR crystallography approach has been demonstrated.

Chapter 4 discussed the self-assembling potential of the pterin subunit, for both low and high molecular weight analogues. In the case of the former, the importance of the pivaloyl amide functionality was demonstrated through a combined approach of experimental NMR (three of the four compounds presented were non-crystalline) and *ab intio* calculations of the relevant NMR parameters *via* the GIPAW method for the crystalline intermediate. Replacing this pivaloyl functional group with a dimethylaminomethylene moiety resulted in a marked difference in the respective ^{1}H DQ MAS spectra, with the latter functional group leading to a broad spectrum consistent only with dimer formation. This was the direct result of the loss of an intramolecular hydrogen bond between the pterin NH and pivaloyl carbonyl oxygen groups. For the higher molecular weight systems, the presence of the deoxycytidine moiety within the same molecule resulted in higher order aggregation, with the data being consistent with some form of stacked trimeric arrangement (or potentially a ribbon-like arrangement for one of the compounds). The ^{1}H DQ MAS spectra for these systems are considerably more complex to analyse when compared to the aforementioned low molecular weight pterin compounds, particularly given the increased hydrogen bonding potential (through the existence of more acceptor and donor functional groups) in the higher molecular weight systems.

In chapter 5, these same methods were employed for three synthetic deoxycytidine analogues. Single crystal X-ray structures existed for two of the three systems, however, the presence of significant disorder in the unit cell of one of these compounds meant that GIPAW calculations were only successfully performed in one case. For two of the systems, for which the NMR and crystallographic data were consistent with a dimeric arrangement in the solid state, the resolution of the ^{1}H DQ MAS and HMQC data was such that the number of crystallographically distinct molecules in the asymmetric unit cell, Z', could be determined, principally through the observed number of distinct amine resonances in the ^{1}H spectra. An NMR crystallographic analysis based on the geometry optimised single crystal X-ray structure, specifically a comparison of the calculated shielding parameters for the full crystal vs. the isolated molecule, allowed for an analysis of relative hydrogen bonding strength for the various NH and OH moieties in the molecules and the solvent, respectively. All three systems were shown to interact through the same hydrogen bonding motif, but in the case of the last compound in which two deoxycytidine moieties across an acetylenic axis are present, this data was consistent with a helical

arrangement which was suggested by the disordered crystal structure (the disorder presented itself away from the main structure).

In terms of structural analysis, chapter 6 was the most challenging, given the non-crystalline nature of *all* intermediates discussed. However, by applying $^{1}H - {}^{1}H$, $^{14}N - {}^{1}H$ and $^{1}H - {}^{13}C$ correlation experiments, solid-state NMR was still capable of commenting on the likely hydrogen bonding and $\pi - \pi$ stacking arrangements of these systems. In addition, the work presented in this chapter involved the novel study of aldehyde and aldoxime functional groups, which in the case of the latter moiety has no literature precedence. Some of the synthetic challenges involved in this series of compounds was also discussed towards the end of the chapter.

Chapter 7 marked a significant change in emphasis. The work presented in this chapter was related to the employment of a selective saturation pulse, of low intensity and long duration, applied immediately prior to three solid-state NMR pulse sequences: one-pulse ^{1}H MAS, $^{1}H - {}^{1}H$ DQ/SQ MAS and $^{14}N - {}^{1}H$ HMQC. It was shown that such a method could be used to suppress the intensity of a strong, mobile methyl resonance in the ^{1}H dimension, thereby reducing observed t_1 noise in two-dimensional spectra. The technique was applied to a deoxycytidine analogue, whose NMR spectra are analysed in chapter 5. Importantly, it was shown that fast MAS frequencies, specifically those over 60 kHz, are needed in order to reduce suppression of nearby (in ppm) resonances of interest. Through analysis of $^{1}H - {}^{1}H$ spin diffusion experiments at 30, 40, 50, 60 and 70 kHz, it was shown that this reduced suppression at higher MAS frequencies is a result of reduced rates of spin diffusion at 60/70 kHz, when compared to lower frequencies.

The recent advances in $^{1}H - {}^{1}H$ solid-state NMR have been intrinsically linked to improved pulse sequence development, in particular the availability of more sophisticated decoupling and recoupling sequences, and the attainability of higher MAS frequencies. As achievable MAS frequencies increase, the workhorse $^{1}H - {}^{1}H$ DQ/SQ MAS, based on BABA recoupling, and $^{14}N - {}^{1}H$ HMQC experiments will become increasingly useful, as observed ^{1}H linewidths are subsequently reduced. In addition, the design and manufacture of higher magnetic field spectrometers (i.e, $\omega_0 < 1$ GHz), will help to increase the sensitivity of NMR experiments moving forward. The principle of dynamic nuclear polarisation (DNP), in which spin polarisation is transferred from electrons to nuclei, has led to the field of DNP-NMR. Since electron spins inherently have larger polarisation when compared to nuclei (660 times higher for electrons when compared to proton), DNP-NMR exploits this phenomenon to significantly enhance NMR signal intensities. Amongst other benefits this has the effect of reducing experimental times.

Of the high resolution options for characterisation in the solid-state, as in solution, there exists no single 'perfect' method. In order to fully appreciate a given system in the solid phase it is necessary to consider both long and short-range order. Diffraction techniques remain the method of choice for highly periodic

materials, however, in a significant number of cases, it is not possible to solve the structure by diffraction, or sometimes the structural models are incomplete, as was seen in chapter 5, where there is disorder which hinders interpretation. Therefore, it is often prudent to complement existing diffraction data with high resolution solid-state NMR, which informs on local atomic structure and which, *via* the chemical shift, is highly attuned to noncovalent phenomena, such as hydrogen bonding. The burgeoning field of NMR crystallography aims to combine these techniques and is capable of providing useful data in its own right, particularly on the strength of noncovalent interactions (see chapter 5), and the confirmation of chemical shift assignments. The latter result allows for, as was seen in chapters 4 and 5, the inference of hydrogen bonding structure for related but non-crystalline materials. This being said, the field is still in its infancy, as continued improvements in experimental methodology and computational power allows for the treatment of ever more complex systems. Ultimately, it can be argued that the overarching objective of NMR crystallography is the effective reversal of the technique as it currently exists, i.e., the inputting of experimental NMR parameters and the outputting of accurate 3D models. However, this requires a number of challenges to be overcome, notably, for the case of moderately sized organic molecules that have been the focus of this thesis, the inclusion of temperature effects into computational calculations.(291)

Chapter 9 : References

1. P. Zeeman, *Versl. Kon. Ak. Wet* **5**, 181 (1896).
2. J. Larmor, *Philos. Mag.* **44**, 503 (1897).
3. I. I. Rabi, *Phys. Rev.* **51**, 652 (1937).
4. I. I. Rabi, J. R. Zacharias, S. Millman, and P. Kusch, *Phys. Rev.* **53**, 318 (1938).
5. I. I. Rabi, S. Millman, P. Kusch, and J. R. Zacharias, *Phys. Rev.* **55**, 526 (1939).
6. B. Lasarew, and L. Schubnikow, *Phys. Z. Sowjetunion* **11**, 445 (1937).
7. C. J. Gorter, and L. J. F. Broer, *Physica* **9**, 591 (1942).
8. E. M. Purcell, H. C. Torrey, and R. V. Pound, *Phys. Rev.* **69**, 37 (1946).
9. F. Bloch, W. W. Hansen, and M. Packard, *Phys. Rev.* **69**, 127 (1946).
10. F. Bloch, *Phys. Rev.* **70**, 460 (1946).
11. F. Bloch, W. W. Hansen, and M. Packard, *Phys. Rev.* **70**, 474 (1946).
12. B. V. Rollin, and J. Hatton, *Nature* **159**, 201 (1947).
13. G. E. Pake, *J. Chem. Phys.* **16**, 327 (1948).
14. J. T. Arnold, S. S. Dharmatti, and M. E. Packard, *J. Chem. Phys.* **19**, 507 (1951).
15. E. L. Hahn, *Phys. Rev.* **76**, 145 (1949).
16. E. L. Hahn, *Phys. Rev.* **80**, 580 (1950).
17. H. C. Torrey, *Phys. Rev.* **76**, 1059 (1949).
18. I. J. Lowe, and R. E. Norberg, *Phys. Rev.* **107**, 46 (1957).
19. R. R. Ernst, and W. A. Anderson, *Rev. Sci. Instrum.* **37**, 93 (1966).
20. E. R. Andrew, A. Bradbury, and R. G. Eades, *Nature* **182**, 1659 (1958).
21. E. R. Andrew, A. Bradbury, and R. G. Eades, *Nature* **183**, 1802 (1959).
22. I. J. Lowe, *Phys. Rev. Lett.* **2**, 285 (1959).
23. P. Mansfield, and D. Ware, *Phys. Lett.* **22**, 133 (1966).
24. E. D. Ostroff, and J. S. Waugh, *Phys. Rev. Lett.* **16**, 1097 (1966).
25. U. Haeberlen, and J. S. Waugh, *Phys. Rev.* **175**, 453 (1968).
26. J. S. Waugh, L. M. Huber, and U. Haeberlen, *Phys. Rev. Lett.* **20**, 180 (1968).
27. R. Tycko, and G. Dabbagh, *Chem. Phys. Lett.* **173**, 461 (1990).
28. M. Hohwy, H. J. Jakobsen, M. Edén, M. H. Levitt, and N. C. Nielsen, *J. Chem. Phys.* **108**, 2686 (1998).
29. W. Sommer, J. Gottwald, D. E. Demco, and H. W. Spiess, *J. Magn. Reson., Ser. A* **113**, 131 (1995).
30. I. Schnell, A. Lupulescu, S. Hafner, D. E. Demco, and H. W. Spiess, *J. Magn. Reson.* **133**, 61 (1998).
31. K. Saalwächter, F. Lange, K. Matyjaszewski, C.-F. Huang, and R. Graf, *J. Magn. Reson.* **212**, 204 (2011).
32. S. R. Hartmann, and E. L. Hahn, *Phys. Rev.* **128**, 2042 (1962).
33. L. R. Sarles, and R. M. Cotts, *Phys. Rev.* **111**, 853 (1958).
34. A. Pines, M. G. Gibby, and J. S. Waugh, *J. Chem. Phys.* **56**, 1776 (1972).
35. A. Pines, M. G. Gibby, and J. S. Waugh, *J. Chem. Phys.* **59**, 569 (1973).
36. J. Schaefer, and E. O. Stejskal, *J. Am. Chem. Soc.* **98**, 1031 (1976).
37. W. P. Aue, E. Bartholdi, and R. R. Ernst, *J. Chem. Phys.* **64**, 2229 (1976).
38. O. W. Sørensen, G. W. Eich, M. H. Levitt, G. Bodenhausen, and R. R. Ernst, *Prog. Nucl. Magn. Reson. Spectrosc.* **16**, 163 (1984).
39. G. Bodenhausen, H. Kogler, and R. R. Ernst, *J. Magn. Reson.* **58**, 370 (1984).
40. M. Lee, and W. I. Goldburg, *Phys. Rev.* **140**, A1261 (1965).
41. A. Bielecki, A. C. Kolbert, and M. H. Levitt, *Chem. Phys. Lett.* **155**, 341 (1989).
42. E. Vinogradov, P. K. Madhu, and S. Vega, *Chem. Phys. Lett.* **314**, 443 (1999).
43. B. C. Gerstein, R. G. Pembleton, R. C. Wilson, and L. M. Ryan, *J. Chem. Phys.* **66**, 361 (1977).
44. S. P. Brown, A. Lesage, B. Elena, and L. Emsley, *J. Am. Chem. Soc.* **126**, 13230 (2004).
45. D. Sakellariou, A. Lesage, P. Hodgkinson, and L. Emsley, *Chem. Phys. Lett.* **319**, 253 (2000).
46. B. Elena, G. de Paepe, and L. Emsley, *Chem. Phys. Lett.* **398**, 532 (2004).

47. J. M. Lamley, D. Iuga, C. Öster, H.-J. Sass, M. Rogowski, A. Oss, J. Past, A. Reinhold, S. Grzesiek, A. Samoson, and J. R. Lewandowski, *J. Am. Chem. Soc.* **136**, 16800 (2014).
48. J.-M. Lehn, *Science* **295**, 2400 (2002).
49. D. Philp, and J. F. Stoddart, *Angew, Chem. Int. Ed. Engl.* **35**, 1154 (1996).
50. G. M. Whitesides, and B. Grzybowski, *Science* **295**, 2418 (2002).
51. G. M. Whitesides, E. E. Simanek, J. P. Mathias, C. T. Seto, D. Chin, M. Mammen, and D. M. Gordon, *Accounts. Chem. Res.* **28**, 37 (1995).
52. J.-M. Lehn, *Proc. Natl. Acad. Sci. USA.* **99**, 4763 (2002).
53. E. A. Appel, M. W. Tibbitt, M. J. Webber, B. A. Mattix, O. Veiseh, and R. Langer, *Nat Commun* **6** (2015).
54. Y. Xu, G. Shi, and X. Duan, *Accounts. Chem. Res.* **48**, 1666 (2015).
55. N. Saito, K. Kanie, M. Matsubara, A. Muramatsu, and M. Yamaguchi, *J. Am. Chem. Soc.* **137**, 6594 (2015).
56. G. Nystrom, A. Marais, E. Karabulut, L. Wagberg, Y. Cui, and M. M. Hamedi, *Nat Commun* **6** (2015).
57. P. K. Kundu, D. Samanta, R. Leizrowice, B. Margulis, H. Zhao, M. Börner, UdayabhaskararaoT, D. Manna, and R. Klajn, *Nat. Chem.* **7**, 646 (2015).
58. E. Busseron, J.-J. Cid, A. Wolf, G. Du, E. Moulin, G. Fuks, M. Maaloum, P. Polavarapu, A. Ruff, A.-K. Saur, S. Ludwigs, and N. Giuseppone, *ACS Nano* **9**, 2760 (2015).
59. W. Zhao, D. Wang, H. Lu, Y. Wang, X. Sun, S. Dong, and J. Hao, *Langmuir* **31**, 2288 (2015).
60. A. Samanta, S. A. Walper, K. Susumu, C. L. Dwyer, and I. L. Medintz, *Nanoscale* **7**, 7603 (2015).
61. J. Roukala, J. Zhu, C. Giri, K. Rissanen, P. Lantto, and V.-V. Telkki, *J. Am. Chem. Soc.* **137**, 2464 (2015).
62. S. Bähring, L. Martín-Gomis, G. Olsen, K. A. Nielsen, D. S. Kim, T. Duedal, Á. Sastre-Santos, J. O. Jeppesen, and J. L. Sessler, *Chem. Eur. J.* **22**, 1958 (2016).
63. V. D. Nguyen, A. Pal, F. Snijkers, M. Colomb-Delsuc, G. Leonetti, S. Otto, and J. van der Gucht, *Soft Matter* **12**, 432 (2016).
64. L. J. Prins, D. N. Reinhoudt, and P. Timmerman, *Angew. Chem. Int. Ed. Engl.* **40**, 2382 (2001).
65. J. E. D. Davies, J. L. Atwood, and J. M. Lehn, *Comprehensive supramolecular chemistry. Volume 9, Templating, self-assembly, and self-organisation*; Pergamon: New York, 1996.
66. C. A. Hunter, and H. L. Anderson, *Angew. Chem. Int. Edit.* **48**, 7488 (2009).
67. A. Mulder, J. Huskens, and D. N. Reinhoudt, *Org. Biomol. Chem.* **2**, 3409 (2004).
68. M. F. Perutz, *Q. Rev. Biophys.* **22**, 139 (1989).
69. G. Ercolani, *J. Am. Chem. Soc.* **125**, 16097 (2003).
70. J. Hamacek, M. Borkovec, and C. Piguet, *Dalton Transactions*, 1473 (2006).
71. J. M. Lehn, A. Rigault, J. Siegel, J. Harrowfield, B. Chevrier, and D. Moras, *Proc. Natl. Acad. Sci. USA.* **84**, 2565 (1987).
72. A. D'Urso, M. E. Fragala, and R. Purrello, *Chem. Commun.* **48**, 8165 (2012).
73. C. Montoro-García, J. Camacho-García, A. M. López-Pérez, N. Bilbao, S. Romero-Pérez, M. J. Mayoral, and D. González-Rodríguez, *Angew. Chem. Int. Edit.* **54**, 6780 (2015).
74. S. Romero-Pérez, J. Camacho-García, C. Montoro-García, A. M. López-Pérez, A. Sanz, M. J. Mayoral, and D. González-Rodríguez, *Org. Lett.* **17**, 2664 (2015).
75. A. Klug, *Angew, Chem. Int. Ed. Engl.* **22**, 565 (1983).
76. A. Klug, *Phil. Trans, R, Soc. Lond. B.* **354**, 531 (1999).
77. H. Fraenkel-Conrat, and R. C. Williams, *Proc. Natl. Acad. Sci. U. S. A.* **41**, 690 (1955).
78. M. Gellert, M. N. Lipsett, and D. R. Davies, *Proc. Natl. Acad. Sci. U. S. A.* **48**, 2013 (1962).
79. P. Tougard, J.-F. Chantot, and W. Guschlbauer, *Biochim. Biophys. Acta.* **308**, 9 (1973).
80. S. Arnott, R. Chandrasekaran, and C. M. Marttila, *Biochem. J.* **141**, 537 (1974).
81. S. B. Zimmerman, G. H. Cohen, and D. R. Davies, *J. Mol. Biol.* **92**, 181 (1975).
82. J. L. Sessler, M. Sathiosatham, K. Doerr, V. Lynch, and K. A. Abboud, *Angew. Chem. Int. Edit.* **39**, 1300 (2000).
83. G. P. Spada, A. Carcuro, F. P. Colonna, A. Garbesi, and G. Gottarelli, *Liq. Cryst.* **3**, 651 (1988).
84. P. Mariani, C. Mazabard, A. Garbesi, and G. P. Spada, *J. Am. Chem. Soc.* **111**, 6369 (1989).

85. S. Bonazzi, M. Capobianco, M. M. De Morais, A. Garbesi, G. Gottarelli, P. Mariani, M. G. Ponzi Bossi, G. P. Spada, and L. Tondelli, *J. Am. Chem. Soc.* **113**, 5809 (1991).
86. J. T. Davis, *Angew. Chem., Int. Ed.* **43**, 668 (2004).
87. J. T. Davis, and G. P. Spada, *Chem. Soc. Rev.* **36**, 296 (2007).
88. S. Lena, S. Masiero, S. Pieraccini, and G. P. Spada, *Chem.-Eur. J.* **15**, 7792 (2009).
89. L. Oganesian, and T. M. Bryan, *BioEssays* **29**, 155 (2007).
90. I. Bang, *Biochem. Z.* **26**, 293 (1910).
91. W. Guo, C.-H. Lu, R. Orbach, F. Wang, X.-J. Qi, A. Cecconello, D. Seliktar, and I. Willner, *Adv. Mater.* **27**, 73 (2015).
92. C. Wu, S. Wan, W. Hou, L. Zhang, J. Xu, C. Cui, Y. Wang, J. Hu, and W. Tan, *Chem. Commun.* **51**, 3723 (2015).
93. J. Li, L. Mo, C.-H. Lu, T. Fu, H.-H. Yang, and W. Tan, *Chem. Soc. Rev.* (2016).
94. S. Lena, G. Brancolini, G. Gottarelli, P. Mariani, S. Masiero, A. Venturini, V. Palermo, O. Pandoli, S. Pieraccini, P. Samorì, and G. P. Spada, *Chem. Eur. J.* **13**, 3757 (2007).
95. J. Lim, and O. S. Miljanic, *Crystengcomm.* **13**, 5309 (2011).
96. M. d. C. Rivera-Sánchez, I. Andújar-de-Sanctis, M. García-Arriaga, V. Gubala, G. Hobley, and J. M. Rivera, *J. Am. Chem. Soc.* **131**, 10403 (2009).
97. P. J. Bates, D. A. Laber, D. M. Miller, S. D. Thomas, and J. O. Trent, *Exp. Mol. Pathol.* **86**, 151 (2009).
98. M.-O. M. Piepenbrock, G. O. Lloyd, N. Clarke, and J. W. Steed, *Chem. Rev.* **110**, 1960 (2010).
99. S. D'Amico, G. Maruccio, P. Visconti, E. D'Amone, R. Cingolani, R. Rinaldi, S. Masiero, G. P. Spada, and G. Gottarelli, *Microelectr. J.* **34**, 961 (2003).
100. A. L. Webber, S. Masiero, S. Pieraccini, J. C. Burey, A. S. Tatton, D. Iuga, T. N. Pham, G. P. Spada, and S. P. Brown, *J. Am. Chem. Soc.* **133**, 19777 (2011).
101. G. M. Peters, L. P. Skala, T. N. Plank, B. J. Hyman, G. N. Manjunatha Reddy, A. Marsh, S. P. Brown, and J. T. Davis, *J. Am. Chem. Soc.* **136**, 12596 (2014).
102. G. M. Peters, L. P. Skala, T. N. Plank, H. Oh, G. N. Manjunatha Reddy, A. Marsh, S. P. Brown, S. R. Raghavan, and J. T. Davis, *J. Am. Chem. Soc.* (2015).
103. G. N. M. Reddy, D. S. Cook, D. Iuga, R. I. Walton, A. Marsh, and S. P. Brown, *Solid. State. Nucl. Mag.* **65**, 41 (2015).
104. G. N. M. Reddy, A. Marsh, J. T. Davis, S. Masiero, and S. P. Brown, *Cryst. Growth Des.* **15**, 5945 (2015).
105. A. Marsh, M. Silvestri, and J. M. Lehn, *Chem. Commun.*, 1527 (1996).
106. S. V. Kolotuchin, and S. C. Zimmerman, *J. Am. Chem. Soc.* **120**, 9092 (1998).
107. M. Mascal, N. M. Hext, R. Warmuth, J. R. Arnall-Culliford, M. H. Moore, and J. P. Turkenburg, *J. Org. Chem.* **64**, 8479 (1999).
108. H. Fenniri, P. Mathivanan, K. L. Vidale, D. M. Sherman, K. Hallenga, K. V. Wood, and J. G. Stowell, *J. Am. Chem. Soc.* **123**, 3854 (2001).
109. H. Fenniri, B.-L. Deng, and A. E. Ribbe, *J. Am. Chem. Soc.* **124**, 11064 (2002).
110. Y. Ma, S. V. Kolotuchin, and S. C. Zimmerman, *J. Am. Chem. Soc.* **124**, 13757 (2002).
111. H. Fenniri, B.-L. Deng, A. E. Ribbe, K. Hallenga, J. Jacob, and P. Thiyagarajan, *Proc. Natl. Acad. Sci. USA.* **99**, 6487 (2002).
112. J. G. Moralez, J. Raez, T. Yamazaki, R. K. Motkuri, A. Kovalenko, and H. Fenniri, *J. Am. Chem. Soc.* **127**, 8307 (2005).
113. M. Mascal, S. C. Farmer, and J. R. Arnall-Culliford, *J. Org. Chem.* **71**, 8146 (2006).
114. R. S. Johnson, T. Yamazaki, A. Kovalenko, and H. Fenniri, *J. Am. Chem. Soc.* **129**, 5735 (2007).
115. A. Asadi, B. O. Patrick, and D. M. Perrin, *J. Am. Chem. Soc.* **130**, 12860 (2008).
116. Y. Yang, M. Xue, J.-F. Xiang, and C.-F. Chen, *J. Am. Chem. Soc.* **131**, 12657 (2009).
117. S. C. Zimmerman, and B. F. Duerr, *J. Org. Chem.* **57**, 2215 (1992).
118. E. Boucher, M. Simard, and J. D. Wuest, *J. Org. Chem.* **60**, 1408 (1995).
119. S. C. Zimmerman, F. Zeng, D. E. C. Reichert, and S. V. Kolotuchin, *Science* **271**, 1095 (1996).
120. P. S. Corbin, L. J. Lawless, Z. Li, Y. Ma, M. J. Witmer, and S. C. Zimmerman, *Proc. Natl. Acad. Sci. USA.* **99**, 5099 (2002).

121. V. Percec, D. A. Wilson, P. Leowanawat, C. J. Wilson, A. D. Hughes, M. S. Kaucher, D. A. Hammer, D. H. Levine, A. J. Kim, F. S. Bates, K. P. Davis, T. P. Lodge, M. L. Klein, R. H. DeVane, E. Aqad, B. M. Rosen, A. O. Argintaru, M. J. Sienkowska, K. Rissanen, S. Nummelin, and J. Ropponen, *Science* **328**, 1009 (2010).
122. S. Zhang, H.-J. Sun, A. D. Hughes, B. Draghici, J. Lejnieks, P. Leowanawat, A. Bertin, L. Otero De Leon, O. V. Kulikov, Y. Chen, D. J. Pochan, P. A. Heiney, and V. Percec, *ACS Nano* **8**, 1554 (2014).
123. E. M. Todd, and S. C. Zimmerman, *J. Am. Chem. Soc.* **129**, 14534 (2007).
124. E. M. Todd, and S. C. Zimmerman, *Tetrahedron* **64**, 8558 (2008).
125. J. E. D. Davies, J. L. Atwood, and J. M. Lehn, *Comprehensive supramolecular chemistry. Volume 8, Physical methods in supramolecular chemistry.*; Pergamon: New York, 1996.
126. V. S. Reddy, S. K. Natchiar, P. L. Stewart, and G. R. Nemerow, *Science* **329**, 1071 (2010).
127. V. Zickermann, C. Wirth, H. Nasiri, K. Siegmund, H. Schwalbe, C. Hunte, and U. Brandt, *Science* **347**, 44 (2015).
128. G. R. Desiraju, *J. Am. Chem. Soc.* **135**, 9952 (2013).
129. G. M. J. Schmidt In *Pure Appl. Chem.*, 1971; Vol. 27, p 647.
130. M. Mammen, E. E. Simanek, and G. M. Whitesides, *J. Am. Chem. Soc.* **118**, 12614 (1996).
131. G. R. Desiraju, *Accounts. Chem. Res.* **35**, 565 (2002).
132. T. Steiner, *Angew. Chem., Int. Ed.* **41**, 48 (2002).
133. P. Metrangolo, H. Neukirch, T. Pilati, and G. Resnati, *Accounts. Chem. Res.* **38**, 386 (2005).
134. P. Metrangolo, F. Meyer, T. Pilati, G. Resnati, and G. Terraneo, *Angew. Chem. Int. Edit.* **47**, 6114 (2008).
135. J. C. Slater, and J. G. Kirkwood, *Phys. Rev.* **37**, 682 (1931).
136. H.-J. Schneider, *Angew. Chem. Int. Edit.* **48**, 3924 (2009).
137. C. A. Hunter, and J. K. M. Sanders, *J. Am. Chem. Soc.* **112**, 5525 (1990).
138. E. A. Meyer, R. K. Castellano, and F. Diederich, *Angew. Chem. Int. Edit.* **42**, 1210 (2003).
139. N. T. Southall, K. A. Dill, and A. D. J. Haymet, *J. Phys. Chem. B.* **106**, 2812 (2002).
140. E. Arunan, R. Desiraju Gautam, A. Klein Roger, J. Sadlej, S. Scheiner, I. Alkorta, C. Clary David, H. Crabtree Robert, J. Dannenberg Joseph, P. Hobza, G. Kjaergaard Henrik, C. Legon Anthony, B. Mennucci, and J. Nesbitt David In *Pure Appl. Chem.*, 2011; Vol. 83, p 1619.
141. E. Arunan, R. Desiraju Gautam, A. Klein Roger, J. Sadlej, S. Scheiner, I. Alkorta, C. Clary David, H. Crabtree Robert, J. Dannenberg Joseph, P. Hobza, G. Kjaergaard Henrik, C. Legon Anthony, B. Mennucci, and J. Nesbitt David In *Pure Appl. Chem.*, 2011; Vol. 83, p 1637.
142. J. P. Bradley, S. P. Velaga, O. N. Antzutkin, and S. P. Brown, *Cryst. Growth Des.* **11**, 3463 (2011).
143. M. R. Chierotti, and R. Gobetto, *Chem. Commun.*, 1621 (2008).
144. R. K. Harris, P. Jackson, L. H. Merwin, B. J. Say, and G. Hagele, *J. Chem. Soc. Faraday Trans.* **84**, 3649 (1988).
145. S. Sharif, D. Schagen, M. D. Toney, and H.-H. Limbach, *J. Am. Chem. Soc.* **129**, 4440 (2007).
146. D. Braga, E. Dichiarante, G. Palladino, F. Grepioni, M. R. Chierotti, R. Gobetto, and L. Pellegrino, *Crystengcomm.* **12**, 3534 (2010).
147. S. P. Brown, *Solid. State. Nucl. Mag.* **41**, 1 (2012).
148. R. K. Harris, P. Y. Ghi, R. B. Hammond, C.-Y. Ma, and K. J. Roberts, *Chem. Commun.*, 2834 (2003).
149. J. R. Yates, T. N. Pham, C. J. Pickard, F. Mauri, A. M. Amado, A. M. Gil, and S. P. Brown, *J. Am. Chem. Soc.* **127**, 10216 (2005).
150. J. Schmidt, A. Hoffmann, H. W. Spiess, and D. Sebastiani, *J. Phys. Chem. B.* **110**, 23204 (2006).
151. A.-C. Uldry, J. M. Griffin, J. R. Yates, M. Pérez-Torralba, M. D. Santa María, A. L. Webber, M. L. L. Beaumont, A. Samoson, R. M. Claramunt, C. J. Pickard, and S. P. Brown, *J. Am. Chem. Soc.* **130**, 945 (2008).
152. A. L. Webber, L. Emsley, R. M. Claramunt, and S. P. Brown, *J. Phys. Chem. A* **114**, 10435 (2010).
153. I. Marin-Montesinos, G. Mollica, M. Carravetta, A. Gansmüller, G. Pileio, M. Bechmann, A. Sebald, and M. H. Levitt, *Chem. Phys. Lett.* **432**, 572 (2006).

154. M. J. Bayro, M. Huber, R. Ramachandran, T. C. Davenport, B. H. Meier, M. Ernst, and R. G. Griffin, *J. Chem. Phys.* **130**, 114506 (2009).
155. C. J. Pickard, and F. Mauri, *Phys. Rev. B* **63**, 245101 (2001).
156. J. R. Yates, C. J. Pickard, and F. Mauri, *Phys. Rev. B* **76**, 024401 (2007).
157. R. K. Harris, P. Hodgkinson, C. J. Pickard, J. R. Yates, and V. Zorin, *Magn. Reson. Chem.* **45**, S174 (2007).
158. C. Bonhomme, C. Gervais, F. Babonneau, C. Coelho, F. Pourpoint, T. Azaïs, S. E. Ashbrook, J. M. Griffin, J. R. Yates, F. Mauri, and C. J. Pickard, *Chem. Rev.* **112**, 5733 (2012).
159. J. Clark Stewart, D. Segall Matthew, J. Pickard Chris, J. Hasnip Phil, I. J. Probert Matt, K. Refson, and C. Payne Mike In *Z. Kristall.*, 2005; Vol. 220, p 567.
160. J. P. Perdew, K. Burke, and M. Ernzerhof, *Phys. Rev. Lett.* **77**, 3865 (1996).
161. C. G. Van de Walle, and P. E. Blöchl, *Phys. Rev. B* **47**, 4244 (1993).
162. P. E. Blöchl, *Phys. Rev. B* **50**, 17953 (1994).
163. A. J. Robertson, M. K. Pandey, A. Marsh, Y. Nishiyama, and S. P. Brown, *J. Magn. Reson.* **260**, 89 (2015).
164. P. J. Hore, J. A. Jones, and S. Wimperis, *NMR, the toolkit*; Oxford University Press: Oxford ; New York, 2000.
165. M. J. Duer, *Introduction to solid-state NMR spectroscopy*; Blackwell: Oxford, UK ; Malden, MA, 2004.
166. J. Keeler, *Understanding NMR spectroscopy*; 2nd ed.; John Wiley and Sons: Chichester, U.K., 2010.
167. U. Haeberlen, *High resolution NMR in solids : selective averaging*; Academic Press: New York, 1976.
168. A. Samoson, E. Lippmaa, and A. Pines, *Mol. Phys.* **65**, 1013 (1988).
169. D. J. States, R. A. Haberkorn, and D. J. Ruben, *J. Magn. Reson.* **48**, 286 (1982).
170. A. E. Bennett, C. M. Rienstra, M. Auger, K. V. Lakshmi, and R. G. Griffin, *J. Chem. Phys.* **103**, 6951 (1995).
171. B. M. Fung, A. K. Khitrin, and K. Ermolaev, *J. Magn. Reson.* **142**, 97 (2000).
172. Z. Gan, and R. R. Ernst, *Solid. State. Nucl. Mag.* **8**, 153 (1997).
173. Y. Yu, and B. M. Fung, *J. Magn. Reson.* **130**, 317 (1998).
174. M. Edén, and M. H. Levitt, *J. Chem. Phys.* **111**, 1511 (1999).
175. K. Takegoshi, J. Mizokami, and T. Terao, *Chem. Phys. Lett.* **341**, 540 (2001).
176. J. R. Lewandowski, J. Sein, H. J. Sass, S. Grzesiek, M. Blackledge, and L. Emsley, *J. Am. Chem. Soc.* **132**, 8252 (2010).
177. A. Equbal, S. Paul, V. S. Mithu, P. K. Madhu, and N. C. Nielsen, *J. Magn. Reson.* **246**, 104 (2014).
178. A. Equbal, M. Bjerring, K. Sharma, P. K. Madhu, and N. C. Nielsen, *Chem. Phys. Lett.* **644**, 243 (2016).
179. A. Lesage, D. Sakellariou, S. Hediger, B. Elena, P. Charmont, S. Steuernagel, and L. Emsley, *J. Magn. Reson.* **163**, 105 (2003).
180. P. K. Madhu, *Solid. State. Nucl. Mag.* **35**, 2 (2009).
181. G. D. Paëpe, *Annu. Rev. Phys. Chem.* **63**, 661 (2012).
182. T. Gullion, and J. Schaefer, *J. Magn. Reson.* **81**, 196 (1989).
183. A. E. Bennett, R. G. Griffin, J. H. Ok, and S. Vega, *J. Chem. Phys.* **96**, 8624 (1992).
184. N. C. Nielsen, H. Bildso/e, H. J. Jakobsen, and M. H. Levitt, *J. Chem. Phys.* **101**, 1805 (1994).
185. Y. K. Lee, N. D. Kurur, M. Helmle, O. G. Johannessen, N. C. Nielsen, and M. H. Levitt, *Chem. Phys. Lett.* **242**, 304 (1995).
186. M. H. Levitt In *eMagRes*; John Wiley & Sons, Ltd, 2007.
187. G. Metz, X. L. Wu, and S. O. Smith, *J. Magn. Reson., Ser. A* **110**, 219 (1994).
188. S. P. Brown, *Prog. Nucl. Magn. Reson. Spectrosc.* **50**, 199 (2007).
189. I. Schnell, and H. W. Spiess, *J. Magn. Reson.* **151**, 153 (2001).
190. S. Hafner, and H. W. Spiess, *Concepts Magn. Resonance* **10**, 99 (1998).
191. M. Feike, R. Graf, I. Schnell, C. Jäger, and H. W. Spiess, *J. Am. Chem. Soc.* **118**, 9631 (1996).
192. W. A. Dollase, M. Feike, H. Förster, T. Schaller, I. Schnell, A. Sebald, and S. Steuernagel, *J. Am. Chem. Soc.* **119**, 3807 (1997).

193. M. Feike, D. E. Demco, R. Graf, J. Gottwald, S. Hafner, and H. W. Spiess, *J. Magn. Reson., Ser. A* **122**, 214 (1996).
194. J. P. Bradley, C. Tripon, C. Filip, and S. P. Brown, *Phys. Chem. Chem. Phys.* **11**, 6941 (2009).
195. C. A. Fyfe, K. C. Wongmoon, Y. Huang, and H. Grondey, *J. Am. Chem. Soc.* **117**, 10397 (1995).
196. B. Elena, A. Lesage, S. Steuernagel, A. Bockmann, and L. Emsley, *J. Am. Chem. Soc.* **127**, 17296 (2005).
197. G. A. Morris, and R. Freeman, *J. Am. Chem. Soc.* **101**, 760 (1979).
198. D. P. Burum, and R. R. Ernst, *J. Magn. Reson.* **39**, 163 (1980).
199. O. W. Sørensen, and R. R. Ernst, *J. Magn. Reson.* **51**, 477 (1983).
200. A. S. Tatton, I. Frantsuzov, S. P. Brown, and P. Hodgkinson, *J. Chem. Phys.* **136**, 084503 (2012).
201. A. S. Tatton, J. P. Bradley, D. Iuga, and S. P. Brown, *Z. Phys. Chemie-Int. J. Res. Phys. Chem. Chem. Phys.* **226**, 1187 (2012).
202. A. S. Tatton, T. N. Pham, F. G. Vogt, D. Iuga, A. J. Edwards, and S. P. Brown, *Mol. Pharmaceut.* **10**, 999 (2013).
203. Z. Gan, *J. Am. Chem. Soc.* **128**, 6040 (2006).
204. S. Cavadini, S. Antonijevic, A. Lupulescu, and G. Bodenhausen, *J. Magn. Reson.* **182**, 168 (2006).
205. S. Cavadini, S. Antonijevic, A. Lupulescu, and G. Bodenhausen, *Chem. Phys. Chem* **8**, 1363 (2007).
206. T. G. Oas, R. G. Griffin, and M. H. Levitt, *J. Chem. Phys.* **89**, 692 (1988).
207. Z. Gan, J. P. Amoureux, and J. Trébosc, *Chem. Phys. Lett.* **435**, 163 (2007).
208. A. Brinkmann, and A. P. M. Kentgens, *J. Am. Chem. Soc.* **128**, 14758 (2006).
209. Y. Nishiyama, Y. Endo, T. Nemoto, H. Utsumi, K. Yamauchi, K. Hioka, and T. Asakura, *J. Magn. Reson.* **208**, 44 (2011).
210. M. K. Pandey, H. Kato, Y. Ishii, and Y. Nishiyama, *Phys. Chem. Chem. Phys.* **18**, 6209 (2016).
211. C. R. Morcombe, and K. W. Zilm, *J. Magn. Reson.* **162**, 479 (2003).
212. S. Hayashi, and K. Hayamizu, *Bull. Chem. Soc. Jpn.* **64**, 685 (1991).
213. S. Hayashi, and K. Hayamizu, *Bull. Chem. Soc. Jpn.* **64**, 688 (1991).
214. K. Harris Robin, D. Becker Edwin, M. Cabral de Menezes Sonia, P. Granger, E. Hoffman Roy, and W. Zilm Kurt In *Pure Appl. Chem.*, 2008; Vol. 80, p 59.
215. G. E. Martin, and C. E. Hadden, *J. Nat. Prod.* **63**, 543 (2000).
216. A. Tkatchenko, and M. Scheffler, *Phys. Rev. Lett.* **102**, 073005 (2009).
217. D. Vanderbilt, *Phys. Rev. B* **41**, 7892 (1990).
218. P. Basu, and S. J. N. Burgmayer, *Coord. Chem. Rev.* **255**, 1016 (2011).
219. T. Kato, T. Yasuda, Y. Kamikawa, and M. Yoshio, *Chem. Commun.*, 729 (2009).
220. E. C. Taylor, and C.-M. Yoon, *Synth. Commun.* **18**, 1187 (1988).
221. E. C. Taylor, and G. S. K. Wong, *J. Org. Chem.* **54**, 3618 (1989).
222. E. C. Taylor, C.-m. Yoon, and J. M. Hamby, *J. Org. Chem.* **59**, 7092 (1994).
223. E. C. Taylor, and C.-m. Yoon, *J. Org. Chem.* **59**, 7096 (1994).
224. H. Fenniri, G. A. Tikhomirov, D. H. Brouwer, S. Bouatra, M. El Bakkari, Z. Yan, J.-Y. Cho, and T. Yamazaki, *J. Am. Chem. Soc.* **138**, 6115 (2016).
225. A. Marsh, N. W. Alcock, W. Errington, and R. Sagar, *Tetrahedron* **59**, 5595 (2003).
226. M.-Q. Zhao, Q. Zhang, G.-L. Tian, and F. Wei, *Nanoscale* **6**, 9339 (2014).
227. K. Cahill, *Phys. Rev. E* **72**, 062901 (2005).
228. D. Pijper, and B. L. Feringa, *Soft Matter* **4**, 1349 (2008).
229. I. Hisaki, T. Sasaki, N. Tohnai, and M. Miyata, *Chem. Eur. J.* **18**, 10066 (2012).
230. C. C. Lee, C. Grenier, E. W. Meijer, and A. P. H. J. Schenning, *Chem. Soc. Rev.* **38**, 671 (2009).
231. P. Pescador, N. Brodersen, H. A. Scheidt, M. Loew, G. Holland, N. Bannert, J. Liebscher, A. Herrmann, D. Huster, and A. Arbuzova, *Chem. Commun.* **46**, 5358 (2010).
232. D. S. Su, *Angew. Chem. Int. Edit.* **50**, 4747 (2011).
233. M. Yang, and N. A. Kotov, *J. Mater. Chem.* **21**, 6775 (2011).
234. V. Allain, C. Bourgaux, and P. Couvreur, *Nucleic Acids Res.* **40**, 1891 (2012).
235. J. Tian, L. Jing, L. Ji, C. Zhang, Q. Liu, and X. Zhang, *RSC Adv.*, **3**, 22461 (2013).

236. A. Ciesielski, P. J. Szabelski, W. Rżysko, A. Cadeddu, T. R. Cook, P. J. Stang, and P. Samorì, *J. Am. Chem. Soc.* **135**, 6942 (2013).
237. S. Ahmed, J. H. Mondal, N. Behera, and D. Das, *Langmuir* **29**, 14274 (2013).
238. T. G. Barclay, K. Constantopoulos, and J. Matisons, *Chem. Rev.* **114**, 10217 (2014).
239. Z. Liu, G. Liu, Y. Wu, D. Cao, J. Sun, S. T. Schneebeli, M. S. Nassar, C. A. Mirkin, and J. F. Stoddart, *J. Am. Chem. Soc.* **136**, 16651 (2014).
240. S. Yagai, M. Suzuki, X. Lin, M. Gushiken, T. Noguchi, T. Karatsu, A. Kitamura, A. Saeki, S. Seki, Y. Kikkawa, Y. Tani, and K.-i. Nakayama, *Chem. Eur. J.* **20**, 16128 (2014).
241. F. Shayeganfar, *J. Phys.: Condens. Matter* **26**, 435305 (2014).
242. M. Ramaekers, I. de Feijter, P. H. H. Bomans, N. A. J. M. Sommerdijk, P. Y. W. Dankers, and E. W. Meijer, *Macromolecules* **47**, 3823 (2014).
243. S.-X. Fa, X.-F. Chen, S. Yang, D.-X. Wang, L. Zhao, E.-Q. Chen, and M.-X. Wang, *Chem. Commun.* **51**, 5112 (2015).
244. T. Nakamura, H. Kimura, T. Okuhara, M. Yamamura, and T. Nabeshima, *J. Am. Chem. Soc.* **138**, 794 (2016).
245. A. R. Hirst, B. Escuder, J. F. Miravet, and D. K. Smith, *Angew. Chem. Int. Edit.* **47**, 8002 (2008).
246. Y. Wu, K. Liu, X. Chen, Y. Chen, S. Zhang, J. Peng, and Y. Fang, *New J. Chem.* **39**, 639 (2015).
247. S. Datta, and S. Bhattacharya, *Soft Matter* **11**, 1945 (2015).
248. J. L. Sessler, C. M. Lawrence, and J. Jayawickramarajah, *Chem. Soc. Rev.* **36**, 314 (2007).
249. E. A. Tanifum, A. Y. Kots, B.-K. Choi, F. Murad, and S. R. Gilbertson, *Bioorg. Med. Chem. Lett.* **19**, 3067 (2009).
250. A. Basiri, V. Murugaiyah, H. Osman, R. S. Kumar, Y. Kia, and M. A. Ali, *Bioorg. Med. Chem.* **21**, 3022 (2013).
251. R. Nakashima, K. Sakurai, S. Yamasaki, K. Hayashi, C. Nagata, K. Hoshino, Y. Onodera, K. Nishino, and A. Yamaguchi, *Nature* **500**, 102 (2013).
252. F. Buron, J. Y. Mérour, M. Akssira, G. Guillaumet, and S. Routier, *Eur. J. Med. Chem.* **95**, 76 (2015).
253. H. Sjuts, A. V. Vargiu, S. M. Kwasny, S. T. Nguyen, H.-S. Kim, X. Ding, A. R. Ornik, P. Ruggerone, T. L. Bowlin, H. Nikaido, K. M. Pos, and T. J. Opperman, *Proc. Natl. Acad. Sci. USA.* **113**, 3509 (2016).
254. R. Kaur, P. Kaur, S. Sharma, G. Singh, S. Mehndiratta, P. M.S. Bedi, and K. Nepali, *Recent Patents on Anti-Cancer Drug Discovery* **10**, 23 (2015).
255. S. Ravez, O. Castillo-Aguilera, P. Depreux, and L. Goossens, *Expert Opinion on Therapeutic Patents* **25**, 789 (2015).
256. A. Durmus, G. Gunbas, S. C. Farmer, M. M. Olmstead, M. Mascal, B. Legese, J.-Y. Cho, R. L. Beingessner, T. Yamazaki, and H. Fenniri, *J. Org. Chem.* **78**, 11421 (2013).
257. V. R. R. Marthala, Y. Jiang, J. Huang, W. Wang, R. Gläser, and M. Hunger, *J. Am. Chem. Soc.* **128**, 14812 (2006).
258. A. B. Fernandez, I. Lezcano-Gonzalez, M. Boronat, T. Blasco, and A. Corma, *Phys. Chem. Chem. Phys.* **11**, 5134 (2009).
259. C. A. Hunter, *Angew. Chem. Int. Edit.* **43**, 5310 (2004).
260. H. Fenniri, G. A. Tikhomirov, D. H. Brouwer, S. Bouatra, M. El Bakkari, Z. Yan, J.-Y. Cho, and T. Yamazaki, *J. Am. Chem. Soc.*, 6115 (2016).
261. J. Granwehr, *Appl. Magn. Reson.* **32**, 113 (2007).
262. A. Gibbs, G. A. Morris, A. G. Swanson, and D. Cowburn, *J. Magn. Reson., Ser. A* **101**, 351 (1993).
263. C. Brissac, T. Malliavin, and M. Delsuc, *J. Biomol. NMR* **6**, 361 (1995).
264. S. Poulding, A. J. Charlton, J. Donarski, and J. C. Wilson, *J. Magn. Reson.* **189**, 190 (2007).
265. G. Bodenhausen, R. Freeman, and G. A. Morris, *J. Magn. Reson.* **23**, 171 (1976).
266. G. A. Morris, and R. Freeman, *J. Magn. Reson.* **29**, 433 (1978).
267. R. Freeman, *Chem. Rev.* **91**, 1397 (1991).
268. M. Piotto, V. Saudek, and V. Sklenář, *J. Biomol. NMR* **2**, 661 (1992).
269. V. Chevelkov, B. J. van Rossum, F. Castellani, K. Rehbein, A. Diehl, M. Hohwy, S. Steuernagel, F. Engelke, H. Oschkinat, and B. Reif, *J. Am. Chem. Soc.* **125**, 7788 (2003).

270. E. K. Paulson, C. R. Morcombe, V. Gaponenko, B. Dancheck, R. A. Byrd, and K. W. Zilm, *J. Am. Chem. Soc.* **125**, 15831 (2003).
271. D. H. Zhou, and C. M. Rienstra, *J. Magn. Reson.* **192**, 167 (2008).
272. J. R. Lewandowski, J.-N. Dumez, Ü. Akbey, S. Lange, L. Emsley, and H. Oschkinat, *J. Phys. Chem. Lett.* **2**, 2205 (2011).
273. I. Fischbach, K. Thieme, A. Hoffmann, M. Hehn, and I. Schnell, *J. Magn. Reson.* **165**, 102 (2003).
274. T. Torring, N. V. Voigt, J. Nangreave, H. Yan, and K. V. Gothelf, *Chem. Soc. Rev.* **40**, 5636 (2011).
275. J. Shimada, T. Maruyama, M. Kitaoka, H. Yoshinaga, K. Nakano, N. Kamiya, and M. Goto, *Chem. Commun.* **48**, 6226 (2012).
276. A. Kuzyk, R. Schreiber, Z. Fan, G. Pardatscher, E.-M. Roller, A. Hogele, F. C. Simmel, A. O. Govorov, and T. Liedl, *Nature* **483**, 311 (2012).
277. Y. Zhang, F. Lu, K. G. Yager, D. van der Lelie, and O. Gang, *Nat Nano* **8**, 865 (2013).
278. S. K. Albert, H. V. P. Thelu, M. Golla, N. Krishnan, S. Chaudhary, and R. Varghese, *Angew. Chem. Int. Edit.* **53**, 8352 (2014).
279. C. Tian, X. Li, Z. Liu, W. Jiang, G. Wang, and C. Mao, *Angew. Chem.* **126**, 8179 (2014).
280. Y. Li, Z. Liu, G. Yu, W. Jiang, and C. Mao, *J. Am. Chem. Soc.* **137**, 4320 (2015).
281. L. Cademartiri, and K. J. M. Bishop, *Nat. Mater.* **14**, 2 (2015).
282. J. Li, C. Zheng, S. Cansiz, C. Wu, J. Xu, C. Cui, Y. Liu, W. Hou, Y. Wang, L. Zhang, I. t. Teng, H.-H. Yang, and W. Tan, *J. Am. Chem. Soc.* **137**, 1412 (2015).
283. M. Cutajar, M. H. Lewis, and S. Wimperis, *Chem. Phys. Lett.* **449**, 86 (2007).
284. J. J. Kweon, R. Fu, J. A. Kitchen, P. L. Gor'kov, W. W. Brey, and N. S. Dalal, *J. Phys. Chem. B.* **119**, 5013 (2015).
285. Y. Ishii, J. P. Yesinowski, and R. Tycko, *J. Am. Chem. Soc.* **123**, 2921 (2001).
286. J.-N. Dumez, M. C. Butler, and L. Emsley, *J. Chem. Phys.* **133**, 224501 (2010).
287. L. Emsley, I. Burghardt, and G. Bodenhausen, *J. Magn. Reson.* **90**, 214 (1990).
288. X. Miao, and R. Freeman, *J. Magn. Reson., Ser. A* **119**, 90 (1996).
289. S. Cadars, A. Lesage, N. Hedin, B. F. Chmelka, and L. Emsley, *J. Phys. Chem. B.* **110**, 16982 (2006).
290. G. Pileio, S. Mamone, G. Mollica, I. M. Montesinos, A. Gansmüller, M. Carravetta, S. P. Brown, and M. H. Levitt, *Chem. Phys. Lett.* **456**, 116 (2008).
291. S. E. Ashbrook, and D. McKay, *Chem. Commun.* **52**, 7186 (2016).